Fuel Pyrolysis at Atmospheric and Elevated Pressure Conditions in Micro-Flow Tube Reactor

A Dissertation

Presented to
the faculty of the School of Engineering and Applied Science
University of Virginia

in partial fulfillment
of the requirements for the degree

Doctor of Philosophy

by

Ujuma Shrestha

May

2017

APPROVAL SHEET

The dissertation
is submitted in partial fulfillment of the requirements
for the degree of
Doctor of Philosophy

AUTHOR

The dissertation has been read and approved by the examining committee:

Harsha K. Chelliah
Advisor

Gabriel Laufer

Christopher Goyne

Haibo Dong

Robert Davis

Accepted for the School of Engineering and Applied Science:

Craig H. Benson, Dean, School of Engineering and Applied Science

May
2017

Abstract

Improved efficiency and reduced emissions are essential elements of more sustainable propulsion systems. In addition to providing energy, the fuel in propulsion systems can be also used as coolant for critical engine components. Both the choice of fuel and understanding the fuel pyrolysis and oxidation behavior is critical for design of future propulsion systems. Specifically, well validated chemical kinetic models are needed in designing such systems. A fundamental approach in developing detailed chemical kinetic models is to start with the simplest fuel molecule and progressively increase the complexity of the molecular structure. Unfortunately, real fuels, and jet fuels in particular, consist of hundreds of hydrocarbon species and therefore the development of appropriate chemical kinetic models is challenging. As part of development of chemical kinetic models for these complex fuels, several surrogate models have been identified in order to simplify the modelling effort. Despite the fact that the surrogate reaction models represent a major simplification, they are still too large and require further simplification before implementation in computational simulation of propulsion systems.

The present research work aims at solving this problem by decoupling the fuel pyrolysis and oxidation processes. The idea of semi-global model with a fast-thermal pyrolysis of large fuel molecules, in combination with more detailed H_2/C_1-C_4 base model, is considered. The work described here is mainly focused on the experimental aspects of fuel decomposition into H_2 and C_1- C_4 species. For this purpose, a novel micro flow tube reactor (MFTR) with a small mixing volume was designed and developed. Extensive investigations were performed to better understand the uncertainties associated with characterization of temperature of the reactor and reactant composition. In particular, traditional reactor temperature measurements by thermocouples were verified by chemical thermometry concept. The fidelity of the reactor was tested by conducting pyrolysis experiments with better understood fuel molecules such as ethane and n-butane. A range of temperatures (950-1100 K), pressures (1-15 atm) and residence times (10- 590 ms) was explored and the experimental results were compared with several predictive models available in the literature as well as experimental data. A key finding is that experimental speciation data generated by MFTR has a much lower uncertainty compared with current model uncertainty. This implies that the MFTR can be a valuable tool in developing accurate chemical kinetic models.

The experimental work was also extended to homogeneous pyrolysis studies of large hydrocarbon fuels such as n-dodecane and JP-8 for a range of temperatures and residence times. Similar to small hydrocarbon fuels, the pyrolysis results were compared with available chemical kinetic models. Additionally, a one-step fast thermal pyrolysis model for JP-8 was also developed based on present experimental results. The model was able to capture most of the key species from the experiments. Finally, homogeneous and heterogeneous catalytic pyrolysis studies of JP-10 were conducted to explore the applicability of reactor to conduct heterogeneous pyrolysis studies in cooling channels of hypersonic engines. The results indicated almost 200 K shift in fuel pyrolysis temperature which can lead to enhance cooling capacity due to endothermicity of pyrolysis process.

Acknowledgements

Firstly, I would like to express my sincere gratitude to my advisor, Prof. Harsha Chelliah for his immense support during the entire course of my graduate school and research work at the University of Virginia. His guidance has always helped me to progress as an independent researcher and without his continuous motivation and enthusiasm, the present work could not have been fulfilled.

I would also like to thank my committee members, Prof. Gabriel Laufer, Prof. Christopher Goyne, Prof. Robert Davis and Prof. Haibo Dong for their guidance, time and critical suggestions.

I am very grateful to Dr. Gaetano Esposito, Dr. Ryan Johnson and Dr. Chowdhury Moniruzzaman for their help and guidance and in particular Dr. Brendyn Sarnacki for providing me proper guidance and support in the lab. I would like to thank my fellow lab-mates Gregory Simms, Dr. Mohammad Rahimi and Khanh Dang for their contribution in experimental and modelling work with the tube reactor and also for all the suggestions they provided to solve various research problems. I would like to acknowledge Ben Huang and Jiahan Xie for their help in preparing the catalytic coated rods for conducting heterogeneous pyrolysis experiments. I am very grateful to Paul Macek from Shimadzu Corporation for his guidance and assistance in learning and troubleshooting GC/GC-MS. I would also like to thank all my other colleagues and friends for their contribution to my intellectual growth during the course of my graduate school and especially Poojan Pyakurel for her help with liquid sample preparation for GC-MS.

Finally, I would like to thank my family for always supporting and encouraging me to pursue my academic goals. They have always helped me find my potential in research or

any other field in general. And most of all my loving husband Dr. Jatin M. Amatya for his enormous support through my undergraduate and graduate degrees.

List of Figures

List of Tables

List of Terms and Symbols

Y_k: Mass fraction of species "k"

MW_{mix}: Mixture molecular weight

AAFRF: Assured aerospace fuel research facility

ATJ: Alcohol-to-jet

C_{pk}: Heat capacity at constant pressure

CFD: Computational fluid dynamics

DAQ: Data aquisition

E_a: Activation energy

FID: Flame ionization detector

GC: Gas chromatography

HC: Hydrocarbon

HF: Hydrofluoric acid

id: Internal diameter

INJ: Injection ports

K: Degree Kelvin

MFTR: Micro-flow tube reactor

MS: Mass spectrometer

NJFCP: National jet fuel combustion program

PAH: Poly aromatic hydrocarbon

PID: Proportional-integral-derivative

$\dot{Q}_{sink}$: Heat sink

R: Specific gas constant

R^o: Universal gas constant

SSR: Solid state relays

t: Residence time

T: Temperature

TCD: Thermal conductivity detector

TMB: Trimethylbenzene

UHP: Ultra-high purity

v: Specific volume

VPFR: Variable pressure flow reactor

W_k: Molecular weight of species "k"

X_k: Mole fraction of species "k"

Δh_{sens}: Sensible heat

φ: Equivalence ratio

$\dot{\omega}_k$: Net chemical production rate

CPD : Cyclopentadiene

Table of Contents

Chapter 1: Introduction

1.1 Motivation

Liquid petroleum-based fuels are the major source of energy driving the aviation industry. Based on the energy consumption by sectors, 2.97 % energy consumption in 2013 is attributed to Jet fuel which is projected to be increased up to 3.79 % by 2040 [1]. Even though these petroleum fuels are limited, projections and historical trends suggest liquid fuels will continue to be a primary source of energy worldwide, see Figure 1.1. The combination of computational fluid dynamics with detailed chemical kinetic models provides a medium to optimize engine performance, explore the variability in pollutants and variability in performance with different fuels at a fundamental level [2]. With regard to these critical factors, the motivation for the current work is described in detail in the following sections.

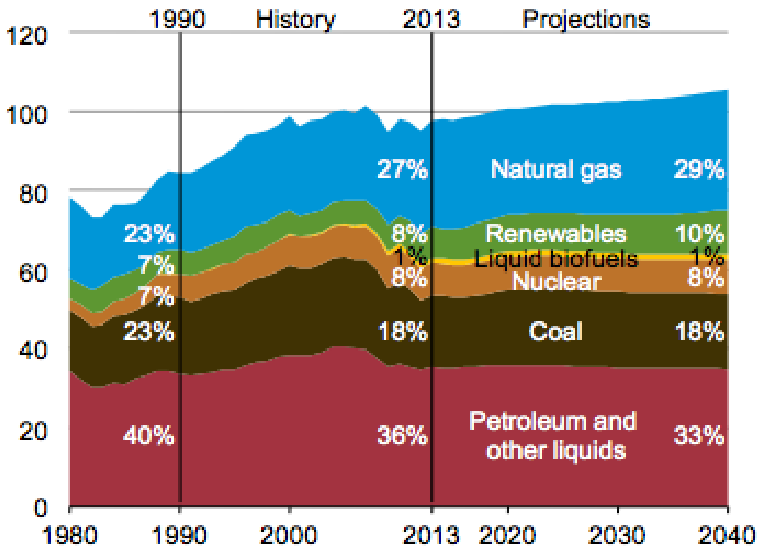

Figure 1.1: Primary energy consumption by fuel type 1980-2040 (quadrillion Btu) [1].

1.1.1 Endothermic Heat Sink

The fuel in propulsion systems can satisfy two purposes. In addition to providing energy for propulsion, the fuel can also be used as a coolant for critical engine components. The components of hypersonic vehicles are exposed to very high temperature (as high as 4950K) and no material can withstand such a high thermal load [3], [4]. Cryogenic fuel such as methane and liquid hydrogen can be used to mitigate the thermal load. However, due to their lower density, they need larger storage and further, there are safety and cost effectiveness issues [5]. One of the approaches of cooling the hot components of hypersonic vehicles and also gas turbine engines is using the high-energy density jet fuel prior to being injected into the combustor as shown in Figure 1.2. In hypersonic vehicles, fuel is sent through the cooling channel in counter-flow direction to the exhaust gases whereas in gas turbine engines, fuel can be passed through the heat exchanger to cool the compressed air and further the air can cool the turbine blades. The decomposition of hydrocarbon (HC) fuel needs energy and is an endothermic reaction. The fuel then acts as

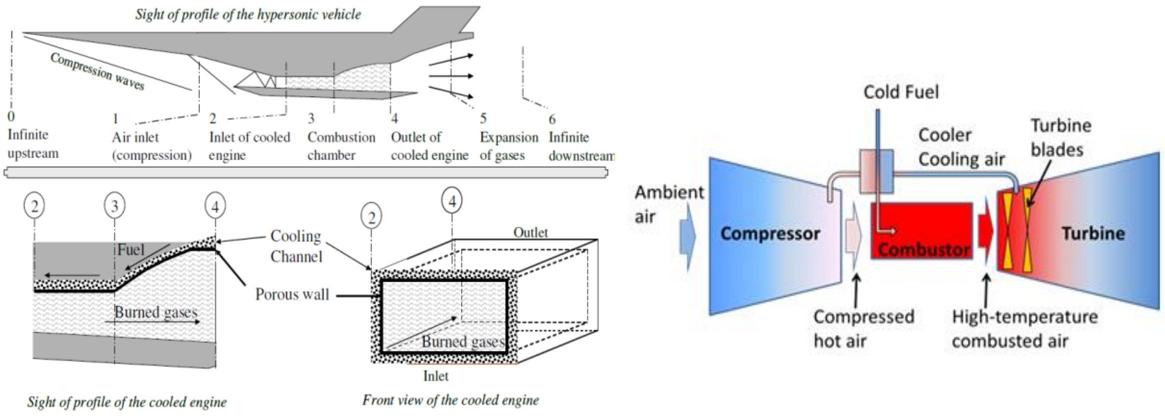

(a) **(b)**

Figure 1.2: Schematic of endothermic cooling using jet fuel as a coolant (a) hypersonic vehicle [4] (b) Gas turbine engine.

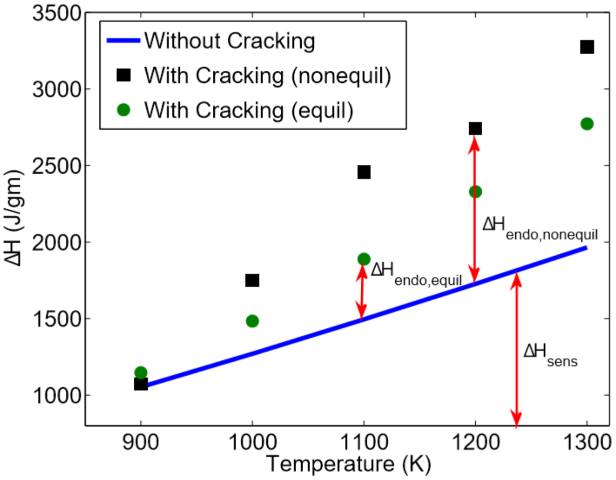

Figure 1.3: Heat Sink in equilibrium and non-equilibrium condition for n-dodecane pyrolysis at different temperature [7].

a heat sink with high cooling potential due to the combination of sensible and chemical enthalpy. This chemical enthalpy is also termed as chemical heat absorption [6]. While the sensible heat increases with increase in temperature, the total heat sink for a particular temperature is higher for non-equilibrium decomposition than at equilibrium. The reason for this is increased chemical heat sink at non equilibrium condition than at equilibrium condition, See Figure 1.3 [7].

The chemical heat absorption or endothermic heat sink is given by [8]

$$\Delta h_{endo} = \frac{\dot{Q}_{sink}}{\dot{m}} - \Delta h_{sens} \ , \qquad (1\text{-}1)$$

Where, the sensible heat Δh_{sens} is a function of specific heat capacity at constant pressure (C_{pk}) and given by

$$\Delta h_{sens} = \int_{T_{inlet}}^{T_{exit}} C_{pk} \, dT \ , \qquad (1\text{-}2)$$

and the total heat sink $\dot{Q}_{sink}$ is the difference between inlet and outlet enthalpies

$$\frac{\dot{Q}_{sink}}{\dot{m}} = h_{exit} - h_{inlet} \ , \tag{1- 3}$$

Here, h_{exit} depends on the product mole fraction (X_k) and enthalpies (h_k) given by

$$h_{exit} = \sum h_k X_k \ , \tag{1- 4}$$

Thus, endothermicity of fuel significantly depends on the product composition and their enthalpies

The typical temperature range in which the fuel starts decomposing is around 700-900 K depending upon the fuel type and residence time. At these temperatures, the cooling capacity of fuel is limited by coke deposition in the cooling channels. The initial building blocks to coke deposition in these cooling channels are regarded as the poly aromatic hydrocarbon (PAH) molecules (See Section 1.1.2 for details in pathway to coke deposition/soot formation). Thus, the maximum heat sink potential can only be utilized by the formation of smaller HC molecules over PAH ring structures [5] [3]. This process can also be enhanced by thermal decomposition of fuel over a catalyst which helps in improving the selectivity of preferred products. Further, integration of active cooling system converts high energy density HC fuel into light molecules such as H_2 and C_2H_4 which leads to short ignition delay times. Thus, the catalytic decomposition can be particularly important for the capability to select the product distribution for shorter ignition delay times and lower emissions [4], [6], [9].

In general, the sensible heat sink can be utilized to cool supersonic air flights and in addition to sensible heat, chemical heat absorption with catalyst can be applicable for hypersonic application [8].

1.1.2 Fuel Pyrolysis Pathways and Soot Precursors

The use of fuels is associated with emissions such as carbon dioxide (CO_2), carbon monoxide (CO), nitrogen oxides (NO_x), sulphur oxides (SO_x), hydrocarbons (HCs) and soot, see Figure 1.4 . Studies have linked these emissions to adverse impact on human health as well as global and local environment [10]–[13]. The emission of soot particles which are formed due to incomplete combustion of fuel results in seeding contrail and cirrus clouds. These clouds are responsible for trapping the radiation from earth and contributes to the greenhouse effect [14]. Further, when fuel is used as heat sink as described in Section 1.1.1, coke deposition in cooling channel can lead to serious problems. Therefore, it is critical to understand pathway to soot formation/coke-deposition in fundamental level

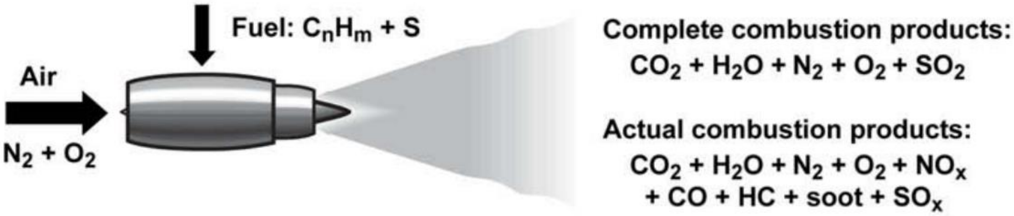

Figure 1.4: Aircraft emissions with ideal/complete and actual combustion [10].

Soot particles are identified as nearly spherical primary particles which have a mean diameter of 2 nm and higher. Soot formation is a combination of complex chemical and physical processes. While the dominant pathway for soot formation varies with fuel composition, the basic model for all fuels include decomposition of fuel molecules into smaller components, formation of molecular soot precursors/smaller aromatics, formation of larger aromatic ring structures, nucleation of soot particles from larger PAH followed by the formation of larger soot particles, see Figure 1.5 (a) [15][16]. Among these steps, the fuel decomposition and formation of smaller soot precursors are the rate limiting steps and play a significant role in soot formation [7] [18].

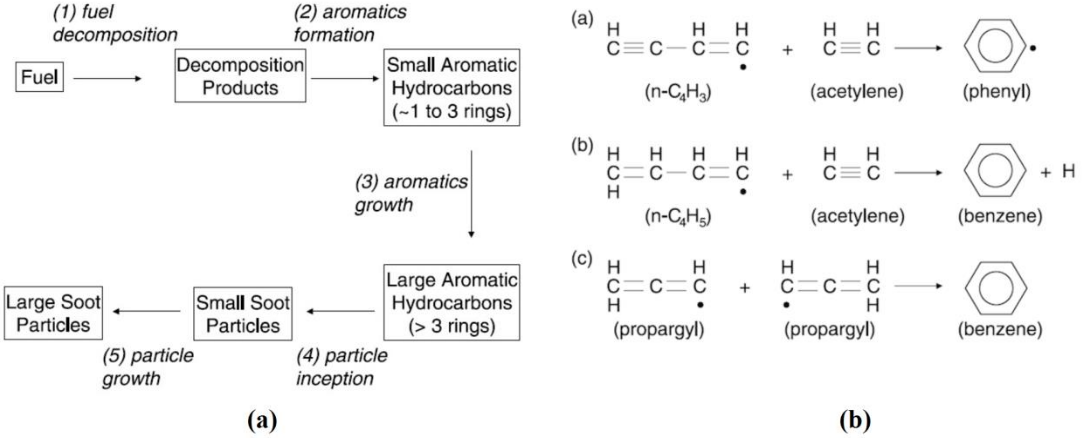

Figure 1.5: (a) Pathway to soot formation (b) Important reactions leading to formation of single ring aromatic hydrocarbons [17].

Several studies have suggested reactions leading to the formation of first aromatic ring which in turn leads to soot particle formation [15][19][20]. Some of these reactions are depicted in Figure 1.5 (b), which includes acetylene as one of the most important soot precursors leading to carbon addition. Also, the recombination reaction of propargyl radical to form benzene is considered to be an important step to the formation of benzene ring in flames. In the other hand, species such as allene and propyne are considered to be a major source of the propargyl radical. Figure 1.6 shows some of the key reactions of allene and propyne leading to formation of propargyl radical. Thus, species such as allene, propyne and also 1,3 butadiene play an important role in soot growth pathways [20]–[22]. These species, along with key intermediate species such as ethylene, ethane and methane are of great interest in development of reaction models defining soot formation.

$$aC_3H_4 + H = C_3H_3 + H_2$$

$$pC_3H_4 + H = C_3H_3 + H_2$$

$$pC_3H_4 + CH_3 = C_3H_3 + CH_4$$

$$pC_3H_4 + C_2H = C_3H_3 + C_2H_2$$

$$pC_3H_4 + C_2H_3 = C_3H_3 + C_2H_4$$

$$pC_3H_4 + C_2H_5 = C_3H_3 + C_2H_6$$

Figure 1.6: Reactions showing formation of propargyl radical from allene (aC_3H_4) and propyne (pC_3H_4) by addition of H-atom [21], [22]

In general, the detailed kinetic model of soot formation comprises of two parts: a gas phase chemistry model and a soot particle dynamic model. The accuracy of particle dynamic model depends on the preciseness of gas phase chemistry [18]. Since fuel decomposition and formation of molecular soot precursors are considered to be critical steps in overall process of soot formation, the current research work is largely focused on the process of fuel decomposition model.

1.1.3 Chemical Kinetic Models

While improved efficiency and reduced emissions are essential elements of more sustainable liquid fuel propulsion system, challenges exist is development of their reaction models. Commercial and military aviation fuels are complex mixtures of hundreds of HCs derived from the distillation of petroleum crude oil. Further, composition of these fuels can vary from batch to batch depending upon the crude oil and the processes involved.

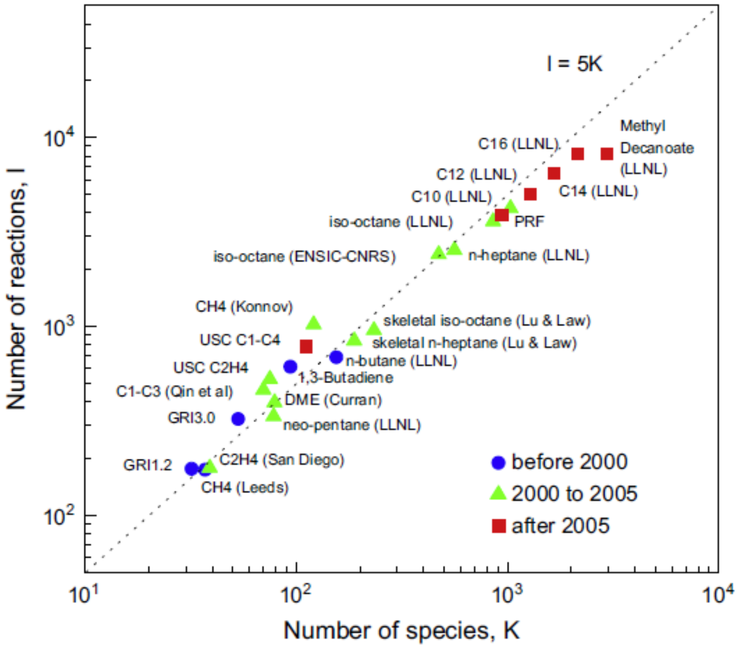

Figure 1.7: Number of species and reactions in published models [126].

As an ensemble of hundreds of HCs consisting mainly n-paraffins, isoparaffins, cycloparaffins and aromatics, a reactive system utilizing these fuels may have a huge number of additional (stable and radical) species involved in thousands of elementary reactions [23]. If a detailed chemical kinetic model for such fuels can be constructed, combustion product yields from these fuels at different conditions can be predicted by coupling Computational Fluid Dynamics (CFD) with combination with the detailed kinetic model. A fundamental way to develop a detailed reaction model of any fuel is to start with the simplest molecule and progressively add more complex ones. However, such a process consists of huge number of species and reaction and complicated to develop. The accuracy of calculation using such model depends on the accuracy of every step of the reaction model.

Figure 1.7 shows (from a review article by Law and Lu [24]) the number of reactions with respect to number of species in various published reaction models. It can be seen from the plot that for smaller HC molecules such as CH_4 and C_2H_6, the number of species and reactions are small. However, the number of species and thus reactions increases to thousands as the size of fuel molecule increases. Each reaction in a reaction model is represented by reaction rate in Arrhenius or modified Arrhenius form, with collision frequency and activation energy. It is extremely hard to obtain the rate constants of every reaction accurately. In fact many of the rate constants have been estimated or guessed [25]. Therefore, the existing reaction models have large uncertainties.

Over a period of time, several efforts have been made to develop well optimized reaction models, particularly for H_2 and C_1- C_4 species. These model development efforts have been supported and validated through the study of experimental laboratory facilities such as shock tubes, well stirred reactors, plug flow reactors and laminar flames. A tremendous amount of experimental and modeling work has been focused on developing and improving the reaction models and is still an ongoing process. Due to complexity in fuel composition, more recent efforts include experimental and model development efforts with surrogate fuels. Such surrogate models still consist of large number of species and reactions, and requires further simplification to be implemented in computational simulations.

The complexity of chemical kinetic models for real fuels can be reduced by using the speciation data from the fuels in developing fast thermal pyrolysis models. The accuracy of such models is highly dependent in the accuracy of experimental data. The current research is thus focused on developing a well-controlled experimental technique to explore such fast thermal pyrolysis models.

1.2 Objectives

The overall combustion process and kinetic research data base can be categorized into several modular components as depicted in Figure 1.8. The key feature is that the combustion process of a multicomponent fuel can be decoupled into pyrolysis and oxidation processes.

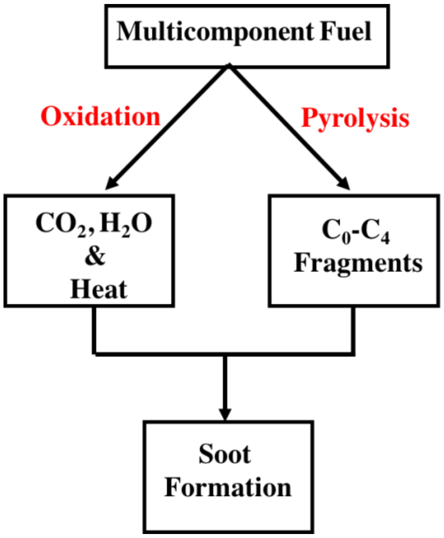

Figure 1.8: Overview of processes occurring in combustion of hydrocarbon fuel [127].

This decoupling process can be explained more clearly by an example as illustrated in Figure 1.9. The figure shows a model (Jet-SurF 2.0 [26]) prediction of dodecane pyrolysis and oxidation ($\varphi = 0.5$) with 98% nitrogen dilution at T=1050 K, p = 1 atm. For the conditions considered here which is typical for pre-heating region of flames the fuel is quickly pyrolyzed and there is formation of intermediate species such as H_2, CH_4, C_2H_2, C_2H_4 etc. As the reaction progresses in time, oxidation of intermediates leads to formation of O_2 and CO_2.

Understanding fuel pyrolysis of real fuels in active cooling system of hypersonic engines is critical. One of the main challenges in the designing of these cooling channels is coke deposition. The pathway to formation of coke in the cooling channels and also gas turbine engines consists of formation of PAH molecules after the fuel decomposition process. The chemical kinetic models defining the decomposition processes are complex and have large uncertainties. These models need to be optimized and reduced to be applicable for CFD calculations.

Considering the need for reliable experimental data at wide range of temperatures, pressures and residence times to reduce uncertainties and complexities in these model, the

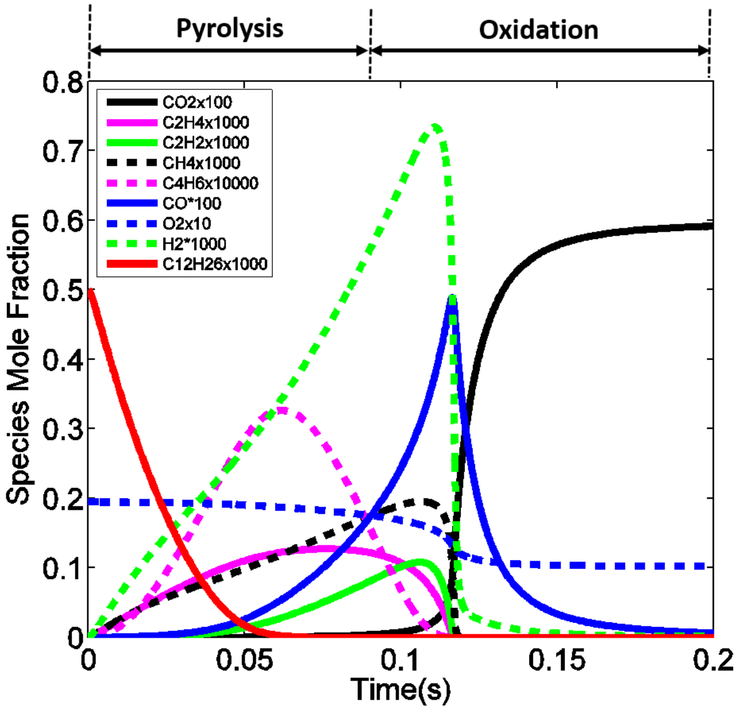

Figure 1.9: Dodecane oxidation process prediction with Jet-SurF 2.0 [26] kinetic model for φ = 0.5, 98% nitrogen dilution, T=1050 K and p=1 atm.

objectives of this study is mainly focused on the experimental aspects of fuel decomposition process into H_2 and C_1-C_4 species. The objectives will be achieved by designing well -controlled experiments employing the MFTR developed as a part of this study and a well-established gas chromatography technique. The details of these systems can be found in chapter 2. The main objectives of the current study are as follows:

1. Design and develop novel micro flow tube reactor (MFTR: Small scale reactors are particularly essential for low cost and easy operation) and a micro probe sampling technique for gas chromatography system capable of conducting fuel pyrolysis experiments with well controlled temperature, pressure and residence time.
2. Characterize the reactor temperature and conduct species mixing and catalytic effect studies on species measurement to validate the developed experimental set up. Study the effects of mass flow rates and pressure in temperature profile of the reactor.
3. Conduct fuel pyrolysis experiments of well-studied small HC fuels to check the fidelity of the reactor in kinetically controlled regimes. Ethane and n-butane are chosen due to availability of chemical kinetic models. Quantify experimental uncertainties associated with species mole fractions.
4. Conduct fuel pyrolysis investigation of n-dodecane (a major component of jet fuel and well-studied surrogate) and JP-8 (a real fuel). Based on the experimental results, develop a fast-thermal pyrolysis model for JP-8.
5. Investigate homogeneous and catalytic fuel pyrolysis studies of JP-10 with and without HY-zeolite catalyst respectively. Study the effect of catalyst on decomposition temperature and major decomposition pathways of JP-10.

1.3 Dissertation Organization

This dissertation includes an extensive experimental work on fuel pyrolysis of HC fuels (ethane, n-butane, n-dodecane, JP-8 and JP-10) in a MFTR at various temperatures, pressures and residence times. The critical need of well quantified experimental data for validation and optimization of chemical kinetic models and the fast-thermal pyrolysis models (developed in the current study) serves as a motivation for the work. The motivations and objectives of the work have already been described in the current chapter. The remaining chapters are organized in the following manner:

In **Chapter 2,** the design of MFTR and general experimental procedures are described in detail. The working of gas chromatography with different detectors, calibration techniques and uncertainty analysis are also presented. In **Chapter 3**, characterization of reactor temperature, species mixing and wall effects on species measurements are presented. The temperature measurements by thermocouple were validated via chemical thermometer concept and the details are also presented in chapter 3. In **Chapter 4**, results on homogeneous thermal pyrolysis of small HC fuels (ethane and n-butane) are presented. The experimental results obtained are compared with available detailed chemical kinetic models as well as literature experimental data reported in literature. In **Chapter 5** results from homogeneous thermal pyrolysis of large HC fuels (n-dodecane, JP-8 and JP-10) and catalytic pyrolysis of JP-10 are presented. A fast-thermal pyrolysis model is developed for JP-8 based on the experimental selectivity data. And finally, in **Chapter 6** a summary of key results and future recommendations are presented.

Chapter 2: Reactor Design and Experimental Methodology

2.1 Background and Introduction: Tube Reactors

Tubular flow reactors have and continued to play a significant role in development of chemical kinetic models [2], [27]–[31]. Generally, flow reactors in the range of 900-1300 K allows investigations of low temperature kinetics of interest to modern gas turbine engines and other propulsion systems.

2.1.1 Types of Reactors

Currently available flow reactors can be primarily categorized into two types: (i) reactors where diluent (and oxidizer) are preheated separately and rapidly mixed with the fuel in the mixing region [28], [32]–[34] and (ii) reactors in which fuel and diluent (and oxidizer) are premixed prior to rapid heating to a target temperature [35]–[39] . Examples of these two types of reactors are shown in Figure 2.1. While the second type of reactors are generally small laminar micro flow reactors which can be subject to significant wall effects,

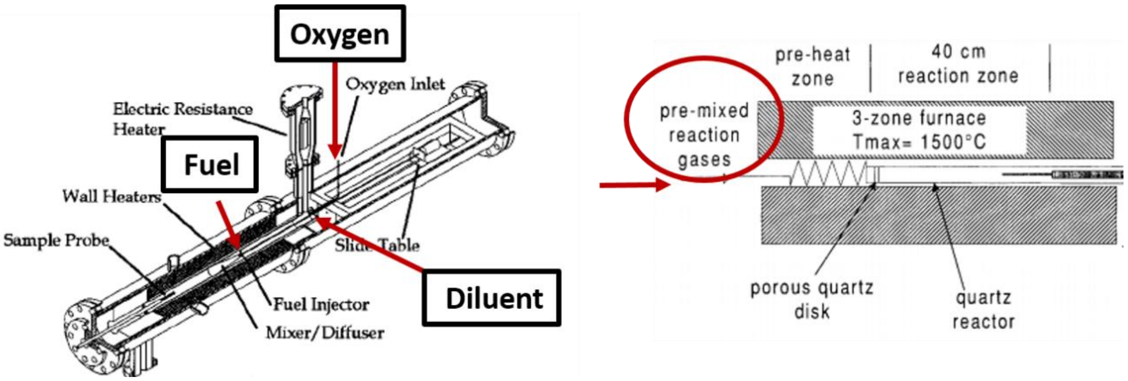

(a) **(b)**

Figure 2.1: Example of two types of currently available reactors (a) Princeton flow reactor [28] (type (i) reactor) with individual preheating of reactants (b) Reactor by Roesler [27] (type (ii)) with premixed reactants.

the first type reactors are turbulent flow reactors with larger diameter and have a high volume to surface area ratio resulting in negligible wall effects. While both large and small reactors have been extensively used to study chemical kinetics, small reactors are convenient and cost effective to use.

The Stanford variable pressure flow reactor (VPFR) is another example of turbulent flow reactor as shown in Figure 2.2. The reactor consists of vertical quartz flow reactor and converging diverging injection section. While the main reactor is heated with electric heated, the McKenna burner with hydrogen-air flame is used to supply hot vitiates to the reaction zone [40], [41]. This type configuration is not only complicated to model but the added vitiates such as O_2, H_2O and H_2 can change the chemical kinetics of the mixture.

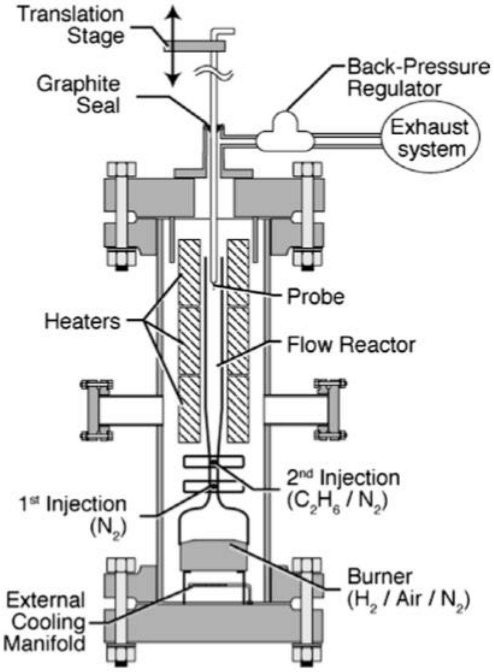

Figure 2.2: Schematic of Stanford VPFR with hot vitiated flow from a McKenna burner [40], [41].

2.1.2 Non- Uniformities in Flow Reactors

In order to derive kinetic data from a flow reactor, a common and convenient way to model the tube reactor is to conduct temporal integration of zero dimensional (0D) governing species and energy conservation equations with no mass transfer across the boundary given by [42]:

$$\frac{dY_k}{dt} = v\dot{\omega}_k W_k \ , \tag{2- 1}$$

$$C_p \frac{d\mathrm{T}}{dt} = v \sum_{k=1}^{K} h_k \dot{\omega}_k W_k \quad , \tag{2- 2}$$

Where, Y_k is the mass fraction of k^{th} species, v is the specific volume, $\dot{\omega}_k$ is the net chemical production rate of k^{th} species, W_k is the molecular weight of k^{th} species, C_p is the mean specific heat of mixture evaluated at constant pressure, h_k is the enthalpy of k^{th} species, T is the temperature and t is time.

In order to solve the equation considered above, the initial conditions of temperature ($T(0) = T_0$), pressure ($P(0)=P_0$) and species mass fraction ($Y_k(0) = Y_{k0}$) are required. As the problem is strongly dependent on initial values of temperature, pressure and species mole or mass fractions, providing accurate initial values in the experiments conducted in tube reactors is crucial. Dryer et al. [43] discussed the reactor initialization problem associated with experiments in tube reactors and attributed two main uncertainties for the definition of zero time: (i) non-negligible mixing time and (ii) change in chemical time scale due to variation in initial temperature.

The radial gradient in large reactors is suppressed by imposing turbulent mixing similar to the study by Mueller et al. [28] who performed H_2/O_2 reaction studies in a variable pressure flow reactor (VPFR) at temperature and pressure ranges of 850-1040 K and 0.3-15.7 atm respectively (See Princeton flow reactor in Figure 2.1 (a)). While the thermal and species gradients were eliminated by high dilution and turbulent mixing at the fuel injection point, the large uncertainties in the mixing region influenced the chemical induction time leading to the requirement of zero time shifting of species profiles. Later, Laskin et al. [44] conducted a 1,3- butadiene pyrolysis and oxidation study in the same flow reactor and shifted the experimental data to match the predicted model trend.

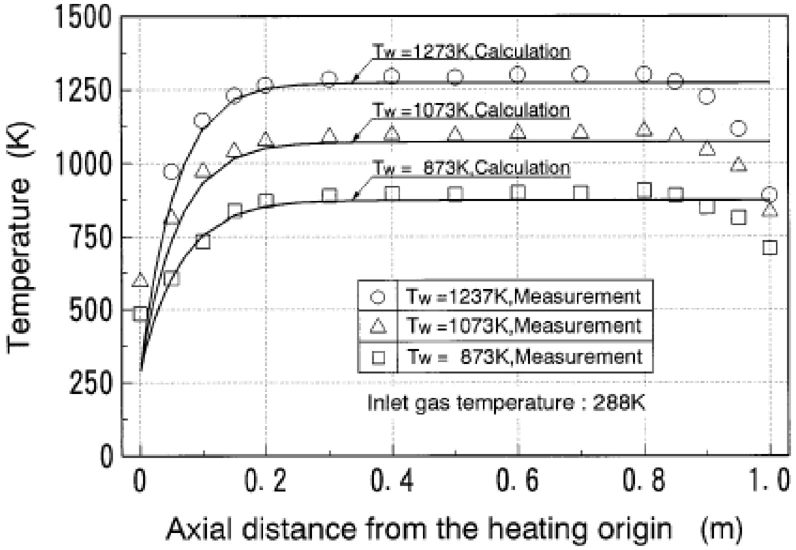

Figure 2.3: Temperature profile of type (ii) reactor [128].

Furthermore, the temperature profile of reactors with premixed reactants is not generic as shown in Figure 2.3 and can lead to uncertainties. Because there cannot be an instantaneous change in the premixed reactants temperature to the set temperature, there exists a temperature ramp up region. Owing to this non-uniformity in temperature, it is necessary to provide individual temperature profile for every experiment. While profile shifting has been a common way to overcome these uncertainties by assuming negligible consumption of initial reactants due to the temperature ramp up and perfectly homogeneous mixing time, this approach has not been applicable for some studies (e.g. dimethyl ether and ethanol oxidation) [43], [45].

One of the key assumptions in 0D modelling studies is to neglect scalar gradient along the radial and axial direction. On the other hand, 1D modelling assumes diffusion along the axial direction and homogeneity in the radial direction. Generally, a plug flow approximation is applied to 1D modelling with uniform properties (concentration, temperature and velocity) along the radial direction and no mixing along the axial direction [46] as shown in Figure 2.4. The latter reduces the 1D problem to be identical to the 0D time varying problem especially for highly diluted conditions.

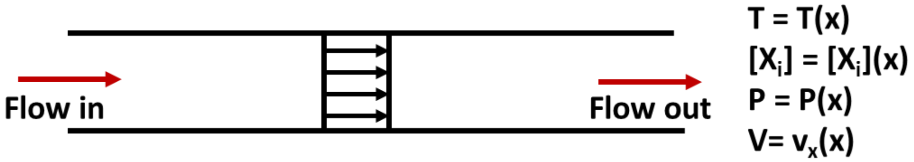

Figure 2.4: Idealized plug flow reactor with uniform velocity, species and temperature profile [46].

Generally, small diameter reactors (Example shown in Figure 2.1 (b)) are associated with laminar flow, but this can result in radial gradients and thus species stratification due to parabolic velocity profile and plug flow assumption may not be valid for these reactors [27]. Lee et al. [47] evaluated the rate parameters of an elementary reaction: $CO + OH \leftrightarrow CO_2 + H$ from a laminar flow reactor in the presence and absence of transport and chemical kinetics. The study emphasized the effects of wall reactions and also illustrated the importance of two-dimensional analysis in processing of experimental data from a laminar flow reactor when radial and axial diffusion are non-negligible. Further, Roesler [27] conducted 2D modeling of a laminar non-plug flow reactor (3 cm i.d.) and included flow stratification in their analysis.

Cutler et al. [48] summarized the criteria for the validity of plug flow idealization for tubular flow reactors. Later, these criteria were adopted by Stewart [49] for the validation of a silica-lined flow reactor to study super-critical and gas phase cycloalkane pyrolysis. The studies emphasized that, even in the presence of laminar parabolic velocity profile, the radial species diffusion time scale can be faster than axial convection or chemical time scale, creating a scope to assume the laminar flow reactors close to plug flow reactors. Table 2.1 lists the criteria for assuming negligible axial diffusion, Poiseuille flow and constant temperature summarized by Cutler et al. [48]. We have recently published a paper which consists of all the details of modeling and characteristic time scales for the current studies [50]. The results for ethane pyrolysis at T=1100 K, satisfied the negligible axial diffusion, constant temperature for all the residence time explored in the present study and negligible Poseuille's flow criteria for residence time above 27 ms.

Table 2.1: Criteria for validity of plug flow assumption summarized by Cutler et al. [48]. c is forced convection, R is radial, L is axial, sd is species diffusion, td is the thermal diffusion and k is the chemical kinetic.

Criteria	Condition	Value
Negligible axial diffusion	$\frac{\tau_{c,R}^2}{(\tau_{sd,R})(\tau_k)}$, $\frac{\tau_{c,L}}{\tau_{sd,R}}$ and $\frac{\tau_{c,R}}{\tau_{sd,L}}$	<<0.1, <0.06 and <0.02
Negligible Poiseuille flow	$\frac{\tau_{sd,R}}{\tau_k}$, $\frac{\tau_{sd,R}}{\tau_{c,L}}$ and $\frac{\tau_{c,R}}{\tau_k}$	< 1, < 0.5 and < 0.05
Constant temperature assumption	$\frac{\tau_{td}}{\tau_{c,L}}$	<<3.7

While accurate modeling of the reactor is extremely important, it is equally critical to design the experiments such that uncertainties are minimized. Indeed, it should be well understood at what conditions the uncertainties become unacceptably high so that the limitations of the experiments are known. This is particularly critical before considering the data extracted from a reactor for model development and optimization.

2.2 Experimental Set-Up

The main components of the experimental set-up which includes a micro flow tube reactor, a fuel and diluent flow system, reactor heating system, a sampling/probing line and quantitative chemical analysis systems/analytical techniques is shown in Figure 2.5. The details of major aspects are discussed below.

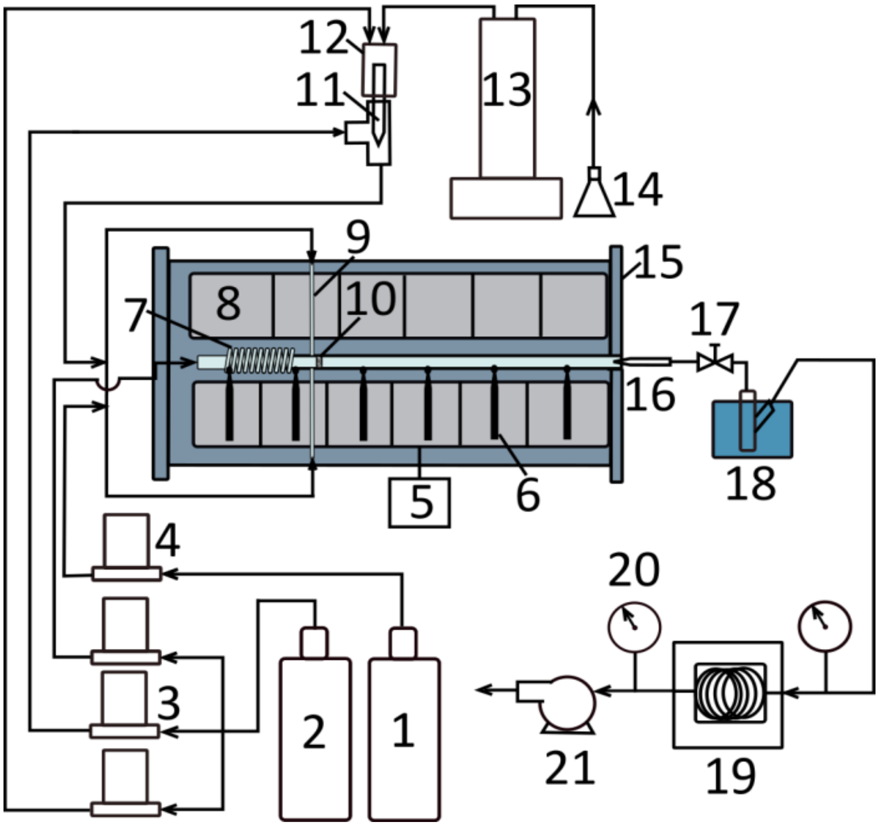

Figure 2.5: Illustration of the microflow tube reactor showing modular heating sections, helical preheat section, fuel addition via side feed tubes, and probing at the exit plane. 1 - fuel gas cylinder, 2 - nitrogen gas cylinder; 3 - Nitrogen mass flow controllers; 4 - Fuel mass flow controller, 5 - PID controller; 6 - thermocouples; 7 - heating coil; 8 - heating elements; 9 - side tubes; 10 - porous quartz frit; 11 - atomizer; 12 - pre-vaporization chamber; 13 - liquid syringe pump; 14 - fuel reservoir; 15 - vented high-pressure enclosure (hydro-tested up to 100 atm); 16 - quartz probe; 17 - valve; 18 - dry ice bath; 19 - GC system ; 20 - pressure gauges; 21 - vacuum pump.

2.2.1 Micro Flow Tube Reactor Design

In order to fulfill the research objectives, two types of micro flow tube reactors (atmospheric pressure and high pressure) have been developed to conduct the experimental work. These reactors were designed to investigate the effects of residence time, temperature and pressure on thermal decomposition of small and large HC fuels. Both reactors are comprised of a 0.4 cm inner diameter quartz tube to minimize the catalytic wall effects. The reactors and heating system sits on a V-shaped metal support and is enclosed within a steel chamber which has been hydro tested up to 100 atm (see Figure 2.7)

2.2.1.1 Atmospheric Pressure Reactor (Ideal Configuration)

The atmospheric pressure reactor is comprised of two 1 mm inner diameter side tubes that direct the fuel into a mixing region, see Figure 2.6(a). The reactor is also equipped with a 125 cm long helical section (coil outer diameter = 2.6 cm) to ensure a complete heating of

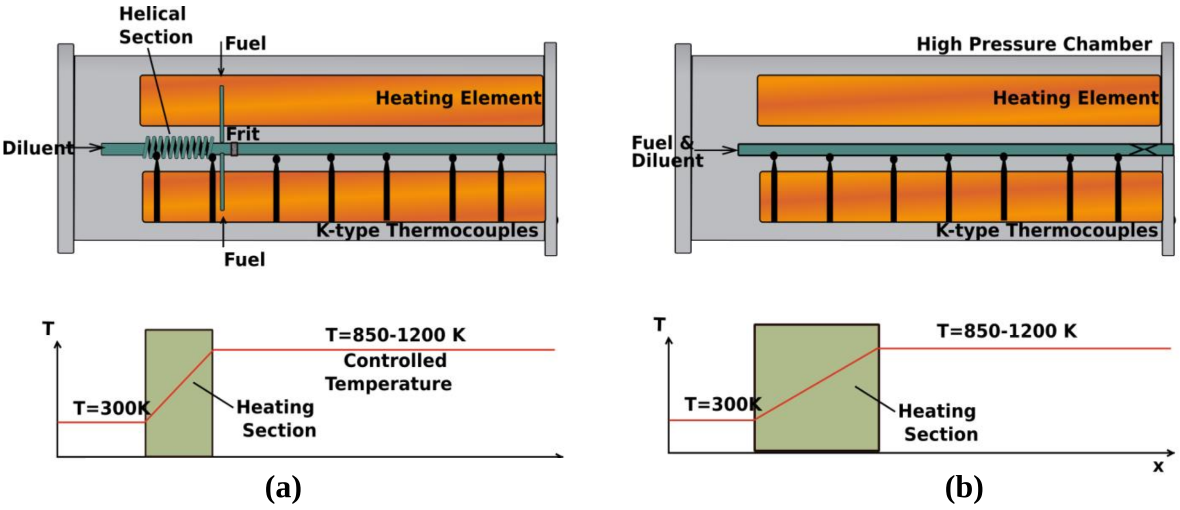

Figure 2.6 : Schematic for micro flow tube reactors. (a) Atmospheric Pressure Reactor (b) High Pressure Reactor.

the diluent, prior to mixing with fuel. The length of the mixing region is kept short and contributes to about 2.5% of the total residence time. After the mixing region, a 37 cm long constant temperature section allows the fuel to decompose at a constant desired temperature (850-1200 K). A glass frit 0.3 cm in length with 200μm pore structure is placed just after the mixing region to enhance mixing between the diluent and fuel before entering the hot section. As small sections of side tubes are exposed to high temperature before the mixing region, the exposed side tubes are equipped with quartz jackets so that fuel remains below pyrolysis temperature.

2.2.1.2 High Pressure Reactor

The high-pressure micro flow tube reactor is comprised of a straight quartz tube with a choked flow orifice at the exit; see Figure 2.6(b) and Figure 2.7. The orifice diameter and length of the reactor can be varied to change the residence time. Compared to the ideal configuration described in Section 2.2.1.1, the high-pressure reactor configuration consists of a temperature ramp up region due to the absence of a preheating section for the diluents and side tubes through which fuel is introduced. In order to back pressure the reactor, a

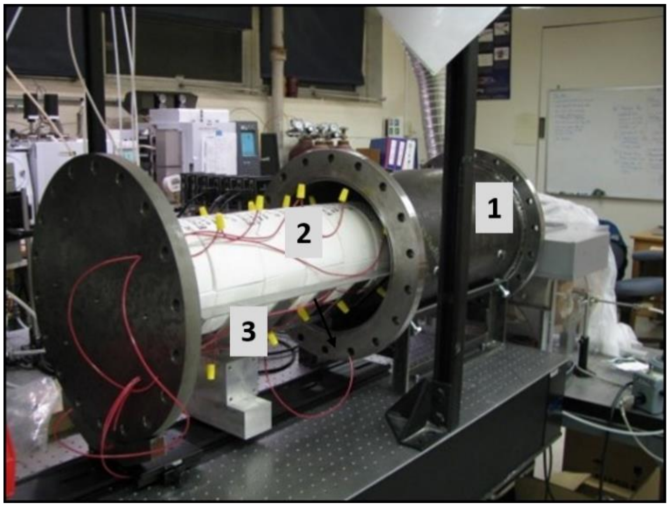

1- High Pressure Chamber

2- Ceramic Heaters

3- V-Shaped Support

Figure 2.7: Photograph of the micro flow tube reactor.

choked orifice is placed exactly at the end of the heater, see Figure 2.8. The expansion of reacted gases through the nozzle leads to cool down and freezing the reaction which is then sampled to analytical devices. A combination of 1/4 " swagelok adapter, nut and vespel ferrule provide support to the glass tube at the exit and prevents the reactor from flying out due to high pressure differential. The inlet of the reactor is also connected with a helical 1/8", thin walled (0.22 cm id) stainless steel tube for flexibility during installation.

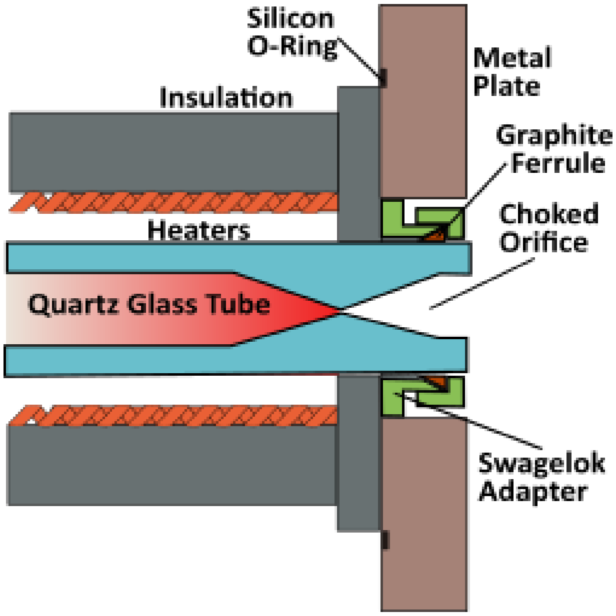

Figure 2.8: Exit of the high-pressure reactor showing the seal made at the exit using a swagelok adaptor, nut and graphite ferrule.

2.2.2 Fuel and Diluent Flow System

In order to accurately supply the required gases to the reactor, a well-arranged fuel and diluent delivery system have been developed. The fluid flow system consists of gaseous fuel/diluent supply system, mass flow controllers, data acquisition (DAQ) system and liquid fuel delivery system.

2.2.2.1 Gaseous Fuel/Diluent Supply System

The fuel (ethane and n-butane), diluent N_2 and reference gas argon for the experiments are supplied from a pressured gas reservoir as shown in Figure 2.5. The gases required for the analytical system namely hydrogen, helium, argon and air are also supplied separately. The gases are regulated to operating pressures of mass flow controllers using gas regulators designed to operate at maximum pressure input and output of 408 and 54 atm respectively. The purities and sources of the gases are listed in Table 2.2.

Table 2.2: List of gases used for experimental studies. UHP: Ultra High Purity

Gases	Purity (%)	Source
Ethane	99.95	Matheson
n-Butane	99.99	Praxair
Nitrogen	99.995	Praxair
Argon	99.999(UHP)	Praxair
Helium	99.999 (UHP)	Praxair
Hydrogen	99.999(UHP)	Praxair
Air	99.999(UHP)	Praxair

The air used as a coolant in the side arm cooling jackets is supplied using a compressor. In order to supply air at required pressure and prevent moisture or particulates to entering the

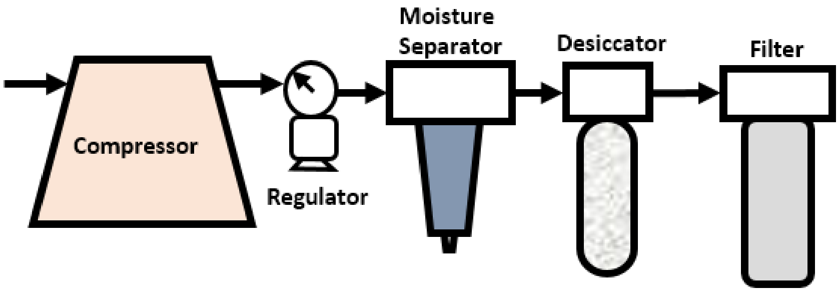

Figure 2.9: Air supply system consisting of air compressor, regulator, moisture separator, desiccator and particulate filter.

flow controller, a combination of air compressor, regulator, moisture separator, desiccator and particulate filter (See Figure 2.9) have been added in the air supply line.

2.2.2.2 Mass Flow Controllers

Sierra mass flow controllers (Series 100) are used to control desired flow rates of fuel or diluent to the tube reactor based on required pressure and residence time. The flow controllers have been calibrated using nitrogen at room temperatures prior to use in actual experiments. The recommended lower operational range of the flow controllers are 20% and above the full scale. In the current work, all the flow controllers are always selected to be within this specified range. Furthermore, individual k factors for all the gases were measured and incorporated in the LabVIEW program. The working principle of mass flow controllers along with the definition of k factor is given in appendix Section A.1.

2.2.2.3 Data Acquisition System

In order to automatically monitor temperatures and set flowrates, a data acquisition system (DAQ) system was developed using NI DAQ input-output system and LabVIEW control program. The program enables separate control of diluent and fuel flowrates to the reactor. In addition, the temperature at 8 different positions of the preheating section are also set and monitored through this program as shown in Figure 2.10

This control has been achieved by incorporating National Instruments (NI) 9215 and 9263 DAQ as an input and output communication bridges between the mass flow controls and the computer. Likewise, two NI 9211 DAQ cards have been incorporated in the DAQ chassis to monitor the temperatures of the preheaters.

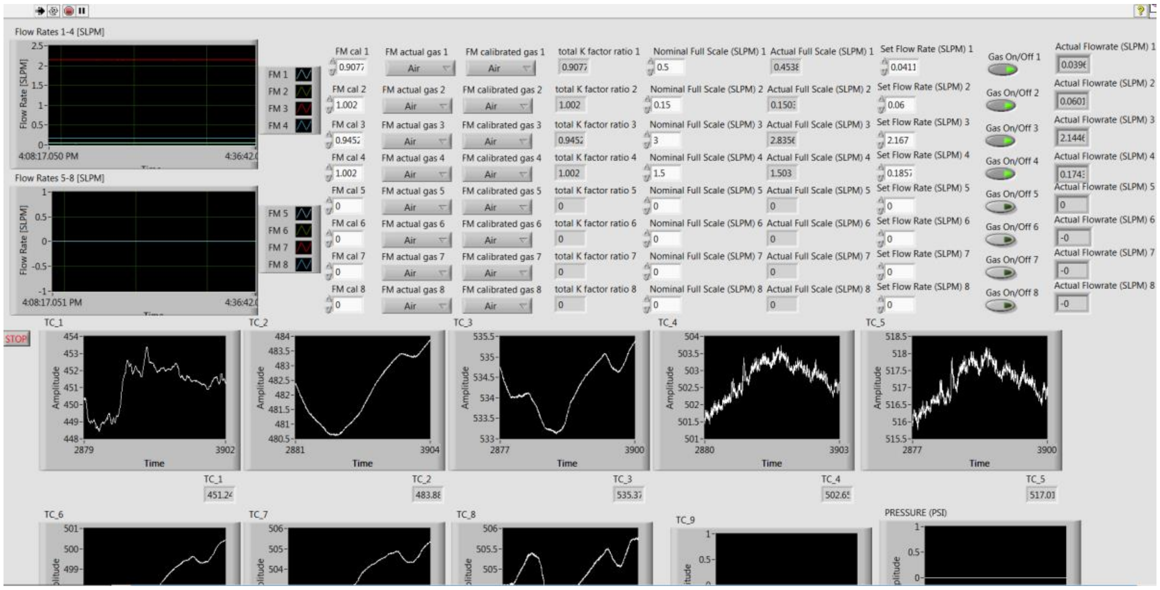

FM cal	FM actual gas	FM calibrated gas	total K factor ratio	Nominal Full Scale (SLPM)	Actual Full Scale (SLPM)	Set Flow Rate (SLPM)	Actual Flowrate (SLPM)
FM cal 1: 0.9077	Air	Air	0.9077	0.5	0.4538	0.0411	0.0396
FM cal 2: 1.002	Air	Air	1.002	0.15	0.1503	0.06	0.0601
FM cal 3: 0.9452	Air	Air	0.9452	3	2.8356	2.167	2.1446
FM cal 4: 1.002	Air	Air	1.002	1.5	1.503	0.1857	0.1743
FM cal 5: 0	Air	Air	0	0	0	0	0
FM cal 6: 0	Air	Air	0	0	0	0	-0
FM cal 7: 0	Air	Air	0	0	0	0	-0
FM cal 8: 0	Air	Air	0	0	0	0	-0

TC_1: 451.24
TC_2: 483.88
TC_3: 535.37
TC_4: 502.65
TC_5: 517.01

Figure 2.10: LabVIEW control panel to set and monitor the flowrates and temperatures.

2.2.2.4 Liquid fuel delivery system

The liquid fuel delivery system consists of a Teledyne ISCO 500D syringe pump with a 507-ml cylinder capacity and Sono-tex atomizer. The pump is capable of flowing 0.001-204 ml /min flow at a pressure range of 10-3750 psi. The atomizer is capable of atomizing the fuel (with mean droplet size of 10-15 µm) and rapid mixing with preheated diluent (N_2). The mixture of fuel and N_2 is kept at a nearly constant temperature (to ensure the fuel remains vaporized), until it is introduced to the reactor. These lines are heated using heavy insulated heating tapes from Omega Engineering and further insulated with high temperature fiberglass fabric strips to minimize any heat losses. Depending on the room temperature and fuel type, a variable heat flux is provided to these heating tapes using adjustable temperature switches or Staco variable transformers.

2.2.3 Reactor Heating System

The heating system of the reactors consists of heaters, PID controllers and thermocouples. A schematic for the connection of single heater with a solid-state relay and a PID controller is shown in Figure 2.11. The heaters are basically modular high temperature electrical heating elements (T_{max}= 1200 °C) from Thermcraft which are a combination of 5.06 and 10.16 cm long semi cylindrical ceramic components (RH211/RH212) and insulation (IP-2.5-2/IP-2.5-4). The reactor is completely enclosed inside 66 cm long and 3.81 cm i.d. heated cavity formed by these components to provide a constant temperature profile along radial and axial direction. Based on the number of heaters used, a series of K-type Omega thermocouples are incorporated to monitor the tube wall temperature adjacent to each heater. Sets of individual PID Proportional- integral-derivative (PID) controllers and solid state relays (SSR) are installed to control and maintain the temperature at desired set value. PID controller is a feedback system which continuously calculates the error between the desired set point and measured temperature by the thermocouple and minimizes the error

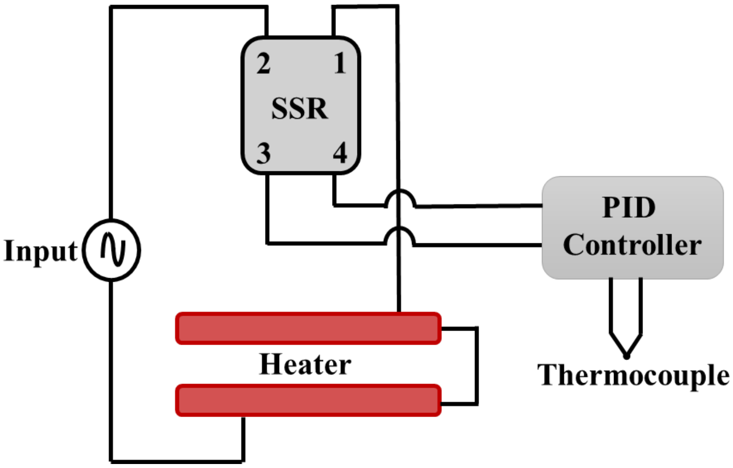

Figure 2.11: Schematic for connection of a single heating element consisting of heater, solid state relay (SSR), proportional integral derivative (PID) controller and a K-type thermocouple.

by adjustment of the power input to the heaters [51]. Variable heat flux is supplied at different conditions with the help of SSR which acts as a switch to turn the heaters on and off. The main advantage such a heating system design is that the modular nature of the heaters allows flexibility in the hot section length and thus easy change of the residence time.

2.2.4 Sampling/Probing Line

The sampling line for the fuel pyrolysis experiments consists of a 75µm probe tip made of a quartz glass, a shut off valve, a needle valve, three omega digital pressure gauges and a vacuum pump as shown in Figure 2.5. The pressure gauges monitor the pressure at the common inlet and exits of GC and GC-MS. A small diameter probe is selected to maintain constant pressure between the inlet and the outlet thereby eliminating any discrepancies in measurements during calibrations and actual experiments. A Shut off valve and a needle valve have been added to the line to evacuate air in the line prior to every experiment and

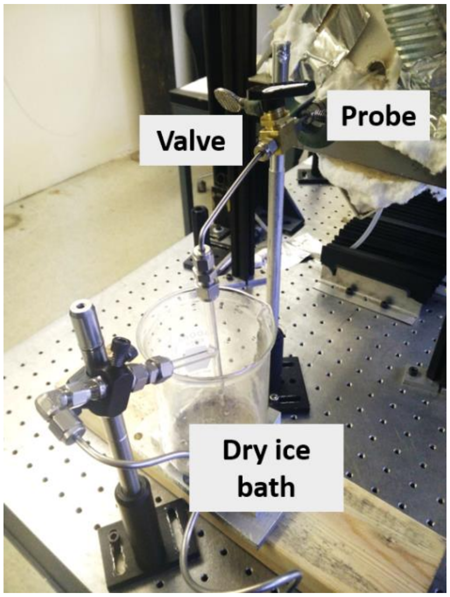

Figure 2.12: Sample probing system consisting of a 75 µm probe and cooling bath.

to regulate pressure in the line, respectively. In all the experiments reported here, pressure of the probe line was maintained at 0.5 atm.

The flow rate through the probe was measured at different temperatures by adding a flow controller in purge mode between the probe and the vacuum pump. The flow rate of the probe plotted with respect to temperature is depicted in Figure 2.13. The volumetric flow rate (Q) through the probe follows the Hagen-Poiseuille equation given by:

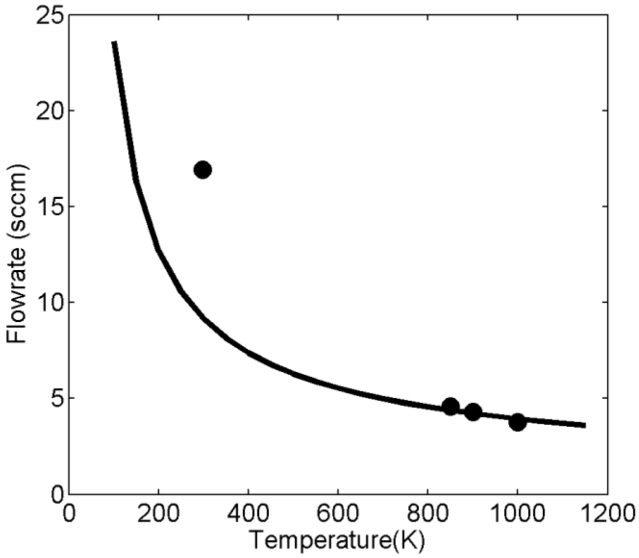

Figure 2.13: Volumetric flow rate through 75$\boldsymbol{\mu}$m probe. Line represents calculated flow rate and symbol represents experimental flow rate.

$$p_2 - p_1 = \mathrm{c}\frac{8\mu Q}{\pi}\int_0^l \frac{dx}{R^4} \quad , \tag{2- 3}$$

where, p_1 and p_2 are pressures at the inlet and the outlet, μ is the dynamic viscosity which is the function of temperature and l is the length of the diverging part of the probe. The radius R is assumed to be changing as a quadratic function of x given by $R = Ax^2 + B$, where A and B are constants found by using the radius of probe at inlet and outlet. c is a constant that depends on the geometry of the probe with an estimated value of 4.5.

In the case of H_2, C_1-C_4 species analysis using the GC described below, the sampled gas mixture is sent through a condenser to separate heavier molecules before sending to the GC as shown in Figure 2.12. This condenser consists of quartz glass trap submerged in a dry ice and ethanol bath at 197 K.

2.2.5 Analytical Techniques

Two gas chromatography systems (i) Shimadzu GC 2014 with two thermal conductivity detectors and a flame ionization detector (GC-TCD/FID) and (ii) Shimadzu GC QP 2010 plus with as mass spectrometer (GC-MS) were used to analyze thermal decomposition products from the tube reactor. Both of these devices work on the same principle except that they have different detectors. The theory/working principle of GC and detectors i.e. TCD, FID and MS are described in Appendix A.

2.2.5.1 GC 2014 (Gas Chromatography with TCD and FID) for H_2 and C_1-C_4 Species

The columns and temperature profile in GC-TCD/FID system was custom designed to analyze species such as O_2, N_2, H_2, CO, CO_2 and light HCs (C_1-C_4) in about 20 mins. The system is equipped with two sets of sampling lines, with each line consisting of its own heated valves, a sample loop and detectors as shown in Figure 2.14. Line 1 consists of a 6 and 10 port valves identified as 92 and 93 with a combination of Hayesep-N and -T, MolSieve-5A, Propak-N, and QS-BOND columns. This line is used to separate and quantify O_2, N_2, CO, CO_2, and C_1-C_4 species via two detectors i.e. TCD2 and methanizer/FID. In particular, Propak-N and QS-BOND columns allow separation of C_2

species, while Haysep-T column allows separation of propane and propylene. Line 2 with a 10-port valve named 91, Hayesep-Q, and Molsieve-5A columns are used to identify and quantify H_2 via a second TCD1. As TCD utilizes the difference in thermal conductivities

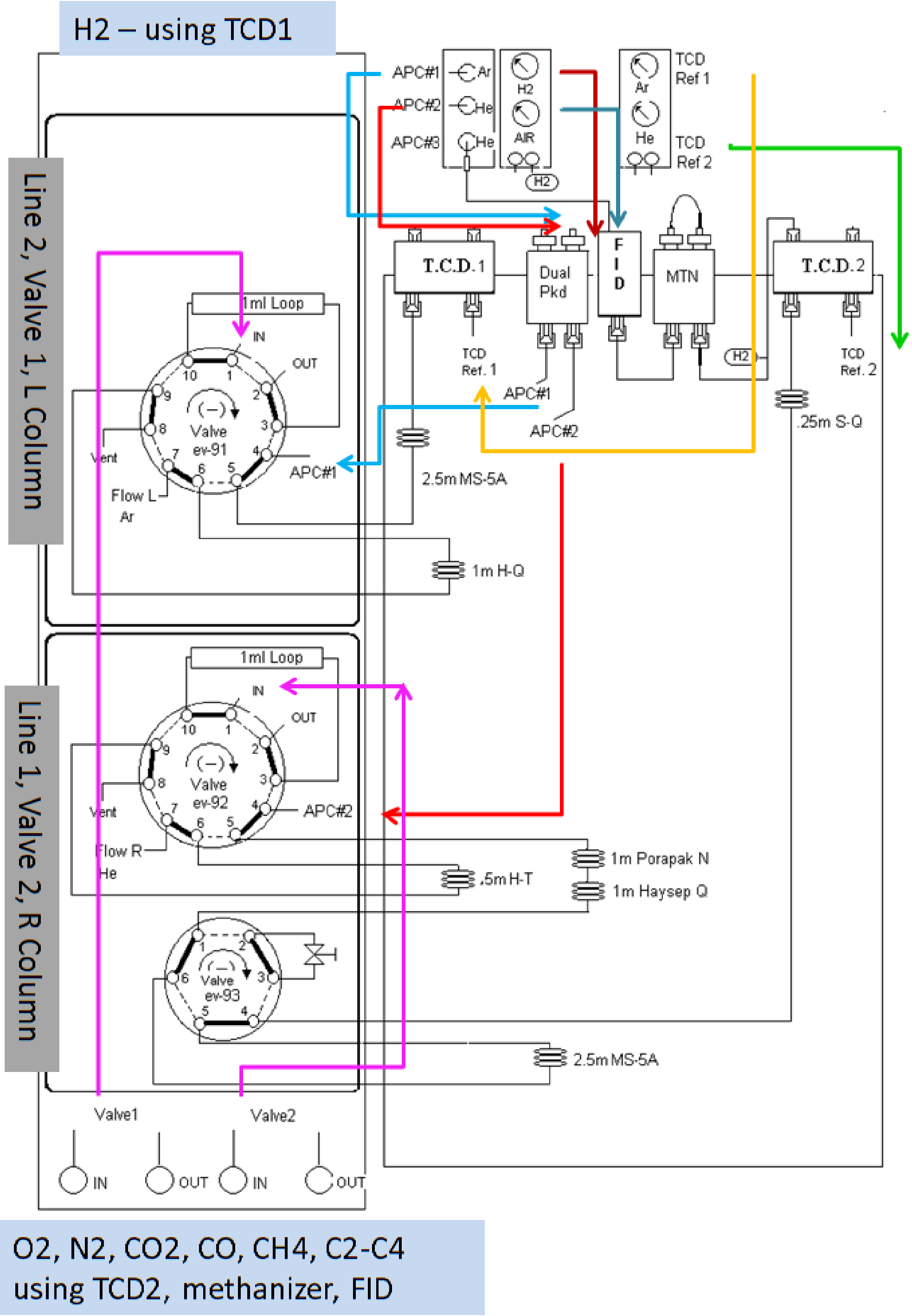

Figure 2.14: Line Diagram of GC 2014 with two lines, 3 multiport valves and 3 detectors.

to identify species, the carrier gas chosen should have a wide differential range in thermal conductivities. While line 1 is supplied with He as a mobile phase/carrier gas, for higher sensitivity Ar is used in line 2 because the thermal conductivities between He and H_2 are not very different.

Table 2.3: Valve time setting in GC-2014 (negative sign indicates turning in anti-clockwise direction)

Time	0.01	0.02	0.75	1.70	5.40	10.80	12.00	20.75
Position/Value	91	92	-91	93	-93	93	-92	-93

Table 2.3 depicts the valve time setting used in the analysis for the combination of valve 91, 92 and 93. Before the GC system is started, a continuous flow of sample from the probe is passed through the loop to the vacuum pump as shown in Figure 2.15 (a). At the same time, a continuous flow of helium is maintained in the columns via APC electronic flow controllers. Once the system is started the valves are actuated (timing according to Table 2.3) and the carrier gas pushes the samples to the columns as shown in Figure 2.15 (b).

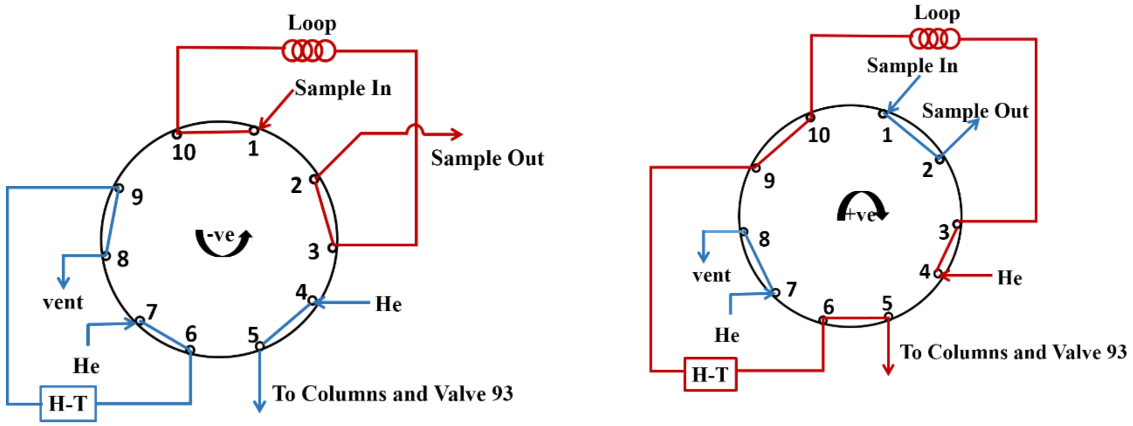

(a) **(b)**

Figure 2.15: Valve timing for 10 port valve in line 1 of GC/FID/TCD (a) flow system during negative position and (b) flow system during positive position.

In line 1 valve 2, the sample from the loop is introduced to 0.5m HayesSep-T(H-T), 1m Porapak- N (P-N) and 1m HayesSep- Q (H-Q) which slows and resolves CO_2, C_2, C_3 and C_4 species. H-T particularly traps water which is vented out with a continuous supply of helium in the negative position of the valve. The permanent gases such as H_2, O_2, N_2, CH_4 and CO are sent to 2.5m Molecular Sieve (MS) -5A. The 6-port valve (93) rotates to trap CH_4 and CO while H_2 and O_2 elute from MS-5A column to TCD2. The slower elutes CO_2 and C_2 next come off the column H-T/P-N/H-Q and reach the TCD2/MTN/FID. The 6-port valve turns back and CH_4 and CO elute into TCD2/MTN/FID. Finally, C_3 and C_4 species elute to the detector and the valve goes back to the minus (-) position and a new sample can be introduced.

Component	**Temperature (°C)**
Methanizer	380
Injection Ports	100
FID	250
TCD1	100
TCD2	100
Valve1	100
Valve 2 &3	100

(a)

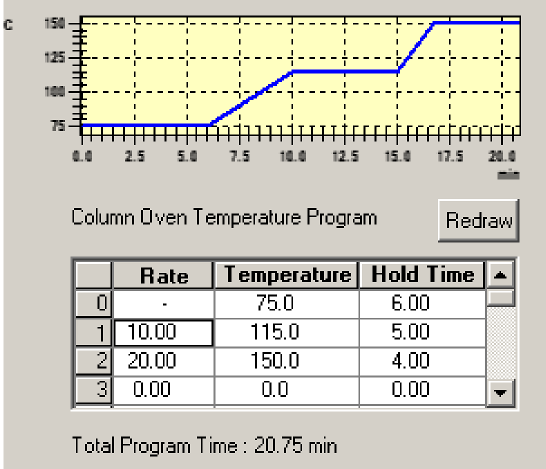

Column Oven Temperature Program

	Rate	Temperature	Hold Time
0	-	75.0	6.00
1	10.00	115.0	5.00
2	20.00	150.0	4.00
3	0.00	0.0	0.00

Total Program Time : 20.75 min

(b)

Figure 2.16: Temperature settings for components GC/FID/TCD (a) Temperature setting for injection ports, Detectors (FID, TCDs) and valve box (Valve1, Valve2 & 3) (b) Temperature program of the column oven with maximum temperature of 150 ºC.

In line 2 valve 1, sample flows to a 1 m H-Q column that slows the CO_2, C_2, C_3 and C_4 species. The H_2 passes through the H-Q column to the MS-5A. The valve rotates back to its original position and CO_2, C_2, C_3 and C_4 are vented to exhaust. H_2 is separated from all other species and elutes first and detected by TCD1. The valve time for valve 93 is similar to 6 port valve system of GC-MS shown in Figure 2.17.

The temperature settings for column, injection ports (INJ), detectors (FID, TCD) and valve boxes (Valve 1-3) are given in Figure 2.16(a). A method file has been developed to specify the set temperatures and flow rates to the device. The method file includes a temperature program of the oven as shown in Figure 2.16(b). The above two-lines with multiport gas sampling valves system allows switching of the samples between different columns and the temperature program controls the elution time of the species thereby minimizing the analysis period to roughly 20 mins.

2.2.5.2 GC QP 2010 Plus (Gas Chromatography with MS) for heavier species

The main advantage of GC QP 2010 plus over GC 2014 is its capability to identify trace amounts of species and also large hydrocarbon molecules because of the capillary column installed. GC QP 2010 Plus is a standard GC-MS system with gas chromatography, a differential pumping system, electron impact ionization (ionization at 70 eV), electron energy/current variable dual filament ion source, quadrupole mass filter and electron multiplier detector [52].

The gas chromatography in the current GC-MS system is achieved by using a capillary column (Zebron Zb-1 capillary GC, 60m X 0.32mm X 3.00μm). In addition to the gas sampling via 6 port valve system (see Figure 2.17) working in a similar manner to the 10-port valve system, the system also consists of liquid sampling capability via an auto sampler. This added feature enables the experimenter to calibrate and quantify larger hydrocarbon molecules using liquid standards whose gaseous standard are not available.

The liquid sample enters the column via split type injection port which enables control of column flow and thus the sensitivity. The amount of sample injected through the column can be defined by the split ratio which is the ratio between the flow through the split valve and the column flow. An increase in split ratio increases the overall flow rate of carrier gas. As the loop volume (1 ml) and column flow rate are fixed, the amount of sample entering the column is decreased with increase in spilt ratio. The column flow rate, total flow and other parameters at split ratio of 50 and 10 are shown in Table 2.4

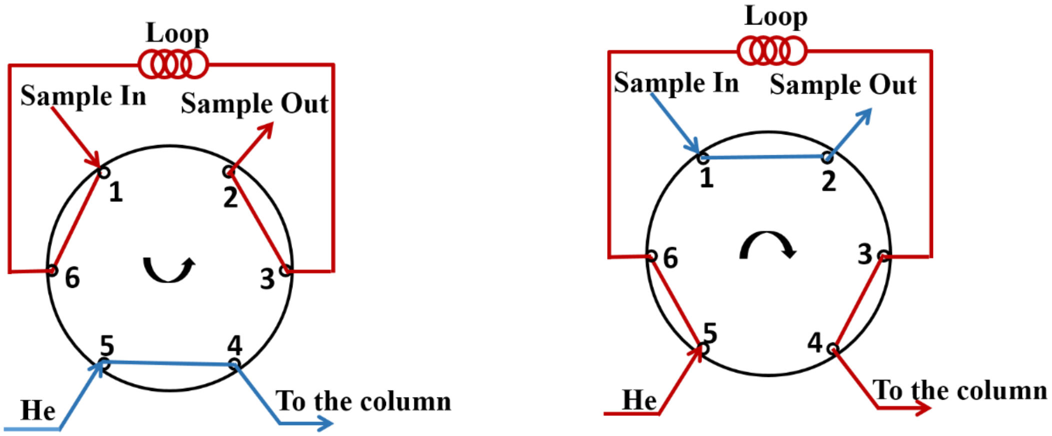

(a) **(b)**

Figure 2.17: Valve timing for 6 port valve system in GC-MS (a) flow system during negative position and (b) flow system during positive position of the valve.

Table 2.4: GCMS 2010 plus parameters at different splits

Split ratio	**Inlet Pressure (KPa)**	**Linear Velocity (cm/sec)**	**Column flow (ml/min)**	**Total flow (ml/min)**	**Carrier gas**
50	83.5	35	1.88	96.5	He
10	83.5	35	1.88	21.2	He

As the MS works on the generation and filtering of ions, low pressure and increased mean free path are crucial for the negligible collision of ions. Thus, in order to fulfill this requirement in the MS, a vacuum differential pumping system with a turbo molecular pump and a rotary backing pump are used with a vacuum pressure of ~ $1.5X10^{-4}$ Pa.

2.3 Experimental Methodology

2.3.1 Ethane and n-Butane Pyrolysis

Ethane and n-butane pyrolysis studies were conducted in the atmospheric pressure reactor. In order to ensure negligible temperature variation due to the endothermic pyrolysis of the fuel, flow reactor experiments were performed in 98% nitrogen diluent bath. Nitrogen was fed through the helical section and preheated to the target temperature before entering the main tube in the experiments. Fuel was introduced through the side tubes accounting for 2% of the total mixture. The schematic of experimental set up for gaseous and liquid fuel pyrolysis is shown in Figure 2.5. After mixing, fuel and diluent then pass through a porous frit to a hot section which is maintained at a constant temperature. As the residence time of fuel in the side tubes is long, a constant cooling supply of air is maintained in the side tube jackets to prevent any undesirable fuel decomposition. In order to eliminate any uncertainty on measured data arising from a transient operating condition, the system was allowed to reach a steady state at the desired temperature prior to each experiment. A fraction of the reacting mixture was then sampled at the exit of the reactor via a quartz probe (75 µm nozzle diameter) into a GC system. Temperature, pressure and residence time explored in the ethane and n-butane experiments are listed in Table 2.5.

Table 2.5: Experimental conditions explored in ethane and n-butane experiments

Fuel Type	**Composition % (by moles)**		**T (K)**	**P (atm)**	**Residence time (ms)**
	Nitrogen	Fuel			
Ethane	98	2	1050-1100 950-1100	1 5 & 15	10-90 590
n-Butane	98	2	1050-1100	1	30-90

2.3.2 Liquid Fuel Pyrolysis (Dodecane, JP-8 and JP-10)

The key challenge in liquid fuel pyrolysis study is the pre-vaporization of fuel without any condensation or pyrolysis until it reaches the hot test section. To minimize the previously mentioned endothermic pyrolysis effects on temperature, an even smaller concentration of fuel (0.25%) is used. Liquid fuel with a flow rate of 0.011-0.176 ml/min is dispensed through liquid syringe pump and delivered to an atomizer via a 1/8" copper tubing before mixing with preheated diluent. Due to the very low liquid fuel flow rates and the fact that real fuels such as JP-8 consist of a broad range of species with different vapor pressures, an atomizer is essential for vaporization and proper mixing. This required 10% of the total nitrogen flow to be sent through the atomizer assembly and also keep the atomizer from overheating. The entire fuel and nitrogen assembly line is kept at a temperature of about 450-550 K (depending upon the vapor pressure) to ensure the vaporization of heavier components of liquid fuels. Uniform heating of the fuel line is attained by wrapping individual heaters/heating tapes and properly insulating different sections of the line up to the side feed tubes of the reactor. In addition, eight K type thermocouples are incorporated inside each heater to monitor the temperature at various points through NI Labview software interface. The nitrogen and pre-vaporized fuel mixture is then allowed to enter the mixing region through side tubes where it was rapidly mixed with preheated nitrogen stream (~90%) from the main tube.

Table 2.6: Experimental conditions explored for liquid fuels

Fuel Type	**Composition % (by moles)**		**T (K)**	**P (atm)**	**Residence time (ms)**
	Nitrogen	Fuel			
n-dodecane	99.75 99	0.25 1	1000-1100	1 5	10-90 590
JP-8 (3733 & 10264)	99.75 99	0.25 1	1050 &1100 950-1100	1 5	30-90 590
JP-10 (with & without catalyst)	99	1	700-950 850-1100	1 1 & 5	400 400 & 590
Cyclohexene	99.77	0.23	950	1	30-60
RP-1 & RP-2[*]	99.75	0.25	1050 &1100	1	10-60

[*] RP-1 & RP-2 data are not reported due to sensitivity of the project

2.3.3 Calculation of Experimental Parameters (Flowrates and Residence Time)

The residence time in the atmospheric pressure flow reactor was varied by changing the inflow velocity of the flow with respect to the probe position at the exit of the reactor. This approach of changing residence time is less expensive than physically altering the length of the reactor. The residence time in the hot section is given by $t_{res} = L/v_H$, where L is the length of the reactor and v_H is the cross-sectional average flow velocity in the hot section.

For incompressible flow mass continuity yields, $\rho_H v_H = \rho_o v_o$, where subscript “H” and “o” refer to hold section and cold inflow condition respectively. The mixture density is given by the equation of state, $\rho_{mix} = \frac{P}{RT_c}$, where $R = \frac{R^0}{MW_{mix}}$ with $MW_{mix} = \sum MW_i\, X_i$. One can readily determine the corresponding mass fraction by $Y_i = X_i \frac{MW_i}{MW_{mix}}$. Thus, knowing density ρ_o and v_o for a target flow residence time, the total mass flow rate at normal temperature and pressure is given by $\dot{m}_{total} = A\, v_0\, \rho_o$, where, A is the area of the reactor. The fractional flow rates of fuel and diluent for a particular mole fraction can be calculated based on their mass fraction. For example, $\dot{m}_F = Y_F \dot{m}_{total}$ and volume flow rate $\dot{V}_F = \frac{\dot{m}_F}{\rho_o}$. Note: If Argon is used as a reference gas, the MW_{mix} and thus mass fractions are calculated including argon. In the experiments with added rods with or without catalyst, the velocity is calculated by compensating for change in volume with and without rods, keeping the residence time constant. The dimension of rods used in the experiment is given in appendix Section B.4 (Figure B.3)

As mentioned in Section 2.1.2, for residence time below 27 ms the criteria for negligible Poseuille's flow is not satisfied and there can be a parabolic velocity profile and thus

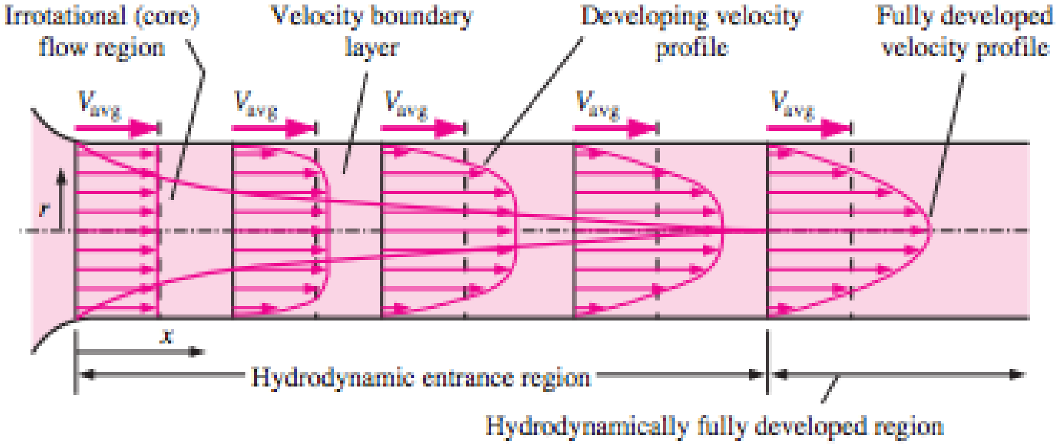

Figure 2.18 : Development of a parabolic velocity profile in a tube with laminar flow [129].

species stratification as shown in Figure 2.18. However, in our recently published paper we have addressed these effects by considering 2D simulation of the MFTR. Specifically, two cases were considered where (i) the inflow velocity was kept constant and species were extracted at different axial locations and (ii) the inflow velocity was changed keeping the length constant. The results showed no significant variation in species concentrations between the two cases [50]. Thus, for convenience, the plug flow or average velocities are used for calculating the residence time in this work.

For the case of high pressure reactor, the residence time is a function of orifice diameter and length of the reactor. The mass flow rate through a chocked orifice is given by $\dot{m} = A_0 \frac{p_0}{\sqrt{T_0}} f(\gamma)$, where, A_o, p_o, T_o and γ are area, pressure, temperature of orifice and gas constant of the mixture respectively. As mentioned earlier, the residence time is calculated by $t_{res} = L/v_H$. In the high-pressure reactor, the fuel and diluent are premixed before entering the hot section. Based on the pressure, there are different temperature time histories creating variation in residence time. This will be discussed in detail in Section 4.2.2. The residence time in the high-pressure reactor in the present study or any reactor with premixed configuration is not precise. In the current study, it is assumed to be bounded by initial formation of H-atom and to the end of the reactor.

2.3.4 GC Calibration Methodologies

The species measured via the two available GCs were calibrated with three different methodologies. The first methodology is the calibration of lower concentration of smaller species (H_2 and C_1- C_4) using gas standards from Air liquid. The calibration process either consisted of direct injection of sample at controller pressure (0.5 atm) from the calibration standards or using the flow controllers with flow rates similar to the probe flow rates in actual experiments (see Section 2.2.4 for details). Both processes generated identical calibration curves.

The second methodology is preferable for the calibration of larger concentration of smaller species (H_2 and C_1- C_4) using combination of flow controllers and gases from tanks. This process involves using a 75µm nozzle tip diameter probe in the same way as in experiments at p=0.5 atm. For every species, a calibration curve with 2-4 points is generated. Further, for every concentration point, 4-5 sample runs are taken to reduce the repeatability uncertainty. A typical calibration curve generated for some species such as ethylene and hydrogen is shown in Figure 2.19. In general, the area under the gas chromatogram peak is proportional to quantitative measure of species. However, for overlapping peaks, height is used as a measure for calibrations which is linear with respect to concentration over the range of species measured. The calibration curves for remaining species are given in appendix Section B.1.

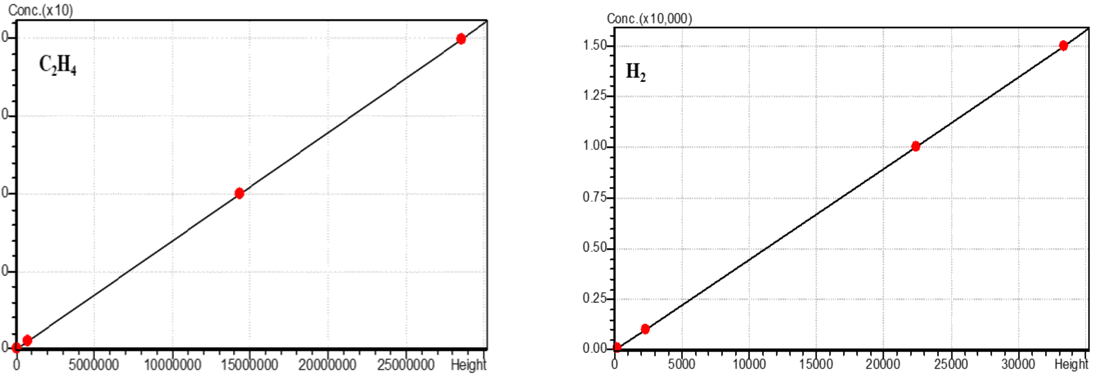

(a) **(b)**

Figure 2.19: Calibration curve for pyrolysis product in GC 2014 (a) Ethylene (b) Hydrogen (Remaining species are given in Appendix B (Figure B.1 and Figure B.2).

The third method involves using of liquid samples through auto sampler in the GCMS. Since the standards for larger species (larger than C_7, cyclopentadiene and cyclopentene) are not available, a process was developed to calibrate the species through liquid samples. However, actual samples from the reactor are in gaseous form, so a correlation between the available gaseous standard and standards of the same components in solutions was established. Note: This method is only utilized in the calibration of cyclopentadiene and cyclopentene in the JP-10 study and is explained in appendix Section B.3.

2.3.5 Uncertainty Analysis

The error in any measurement is composed of two parts: systematic error or bias error and random error. Bias error is the same for every measurement while random error varies from measurement to measurement and eventually becomes negligible in long run. Accuracy in data can be determined by the bias which is the difference between mean and true value. Precision of the data can be determined by repeatability of the data and expressed as standard deviation (σ). This degree of agreement between different measurements is the uncertainty and can be estimated by repeated measurements. In the contrary bias is difficult to estimate and calibration is an essential way to estimate bias [53].

In the current study, bias in the results is reduced in the measurements using calibration standards and calibrated flow controllers while the uncertainty is reduced by repeated measurements during experiments as well as calibrations. Further, the NIST Technical Note 1297 is used as a guideline for uncertainty analysis of the measurements [54]. Based on the NIST handbook, the sources of error can be categorized into type A and type B error. Type A uncertainty is associated with repeated measurements and is evaluated by statistical methods. It is generally expressed as standard deviation for a measurand x_i given by

$$\sigma = \sqrt{\sum_{i=1}^{n} \frac{(x_i - M)^2}{n-1}} \quad , \qquad (2\text{- }4)$$

where, σ is the standard deviation, n is the number of samples, and M is the mean of the samples.

Type B uncertainty is based on scientific judgment made from previous experience, manufacturers, specifications etc. Different models can be used to get the uncertainty associated with this type of uncertainty if the level of confidence is not specified. The common examples may be rectangular, triangular or normal models. In the current study, the type B uncertainties are the errors of standard gases and the flow controllers. These uncertainties are taken as normal standard error.

The general steps used to estimate the uncertainties are specification of the measurand, listing of experimental processes, identification of sources of uncertainties in these processes, estimation of uncertainties from each source, combination of all the uncertainties and finally expansion of uncertainties based on coverage factor [55]. The quantification of species mole fractions from the MFTR is associated with two types of experimental uncertainties. One is due to the uncertainty associated with calibration gases (or standards) used, $\mathrm{u_{cal}}$ and the second is due to the uncertainty associated with measurements, $\mathrm{u_{meas}}$. The details of $\mathrm{u_{cal}}$ and $\mathrm{u_{meas}}$ are discussed below.

2.3.5.1 Calibration uncertainty

Calibration uncertainty is associated with the dispersion of calibration species concentrations. Two different methods were used to generate the gas mixtures for calibration species concentrations, either using commercially available standards or synthesis of gas mixtures using well calibrated mass-flow controllers available in the laboratory as explained in Section 2.3.4. Since the uncertainty of calibration gas mixtures provided by Air Liquide had no confidence intervals reported, the specified errors are assumed as the standard uncertainty. The uncertainties due to mass-flow controllers depend on the capacity of the flow controllers utilized and the typical uncertainty is one percent of the full scale of the mass-flow rate. The uncertainty of measurements in between the calibration points is estimated by interpolation of uncertainty of the points considered. As part of estimating the calibration repeatability uncertainty, a number of samples were used to calculate the unbiased standard deviation to obtain the repeatability uncertainty. The resulting combined calibration uncertainty was estimated from an error propagation equation, given by

$$\mathrm{u_{cal}} = \sqrt{\mathrm{u_{sf}^2 + u_{r1}^2}} \quad , \tag{2- 5}$$

where, $\mathrm{u_{sf}}$ is the standard gas mixture or flow controller uncertainty and $\mathrm{u_{r1}}$ is the repeatability uncertainty of calibration experiments. The list of species calibrated with standards and combination of standards and flow controllers including their uncertainty are given in Table B.1 and Table B.2 respectively.

2.3.5.2 Measurement Uncertainty

Measurement uncertainty is associated with the actual fuel pyrolysis experimental uncertainties that arise due to sets of flow controllers, liquid fuel pump and random errors due to repeatability uncertainty of measurements. A combined propagation of these two yields the net measurement uncertainty, given by

$$\mathrm{u_{meas}} = \sqrt{\mathrm{u_{f/l}^2 + u_{r2}^2}} \quad , \qquad (2\text{- }6)$$

where, $\mathrm{u_{f/l}}$ is the combination of flow controller and liquid fuel pump uncertainty and $\mathrm{u_{r2}}$ is the repeatability uncertainty of measurements.

2.3.5.3 Total and Expanded Uncertainty

The total combined uncertainty of species is calculated via propagation of uncertainty, which is given by,

$$\mathrm{u_{total}} = \sqrt{\mathrm{u_{cal}^2 + u_{meas}^2}} \quad , \qquad (2\text{- }7)$$

In order to provide uncertainties with a level of confidence, extended uncertainties (U) were calculated using a coverage factor (k=2) equivalent to 95 percent confidence level given as,

$$U = k\, u_{total} \quad , \qquad (2\text{- }8)$$

Table 2.7 shows the calibration uncertainties, measurement uncertainties, total uncertainty, and expanded uncertainty, for ethane pyrolysis at p=1 atm, T=1100 K, t_{res}=90 ms, and inflow composition of $X_{C_2H_6}$ = 0.02, X_{N_2}=0.98. Note that the calibration uncertainty (7%) of C_2H_6 is higher that the measurement uncertainty (3.9%) because of larger uncertainty associated with calibration standard. Further, the repeatability uncertainties for both measurement and calibration are relatively lower than the standard flow controller and liquid fuel pump uncertainties.

Table 2.7: A typical list of uncertainties in species quantification in MFTR using GC 2014

Species	u_{cal}	u_{meas}	u_{total}	Expanded Uncertainty
H_2	0.0547	0.0390	0.0672	0.1344
CH_4	0.0488	0.0390	0.0625	0.1250
C_2H_2	0.0374	0.0391	0.0541	0.1081
C_2H_4	0.0284	0.0391	0.0483	0.0966
C_2H_6	0.0702	0.0392	0.0804	0.1608
C_3H_6	0.0497	0.0392	0.0633	0.1267
C_3H_8	0.0227	0.0391	0.0452	0.0904
aC_3H_4	0.0534	0.0457	0.0703	0.1406
pC_3H_4	0.0586	0.0480	0.0757	0.1515

2.4 Summary

Tube reactors have and continued to play a significant role in the development of chemical kinetics models. While both large and small reactors have been extensively used to study chemical kinetics, small reactors are convenient and cost effective to use. Even though, the concept of using small laminar flow tube reactors is not new, a novel small scale MFTR with well controlled temperature and residence time was developed in this study. To minimize the effects of reaction initialization, the atmospheric pressure reactor featured a preheating helical section for supplying diluent, air cooled side tubes for supplying fuel, a small mixing volume, and a porous glass frit. In addition, a high-pressure reactor was also designed and developed to conduct pyrolysis experiments at elevated pressure. The high-pressure reactor was back pressurized by a chocked orifice. The proper heating of the gases in both the reactors were assured by a well-controlled heating system consisting of heaters, PID controllers and thermocouples.

Apart from MFTR and its heating system, the main components of the experimental set-up also include, a fuel and diluent flow system (gaseous and liquid fuel supply), a sampling/probing line and two quantitative chemical analysis systems (GC/FID/TCD and GC/MS). Columns and temperature profile in GC/FID/TCD system was custom designed to analyze species such as O_2, N_2, H_2, CO, CO_2 and light HCs (C_1-C_4) in about 20 mins. The main advantage of GC/MS is its capability to identify trace amounts of species and also large HC molecules because of the capillary column installed.

Gaseous (ethane and n-butane) and liquid (dodecane, JP-8 and JP-10) fuel pyrolysis experiments were conducted in atmospheric pressure reactor at various temperatures and residence times. Experiments at elevated pressures (5 and 15 atm) and different temperatures were conducted in the high-pressure reactor. To minimize the endothermic pyrolysis effects on temperature, small concentrations of fuels (generally 2% for gaseous fuel and 0.25% for liquid fuel) were used. Careful calibration methodologies were developed to quantify the species measured via the GC systems. Extensive uncertainty analysis was also performed considering both calibrations and measurement uncertainties.

Chapter 3: Reactor Characterization

Reactor characterization aims at identifying non-idealities which results in experimental uncertainties in the data obtained from the tube reactor. Chapter 2 described different types of tube reactors and non- idealities associated with them. In this chapter, the various non-idealities associated with experimental studies in the MFTR are categorized into: (1) Non-uniformity of temperature along the length of the reactor, (2) Fuel and diluent mixing effects and, (3) Wall effects on fuel pyrolysis as shown in Figure 3.1. Various experiments were carefully designed and performed to understand these non-idealities which are described in detail in the following sections.

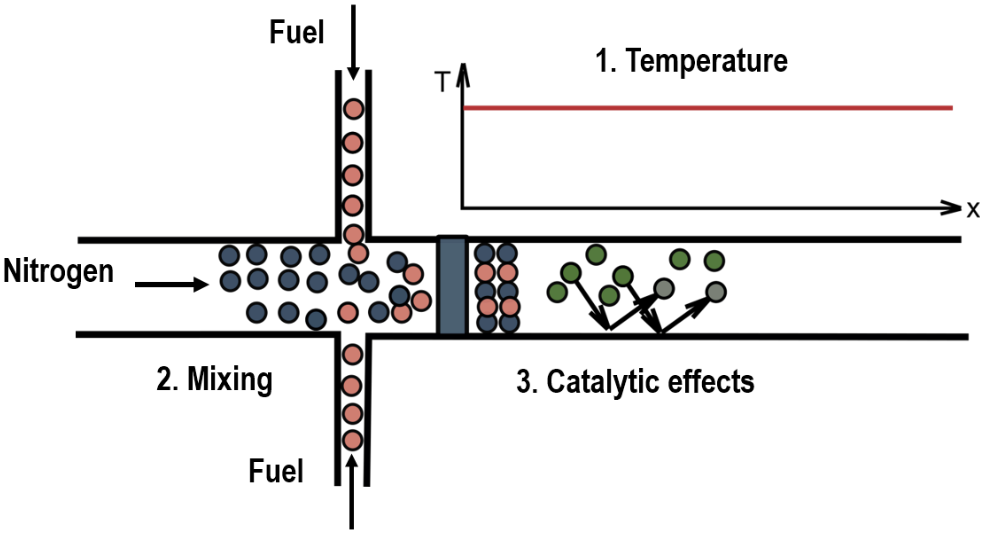

Figure 3.1: Schematic for understanding the reactor non-idealities: (1) Non-uniformity of temperature along the length of the reactor (2) Mixing effects of fuel and diluent and (3) Wall effects in fuel pyrolysis.

3.1 Non-Uniformity of Temperature along the Length of the Reactor

3.1.1 Reactor Temperature Analysis with Thermocouple Measurements

One of the most important parameters in chemical kinetics is temperature. In order to verify the temperature of fluid inside the hot section of both the reactors, a series of temperature measurement experiments were conducted using 45 cm long Omega K-Type thermocouple. No radiation corrections were applied as thermocouple was inside the cavity except near the exit of reactor. A quartz glass sleeve was carefully designed to prevent any catalytic effects or accumulation of impurities inside the reactor. Further, the glass reactors were often cleaned with 1% HF solution to eliminate any unwanted impurities. Temperature measurement experiments in the atmospheric pressure reactor were conducted by inserting a thermocouple from the exit of the reactor, measuring temperature at equal distances along the length. Figure 3.2 shows the resulting temperature profiles for typical flow rates and temperatures used in the experiments by flowing nitrogen from main

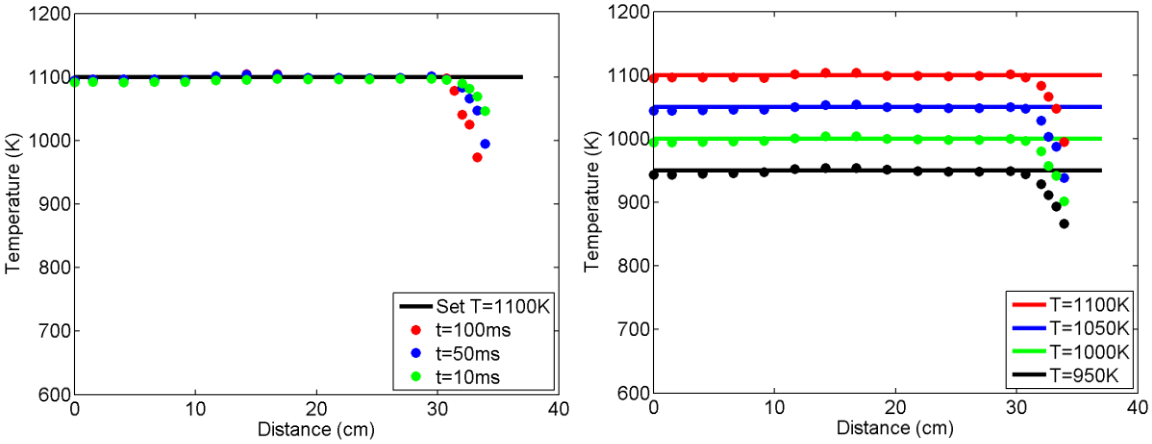

(a) **(b)**

Figure 3.2: Measured temperature inside the atmospheric pressure reactor for set wall temperature, (a) for a target wall temperature of 1100 K at different flow rates corresponding10-100 ms residence time and (b) for 10 ms residence time with varying wall temperature from 950-1100 K.

and side tubes. For a target wall temperature of 1100 K, no significant change in temperatures (±(5-10) K) along the hot section was observed. A separate series of experiments (not presented here) conducted by the addition of fuel and fuel-oxygen to check for endothermic and exothermic effect respectively showed similar trend. However, even with the careful insulation of the reactor exit in all the experiments, a temperature drop of 100-150 K was observed over the last 2.5-4 cm length.

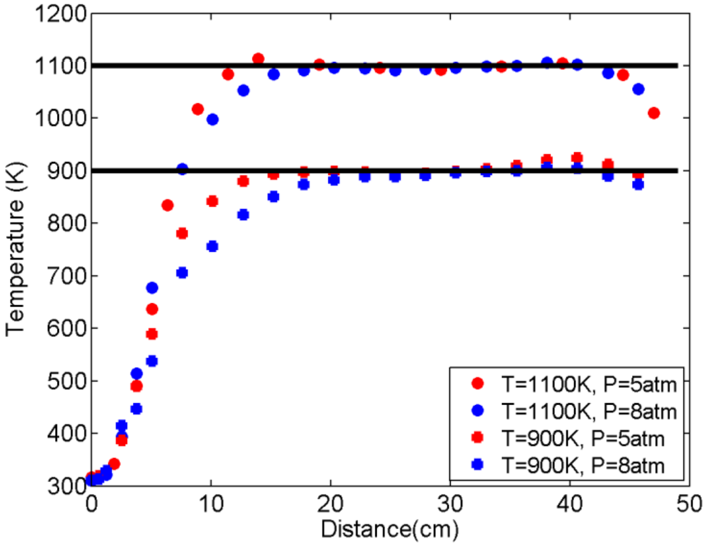

Figure 3.3: Measured temperature profile inside the high-pressure reactor for set wall temperature at p=5 and 8 atm.

Another series of temperature experiments were performed in the high-pressure reactor at 5 and 8 atmospheric pressures. As a chocked orifice was present at the exit, these experiments were conducted by inserting a thermocouple from the inlet of the reactor using a swagelok three-way fitting. The system was allowed to come to a steady state prior to collecting data. Since the high-pressure reactor configuration lacked a preheating helical section as described in Section 2.2.1.2, a transient region of approximately 15 cm was observed in all the experiments as shown in Figure 3.3. In this type of configuration, the reactor can be basically separated into a preheat transient section and a hot, constant temperature, section. Also, a small temperature drop was observed at the exit of the nozzle and radiation correction for temperature may be used to accurately quantify temperature variation. Such corrected temperature vs distance or time plot data can be used in reacting flow calculations as an input to accurately model the system.

3.1.2 Reactor Temperature Validation with Chemical Thermometer

In addition to temperature measurement experiments described above, the temperature of the reactor is further verified by the concept of chemical thermometer. Here, reverse Diels-Alder reaction for unimolecular decomposition of cyclohexene to 1,3-butadiene and ethylene is considered which is given by,

$$\mathrm{cC_6H_{10} \rightarrow C_4H_6 + C_2H_4} \quad , \qquad (3\text{- }1)$$

3.1.2.1 Introduction to Chemical Thermometer

A unimolecular reaction, whose rate parameters for decomposition have been well established from earlier studies, can be used as a standard reaction for this purpose. In general, the process of determining the temperature through this method is known as the chemical thermometry [56].

The rate constant for these standard equations described in Arrhenius or modified Arrhenius form are given by Eq. (3- 2)

$$k = A\,exp\left(-\frac{E_a}{RT}\right)\ or\ k = A\,T^n exp\left(-\frac{E_a}{RT}\right) \quad , \qquad (3\text{- }2)$$

where k is the rate constant, A is a pre-exponential factor, E_a is the activation energy, R is the universal gas constant, T is the temperature and n is a temperature exponent [57].

Equation (3- 2) can be inverted to get the temperature based on rate parameters. In fact, the exponential dependence of rate constant in temperature can be utilized as sensitive and highly accurate measure of temperature [56].

The rate constant of cyclohexene decomposition given by Eq. (3- 1) can be expressed in terms of initial and final mole fraction of cyclohexene and residence time as,

$$k[s^{-1}] = \frac{-ln\left(\frac{[cC_6H_{10}]_f}{[cC_6H_{10}]_i}\right)}{t} \quad , \qquad (3\text{- }3)$$

This reaction is commonly used as chemical thermometer because of the thermal stability of ethylene and 1,3- butadiene offering a wide range of temperatures. The decomposition pathway of cyclohexene into 1,3-butadiene and ethylene is considered to be a major decomposition pathway and regarded as a reference reaction between temperatures 950 - 1100 K. Moreover, ethylene and butadiene are produced in one to one ratio under this condition and mole fraction of cyclohexene at any time *t* can be related to ethylene or butadiene by the following relation [58]:

$$[\mathrm{X}]_{\mathrm{cyclohexene,t}} = [\mathrm{X}]_{\mathrm{cyclohexene,i}} - [\mathrm{X}]_{\mathrm{ethylene/butadiene,t}} \quad , \qquad (3\text{- }4)$$

where, $[\mathrm{X}]_{\mathrm{cyclohexene,i}}$ is initial mole fraction of cyclohexene and $[\mathrm{X}]_{\mathrm{ethylene/butadiene,t}}$ is the mole fraction of ethylene or 1,3-butadiene at time *t*.

Several groups have estimated the rate constant for Eq. (3- 1) based on experimental observations [56], [58]–[62]. Experimental study of thermal decomposition of cyclohexene by Uchiyama et al. [61] in a flow system is one of the earlier work in determining the rate constant at low pressure and temperatures. While their work reports 96% of the total products as ethylene and 1,3-butadiene, the measured 1,3-butadiene was consistently less than ethylene. The reason for this was attributed to formation of 4-vinlycyclohexene from 1,3-butadiene in the temperatures considered. Other species like ethane, propane, propylene, butenes, benzene, 1,3-cyclohexadiene, 1,4-cyclohexadiene and cyclohexane were also observed as products in the experiment. Kiefer and Shah [59] reported a modified Arrhenius expression for very high temperature and low pressure range using a RRKM model. Later, Tranter et al. [60] offered high pressure limit rate coefficient and used to calibrate temperatures behind reflected shock wave. Heyne and Dryer [62] developed a general method to evaluate uncertainties of temperature derived from the decomposition reaction of cyclohexene. Based on the data from shock tubes and static reactors an uncertainty (1σ) of ± 20 K (at 1000K) was reported in the work. However, recently Tsang and Rosado–Reyes [56] pointed out that the temperature determination by Heyne and Dryer is subjected to erroneous results for the reason that they neglected secondary chemistry. The work by Tsang and Rosado –Reyes [56] also offered a comparative rate constant expression based on single pulse shock tube and low pressure flow experiments by Uchiyama et al. [61].

All the important rate expressions with the condition of applicability are summarized in Table 3.1. While the rate constant by Kiefer and Shah [59] and Tranter et al. [60] are applicable for high temperature and pressure, rate constant by Uchiyama et al. [61], Stranic et al. [58] and Tsang and Rosado–Reyes [56] are in the range of pressure applicable for current work. Because of this reason, the plots in the following section will only include rate constants from these expressions.

Table 3.1: Rate Constants from literature at different conditions.

Literature	Rate Constant expression (s^{-1})	Conditions	
		Temperature (K)	**Pressure (atm)**
Uchiyama et. al (1964)	$1.5\times10^{15}\exp\left(-\frac{33233[K]}{T}\right)$	814-902	0.0328
Kiefer and Shah (1987)	$10^{96.37}\,T^{-23.6}\exp\left(-\frac{55953.7}{T}\right)$	1200-2000	0.473-0.723
Tranter et al. (2001)	$4\times10^{15}T^{-0.005}\exp\left(-\frac{33467}{T}\right)$	1050-1350	340.2
Stranic et al. (2013)	$4.84\times10^{14}\exp\left(-\frac{31900[K]}{T}\right)$	950-1300	0.8-3.7
Tsang and Rosado–Reyes (2015)	$10^{15.02\pm0.35}\exp\left(\frac{-33170\pm1000[K]}{T}\right)$		

3.1.2.2 Temperature Measurement in the Reactor Using Chemical Thermometer

Thermal decomposition of 0.23% cyclohexene (purity 99% from Sigma Aldrich) was conducted in the atmospheric pressure micro flow tube reactor. In order to minimize secondary reactions, a very small conversion (2-6%) was achieved by keeping the temperature relatively low at 950 K and residence time was varied from 0.03-0.06 seconds. Nitrogen and argon were used as carrier and reference gases respectively.

The rate constants were calculated from Eq. (3-4) and (3-5) based on both conversion of cyclohexene into ethylene and 1, 3-butadiene mole fraction from experiments. For different residence times, the rate constants and calculated reactor temperatures (using rate constant expression from Table 3.1) are summarized in Table 3.2 and Table 3.3. The temperatures given in Table 3.2 and Table 3.3 have been calculated using ethylene and 1-3,butadiene concentrations respectively. A key point to notice here is the temperatures are very similar using either of the product mole fractions.

The temperatures calculated using the rate constant expression offered by Uchiyama et al.[61] and Tsang and Rosado –Reyes [56] are in very good agreement with the current set temperature (within ±5-10K). As tabulated in Table 3.1, the rate expressions offered by these groups are in a closer range of temperature and pressure to the current study. In spite of the rate expression offered by Stranic et al. [58] being in the range of current experimental condition, the calculated temperatures are within ±15K. The maximum uncertainty of the rate constant offered by Stranic et al. is reported as ±36% for temperature below 1000K. Based on the rate expression offered by Stranic et al. the value of rate constant at T=950K is 1.2638. This value can vary from 0.808-1.718 with maximum uncertainty equivalent to temperature of 937.53-958.77 K. The calculated temperatures using rate constant from Stranic et al. are within this range (See Table 3.2 and Table 3.3.).

Table 3.2: Temperature estimated from experimentally measured decomposition rate of cyclohexene at 950 K and 1 atm for range flow reactor residence time. Temperatures are calculated from rate parameters reported in literature and ethylene mole fractions are used for calculations

Residence time (sec)	**Measured rate constant (s^{-1})**	**Temperature (K)**				
		Uchiyama et al.[61]	**Kiefer and Shah** [59]	**Tranter et al.**[60]	**Stranic et al.**[58]	**Tsang et al.**[56]
0.0295	0.7693	945.55	912.95	925.70	936.16	951.87
0.0393	0.7266	944.02	911.57	924.24	934.59	950.31
0.0487	0.832	947.66	914.85	927.71	938.31	954.01
0.0592	1.0737	954.61	921.12	934.31	945.40	961.06

Table 3.3: Temperature estimated from experimentally measured decomposition rate of cyclohexene at 950 K and 1 atm for range flow reactor residence time. Temperature are calculated from rate parameters reported in literature and 1,3-butadiene mole fractions are used for calculation

Residence time (sec)	**Measured rate constant (s^{-1})**	**Temperature (K)**				
		Uchiyama et al.[61]	**Kiefer and Shah** [59]	**Tranter et al.**[60]	**Stranic et al.**[58]	**Tsang et al.**[56]
0.0295	0.7958	946.47	913.77	926.56	937.09	952.79
0.0393	0.8181	947.21	914.44	927.27	937.85	953.55
0.0487	0.9027	949.87	916.84	930.50	940.57	956.26
0.0592	0.9908	952.41	919.13	932.22	943.16	958.83

As mentioned earlier, the recently proposed rate constant by Tsang and Rosado–Reyes [56] is an averaged rate constant from single pulse experiments and low pressure flow experiments . Their work also reports the uncertainty of $\pm 10^{0.35}\ s^{-1}$ in the rate constant (see Table 3.1) from the expression. Table 3.4 lists the activation energy, the A- factors and the temperature of the reactor considering uncertainties of all the factors reported in the study by Tsang and Rosado–Reyes [56]. The temperature varied from 902-1013 K for the set temperature of 950K at different residence time. Nevertheless, the temperature of the reactor is very close to the nominal value which is very encouraging.

Table 3.4: Temperature of reactor based on uncertainties of E_a and A-factors as reported by Tsang and Rosado–Reyes [56]

E_a/R	**A -Factor**	**Temperature (K)**			
		t=0.0295	**t=0.0393**	**t=0.0487**	**t=0.0592**
32170	2.34E+15	902.31	900.86	904.29	910.83
32170	4.68E+14	945.03	943.45	947.21	954.38
34170	2.34E+15	958.40	956.87	960.51	967.45
34170	4.68E+14	1003.78	1002.10	1006.10	1013.71
33170	2.34E+15	930.36	928.87	932.40	939.14
33170	4.68E+14	974.41	972.78	976.65	984.04
33170	1.05E+15	951.87	950.31	954.02	961.07

3.1.2.3 Comparison of Reaction Rates and Species of Cyclohexene Decomposition

Figure 3.4 compares rate constants for cyclohexene decomposition from the present experimental data at different residence time with rate constant from literature studies. It is seen that the rate constant obtained from the present study is in a very good agreement with the literature rate constants. The models reported by Kiefer and Shah [59] and Tranter et al. [60] are not shown in the figures because the rate constants were inferred from shock tube experimental data performed at high pressures and thus resulted in large discrepancies with current study.

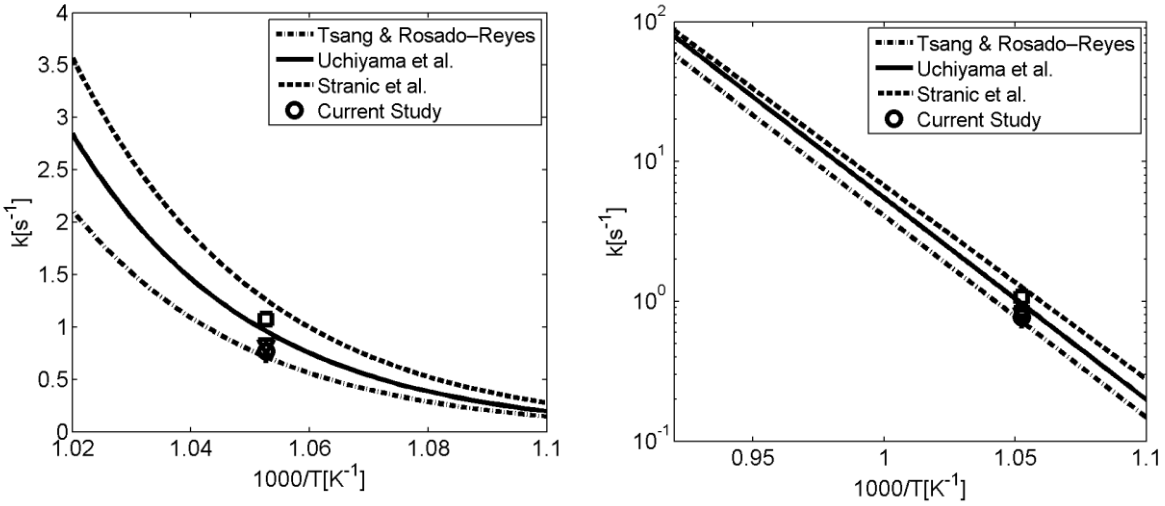

(a) **(b)**

Figure 3.4: Comparison of rate constant for cyclohexene decomposition from present study with rate constant from literature data. Symbol represents results from current study (circle, plus, triangle and square represents residence time from 0.030 to .06 sec). (a) Rate constant with respect to 1000/T (b) log of rate constant with respect to 1000/T.

A standard zero-dimensional Sandia Senkin code in combination with rate parameters for Eq. (3- 1) given by Uchiyama et al. [61], Stranic et al. [58] and Tsang and Rosado –Reyes [56] were considered to analyze the chemical kinetic behavior in the tube reactor. As

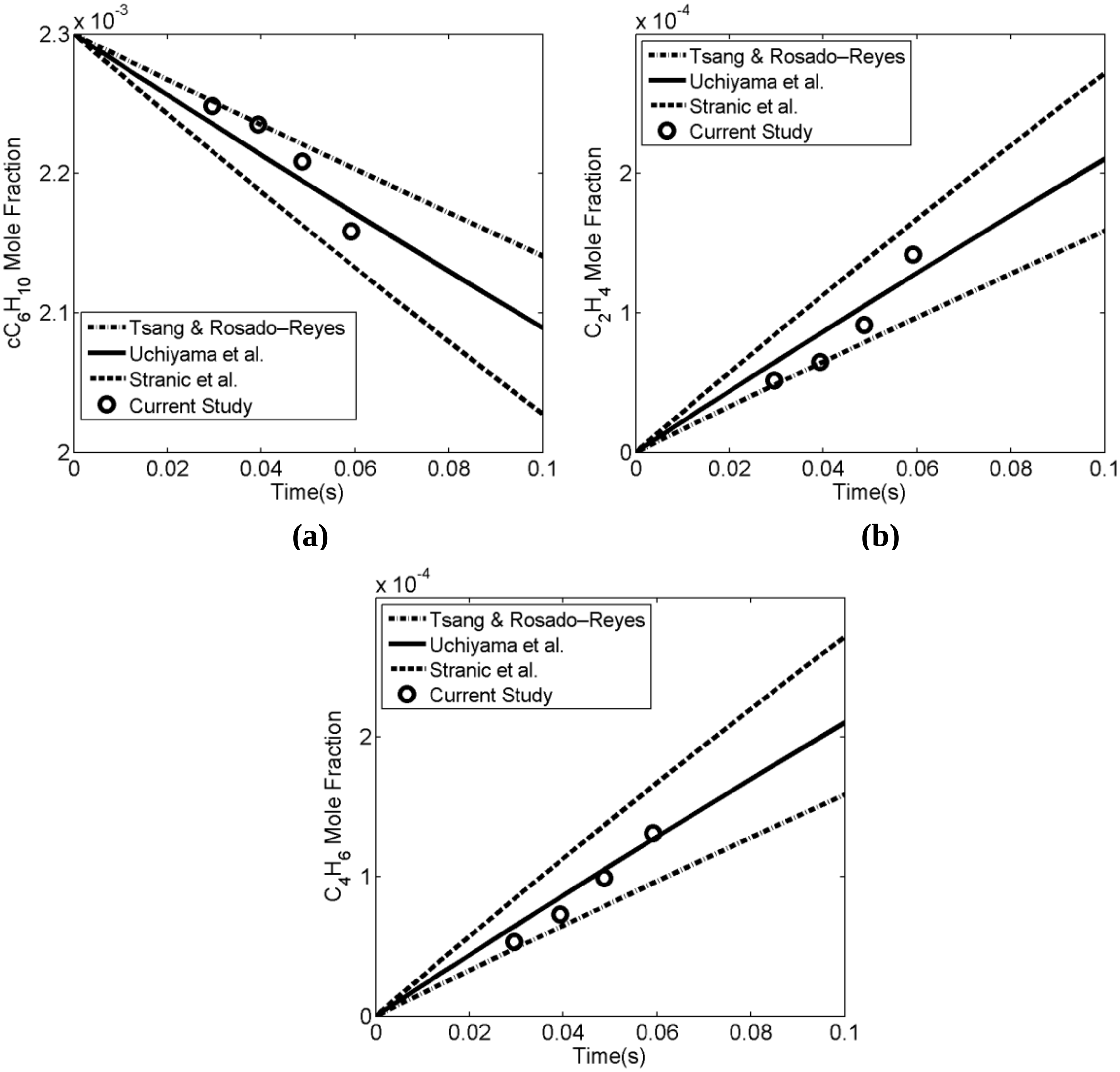

(a) **(b)**

(c)

Figure 3.5: Comparison of species mole fraction in cyclohexene decomposition with respect to residence time with inlet condition [cC_6H_{10}] = 0.23%, [N_2] = 98.77%, [Ar] = 1% and T = 950K (a) cC_6H_{10} (b) C_2H_4 and (c) C_4H_6.

mentioned earlier the current results agree well with the model by Uchiyama et al. [61] and Tsang and Rosado –Reyes [56], which can also be seen in the species mole fractions shown in Figure 3.5. With reference to the temperature results in Table 3.2 and Table 3.3, based on ethylene and 1-3,butadiene respectively and also their mole fractions, these two species were very close to equimolar in concentration. The accuracy of the results is also supported by the fact that there is no discernible concentration of species other than ethylene and 1-3, butadiene in GC chromatograms.

3.2 Fuel and Diluent Mixing Effects

As described in Section 2.1.2, a common way to model the tube reactor is to conduct temporal integration of zero dimensional (0D) governing equations. One of the key assumptions in 0D modelling studies is to neglect flow property gradients in the radial and axial direction. Also, the problem is strongly dependent on initial values of temperature, and species concentrations. In order to use flow reactor data for the development and optimization of chemical kinetic models, it is crucial to understand the limits of experiment. As mentioned in Section 2.2.1.1, a 200 µm porous frit has been added in the reactor just after the mixing section to attain a uniform species profile by improving the mixing of gases coming out from the main and side tubes. To evaluate the extent of mixing in radial and axial direction, mixing quantification studies were conducted before fusing the hot section of the reactor. A 15 µm probe was placed very close to the frit and samples were

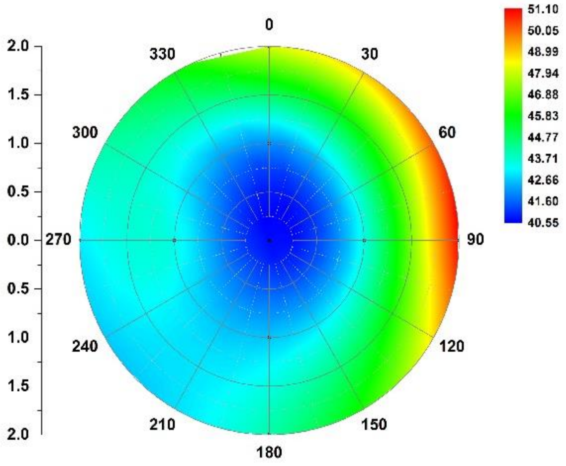

Figure 3.6: Concentration (ppt) of C_2H_4 along the radial direction of the reactor. In flow species composition are $X_{C_2H_4}$=0.042, X_{N_2}=0.757 and X_{O_2}=0.201 at p=1 atm.

taken along the x and y directions and at the center of the reactor. In the mixing investigation, the inflow concentrations of C_2H_4, O_2 and N_2 were selected as 42.2, 20.1 and 75.7 ppt, respectively. Figure 3.6 shows a contour plot for the concentration (ppt) of C_2H_4 at p=1 atm along the radial direction. The plot shows that C_2H_4 is fairly well mixed after the frit except for a small portion on the right side, which may be a result of probe being very close to the reactor wall.

Figure 3.7 (a) shows a schematic of the study conducted to explore mixing along the axial direction of the reactor. Here, 2% C_2H_4 was allowed to flow through the side tube and diluent was allowed to flow from the main tube. Five different locations were sampled using a micro probe. For high pressure study, a needle valve was added at the exit to regulate flow. Further, a good seal was maintained between the reactor and probe using vespel ferrules in combination with swagelok fittings. Figure 3.7 (b) shows experimental results from the mixing study. The plot also include the predicted mixing length by a 3D simulation conducted with and without a frit; the frit was modeled by three layers of equally spaced orthogonal rods in the position of frit [63]. Both the experimental and modeling results show a very good mixing in the current flow reactor. As only three orthogonal rods were used in the modelling study, mixing in experiments appears to be slightly better. The experimental results show the streams are well mixed within 1.36 cm of the length which is equivalent to 3.6% of the total length of the reactor.

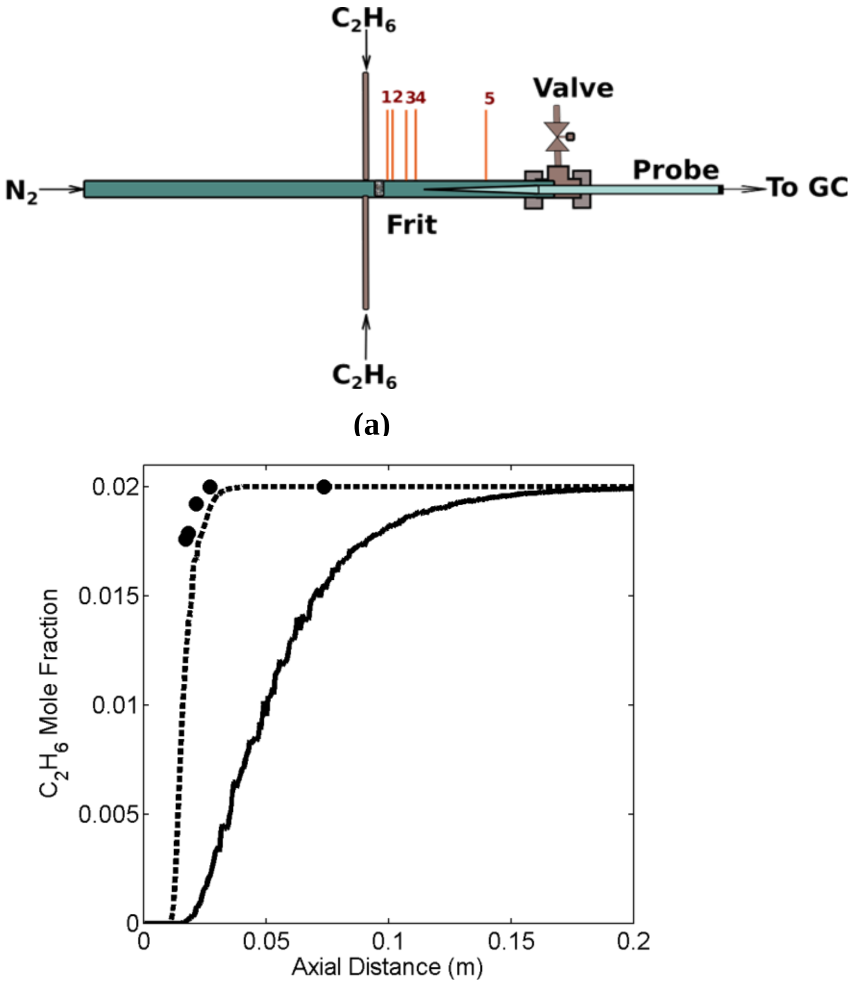

(a)

(b)

Figure 3.7: (a) Schematic for high pressure mixing study depicting positions of the sampling probe (b) Mixing length based on measured species profile along the length. In flow species composition are $X_{C_2H_4}$=0.02, X_{N_2}=0.98 and p=7.6 atm. Symbols represents experimental results, dashed line represents prediction of mixing length with the frit and solid line without the frit.

3.3 Wall Effects on Fuel Pyrolysis

Due to the small reactor diameter, there is a possibility of radical deactivation on the walls of reactor. Even if quartz is a relatively non-reactive material compared to stainless steel, it is essential to understand catalytic effects due to quartz. To determine any catalytic activity of quartz tube walls, fuel pyrolysis experiments were performed with three solid quartz rods 1 mm diameter and 35 cm length placed inside the hot section of the reactor, basically doubling the surface to volume ratio (a schematic of the experimental set up is shown in chapter 5, Figure 5.16 and the dimensions of the rods can be found in Appendix B, Figure B.3). The mass flow rates were adjusted based on the volume occupied by the quartz rods to obtain equivalent flow residence time with and without quartz rods.

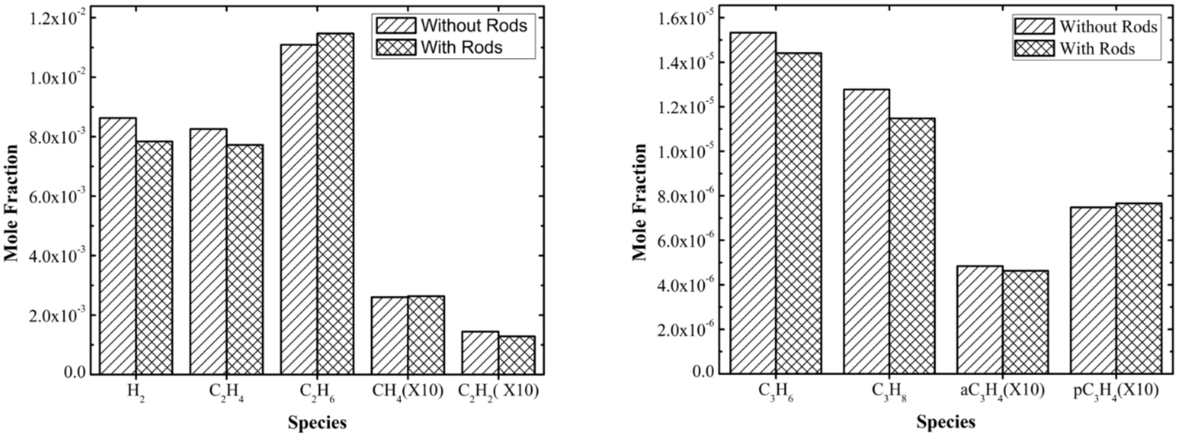

(a) **(b)**

Figure 3.8: Measured (a) Major species and (b) Minor species mole fractions without and with 1mm quartz rods to double the surface to volume ratio, for a case at p=1 atm, T=1100 K, t_{res}= 90 ms, and $X_{C_2H_6}$=0.02, X_{N_2}=0.98.

Figure 3.8 shows that the major and minor species measured at the exit of reactor were generally within the experimental uncertainties. Although some species variations were slightly greater than the experimental uncertainty, one would expect to see that radical species converted to stable species at the reactor wall would lead to an increase in moles of measured stable species. However, a slight overall decrease of stable species was observed which supports the conclusion that there is no significant catalytic effect from wall reactions.

3.4 Summary

Experiments were performed to understand the uniformity of temperature along the length of the reactor, establish the degree of mixing of fuel and diluent after the frit, and to determine the presence of any catalytic/wall effects of quartz. Based on the traditional thermocouple measurement in both the reactors, no significant change in temperatures (±(5-10) K) along the hot section were observed. As anticipated, in the atmospheric pressure reactor with a preheated helical section, a uniform temperature profile was observed. Since, the high-pressure reactor configuration lacked a preheating helical section, a transient region of approximately 15 cm was observed. Temperature being an important kinetic property, the temperature of the reactor was further validated by the concept of chemical thermometer. A standard unimolecular decomposition of cyclohexene into 1,3-butadiene and ethylene whose rate constant has been well established was utilized as a measure of temperature. Similar to the thermocouple measurements, the results indicated the temperature variation within ±5-10K. To evaluate the extent of mixing in radial and axial direction, mixing studies were conducted in atmospheric and high pressure conditions using a microprobe and GC system. The results indicated well mixed fuel and diluent along radial direction and a very well mixed mixture within 3.6% of the length in axial direction. Finally, the catalytic study with three solid quartz rods indicated no significant catalytic effect from wall reactions.

Chapter 4: Homogeneous Thermal Decomposition of Small Hydrocarbon Fuel

4.1 Introduction and Background

Thermal decomposition pathways of smaller hydrocarbon fuels are considered to be reasonably well-understood and have reliable detailed reaction models. Species profile from experimental techniques especially tube reactors and jet stirred reactors (JSR) have contributed significantly in understanding thermal decomposition behavior of these fuels. Dryer et al. [28], [64] developed a variable pressure flow reactor (Princeton turbulent flow reactor, see Figure 2.1 (a)) which consisted of movable injector-diffuser assembly, fixed sampling probe and back pressure valve to conduct chemical kinetic studies at various temperatures, pressures and residence times. Dagaut et al. [65] designed and fabricated a fused silica JSR to study homogeneous gas reactions. The reactor comprised of four nozzles and was capable of withstanding pressure of up to 10 atm while the residence time could be varied from 0.01-3 s. Various other available experiments for small hydrocarbon fuels such as methane, ethane, ethylene, ethyne, propane, propylene, propyne, butane, butenes, and butynes including other larger HC fuels used to validate the chemical kinetic models can be found in a review article by Simmie [66].

With various experimental data available to validate the chemical kinetic models, in 1990s GRI Mech is one of the first considerable efforts to model natural gas combustion (C_1 chemistry with propane and C_2 oxidation products) consisting of 53 species and 325 elementary reactions [67], [68]. The model has been optimized for methane but does not include reactions for combustion of larger fuels. Later, a more comprehensive high temperature model (USC Mech) for H_2/CO/C_1-C_4 with 111 species and 784 reactions was proposed [69]. Follow up kinetic model JetSurF 2.0 [26] consisting of 348 species and 2163 reactions which includes n-dodecane chemistry has also been proposed. Recently, a reaction model (AramcoMech 2.0) focusing on most important reactions of C_1-C_2 species consisting of 493 species and 2716 reactions has been developed by Combustion Chemistry Centre in NUI Galway. The model has been validated against a large array of experimental measurements from shock tubes, rapid compression machines, flames, jet stirred reactors and plug flow reactors [70]. Since considerable efforts have been made in developing H_2, C_1-C_4 reaction models, experimental data obtained for these fuels in the tube reactor can be compared with available reaction model for further verification tube reactor design.

Thermal pyrolysis of two different fuels, ethane and n-butane, was selected for the current study. Along with the reactor characterization studies described in chapter 3, pyrolysis studies will contribute in better understanding temperature of the reactor, need of any zero-time shifting, proper control of residence time, wall effects, mixing issues, effects of sample probing technique and species quantification approach. As described in our recently published paper, for a highly diluted cases such as 2% ethane and n-butane and 0.25% n-dodecane pyrolysis, the variations between 0D, 1D constant temperature and 2D modelling calculations are within experimental uncertainties [50]. Due to this reason, the result section will compare the obtained experimental results with model calculations using standard 0D Senkin code in combinations with various reaction models from the literature.

4.1.1 Ethane Experimental Studies and Kinetic Models in Literature

Due to the fact that ethane is an intermediate species for pyrolysis and oxidation of many lighter and heavier HC fuels, several researches have shown a deep interest in ethane pyrolysis and oxidation. For example, an ethane oxidation study was carried out by Dagaut et al. [71] in a JSR for the temperature and pressure range of 800-1200 K and 1-10 atm using a GC sampling technique. A kinetic reaction model was proposed which was validated against the obtained JSR data and ignition delay time from shock tube experiments. Later, ethane oxidation experiments and modelling work were conducted by Hunter et al. [29] at approximately T=925 K and p=3,6 and 10 atm in a high pressure flow reactor in an effort to expand GRI mech 1.1 to include ethane oxidation at intermediate temperatures and higher pressures. The species profiles were explored using GC/FID/TCD and GCMS. Realizing the lack of combined study of ethane pyrolysis and oxidation, Hidaka et al. [72] carried out these studies in 4.1 cm i.d. shock tubes. A temperature range of 950-1900 K was explored and the product species were analyzed with GC and other spectroscopic techniques. However, the residence time was fairly short i.e. in the micro second range (around 100-3000 µs).

Tranter et al. [73], [74] explored ethane pyrolysis and oxidation experiments in a high-pressure shock tube, ranging from 5 to 1000 bar, at intermediate temperatures and offered a reaction model based on previously published models (Miller 2001 and GRI mech 3.0). Later, Naik and Dean [75] developed a detailed chemical kinetic model for ethane oxidation covering a wide temperature range and compared their model with data at low, intermediate, and high temperature regimes with pressure up to 10 atm. More recently, the model was extended covering a much higher pressure (0.1-1000 atm) and temperature (298-2500 K). The model consists of 181 species and 2066 reactions [76]. Their model has been compared to experimental data from stirred reactors, flow reactors and shock tubes. However, the rate constants have not been adjusted to match the experimental data to eliminate any effects on reaction rates from one temperature regime to another.

4.1.2 n-Butane Experimental Studies and Kinetic Models in Literature

In contrast to ethane, relatively few studies have been performed with n-butane. Marinov et al. [77] performed an experimental and modelling investigation of an atmospheric pressure laminar n-butane-oxygen-argon flame with an objective to identify reaction sequence for the formation of aromatic and polycyclic aromatic HC. Online GC/TCD/MS in combination with micro-probes were used for gas sampling. The model was able to predict most of the smaller HCs reasonably well. However, the model was unable to capture the trend of some of the important intermediate species such as C_2H_4. Dagaut et al. [78] conducted a study on reduction of NO in a JSR at 1 atm. Apart from experiments with added NO, a neat n-butane oxidation (0.22%) experiments was also included in the study. The experiments were conducted with temperature and equivalence ratio varied from 1000-1450 K and 0.5-1.5, respectively, and at a residence time of 0.16 s. The concentration profiles were obtained by using an in-line FTIR (Fourier Transform Infrared Spectroscopy) and off-line GC-TCD/FID and a detailed chemical kinetic model was also proposed which matched reasonably well with the experimental data. The decomposition rates of n-butane and iso-butane were studied from 1297 K-1600 K at 0.2-0.88 atm in a shock tube using a UV laser absorption spectroscopy by Oehlschlaeger et al. [79]. The study offered updated rate coefficients for the key reactions $i\text{-}C_4H_{10} \rightarrow CH_3 + i\text{-}C_3H_7$, $n\text{-}C_4H_{10} \rightarrow CH_3 + n\text{-}C_3H_7$ and $n\text{-}C_4H_{10} \rightarrow C_2H_5 + C_2H_4$.

More recently, Pyun et al. [80] conducted n-butane and n-heptane pyrolysis experiments in a shock tube at temperatures of 1254 K-1565 K and pressure in the range of 1.45-1.64

atm with 1% fuel in an effort to improve time history measurements of CH_4 and C_2H_4 using laser absorption diagnostic technique. Four different reactions for n-butane, two of which are decomposition reaction rates from Oehlschlaeger et al. [79], and six reactions for n-heptane were modified in the model to match mole fraction profile of CH_4 and C_2H_4. Recently, Su and Zhang [81] conducted a quantitative measurement of methane from n-butane pyrolysis experiments in a flow reactor. The investigation was focused on measurement of methane at atmospheric pressure using absorption spectroscopy. While some of these studies have proved pioneering to the lower alkane reaction model uncertainty, the need of accurate experimental data especially for n-butane is considerable.

4.2 Ethane Pyrolysis Results Comparison with Detailed Chemical Kinetic Models

4.2.1 Ethane Pyrolysis Results at Atmospheric Pressure

Ethane pyrolysis experiments were conducted at atmospheric pressure in the UVa MFTR by varying the flow velocity to capture the residence time effect in species profile at two different temperatures.

Figure 4.1 shows the ethane conversion as a function of temperature in comparison with numerically predicted ethane pyrolysis results using three models: (i) JetSurF 2.0 chemical kinetic model by Wang et al. [26], (ii) an optimized ethane pyrolysis model by Naik and Dean [76], and (ii) a recent model by Curran and coworkers (AramcoMech 2.0) [70]. As seen from the figure, at the temperature of 1100K, about 40% ethane has been converted to the other species, namely C_2H_4, H_2, CH_4, C_2H_2, C_3H_6, C_3H_8, aC_3H_4 and pC_3H_4, in descending order. The plots of species profile with respect to residence times for two different temperatures are depicted in Figure 4.2 to Figure 4.5 separated between major and minor species for temperatures of 1050K and 1100K. Lists of these species in the present study are consistent with shock tube experiments by Hidaka et al. [72] and Tranter et al. [73], [74].

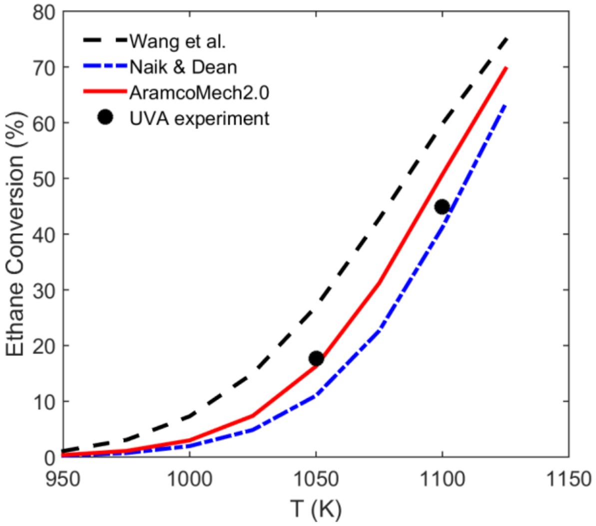

Figure 4.1: Comparison of ethane conversion as a function of temperature. Symbols represent experimental results and lines represent predictions with three models by Wang et al. [26], Naik and Dean [76] and Curran and co-workers (AramcoMech 2.0 [70]), for inflow species compositions of $X_{C_2H_6} = 0.02$, $X_{N_2} = 0.98$ and p=1 atm and residence time of 90 ms.

One of the important factors to be concluded from these comparisons is the fact that there is no issue of profile shifting (zero time) to match the experimental data with model predictions. The reason for this can be attributed to the small mixing volume (0.2 cm^3) of the reactor which has negligible effect on the overall experimental results. Further, the overall trend of the experimental results is very close to the simulation results in terms of time as well as temperature.

Reaction pathway and sensitivity analysis described in the paper by Shrestha et al. [50] highlights the dominant reactions controlling the ethane pyrolysis at T=1100 K from 0.1

ms to 100 ms. At peak ethane pyrolysis conditions, the dominant path is the hydrogen abstraction leading to the formation of ethyl radical, followed by the third-body collision reactions forming ethylene. In addition, ethane reaction with methyl contributes to about 1% of ethane destruction at 50 ms and to some extent explains the delayed methane formation by this reaction (or large ethylene to methane ratio at low residence times). Difficultly in methane peak integration in shock tube experiments conducted by Tranter et

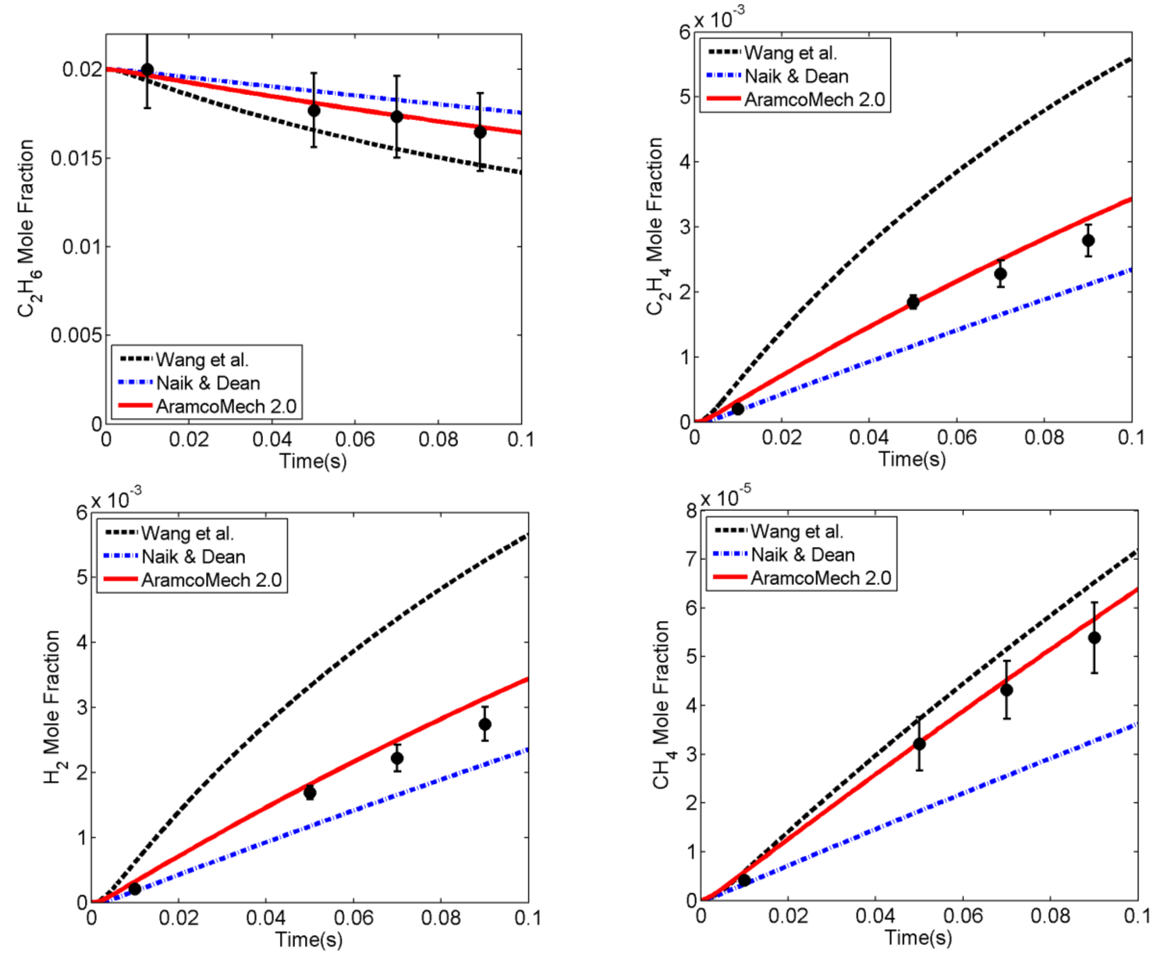

Figure 4.2: Comparison of **major** species mole fraction as a function of time for the hot section temperature of **1050 K**. Symbols represent experimental results and lines represent predictions with three models by Wang et al. [26] , Naik and Dean [76] and Curran and co-workers (AramcoMech 2.0 [70]), for inflow species compositions of $X_{C_2H_6}$ = 0.02, X_{N_2} = 0.98 and p=1 atm.

al. [73] is also explained by the delay in methane formations. Reaction pathway flux analysis for the residence time of 100 ms and 1100 K temperature indicates that 1,3-butadiene leads to the formation of allene and propyne and are consistent with the experimental results.

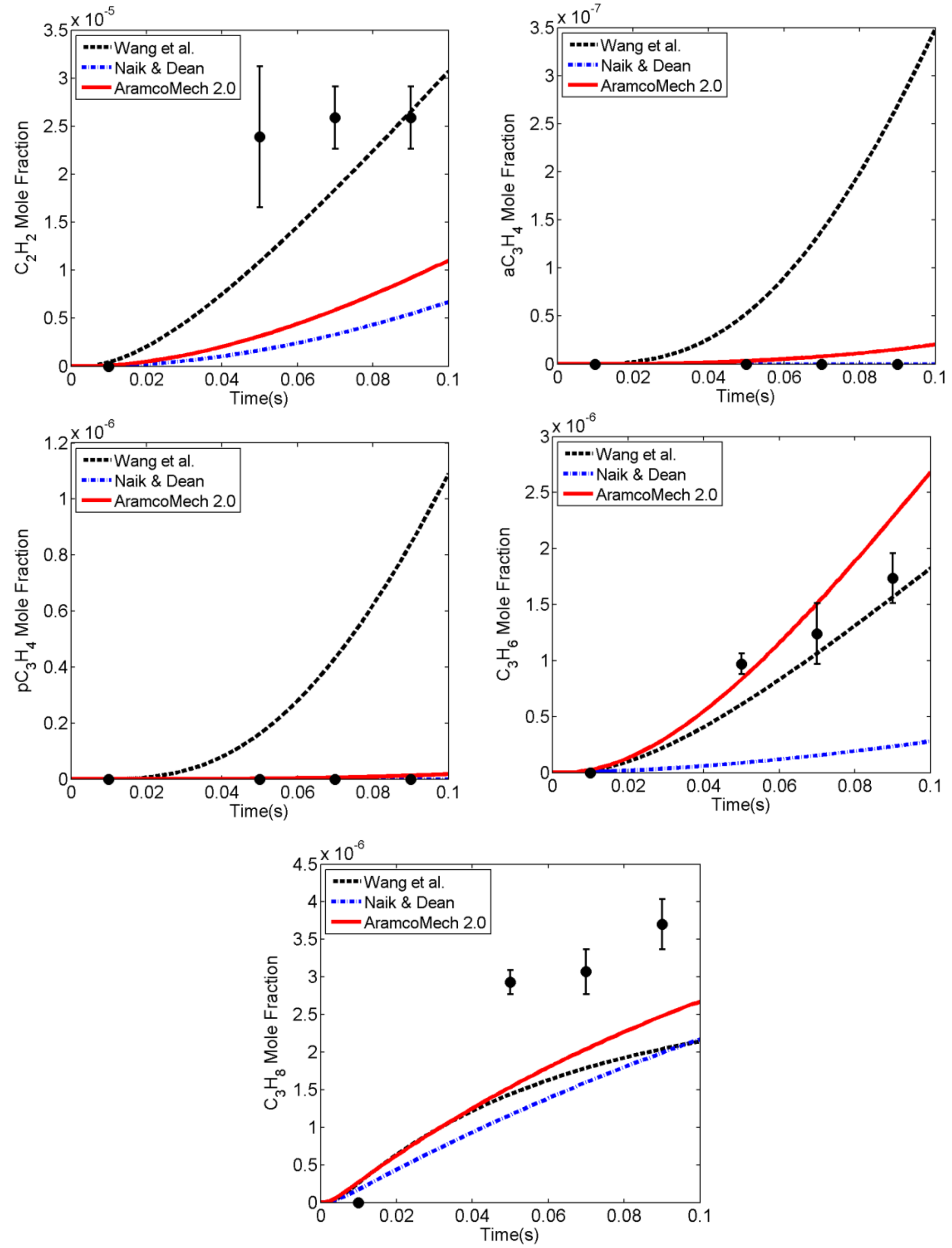

Figure 4.3: Comparison of **minor** species mole fraction as a function of time for the hot section temperature of **1050 K**. Symbols represent experimental results and lines represent predictions with three models by Wang et al. [26] , Naik and Dean [76] and Curran and co-workers (AramcoMech 2.0 [70]), for inflow species compositions of $X_{C_2H_6}$ = 0.02, X_{N_2} = 0.98 and p=1 atm.

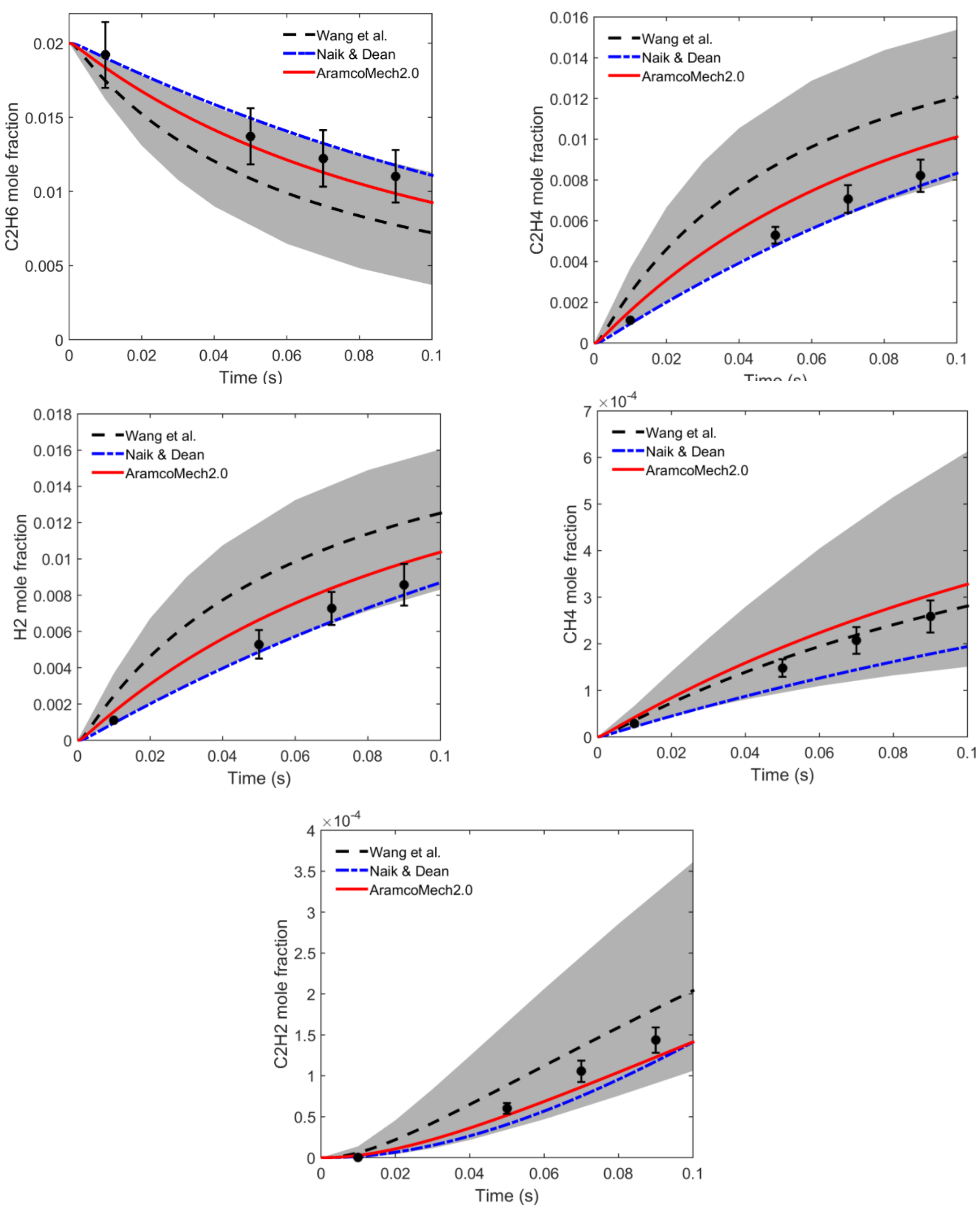

Figure 4.4: Comparison of **major** species mole fraction as a function of time for the hot section temperature of **1100 K**. Symbols represent experimental results and lines represent predictions with three models by Wang et al. [26] , Naik and Dean [76] and Curran and co-workers (AramcoMech 2.0 [70]), for inflow species compositions of $X_{C_2H_6}$ = 0.02, X_{N_2} = 0.98 and p=1 atm. The shaded area indicates the 2σ model prediction uncertainty.

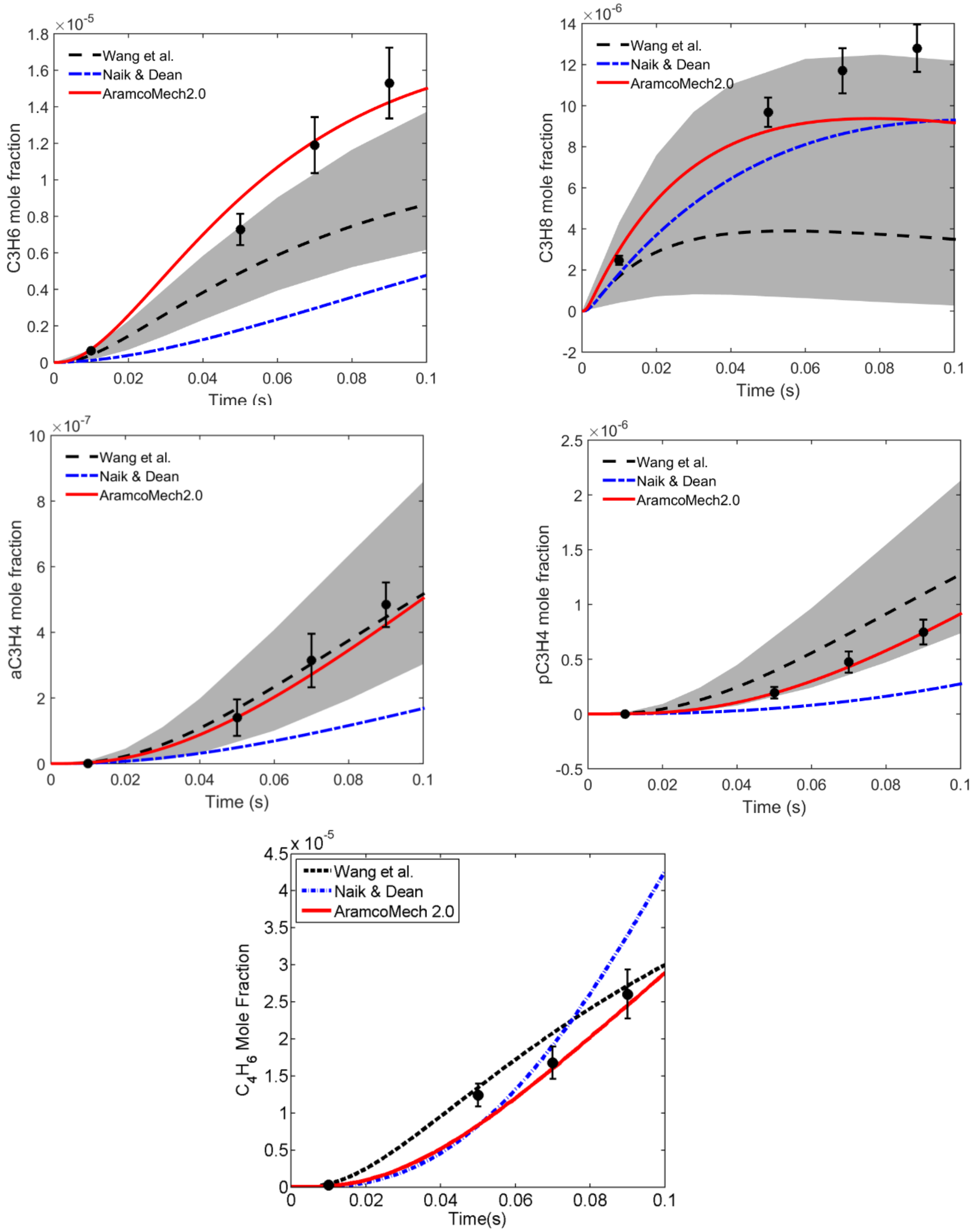

Figure 4.5: Comparison of **minor** species mole fraction as a function of time for the hot section temperature of **1100 K**. Symbols represent experimental results and lines represent predictions with three models by Wang et al. [26] , Naik and Dean [76] and Curran and co-workers (AramcoMech 2.0 [70]), for inflow species compositions of $X_{C_2H_6} = 0.02$, $X_{N_2} = 0.98$ and p=1 atm. The shaded area indicates the 2σ model prediction uncertainty.

The two models considered here predict to a certain extent different reactant decomposition and product formation. The Naik and Dean model [76] is able to capture the tube reactor results for C_2H_4, C_2H_6 and H_2, while it is less accurate for other species. The reason for this might be the fact that this model has been optimized for concentration profiles of C_2H_4, C_2H_6 and H_2 with experimental results reported by Dagaut et al. [71] at the temperatures close to that explored in our present study. However, they didn't consider methane and other C_3 species in their comparison which might be a reason for the model's difficulty in capturing the time evolution of such important species accurately. Also, as JetSurF 2.0 is intended for dodecane, it is expected to capture smaller alkane pyrolysis experiments well. However, the model's result did not match experimental data as well as Naik and Dean's model.

The experimental results show a very good agreement with the recently published Aramco Model [70]. As explained in the introduction this model has been extensively validated with experimental results from shock tubes, rapid compression machines, flames, jet stirred reactors and plug flow reactors and covers C_1 to C_4 species including ethane [82]. The agreement between the results of the present experiment and the most recent rigorously developed model is an encouraging sign that the MFTR is indeed well suited for investigations of species-time evolution at the range of temperatures and residence times studied.

Another key observation is that there exists a huge variation of results between the available models. Due to large number of elementary reactions involved in these models, large uncertainties exist in chemical kinetic parameters used in these models. These parameters are often derived either from theoretical calculations or obtained from experimental results. Due to the extreme difficulty in accurately determining all the parameters required to define the reactions, some parameters are assumed or guessed based on similar reactions whose parameters have been derived from any of the methods mentioned earlier. The process of determining rate constants becomes especially difficult for radical species which contribute further to uncertainties in the overall model. As seen in Figure 4.2 to Figure 4.5, the three models predict significantly different product distribution. The reason for the variation lies in the difference in reaction rates of sensitive reactions used in these models. The details of sensitivity analysis and reaction rates for these models can be found in the recently published paper by Shrestha et al. [50]. Further, Figure 4.4 and Figure 4.5 also includes the bound to bound uncertainty of model parameters (shaded area) based on Monte Carlo calculations by perturbing the top 15 sensitive reactions of Wang et al. [26] model. It can be observed that compared to model uncertainty, the experimental uncertainty is much narrower implying that the present data can be used to minimize the uncertainty of the key rate controlling reactions.

Another encouraging factor of the current results is the prediction of minor species such as aC_3H_4, pC_3H_4 and C_2H_2, which matched well with Aramco Mech 2.0 at 1100K. As explained in chapter 1, while C_2H_2 is one of the key soot precursors, aC_3H_4 and pC_3H_4 are also primary source of propargyl radicals, which is related to formation of benzene and PAH molecules [22], [83]. Thus, the results from the current study can be used to further improve these reaction models and help accurate prediction of soot precursors.

4.2.1.1 Uncertainties of peak integration in GC analysis

One of the main contributions to uncertainty of measured species is improper GC peak integration [84][85]. The following critical peak integration issues where observed during this study.

Measurement of C_4 species

As mentioned in species quantitation section, the current GC system consists of series of packed columns designed to minimize the species analysis duration, typically about 20 mins. The system has a good retention time resolution for C_1-C_3 species, while C_4 species quantification suffer from overlapping peaks of as shown in Figure 4.6. Even though this chromatogram for propylene and propane generated from standards are very close to each other, they are still identifiable and have been quantified accurately. On other hand, retention times for standards of isobutylene, 1-butene, butane, trans-2-butene and 1,3-butadiene are given by 19.197, 19.245, 19.623, 19.906 and 19.907 mins, respectively, and can introduce significant uncertainties. It can also be seen that the peaks of isobutylene and1-butene, and the peaks of trans-2-butene and 1,3-butadiene overlap with each other, while retention time for butane is noticeably different from other C_4 species.

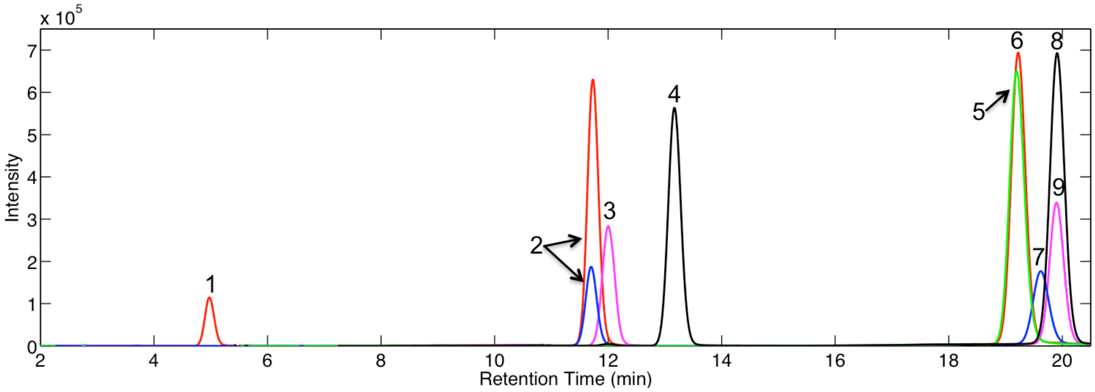

Figure 4.6: GC Chromatogram using standards. 1 - Acetylene, 2 - Propylene, 3 - Propane, 4 - Propadiene, 5 - Isobutylene, 6 - 1-Butene, 7 - Butane, 8 - Trans-2-butene, 9 - 1,3 Butadiene.

Figure 4.7 shows an actual chromatogram for an ethane pyrolysis experiment, for inflow species composition of $X_{C2H6} = 0:02$, $X_{N2} = 0.98$, p = 1 atm and T = 1100K and for several

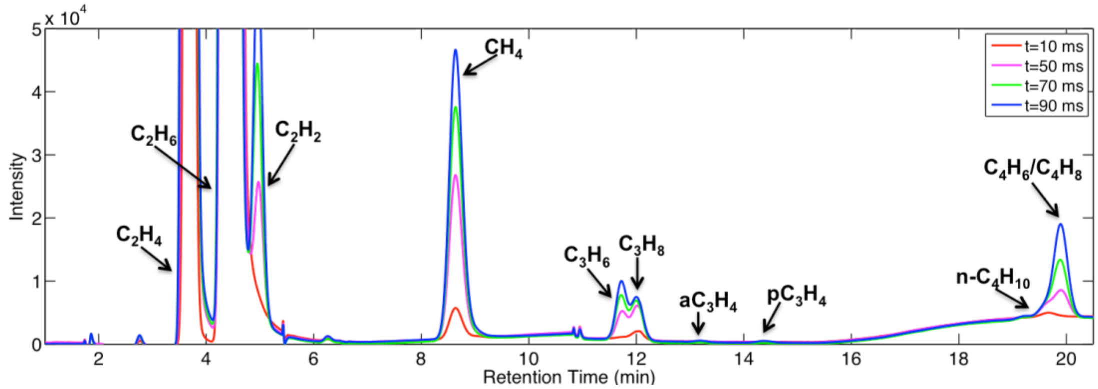

Figure 4.7: GC Chromatogram from actual ethane pyrolysis experiment, for inflow species composition of $XC_{2H_6} = 0.02$, $X_{N_2}=0.98$, T=1100K, p=1 atm, and several reactor flow residence times.

residence times. The increase in area peaks clearly correlates with increase in residence times in the reactor. In particular, the chromatogram shows that at reactor residence time of 10ms, there are clear signs on formation of n-butane but as the residence time is increased, the chromatogram of either trans-2-butene or 1,3-butadiene swallows the n-butane peak. Thus, a better resolution of chromatogram is required for proper quantification of C_4 species or the use of the GC-MS system available with capillary columns. Nevertheless, the results for 1,3-butadiene matched well with model prediction at T=1100K.

Measurement of Acetylene

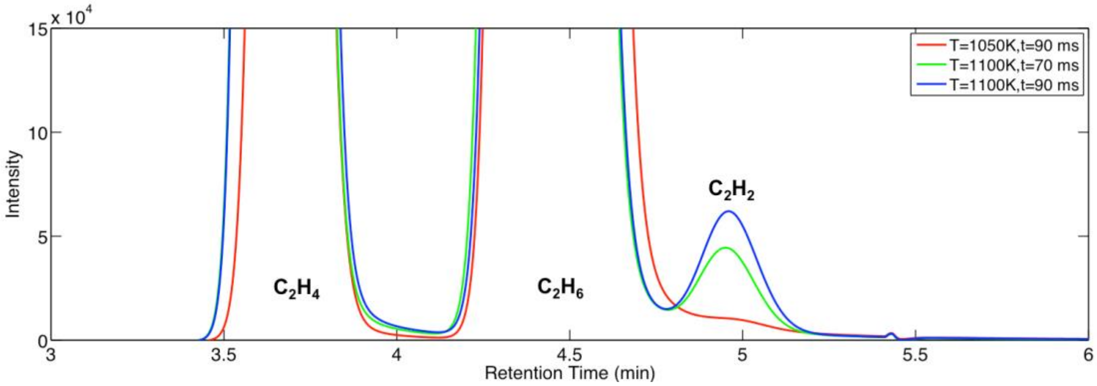

Figure 4.8: GC Chromatogram from an actual ethane pyrolysis experiment showing ethylene, ethane, and acetylene peaks for selected residence times and temperatures at p=1 atm and inflow species composition of $XC_{2H_6} = 0.02$, $X_{N_2}=0.98$.

Figure 4.8 shows GC chromatograms with peaks of ethylene, ethane, and acetylene for selected residence times and reactor temperature of 1050K and 1100K. It can be observed that the retention time of these C_3 species are quite close. Also, the acetylene peak at T=1050K and residence time of 90 ms is not completely resolved, mainly due to the asymmetric peak of ethane at higher concentrations.

Tailing of peaks are also inevitable in chromatographic investigations and clearly seen in this study. These effects were mostly prominent for large concentrations, such as those seen of ethane. In order to avoid any errors associated with overlapping or tailing peaks, method of peak heights was used as a calibration and measurement parameter to quantify the pyrolyzed species concentrations instead of areas. Specifically, it was verified that the peak heights were linear for a range of concentrations used in this study (Figures are given in Appendix B i.e. Figure B.1 and Figure B.2)

4.2.2 Ethane Pyrolysis Results at Elevated Pressures

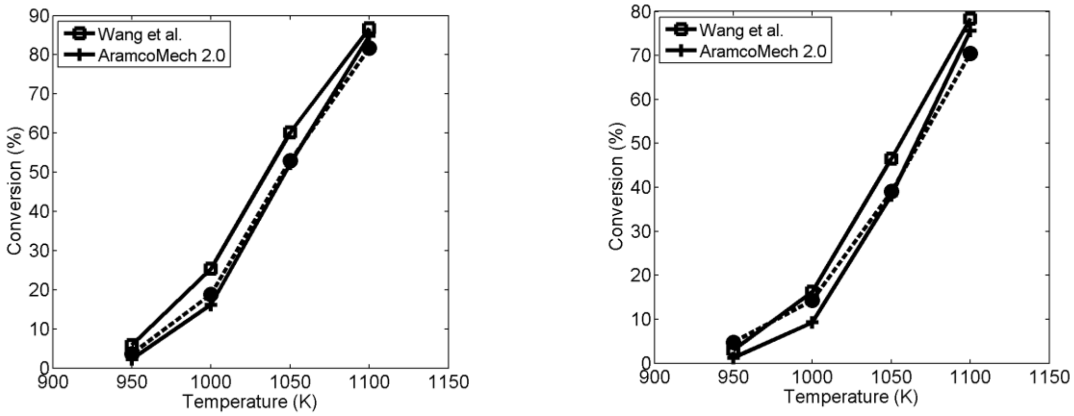

(a) **(b)**

Figure 4.9: Comparison of ethane conversion from the current experiments as a function of temperature with two models by Wang et al. [26] and AramcoMech 2.0 [70] at (a) **p=5 atm** and (b) **15 atm**. Solid lines/square symbols represent prediction with model by Wang et al., solid lines/plus symbol represent prediction with AramcoMech 2.0 and dashed line/ filled circles represent present experimental results. Inflow species compositions of $X_{C_2H_6}$ = 0.02, X_{N_2} = 0.98 and residence time ~ 590 ms.

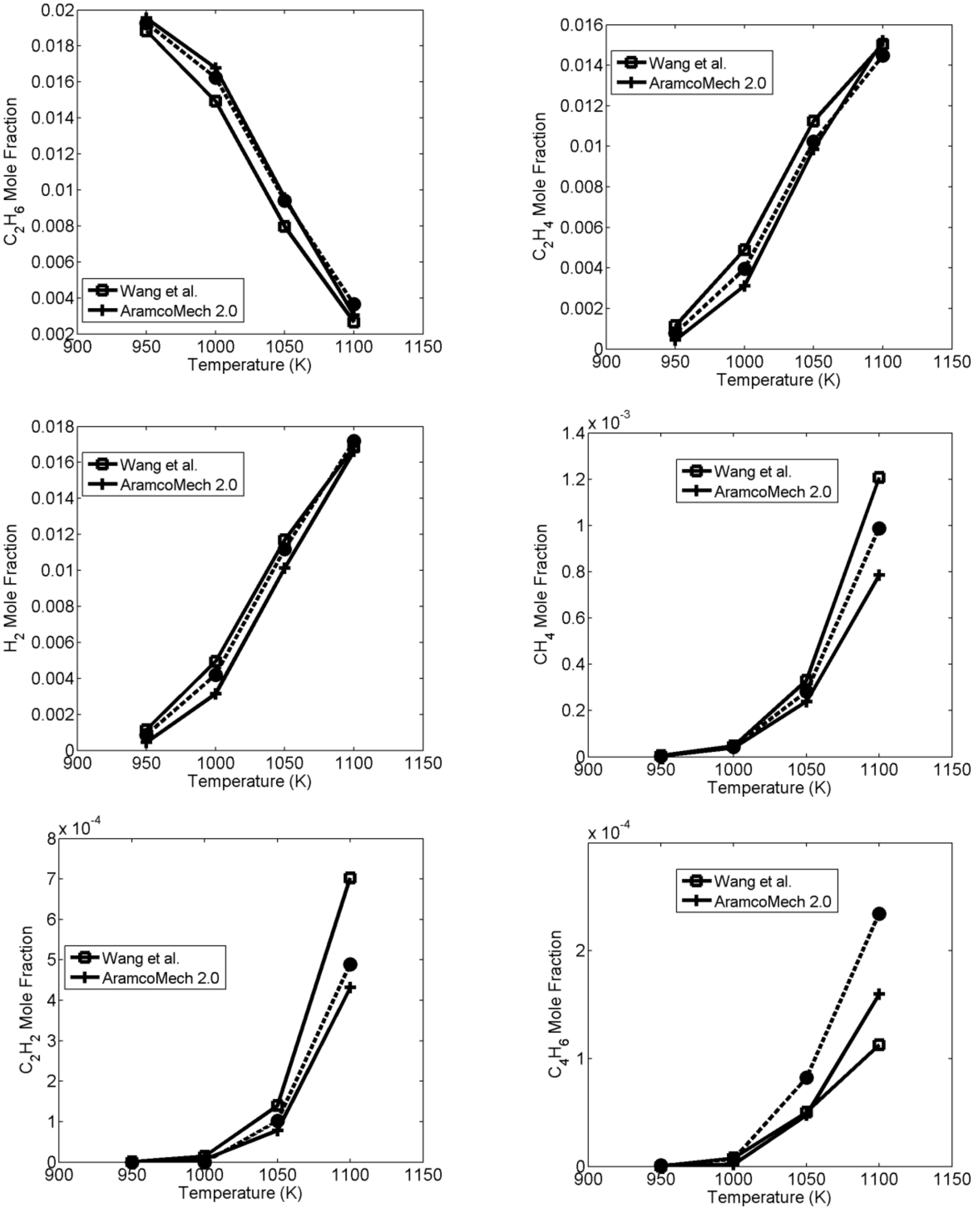

Figure 4.10: Comparison of species mole fraction (**major species**) from the current experiments at **p=5 atm** as a function of temperature with two models by Wang et al. [26] and AramcoMech 2.0 [70]. Solid lines/square symbols represent prediction with model by Wang et al., solid lines/plus symbols represent prediction with AramcoMech 2.0 and dashed line/ filled circles represent present experimental results for inflow species compositions of $X_{C_2H_6} = 0.02$, $X_{N_2} = 0.98$ and residence time ~ 590 ms.

Ethane pyrolysis experiments were conducted in the high-pressure reactor for pressure range of 5 to 15 atm, temperature from 950 to1100K, and residence time ~ 590 ms. While species measurements are presented for pressures up to 15 atm, the reactor assembly have been tested to a differential pressure of 25 atm at 1100K. Figure 4.9(a) and Figure 4.9(b) shows ethane conversion at various temperatures at 5 and 15 atm compared to with two models by Wang et al. [26] and AramcoMech 2.0 [70]. Aramco Mech 2.0 was chosen for

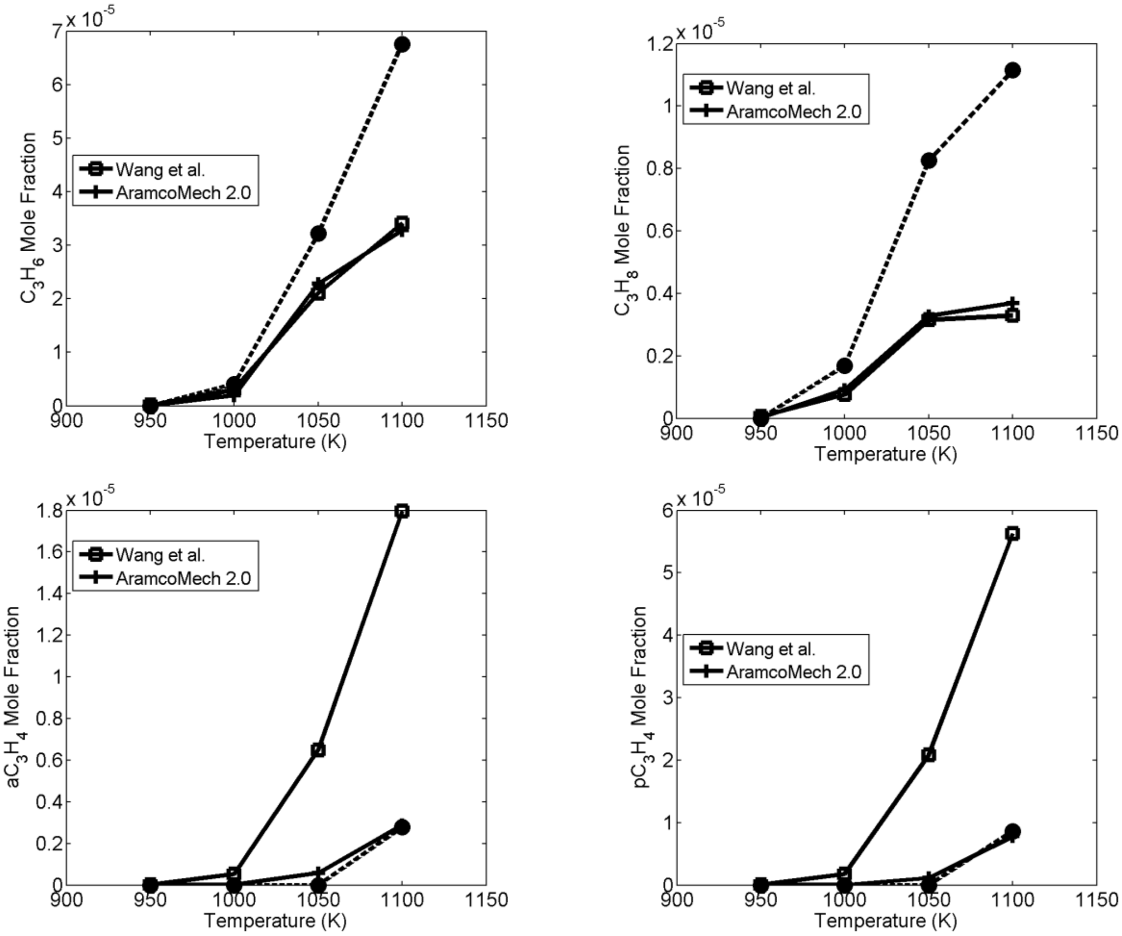

Figure 4.11: Comparison of species mole fraction (**minor species**) from the current experiments at **p=5 atm** as a function of temperature with two models by Wang et al. [26] and AramcoMech 2.0 [70]. Solid lines/square symbols represent prediction with model by Wang et al., solid lines/plus symbol represent prediction with AramcoMech 2.0 and dashed line/ filled circles represent present experimental results for inflow species compositions of X $_{C_2H_6}$ = 0.02, X_{N_2} = 0.98 and residence time ~ 590 ms.

comparison because the experimental results for ethane pyrolysis at p=1 atm was well predicted by AramcoMech 2.0. Over the temperature range from 950 to 1100K ethane conversion varied almost linearly from 5% to 90% for both p=5 atm and p=15 atm. At the same temperature of 1100K, compared to ethane conversion at p=1 atm and t_{res}=90 ms (see Figure 4.1), ethane conversion at p=5 atm and t_{res} ~ 590 ms almost doubled and converted into similar species such as ethylene, hydrogen, methane, acetylene, 1-3 butadiene, propylene and propane as shown in Figure 4.10 and Figure 4.11. While both models predicted ethane, ethylene and hydrogen well, the prediction by AramcoMech 2.0 is slightly better for ethane and ethylene. Also, AramcoMech 2.0 captured the important species trends such as acetylene, allene, and propyne from the current study. However, both models are not able to capture the trends of species such as methane, propylene, propane and butadiene. The experimental results along with model prediction followed similar trends at other pressures and can be found in Appendix C (Figure C.1 to Figure C.4).

As explained in chapter 3, the fuel and diluent is premixed before entering the heated section. While the atmospheric pressure reactor consisted of a well-controlled temperature profile, the high-pressure reactor consists of a temperature ramp up region before the hot section. Thus, temperature profiles were used as an input in the calculations. One of the disadvantages of using such reactor is slight variation in residence time with change in pressure.

With increase in pressure, the ratio of residence time in constant temperature hot section to time spend in the pre-heating section decreases considerably as shown in Figure 4.12. Unlike in the nearly ideal case achieved in the atmospheric pressure reactor, the total residence time is dependent on the overall flowrate, which is in turn dictated by the target pressure, as the fuel and diluent are premixed. This creates difficulty in defining the exact point of reaction initiation. For example, if the reaction threshold is taken as 0.1× maximum mole fraction of H atoms as shown in Figure 4.12, then a residence time of 590 and 540 ms is found for pressure of 5 and 15 atm, respectively. Thus, the premixed configuration presents uncertainty in defining exact residence time for the reacting flow. While the results presented at elevated pressure have small variation in residence time, a temperature profile has always been input into the model to obtain the temporally-resolved

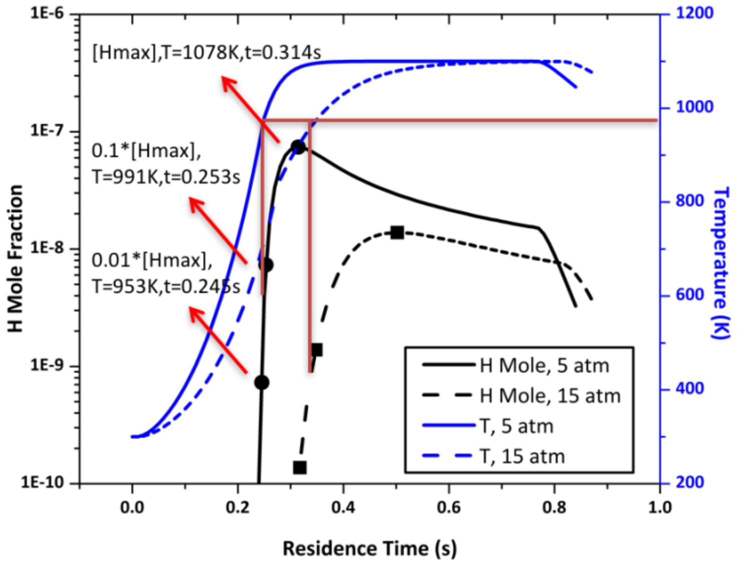

Figure 4.12: Effect of temperature ramp up on residence time. H-atom mole fraction and temperature (at T=1100K) plot with residence time at p = 5atm and p = 10atm. Inflow condition $X_{C_2H_6} = 0.02$, $X_{N_2} = 0.98$.

species profile. The mole fractions of major and minor species with respect to time are compared with the model by Wang et al. [26] and are depicted in Figure 4.13 and Figure 4.14. It can be observed from these figures that the reaction in the reactor is not initiated until t ~ 300-400 ms. Nevertheless, if accurate temperature profiles are included in calculations, the reactor is capable of capturing the species distribution.

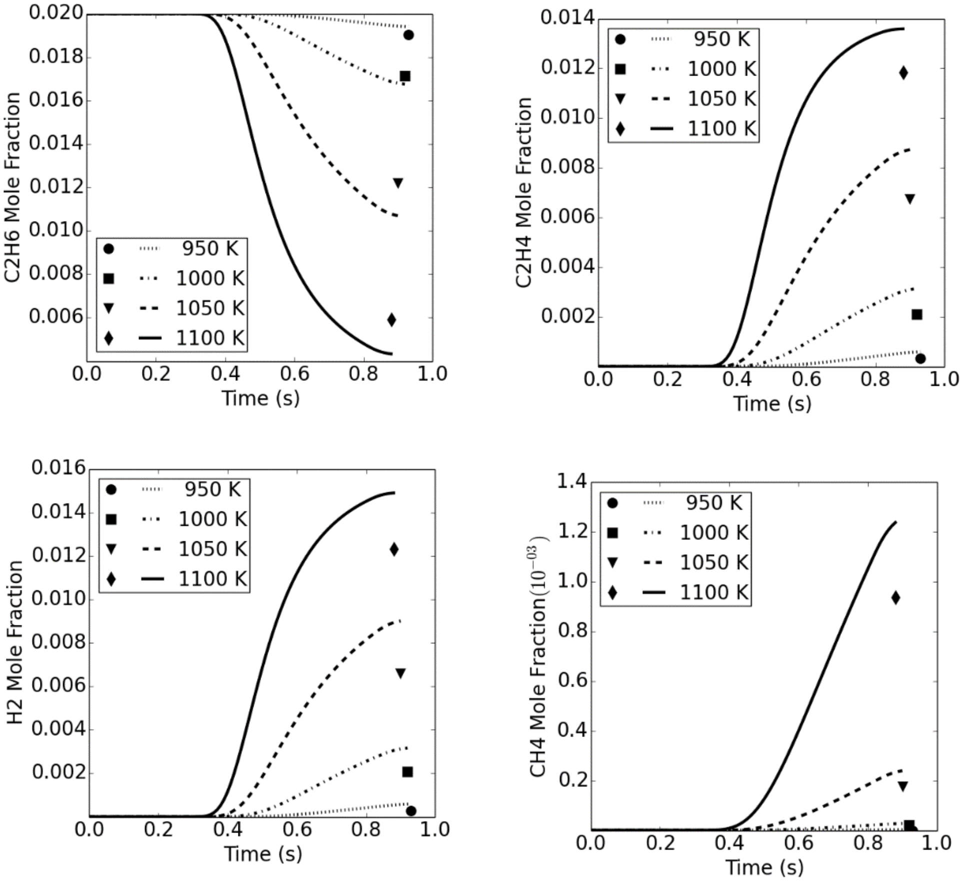

Figure 4.13: Comparison of **major** species mole fraction in ethane pyrolysis with respect to time, at different temperatures (experiments (symbols) and predictions (lines)) with model by Wang et al. [26], In flow species composition are $X_{C_2H_6}$=0.02, X_{N_2}=0.98 and p=15 atm.

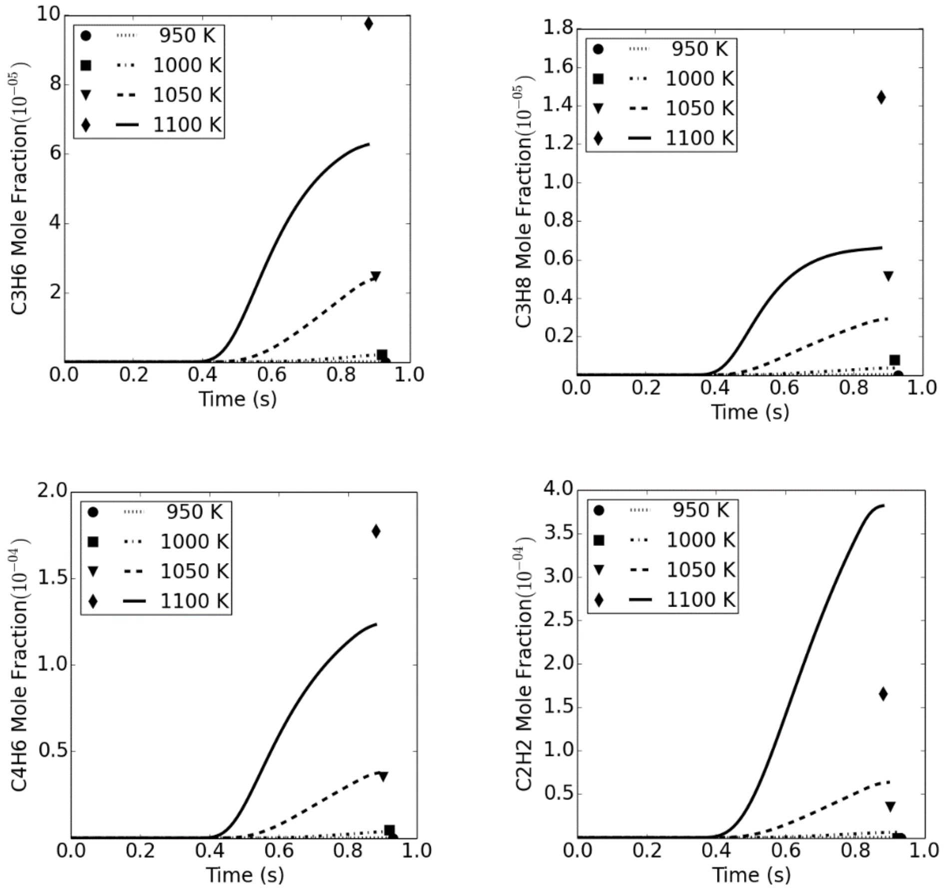

Figure 4.14: Comparison of **minor** species mole fraction in ethane pyrolysis with respect to time, at different temperatures (experiments (symbols) and predictions (lines)) with model by Wang et al. [26], In flow species composition are $X_{C_2H_6}$=0.02, X_{N_2}=0.98 and p=15 atm.

Another important point to be noted is the effect of pressure in the species mole fraction at different temperatures. It can be observed from Figure C.5 and Figure C.6 in the Appendix C, that with increase in pressure there is less consumption of fuel or synthesis of products. However, with the uncertainty in the residence time due to preheating, the variations seen in these plots cannot be precisely related to pressure effects. At p=5 atm, the gases spend more time in the hot section, leading to more consumption of fuel and production of species as can be seen in Figure 4.12. To explain this, Figure 4.15 shows the ethane consumption with respect to residence time at p=5 atm and p=15 atm. The calculation is conducted using constant temperature profile and then using the actual temperature profile of the reactor. It can be observed from the plot that while there is prominent difference in ethane consumption due to temperature effects at two pressures, there is only a slight pressure effect at constant temperature. While no quantitative conclusion can be made from the experimental results, both experimental and model shows that with increase in pressure, the ethane conversion decreases. Since changing the residence time requires changing the length or diameter of the choked orifice, the current study focuses on variation of pressure and temperature.

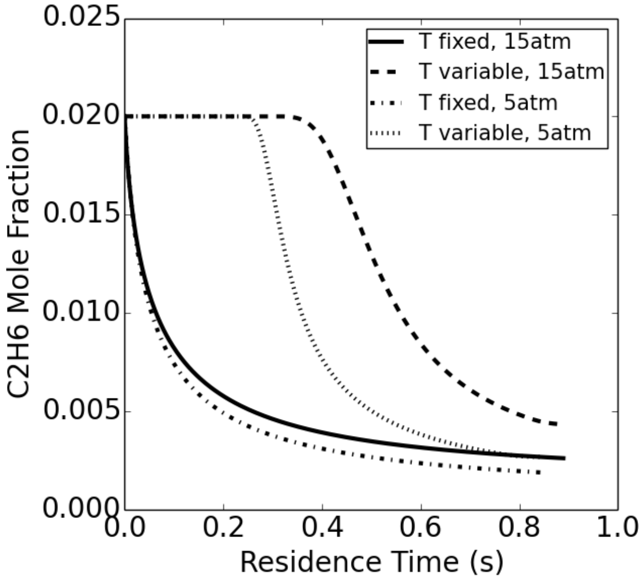

Figure 4.15: Effect of temperature ramp up on ethane pyrolysis. Ethane consumption with ideal constant and actual temperature profile at set temperature of 1100K. Inflow condition $X_{C_2H_6} = 0.02$, $X_{N_2} = 0.98$.

4.3 n-Butane Pyrolysis Results Comparison with Detailed Chemical Kinetic Models

Due to the availability of several detailed kinetic models, n-butane was another fuel considered for pyrolysis study. Similar to ethane pyrolysis, dilution was kept at 98% to reduce any uncertainty in temperature due to endothermic effect of fuel. Unlike ethane, one of the difficulties in handling n-butane was the low vapor pressure of n-butane (35 psia at 25°C). Since the flow controllers needed differential pressure of 30-40 psig to operate precisely, the fuel line was kept warm in order to eliminate condensation during the experiments.

Figure 4.16 to Figure 4.19 show the concentration profiles of major and minor species observed in butane pyrolysis compared to three different models proposed by Pyun et al. [80], Curran and co-workers (AramcoMech 2.0 [70] and Wang et al. [26] at T= 1050K and 1100K. Similar to ethane pyrolysis, the parent molecule C_4H_{10} is mostly converted to C_2H_4, H_2, CH_4, C_2H_6, C_2H_2, C_3H_6, C_3H_8, aC_3H_4 and pC_3H_4. As mentioned in the Section 4.1.2, Pyun et al.'s model is a modified version of Wang et al.'s model which has been recently optimized for CH_4 and C_2H_4 at higher temperatures (T>1200 K) and lower residence time (1.5 ms). Thus, Pyun et al.'s model appears to agree better with CH_4 and C_2H_4 at both temperatures.

While none of the models can capture the tube reactor data perfectly well and show significant variation between them, the experimental results lie mostly between these models at T=1050K and show closer agreement with AramcoMech 2.0 [70] at T=1100K. Similar to ethane pyrolysis, the reason for this large variation is the difference in reaction rates used in the sensitive reactions and the details can be found in the recently published paper by Shrestha et al. [50]. Figure 4.18 and Figure 4.19 also includes the bound to bound uncertainty of model parameters (shaded area) based on Monte Carlo calculations by perturbing the top 15 sensitive reactions of the Wang et al. [26] model. It can be observed that compared to model uncertainty, the experimental uncertainty is much lower for all the species except C_2H_6 implying that the present data can be used to minimize the uncertainty of the key rate controlling reactions. The large uncertainty in ethane mole fraction in experiments is due to the large uncertainty in standards from Air Liquide.

Further, the reason for this variation can also be attributed to lack of experimental results for n-butane pyrolysis. The disagreement between the models shows that there is room for improvement and the results from the MFTR can be used to optimize the current existing models.

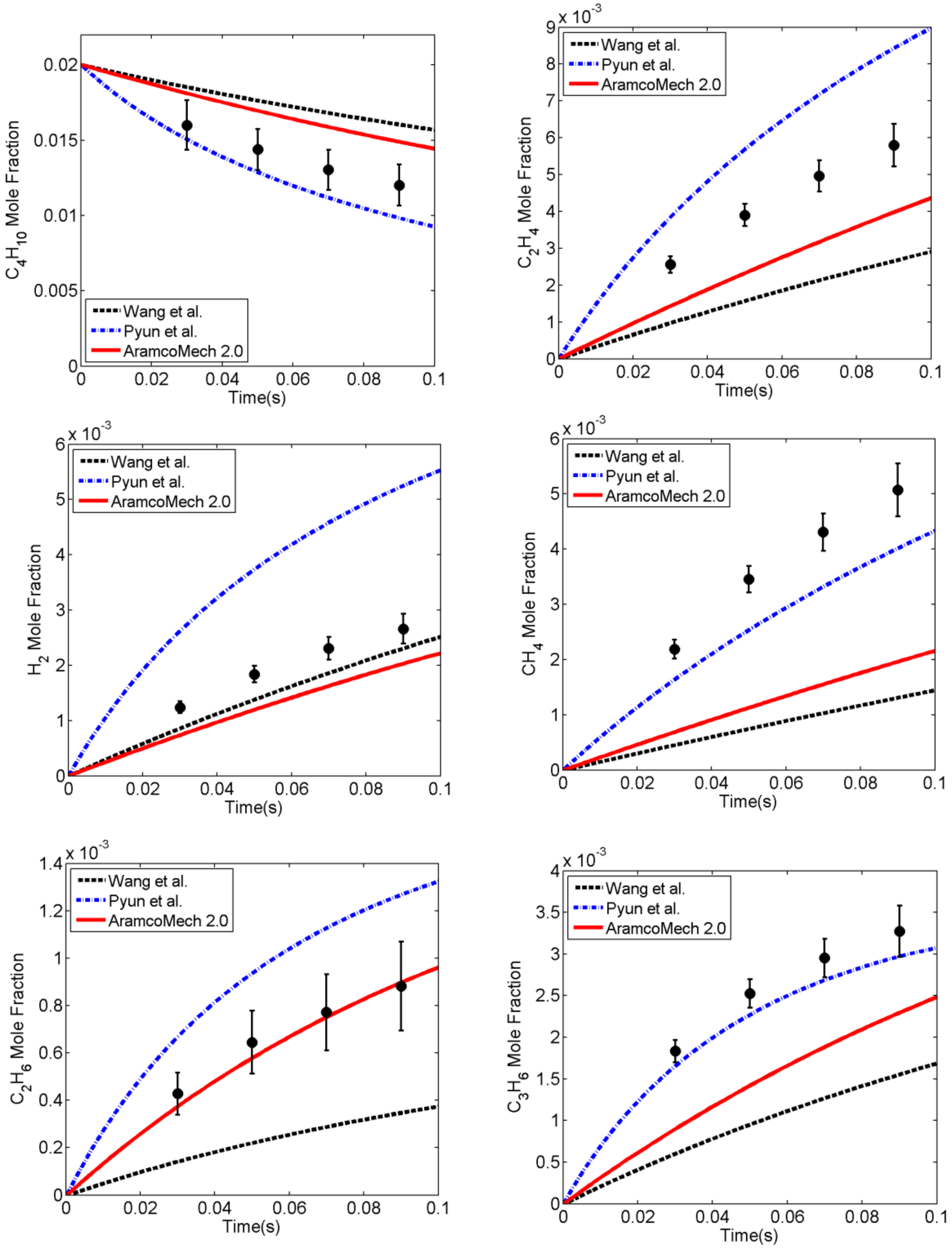

Figure 4.16: Comparison of **major** species mole fraction in n-butane pyrolysis vs time, for hot section temperatures **1050 K** (experiments (symbols) and predictions (lines)) with three different models by Wang et al. [26], Pyun et al. [80] and Curran and co-workers (AramcoMech 2.0 [70]). In flow species composition are $X_{C_4H_{10}}$=0.02, X_{N_2}=0.98 and p=1 atm.

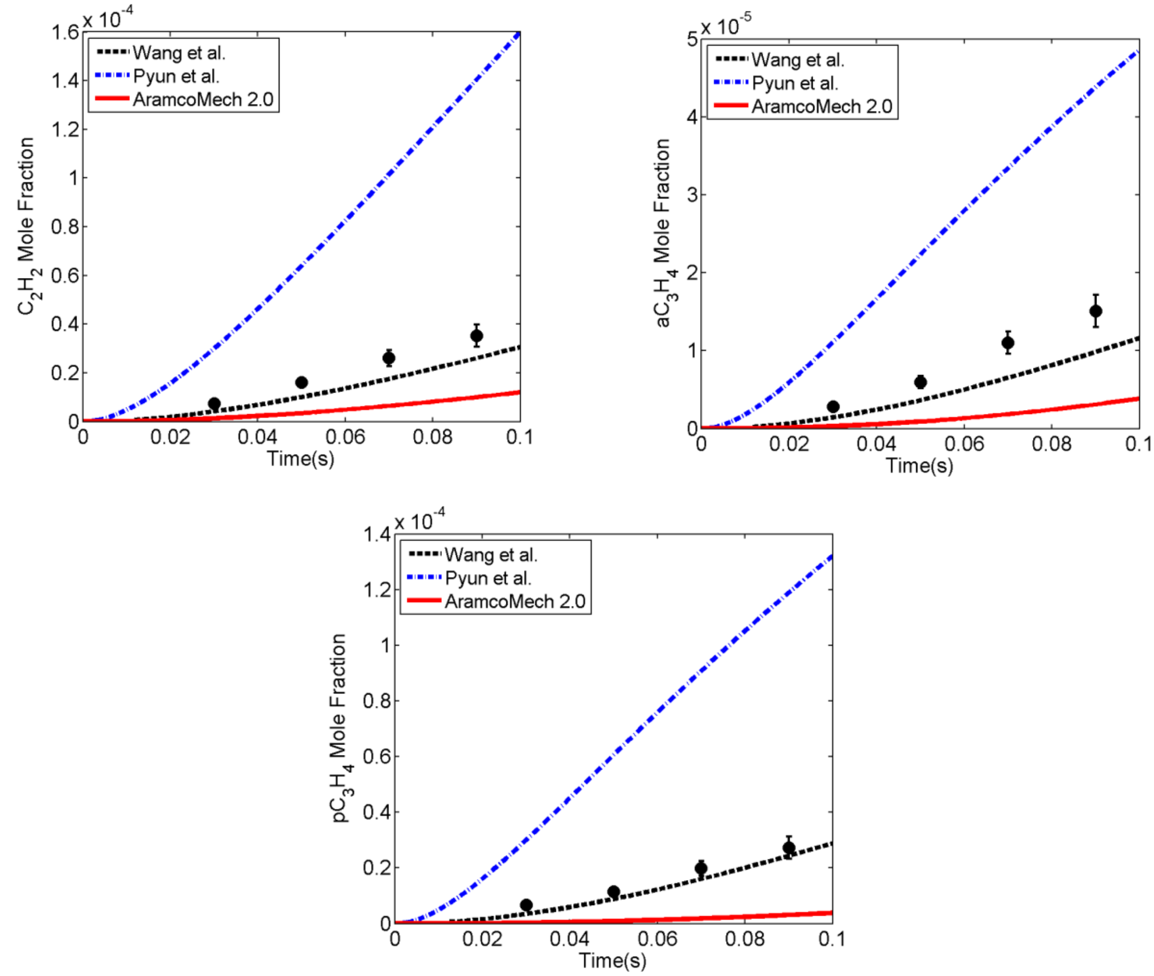

Figure 4.17: Comparison of **minor** species mole fraction in n-butane pyrolysis vs time, for hot section temperatures **1050 K** (experiments (symbols) and predictions (lines)) with three different models by Wang et al. [26], Pyun et al. [80]and Curran and co-workers (AramcoMech 2.0) [70]. In flow species composition are $X_{C_4H_{10}}$=0.02, X_{N_2}=0.98 and p=1 atm.

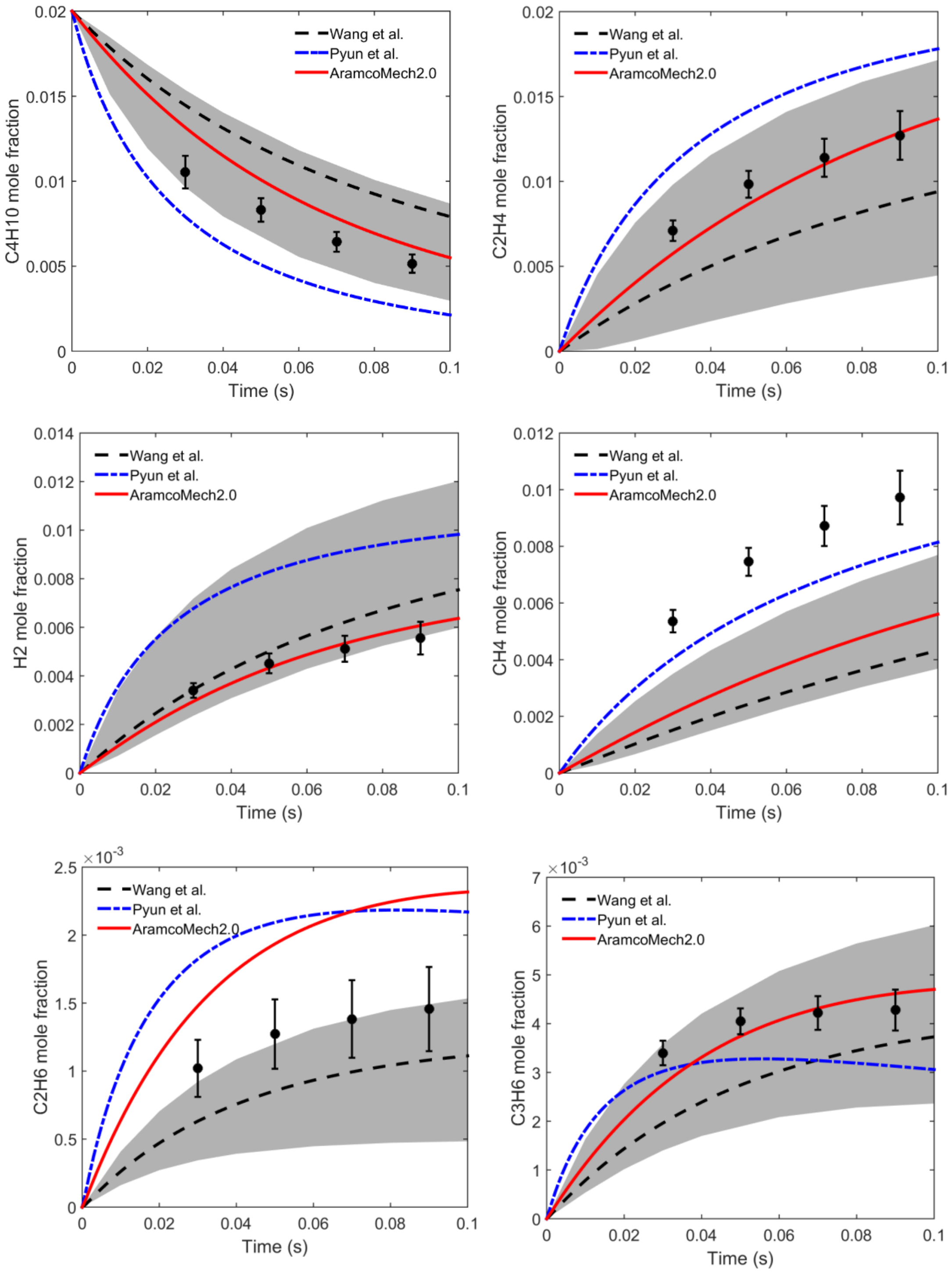

Figure 4.18: Comparison of **major** species mole fraction in n-butane pyrolysis vs time, for hot section temperatures **1100 K** (experiments (symbols) and predictions (lines)) with three different models by Wang et al. [26], Pyun et al. [80] and Curran and co-workers (AramcoMech 2.0 [70]). In flow species composition are $X_{C_4H_{10}}$=0.02, X_{N_2}=0.98 and p=1 atm. The shaded area indicates the 2σ model prediction uncertainty.

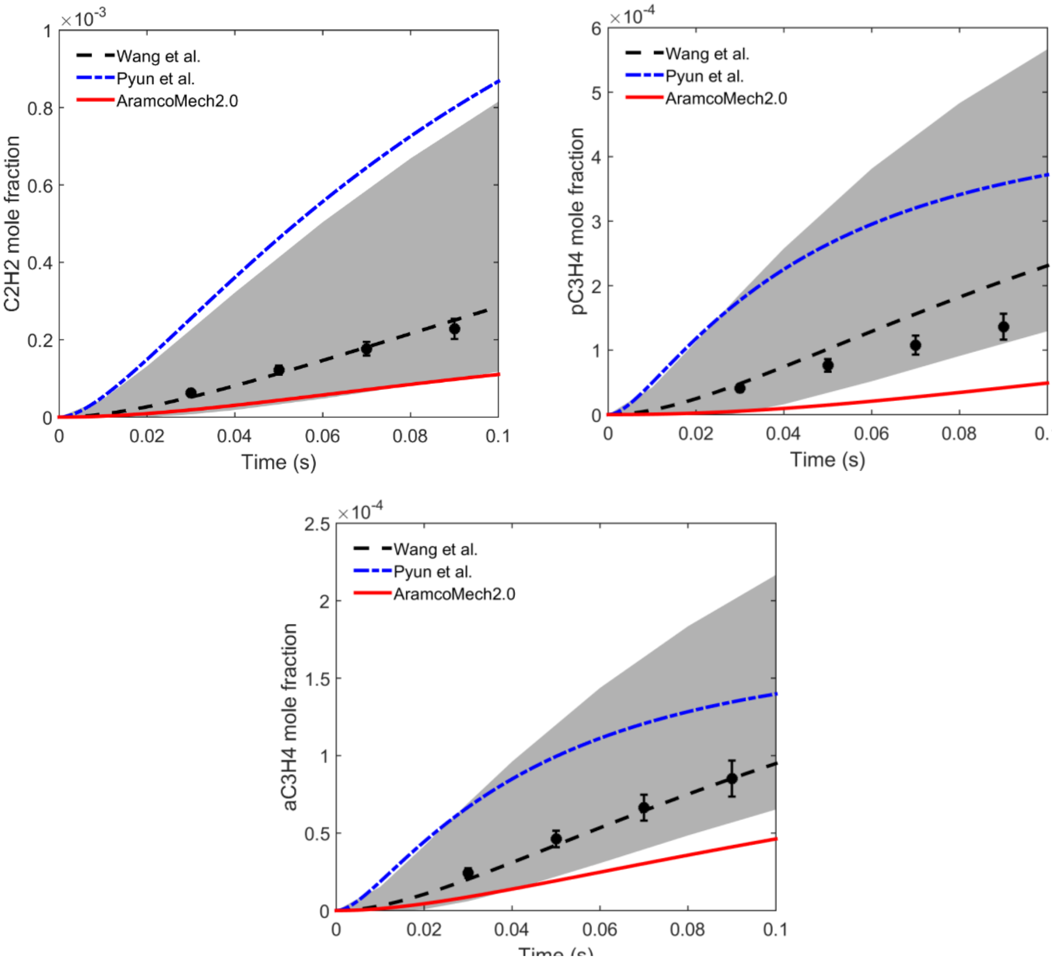

Figure 4.19: Comparison of **minor** species mole fraction in n-butane pyrolysis vs time, for hot section temperatures **1100 K** (experiments (symbols) and predictions (lines)) with three different models by Wang et al. [26], Pyun et al. [80] and Curran and co-workers (AramcoMech 2.0 [70]). In flow species composition are $X_{C_4H_{10}}$=0.02, X_{N_2}=0.98 and p=1 atm. The shaded area indicates the 2σ model prediction uncertainty.

4.4 Carbon Hydrogen Balance

In order to verify that most of the pyrolysis products are quantified in the current study, the carbon balance was investigated for ethane and butane experiments. The analysis was performed by sending 10 ppt of ultra-high purity argon from Praxiar (99.999% purity) as an internal standard. Argon was calibrated using mass flow controllers before the actual data collection and was analyzed in TCD. The carbon balance for ethane pyrolysis at

T=1100K and t_{res}=90 ms was 99.45% and for n-butane cracking at t_{res}=70 ms was 92.4%. The lower carbon balance for n-butane pyrolysis can be attributed to the formation of unquantified larger molecules during n-butane pyrolysis in comparison to ethane pyrolysis. Also, Table 4.1 lists the carbon to hydrogen ratio of outflow (products) for ethane and butane pyrolysis at different temperatures. While, the inflow and outflow C/H is very close for ethane pyrolysis indicating most of the species have been quantified in the current study of ethane pyrolysis, they are slightly lower in case of n-butane pyrolysis. Further, the C/H is even lower at T=1100K than at T=1050K indicating the presence of unquantified larger hydrocarbon.

Table 4.1: Carbon to Hydrogen ratio for different temperatures for inflow condition XC_2H_6/ XC_4H_{10}=0.02, X_{N_2}=0.98 and p=1 atm.

Fuel Type	Temperature (K)	C/H (inflow)	C/H (outflow)
Ethane	1050	0.3333	0.3339
	1100	0.3333	0.3328
n-Butane	1050	0.4	0.394
	1100	0.4	0.389

4.5 Ethane and n-Butane Pyrolysis Results Comparison with Literature Experimental Studies

The comparison of experimental results with various models in Section 4.2 indicated the large disagreement between available models. Thus, to further validate the current experimental configuration, the results from pyrolysis experiments are compared to experimental data available in the literature in the following sections.

4.5.1 Ethane Pyrolysis Results Comparison with Literature Experimental Studies

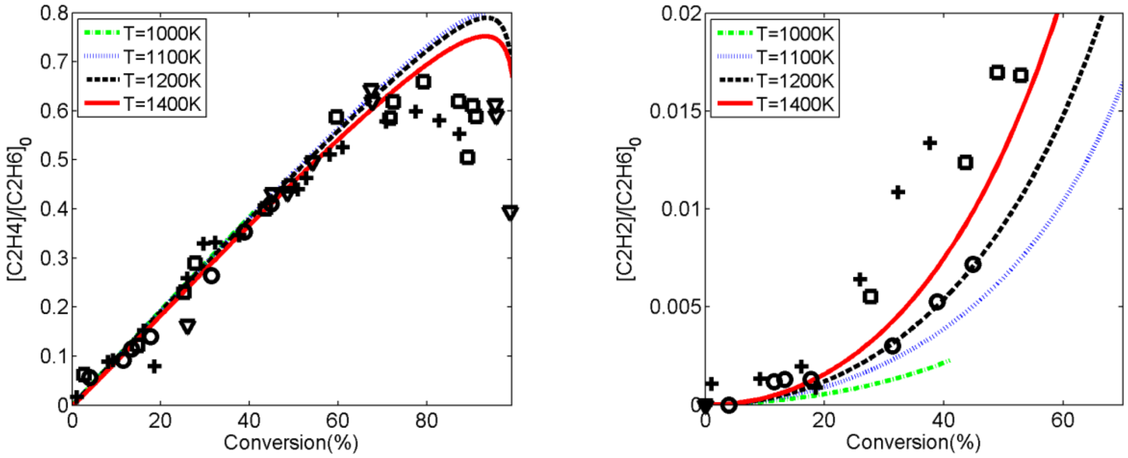

Figure 4.20: Comparison plot of ethylene and acetylene yield with respect to conversion at various temperatures. $[C_2H_6]_0$ is the initial ethane mole fraction. + represents experimental results from a shock tube by Tranter et al. [73] at p = 335.55 atm, Δ represents experimental results from a shock tube by Tranter et al. [74] at p =986.92 atm, □ represents experimental results from a shock tube by Hidaka et al. [72] at p =0.066 atm, O represents current experimental results from the current study at p = 1 atm and Line represents model by Wang et al. [26] at T=1000K-1400K. For current study, inflow species compositions of $X_{C_2H_6} = 0.02$, $X_{N_2} = 0.98$.

In spite of large amount of experimental work conducted on ethane pyrolysis, the experimental conditions explored by various groups differ in residence time, temperatures and pressures to the current study (See Table 4.2 for list of experiments). While the experimental conditions vary between different studies creating difficulty in direct comparison of species data, the product yields of species such as ethylene and acetylene at iso-conversion are compared here. Since, shock tube experiments are not influenced by mixing effects, they are ideal for comparison with present flow reactor data.

Table 4.2: Experimental Conditions and configuration explored in literature studies

Literature	**Configuration**	**Temperature (K)**	**Pressure (atm)**	**Residence time (ms)**	**Quantified Species**
Tranter et al. [73] [74]	Shock Tube	1050-1450	336-987	1.1-1.6	C_2H_6, C_2H4 and C_2H_2
Hidaka et al. [72]	Shock Tube	1100 – 1900	0.0657	0.69-2.73	C_2H_6, C_2H4 C_2H_2, CH_4, C_3H_6 C_3H_8, C_4H_6 and aC_3H_4

Figure 4.20 depicts the C_2H_4 and C_2H_2 yield (species mole fraction with respect to initial fuel mole fraction $[C_2H_6]_0$) as a function of ethane conversion in the current study, with comparison to the literature experimental data by Tranter et al. [73] [74] and Hidaka et al. [72]. Likewise, the yield for these species at different conversion using model predictions by Wang et al. [26] at T=1000K-1400K is also presented for comparison. While yield of C_2H_4 in the experiments as well as model prediction at a particular conversion didn't show much variation at different temperatures, C_2H_2 yield shows relatively more variation than C_2H_4. Nevertheless, the current experimental results matched very well with the other experiments and provides further validation of MFTR results.

While Tranter et al. [73] [74] only conducted quantitative measurement of C_2H_4 and C_2H_2, Hidaka et al. [72] presented the results for species such as CH_4, C_3H_6, aC_3H_4, and C_4H_6.

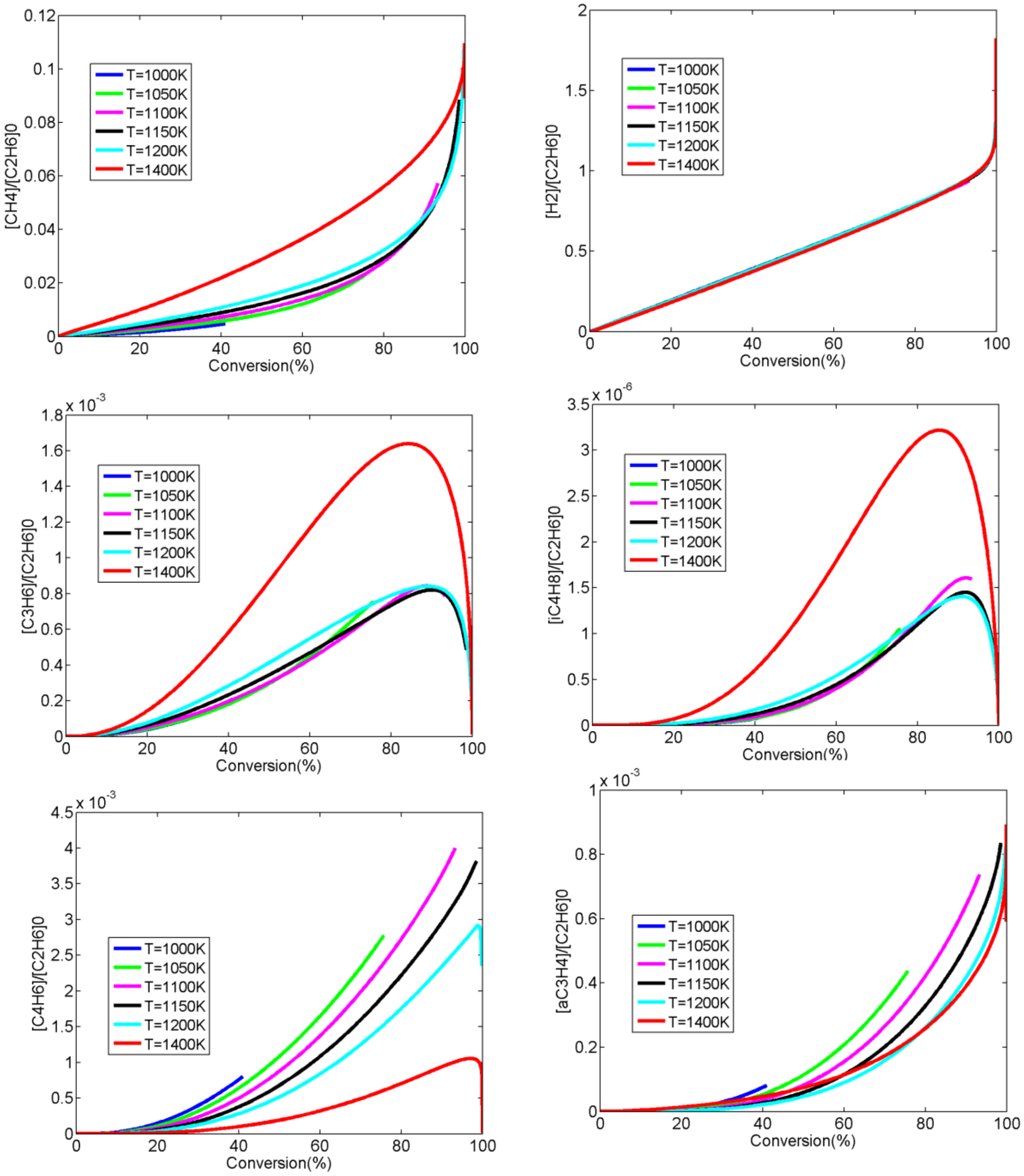

Figure 4.21: Species yield with respect to conversion using model by Wang et al. [26] at various temperatures (T = 1000 K -1400K). Inflow species compositions of $X_{C_2H_6} = 0.02$, $X_{N_2} = 0.98$.

However, the current result for other species is not compared with other data from Hidaka et al. [72]. The reason for this is that CH_4, H_2, C_3H_6, i-C_4H_8, C_4H_6 and aC_3H_4 yields at different conversions are highly dependent on reactor operating temperature as shown in Figure 4.21.

4.5.2 n-Butane Pyrolysis Results Comparison with Literature Experimental Studies

Only limited butane pyrolysis results were found in the literature prohibiting detailed comparison with the MFTR study. Nevertheless, the methane production in the current study is compared with tube reactor results by Su and Zhang [81]. While the range in residence time, initial fuel concentration and one of the species (methane) in the current study matched the condition explored by Su and Zhang, their explored temperature is slightly lower than the current study of T=1100K.

Figure 4.22 shows the methane production in butane pyrolysis with respect to time compared with tube reactor data by Su and Zhang [81] and model by Pyun et al [80]. The reason for choosing the model by Pyun et al. [80] for comparison is because the model has been tuned to match CH_4 concentration using laser absorption diagnostic technique. It can be observed from Figure 4.22 that the methane production measured by Su and Zhang is smaller than the prediction by the model. In the study by Su and Zhang [81], the gases are premixed and sent through a stainless-steel tube. The reason for the discrepancy between the experimental results and the model could be that the temperature ramp up region in their premixed reactor is not considered and there exists heating non-uniformities of the reactor which are not properly addressed in the study. This reason can be supported by their experimental results requiring zero-time shifting as seen in Figure 4.22 Based on the detailed reactor characterization studies especially the chemical thermometer study and agreement of ethane pyrolysis results with recent chemical kinetic model and experimental results have validated the design of the current flow reactor. Further, the lack of experimental data for n-butane pyrolysis compared to ethane explains the discrepancy of current results for n-butane pyrolysis with the models. Thus, experimental data presented in this study can be a source to improve these chemical kinetic models.

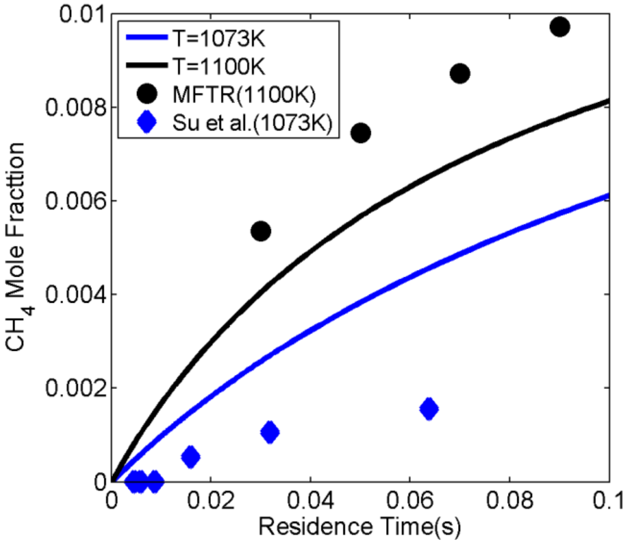

Figure 4.22: Comparison plot of methane mole fraction at different residence time with tube reactor data by Liu and Zhang [81] and model by Pyun et al.[80]. Lines represent prediction by Pyun et al. model, circle symbols represent results from current study and square symbols represent tube reactor result by Liu and Zhang. Inflow species compositions of $X_{C_4H_{10}} = 0.02$, $X_{N_2} = 0.98$.

4.6 Summary

Smaller hydrocarbon fuels are considered to be reasonably well-studied and have reliable detailed reaction models. The fidelity of the MFTR was tested by conducting ethane and n-butane pyrolysis studies at various temperatures, pressures, and residence times. The experimental results were compared with several models' predictions as well as with available experimental results from the literature. Due to the small mixing volume of the reactor, one of the important factors concluded from the results is the fact that there is no issue of profile shifting or zero time shifting to match the experimental data with model predictions. For ethane pyrolysis, the models showed significant variation with each other. The experimental results show the best agreement with the recently published Aramco model. Furthermore, product yield of ethylene and acetylene matched well with literature experimental data. However, for n-butane pyrolysis, none of the models captured the tube reactor data perfectly well and show significant variation between themselves. Unlike ethane pyrolysis, only few experimental studies have been performed for n-butane. The lack of experimental data for n-butane pyrolysis explains the discrepancy of current results for n-butane pyrolysis with the model predictions. A key finding is that experimental speciation data generated by MFTR has a much lower uncertainty compared with current model uncertainty. This implies that the MFTR can be a valuable tool in developing accurate chemical kinetic models.

Chapter 5: Homogeneous and Catalytic Thermal Decomposition of Large Hydrocarbon Fuels: Dodecane, JP-8, and JP-10

5.1 Introduction and Background on Jet Fuel and Jet Fuel Surrogate

There are various types of Jet fuels used in the commercial and military aviation industries. The National Jet Fuel Combustion Program (NJFCP) has categorized these fuels into Category A and C types fuels [25]. Some of the fuels investigated by NJFCP along with surrogate and single component fuels are listed in Table 5.1. Among these fuels, Category A fuels are conventional petroleum-derived fuels which have been identified as A1, A2, or A3 for low, nominal, or high flashpoint, viscosity, and aromatic content. The fuel used in commercial aviation in the United States and parts of Canada is Jet A2. JP-8 is Jet A1 with an additive package used currently in US military aviation [86]. Category C fuels are synthetic fuels or alternative fuels derived from alternative raw material (bio-derived). These fuels consist of wide range of hydrocarbons and therefore have different decomposition behavior and soot formation pathways.

Further, n-dodecane is one of the primary components of JP-8 (see Figure 5.1) and regarded as a representative of n-alkanes in jet fuel surrogates. The pyrolysis and oxidation behaviors of n-dodecane have been investigated by various groups from experimental as well as modeling perspectives [30], [41], [86]–[89].

Table 5.1: List of Fuels considered by National Jet Fuels Combustion program including some surrogate and single component fuels [25]. (ATJ: alcohol-to-jet, AAFRF: assured aerospace fuel research facility, TMB: trimethylbenzene)

Name	POSF	Description	MW (g/mol)	Composition	Application
A-1	10264	JP-8 (best case)	151.9	Blend of HCs	Military Aviation
A-2	10325	Jet-A	158.6	Blend of HCs	Commercial Aviation
A-3	10289	JP-5	166.1	Blend of HCs	Military Aviation
C-1	11498	Gevo ATJ	178.0	85% C_{12} iso-paraffins/15% C_{16} iso-paraffins	Synthetic
C-2	12223	blend	173.0	84% C_{14} iso-paraffins/16%TMB	Synthetic
C-5	12345	blend	135	73% C_{10} iso-paraffins/27%TMB	Synthetic
Dodecane	-	Surrogate	170.3	Dodecane	Surrogate
JP-10	7478	Single component	136.2	exo-tetrahydrodicyclopentadiene	Military Aviation

Due to complexity of real fuel, mainly two methods have been applied to model the real fuels. The first method is recognizing the fuel surrogate or surrogate mixture and design a detailed kinetic model. The second approach consists of fast thermal pyrolysis model (one step or few steps) development in conjunction with a detailed or reduced H_2, C_1-C_4 base model. The background for these two approaches are given in the following sections.

5.1.1 Jet Fuel Surrogate Mixture Investigations and Kinetic Models

Several surrogates consisting of alkanes, iso-alkanes, cyclo-alkanes and aromatics have also been proposed to mimic the characteristic of jet fuels. Figure 5.2 shows some of the proposed JP-8 surrogates by different groups [90]. Violi et al. [91] proposed six component surrogate fuels for JP-8 by comparing volatility, sooting propensity and boiling point curves of JP-8 with three different surrogates as a means to simulate complex fuel. Thermal decomposition of dodecane was performed by Dahm et al. [30] in a stainless-steel plug flow reactor at atmospheric pressure and similar temperature range (950-1050 K) as in the current study. The end products were analyzed with a GC-FID/TCD. This is one of the few studies which considered residence time variation along with temperature effects for analysis. A detailed kinetic model consisting of 1175 reactions was also proposed and showed reasonable agreement with the data. Dagaut [92] developed a surrogate model consisting of 74% n-decane, 15% n-propylenebenzene and 11% n-propylcyclohexane

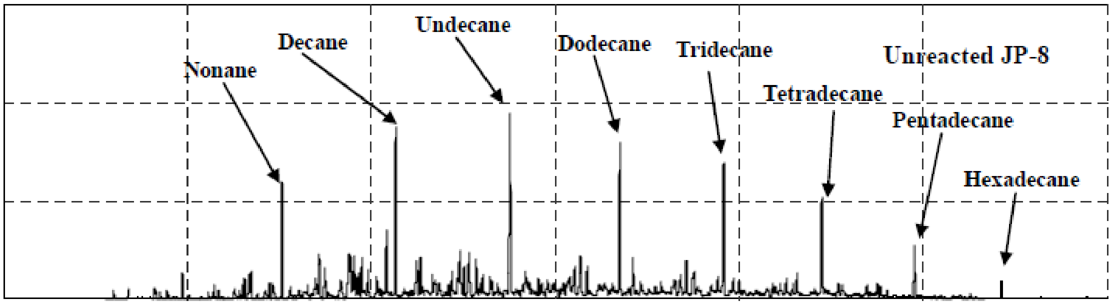

Figure 5.1: GC-MS spectra of unreacted JP-8 [130].

based on the experimental data from oxidation of kerosene fuel (Jet-A1) in a jet stirred reactor (JSR) at 1 atm and shock tube results obtained from the literature. Sub-models for individual pure compounds were established and validated before merging into a kerosene reaction model and it matched fairly well with the experimental results. However, the studies were conducted with only temperature variations and lacked variations in time and pressure. Thermal decomposition of n-dodecane has also been studied by Herbinet et al. [89] in a jet stirred reactor at T=773-1073 K, p=1 atm and residence time of 1-5 s. The study involved identification and quantification of a large number of gaseous and liquid products in GC-FID/TCD and GC-MS. A detailed chemical kinetic model with 1449 reactions and 271 species was also generated and validated against previously obtained plug flow reactor data.

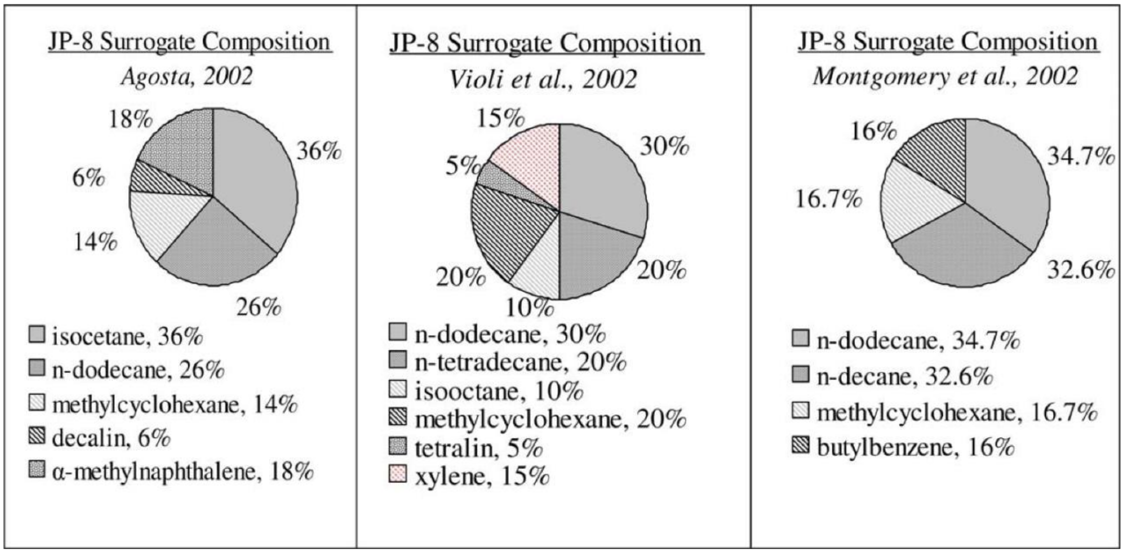

Figure 5.2: Examples of surrogate fuels proposed by different groups [90].

With an aim to obtain consistent kinetic parameters for a wide range of HCs, a surrogate reaction model for jet fuels, JetSurF 2.0 model, consisting of 348 species in 784 reactions has been proposed [26]. The model has been validated against laminar flame speeds, ignition delay times behind shock waves, species profiles in tube reactors and burner stabilized flames. The model is meant to be used for the pyrolysis and oxidation of n-alkanes (up to n-dodecane), cyclohexane and mono-alkylated cylcohexanes (up to n-butyl-cylcohexane) at high temperatures [26].

A surrogate model for Jet-A (POSF 4658) consisting of n-decane, iso-octane and toluene (1st generation surrogate model) has been formulated and tested against data from each of a variable pressure flow reactor, counter-flow burner, shock tube and rapid compression machine at intermediate and low temperature ranges by Dooley et al. [2]. While the model was validated by checking the chemical reactivity via oxidation of a 0.3% surrogate and Jet-A at p=12.5 atm and T=500-1000 K, only concentration of CO, CO_2, O_2 and H_2O were analyzed. Later, a surrogate fuel mixture consisting of n-dodecane, iso-octane, n-propylbenzene and 1,3,5-trimethylbenzene (2nd generation surrogate) based on molecular weight, hydrogen to carbon ratio, derived cetane number and threshold sooting index was proposed [31], [93]. Various experiments in combustion systems, for instance shock tubes, rapid compression machines, variable pressure flow reactors, premixed and non-premixed flames showed the 2nd generation surrogate closely matches Jet-A. However, the proposed model still consisted of 2080 species and 8310 reactions. Further, the shock tube experiments at shorter residence time considered larger species, while for longer residence time, only species such as CO, CO_2, O_2 and H_2O were considered for validation [31], [93].

Mze-Ahmed et al. [94] conducted an experimental oxidation study of n-undecane and n-dodecane in a jet stirred reactor at temperature ranging from 550 to 1150 K, p = 10 atm, residence time of 1 s and equivalence ratio of 0.5, 1.0 and 2.0. Fourier transform infrared spectrometer and GC systems were used for analysis. The experimental results were used to validate a chemical kinetic model involving 1377 species and 5865 reactions. Recently, Banerjee et al. [41] investigated n-dodecane pyrolysis and oxidation in the Standford Variable Flow Reactor at a temperature range of 1000-1300 K, p=1 atm and residence time 1-40 ms using GC. While the experimental conditions for this investigation are close to the present study, the reactor assembly is complex with converging- diverging duct before the reaction zone and heated by vitiated inflow from a McKenna burner as explained in chapter 2. The modeling for such system is relatively complex compared to the UVa MFTR and the system can also be subject to reaction initialization problem.

In general, most of the surrogate fuels were proposed on the basis of few tests while others having extensive study are more fuel specific and not universal. Additionally, the physical characteristics such as single phase heat transfer can be mimicked by a single component physical surrogate (e.g. n-dodecane). However, to reproduce properties such as ignition, emission, pyrolysis and oxidation behavior, a chemical surrogate with various classes of components is necessary [95]. As a result, the available surrogate models still consist many of species and reactions and further simplification is needed for both applications and research purposes.

5.1.2 Fast Thermal Pyrolysis Model

The initial investigations on jet fuel started with the need to get insights on thermal stability and deposit formations on critical engine components. Moler't et al. [96] conducted JP-8 pyrolysis experiments from 623 K to 1123 K in a quartz test cell and analyzed the decomposition products using gas chromatography equipped with flame ionization detector and a mass spectrometer (GC-FID/MS). The initial modelling efforts included a very simple fast thermal pyrolysis model. Lee and Kundu proposed a simplified 5 step kinetic model for Jet-A and validated it through CO and CO_2 concentration using a gas analyzer in a flame-tube combustor [97]. Ranzi et al. [98] described the process of lumping species and reactions in detailed kinetic models. This approach is attractive to reduce the number of species and reactions in complex models and uses a simplified description of primary propagation reactions and intermediates in combination with detailed reaction model for smaller molecules [91]. Violi et al. [91] also incorporated the a semi-detailed kinetic scheme (lumped chemical kinetic model) developed by Ranzi et al. [98] in combination with already available alkane kinetic model to describe the surrogate components of JP-8.

Recently, employing the concept of fast kinetics of fuel cracking to form smaller fragments, a fast-thermal pyrolysis model for dodecane consisting of 4 species and 20 reaction steps in conjunction with a detailed C_1 to C_4 model was proposed by You et al [88]. Similar to detailed kinetic model, the fast-thermal pyrolysis model was able to capture H_2 concentration fairly well as a function of time. However, the model was not able to predict the species profiles of C_2H_4, C_3H_6 and CH_4 very well. In an effort to study the preliminary version of Wang's Hybrid model, Zhu et al. [99] recently conducted shock tube/laser absorption experiments of JP-8 (POSF 10264) at T=1000-1400 K and p=1-60 atm and reported the time history measurement of CH_4, C_2H_4 and C_3H_6.

Examination of the literature suggests that much time has been devoted to validating these detailed models which are very complex and expensive, while relatively less effort has been made in developing simplified models such as the approach suggested in the present work. The current work is focused on further confirming the fidelity of the data produced by the micro flow tube reactor by comparing dodecane pyrolysis species measurements at the reactor exit to models in the literature. The study will then be extended to pyrolysis of a real fuel (JP-8) and development of a fast-thermal pyrolysis model in an effort to reduce the complexity of chemical kinetic models. Finally, homogeneous and catalytic pyrolysis studies of JP-10 will be conducted in the reactor to show the applicability of reactor to conduct heterogeneous pyrolysis studies.

5.2 Fast Thermal Pyrolysis Model Developed from Current Experimental Results

In the current study, a semi-global model was developed by considering a fast-thermal pyrolysis of a real fuel (JP-8) which can be combined with more detailed H_2/CO/C_1-C_4 base model to form a complete model. If we considered a fast-thermal pyrolysis of a model fuel C_xH_y into major C_0-C_4 species, the reaction can be represented by:

$$C_xH_y \rightarrow aC_2H_4 + bC_3H_6 + cH_2 + dCH_4 + eC_2H_6 + fC_4H_6 + gC_4H_8 \text{ (isobutylene)} + hC_2H_2 + iC_3H_4 \text{ (propyne)} + jC_3H_4 \text{ (allene)} + k\,C_6H_6, \quad (5\text{- }1)$$

where a-k are stoichiometric coefficients. These stoichiometric coefficients can be determined from known species selectivity ratios. The selectivity ratios are defined as the ratio between different species and a reference species, C_2H_4 in this case, as follows:

$$\frac{C_3H_6}{C_2H_4} = \alpha \quad , \qquad (5\text{- }2)$$

$$\frac{H_2}{C_2H_4} = \beta \quad , \qquad (5\text{- }3)$$

$$\frac{CH_4}{C_2H_4} = \gamma \quad , \qquad (5\text{- }4)$$

$$\frac{C_2H_6}{C_2H_4} = \delta \quad , \tag{5- 5}$$

$$\frac{C_4H_6}{C_2H_4} = \theta \quad , \tag{5- 6}$$

$$\frac{C_4H_8}{C_2H_4} = \lambda \quad , \tag{5- 7}$$

$$\frac{C_2H_2}{C_2H_4} = \varepsilon \quad , \tag{5- 8}$$

$$\frac{aC_3H_4}{C_2H_4} = \rho \quad , \tag{5- 9}$$

$$\frac{pC_3H_4}{C_2H_4} = \eta \quad , \tag{5- 10}$$

Based on the elemental conservation, the stoichiometric coefficients (a-k) can be obtained from:

$$a = \frac{(y-x)}{3\alpha + 2\beta + \gamma + 4\delta + 2\theta + 4\lambda + \rho + \eta + 2} \ , \tag{5- 11}$$

$$b = \frac{(y-x)\alpha}{3\alpha + 2\beta + \gamma + 4\delta + 2\theta + 4\lambda + \rho + \eta + 2} \ , \tag{5- 12}$$

$$c = \frac{(y-x)\beta}{3\alpha + 2\beta + \gamma + 4\delta + 2\theta + 4\lambda + \rho + \eta + 2} \ , \tag{5- 13}$$

$$d = \frac{(y-x)\gamma}{3\alpha + 2\beta + \gamma + 4\delta + 2\theta + 4\lambda + \rho + \eta + 2} \tag{5- 14}$$

,

$$e = \frac{(y-x)\delta}{3\alpha+2\beta+\gamma+4\delta+2\theta+4\lambda+\rho+\eta+2} \ , \tag{5- 15}$$

$$f = \frac{(y-x)\theta}{3\alpha+2\beta+\gamma+4\delta+2\theta+4\lambda+\rho+\eta+2} \ , \tag{5- 16}$$

$$g = \frac{(y-x)\lambda}{3\alpha+2\beta+\gamma+4\delta+2\theta+4\lambda+\rho+\eta+2} \ , \tag{5- 17}$$

$$h = \frac{(y-x)\varepsilon}{3\alpha+2\beta+\gamma+4\delta+2\theta+4\lambda+\rho+\eta+2} \ , \tag{5- 18}$$

$$i = \frac{(y-x)\rho}{3\alpha+2\beta+\gamma+4\delta+2\theta+4\lambda+\rho+\eta+2} \ , \tag{5- 19}$$

$$j = \frac{(y-x)\eta}{3\alpha+2\beta+\gamma+4\delta+2\theta+4\lambda+\rho+\eta+2} \ , \tag{5- 20}$$

$$k = \frac{1}{6}\left(x - \frac{(y-x)(3\alpha+\gamma+2\delta+4\theta+4\lambda+2\varepsilon+3\rho+3\eta+2)}{3\alpha+2\beta+\gamma+4\delta+2\theta+4\lambda+\rho+\eta+2}\right), \tag{5- 21}$$

These stoichiometric coefficients extracted from well characterized experimental data can be utilized to develop a reduced order pyrolysis model. In general, a fast-thermal pyrolysis model of larger fuels in combination with a well-studied H_2/C_1-C_4 oxidation model can play a significant role in reducing the complexity of reaction models.

5.3 Results and Discussion on Homogeneous Thermal Decomposition

5.3.1 n-Dodecane Pyrolysis at Atmospheric Pressure

n-Dodecane experiments were conducted in the micro flow tube reactor in temperature range of T= 1000K-1100K, residence time t_{res}=10-60 ms and p=1atm. In order to maintain a constant temperature or reduce endothermic effect, the fuel concentration was kept at 0.25% by volume.

Figure 5.3 and Figure 5.4 show the major and minor product distributions of n-dodecane pyrolysis at 1000K with respect to residence time. Also, Figure 5.5 and Figure 5.6 show the major and minor product distributions at 1100 K with respect to residence time. The quantified species include C_2H_4, C_3H_6, H_2, CH_4, C_4H_8, C_2H_6, C_4H_6, aC_3H_4, C_2H_2, and pC_3H_4, respectively. The results have been compared with predictions using three different models: JetSurF 2.0 by Wang et al. [26], and models by Banerjee et al. [41] and Mze-Ahmed et al. [94].

For reactor temperature 1000K, the major pyrolysis species shown in Figure 5.3 are in good agreement with the model by Banerjee et al. [41], except for CH_4 which matches well with the model by Mze-Ahmed et al. [94]. In contrast, the minor species profiles shown in Figure 5.4 do not agree well with any of the models except for C_4H_6 which matches well with the model by Mze-Ahmed et al. [94] .

On the other hand, for a reactor temperature of 1100K, both the major and minor species shown in Figure 5.5 and Figure 5.6, agree well with the model by Mze-Ahmed et al.[94], except for C_2H_6 and C_3H_6. Similar to ethane and n-butane, the models for n-dodecane showed a large disagreement with each other for almost all the species.

Based on model predictions as well as experimental studies conducted by Wang et al. [26], Banerjee et al. [41] and Mze-Ahmed et al. [94], larger species such as 1-hexene, 1-pentene, 1- heptene, benzene and toluene are also produced during n-dodecane pyrolysis in addition to the H_2 and C_1-C_4 species observed in the GC/FID/TCD. However, these species have not been quantified in the current study due to the measurement limitation of GC columns used. Also, as explained in chapter 2, a dry ice ethanol bath has been used to prevent the larger species from entering the packed columns of the GC system. However, the actual mole fraction of species was not affected by absence of these larger species in the sample. The dilution used in the current study is very high (99.75% of N_2) which changes to 98.54% at the highest conversion. This can introduce a maximum error of only 0.15% in species mole fractions.

The model by Banerjee et al. [41] is an optimized JetSurF 1.0 [100] model which predicts major species (C_2H_6, CH_4 and C_3H_6) yield of n-dodecane pyrolysis experiments conducted in Stanford Variable Pressure Flow Reactor (VPFR) well**.** While the reactor is heated by vitiated gases such as N_2, H_2O, O_2 and H_2 and also consists of converging-diverging duct (details about the reactor is in chapter 2) creating uncertainty in residence time, the model captures well the species yield from the experiments on the VPFR at similar conditions to those investigated in the UVa MFTR. However, the residence time varies due to different reaction initialization in the VPFR compared to the current study with well-defined initial conditions. Nevertheless, product yield at the same conversion can be compared between the two experimental setups at UVa and Stanford as was performed in the ethane pyrolysis study discussed in chapter 4.

Table 5.2: Total mole fraction of C_1-C_4 species and n-dodecane mole fraction in the current study compared to (Banerjee et al. [41]) at T=1000-1100K and residence time 10-60 ms. Note: [X] is the mole fraction.

Residence time (ms)	**10.91**	**20**	**30**	**40**	**50.50**	**59.99**	**Temp (K)**
Total [X] of C_1-C_4 Species from Banerjee et al. [41]	0.00028	0.00056	0.0008	0.0011	0.0014	0.0017	1000
	0.007313	0.0108	0.012299	0.013163	0.013588	0.013854	1100
Total [X] of C_1-C_4 Species in Current Study	0.00033	0.0006	0.00078	0.0011	0.0015	0.0016	1000
	0.006517	0.008559	0.009997	0.010958	0.011975	0.011515	1100
$[X]_{n\text{-}C_{12}H_{26}}$	0.0024	0.0023	0.0022	0.0021	0.00207	0.0019	1000
	8.13E-5	3.30E-4	1.76E-4	9.79E-5	6.16E-5	3.95E-5	1100

Since n-dodecane was not quantified in the current study, there is an added complication in comparing species yield at a particular conversion as the conversion of dodecane must be estimated. Based on the good agreement of C_1-C_4 species mole fractions to the model by Banerjee et al. especially at T=1000K (see Figure 5.3), the n-dodecane mole fraction from the model is used to calculate conversion. The total mole fractions of C_1-C_4 species from the current study and model by Banerjee et al. [41] including the n-dodecane at T=1000-1100K and residence time 10-60 ms are given in Table 5.2.

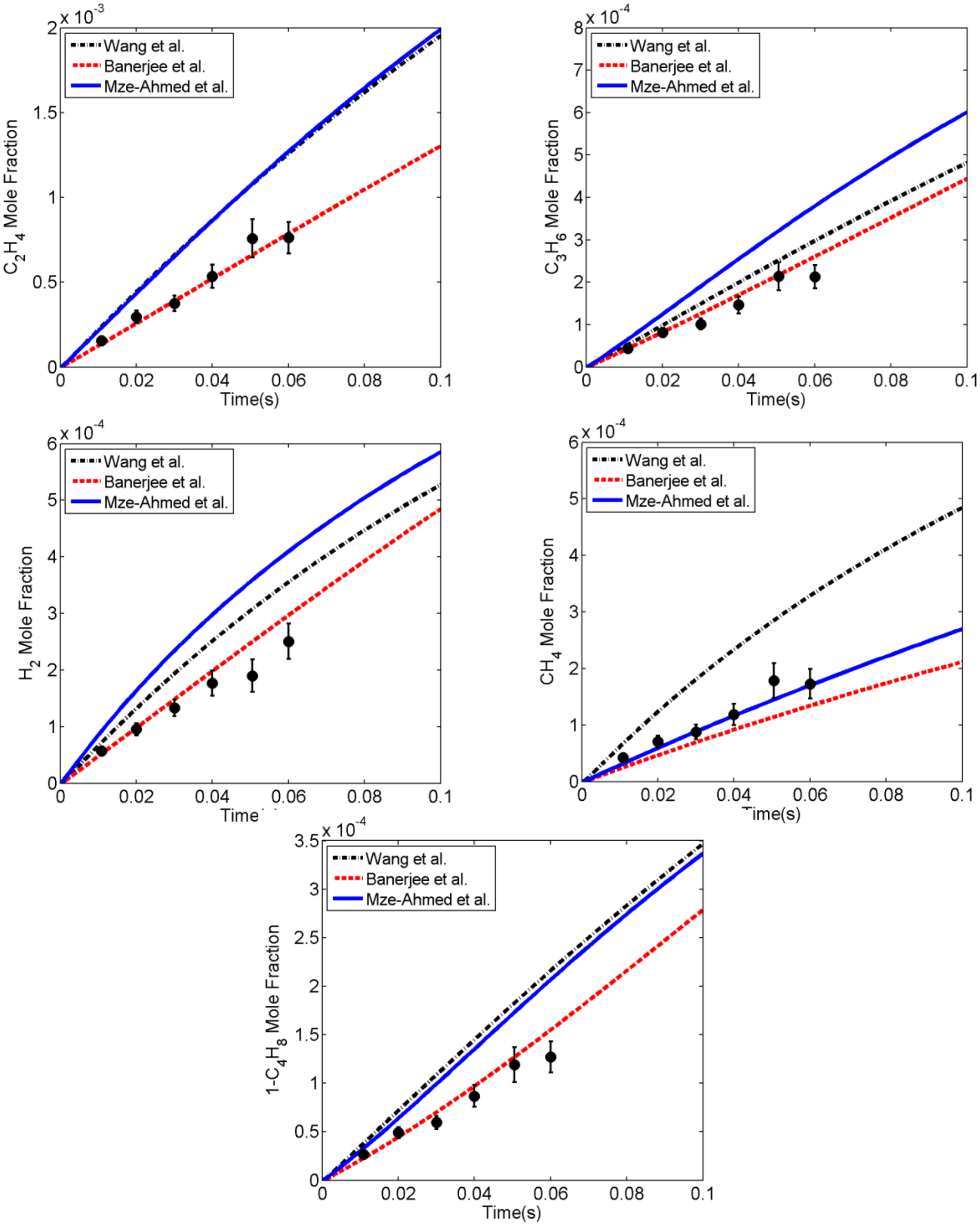

Figure 5.3: Comparison of species mole fraction (**major species**) as a function of time for the hot section temperature of **1000 K.** Symbols represent experimental results and lines represent predictions with three models by Wang et al. [26], Banerjee et al. [41] and Mze-Ahmed et al. [94] for inflow species compositions of $X_{C_{12}H_{26}}$ = 0.0025, X_{N_2} = 0.9975 and p = 1 atm.

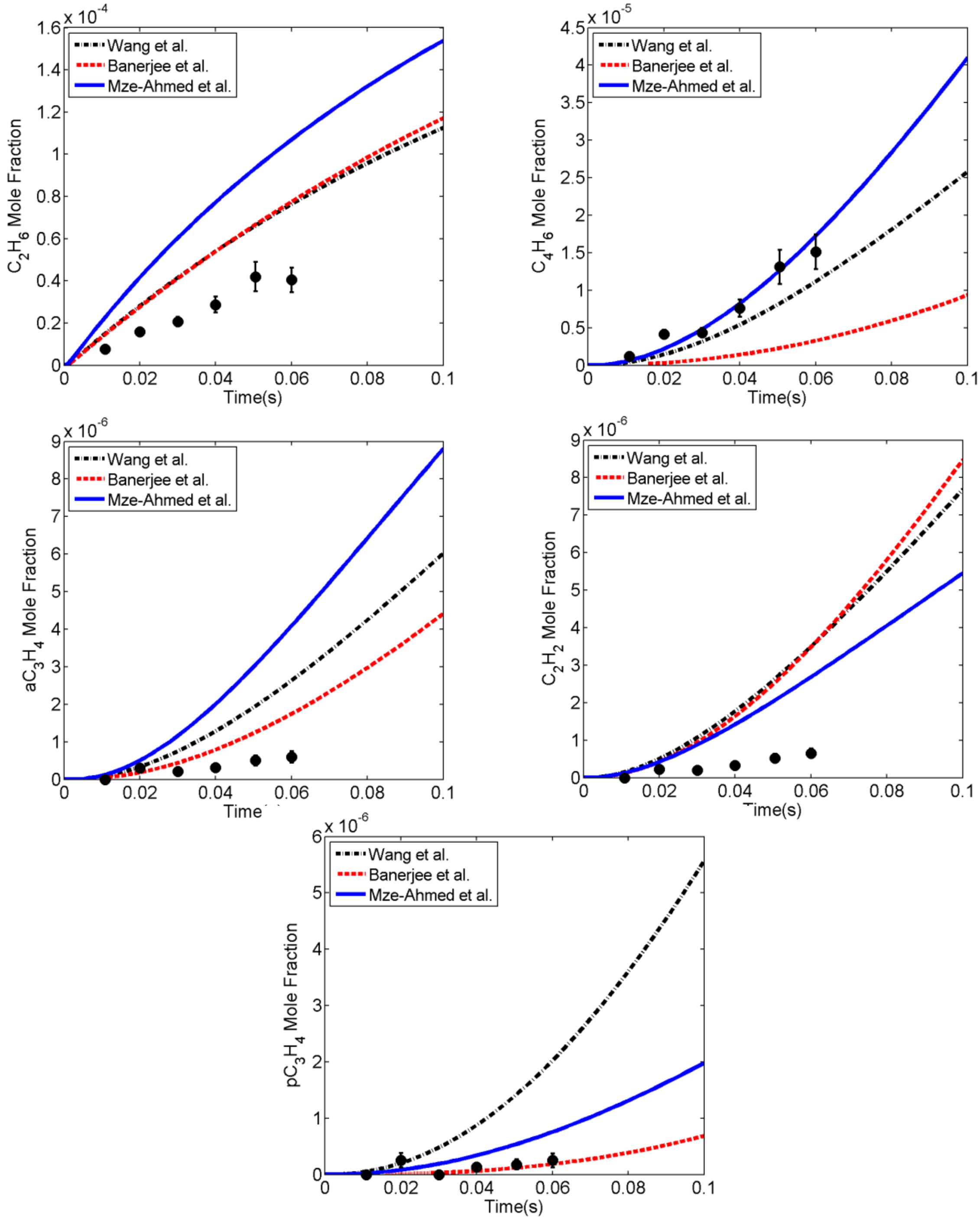

Figure 5.4: Comparison of species mole fraction (**minor species**) as a function of time for the hot section temperature of **1000 K**. Symbols represent experimental results and lines represent predictions with three models by Wang et al. [26], Banerjee et al. [41] and Mze-Ahmed et al. [94] for inflow species compositions of $X_{C_{12}H_{26}} = 0.0025$, $X_{N_2} = 0.9975$ and p = 1 atm.

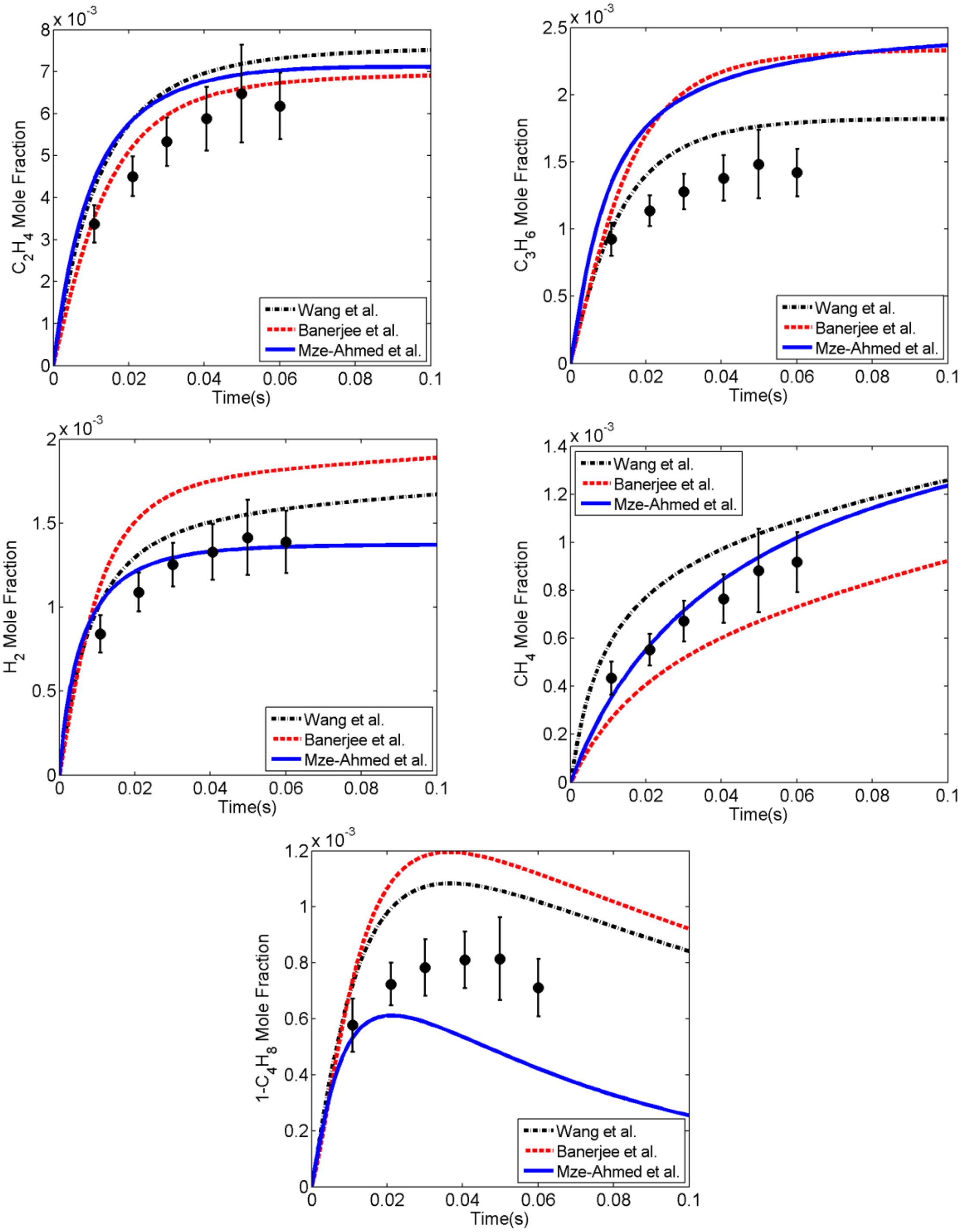

Figure 5.5: Comparison of species mole fraction (**major species**) as a function of time for the hot section temperature of **1100 K**. Symbols represent experimental results and lines represent predictions with three models by Wang et al. [26], Banerjee et al. [41] and Mze-Ahmed et al. [94] for inflow species compositions of $X_{C_{12}H_{26}} = 0.0025$, $X_{N_2} = 0.9975$ and p = 1 atm.

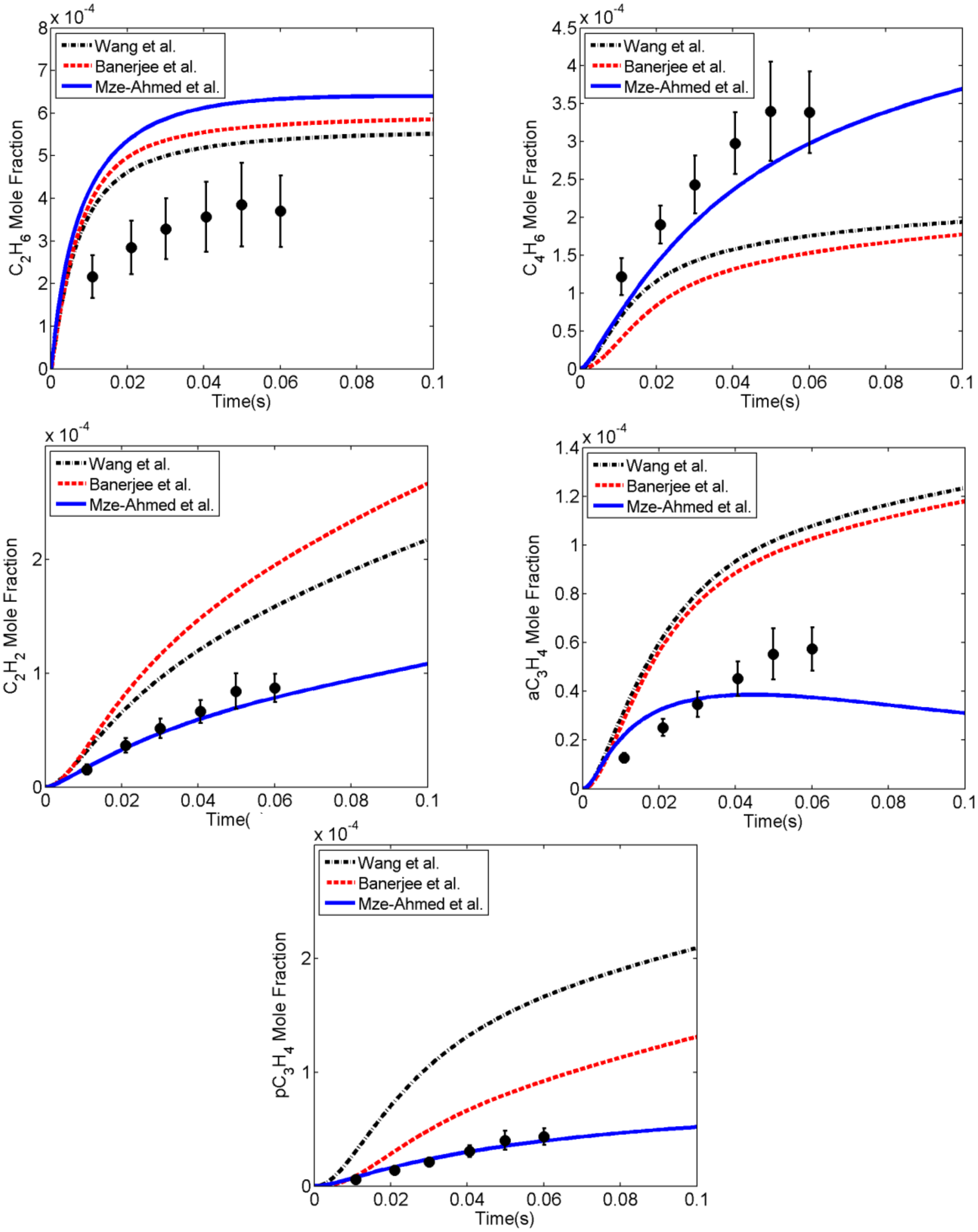

Figure 5.6: Comparison of species mole fraction (**minor species**) as a function of time for the hot section temperature of **1100K**. Symbols represent experimental results and lines represent predictions with three models by Wang et al. [26], Banerjee et al. [41] and Mze-Ahmed et al. [94] for inflow species compositions of $X_{C_{12}H_{26}} = 0.0025$, $X_{N_2} = 0.9975$ and p = 1 atm.

Even though the residence time reported in the Banerjee et al. study is similar to the current study, the conversion is much larger**.** Figure 5.7 depicts the product yield from current study with respect to conversion (C_2H_4 and C_3H_6) compared with experimental and modeling results by Banerjee et al. [41]. The present results are well captured by the model and consistent with experimental results by Banerjee et al. [41] for ethylene. For propylene, the results match well with the model at lower conversion but shows discrepancies at higher conversion. Nonetheless, the present results offer well defined and intermediate residence times and temperature regimes which have not been well studied in literature.

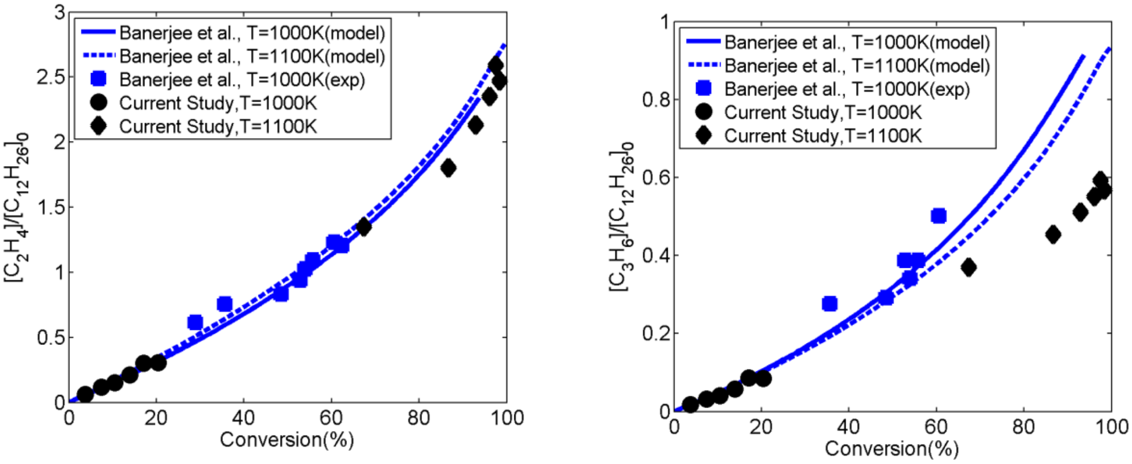

Figure 5.7: Comparison of current n-dodecane pyrolysis results at T=1000-1100K with literature data by Banerjee et al. [41]. Line represents model by Banerjee et al. and symbols represents experimental results from Banerjee et al. [41] and current data.

The products mole fractions with respect to temperature compared with three models are also presented in Figure D.1 and Figure D.2. The model by Mze-Ahmed et al. [94] shows good agreement with the present results from the reactor for most of the C_1-C_4 species. Also, the experimental uncertainties are comparatively smaller than the variation in these models and can be essentially used to improve the model prediction [7].

5.3.2 JP-8 Pyrolysis at Atmospheric Pressure

A JP-8 pyrolysis experiment was conducted in the atmospheric pressure tube reactor at T=1000 K, 1100K and residence time from 20-60 ms. In addition, with an attempt to reduce the chemical reaction model, a one-step fast thermal pyrolysis model (given by Eq. (5- 1)) has been developed for JP-8 (POSF-10264) in the current study. The selectivity ratios α to η (given by Eq. (5- 2) to (5- 10)) have been calculated using mole fractions of species from experiments. The obtained selectivities are then used to calculate the stoichiometric coefficients “a” to “k” using Eq. (5- 11) to (5- 21).

Figure 5.8 and Figure 5.9 show the major and minor product distribution at 1000K with respect to residence time. Also, Figure 5.10 and Figure 5.11 show the major and minor product distribution at 1100 K with respect to residence time. The experimental results from current study have been compared with predictions using two different models: Dagaut et al. [95] and the one step model from the current study. The model by Dagaut et al. [95] represents a surrogate mixture of 74% n-decane, 15% n-propylbenzene and 11% n-propylcyclohexane and consists of 209 species in 1673 reversible reactions. The model has been validated with kerosene (TR0) oxidation results in jet stirred reactor from T=900K to 1400 K [95]. The key observation is that the one step model is able to capture all the important species at T=1000K. In fact, the model is able to capture the MFTR results even better than the multi-step surrogate model. At T=1100K, the one step model can capture the MFTR results trend as well as the model by the Dagaut et al. [95] except for C_2H_2, aC_3H_4 and pC_3H_4.

The stoichiometric coefficients (a-k) at different temperatures and residence time are shown Figure 5.12 and Figure 5.13. The stoichiometric coefficients (a-g) remain nearly constant with respect to residence time while they vary with temperatures. Thus, the modelling was conducted using two separate sets of coefficients for T=1000K and T=1100K. In contrast, selectivity ratios of some minor species such as C_2H_2, aC_3H_4 and pC_3H_4 at T=1100K show a significant variation with respect to temperature as well residence time. This disagreement can explain the incapability of the current one step model to capture the experimental trend of these species shown in Figure 5.11. It also indicates the need of more reactions to define the formation of such species i.e. a multi-step model with additional stoichiometric coefficient as described in ref. [101] to improve their prediction.

Thus, the reasonable agreement between the one step model and experimental data indicate a potential use of the one step model in conjunction with available C_1-C_4 base models for limited range of temperature.

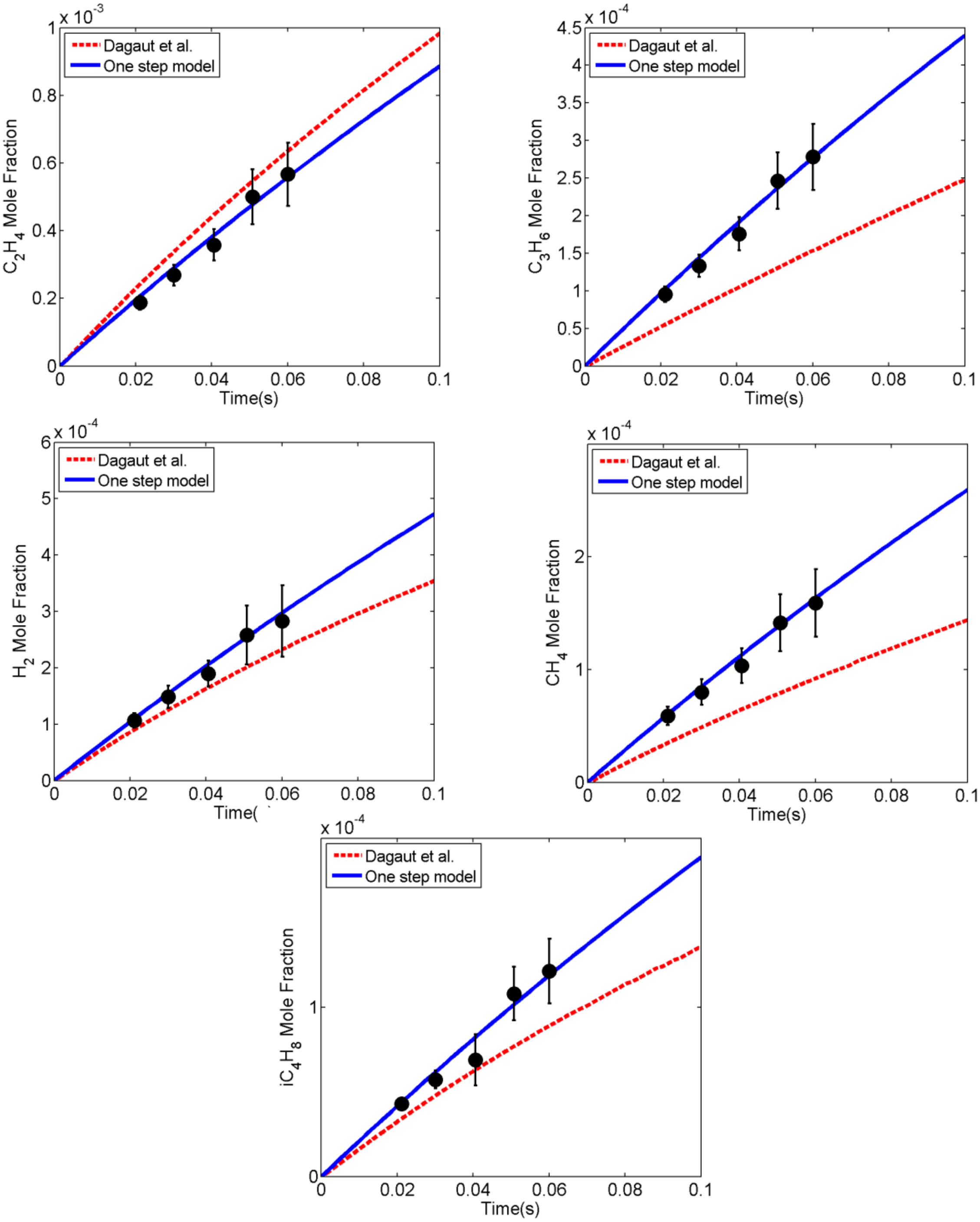

Figure 5.8: Comparison of species mole fraction (**major species**) as a function of time for the hot section temperature of **1000 K**. Symbols represent experimental results and lines represent predictions with two models by Dagaut et al. [95] and the one step model for inflow species compositions of $X_{C_{11}H_{22}} = 0.0025$, $X_{N_2} = 0.9975$ and p = 1 atm.

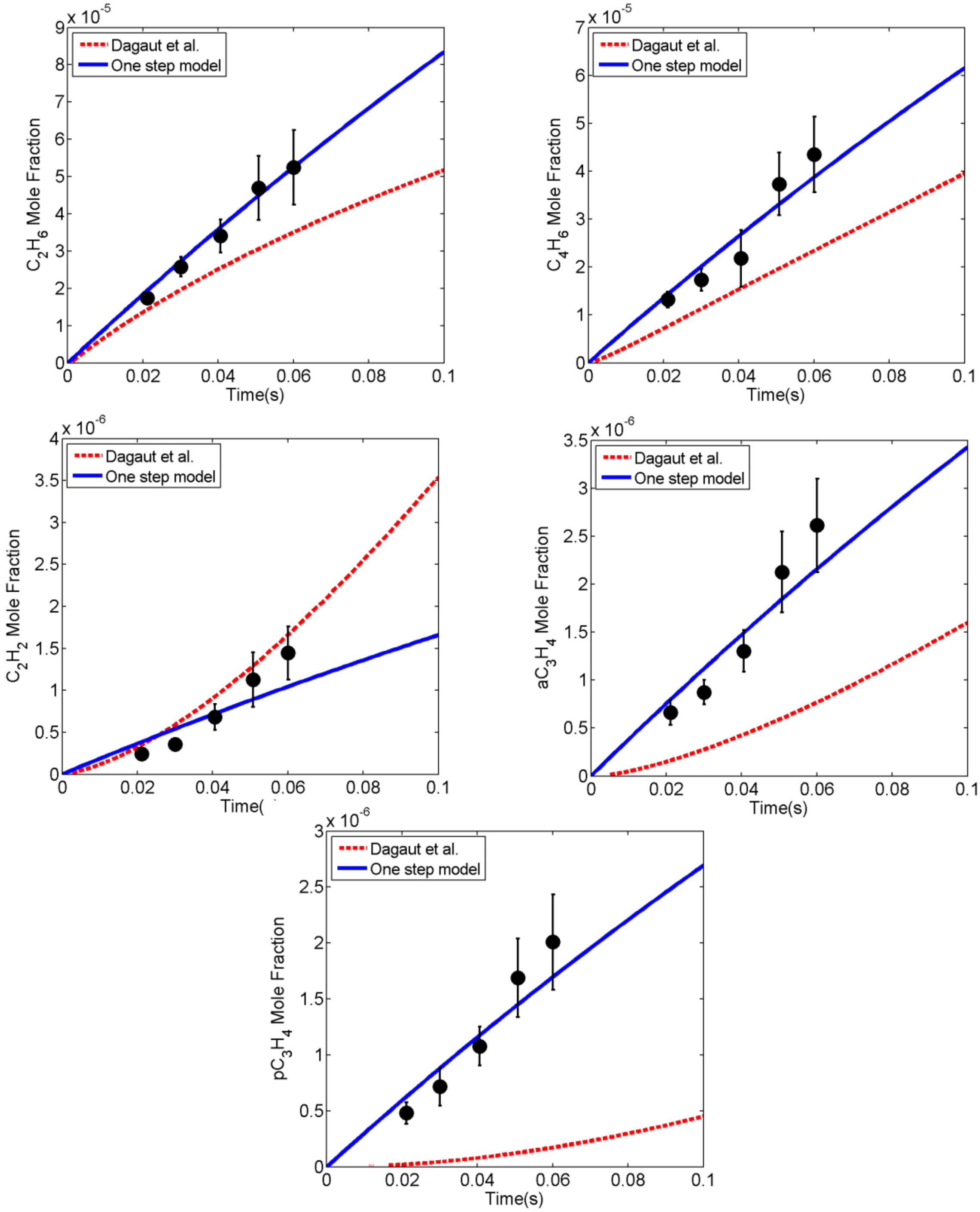

Figure 5.9: Comparison of species mole fraction (**minor species**) as a function of time for the hot section temperature of **1000 K**. Symbols represent experimental results and lines represent predictions with two models by Dagaut et al. [95] and the one step model for inflow species compositions of $X_{C_{11}H_{22}} = 0.0025$, $X_{N_2} = 0.9975$ and p = 1 atm.

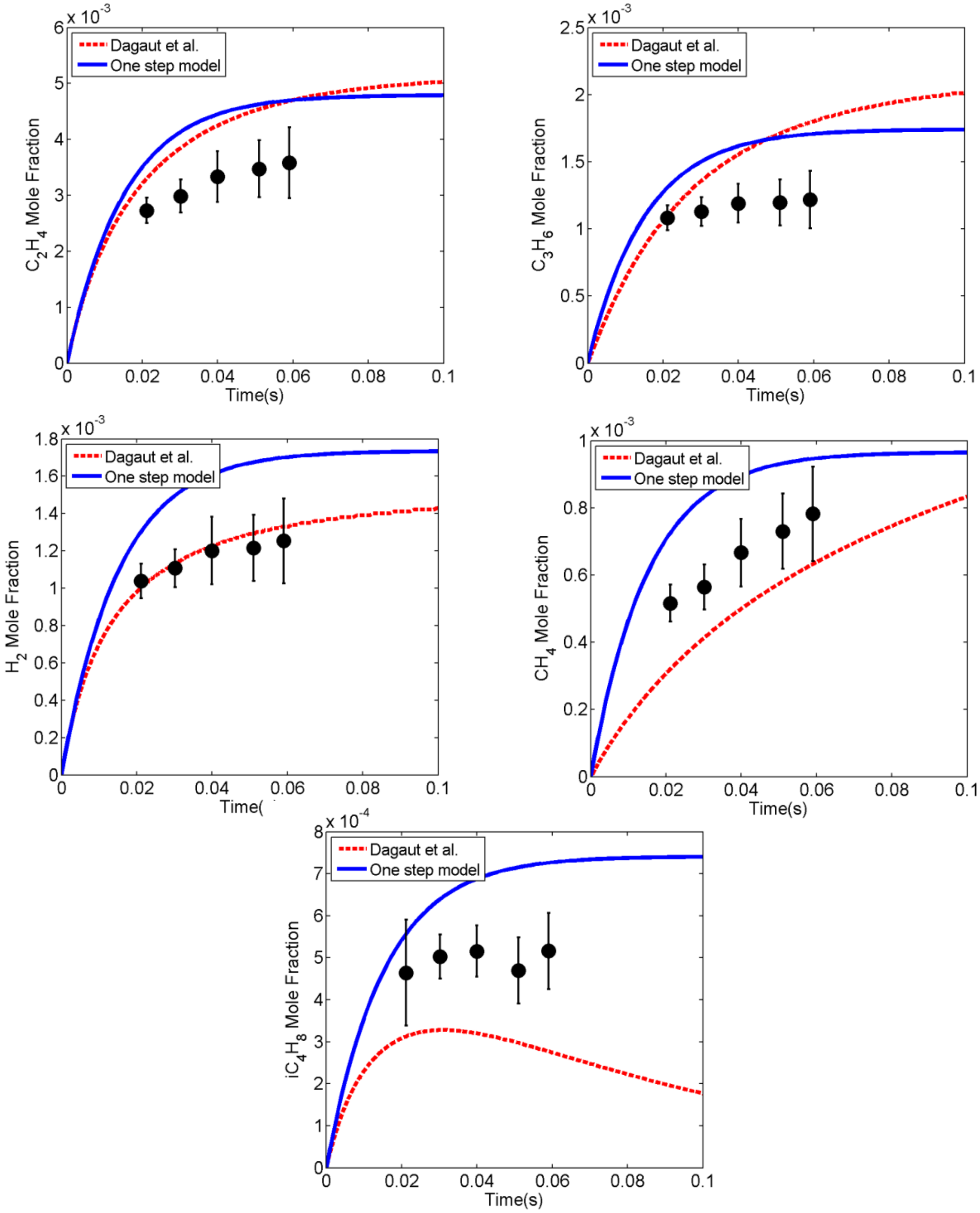

Figure 5.10: Comparison of species mole fraction (**major species**) as a function of time for the hot section temperature of **1100 K**. Symbols represent experimental results and lines represent predictions with two models by Dagaut et al. [95] and the one step model for inflow species compositions of $X_{C_{11}H_{22}}$ = 0.0025, X_{N_2} = 0.9975 and p = 1 atm.

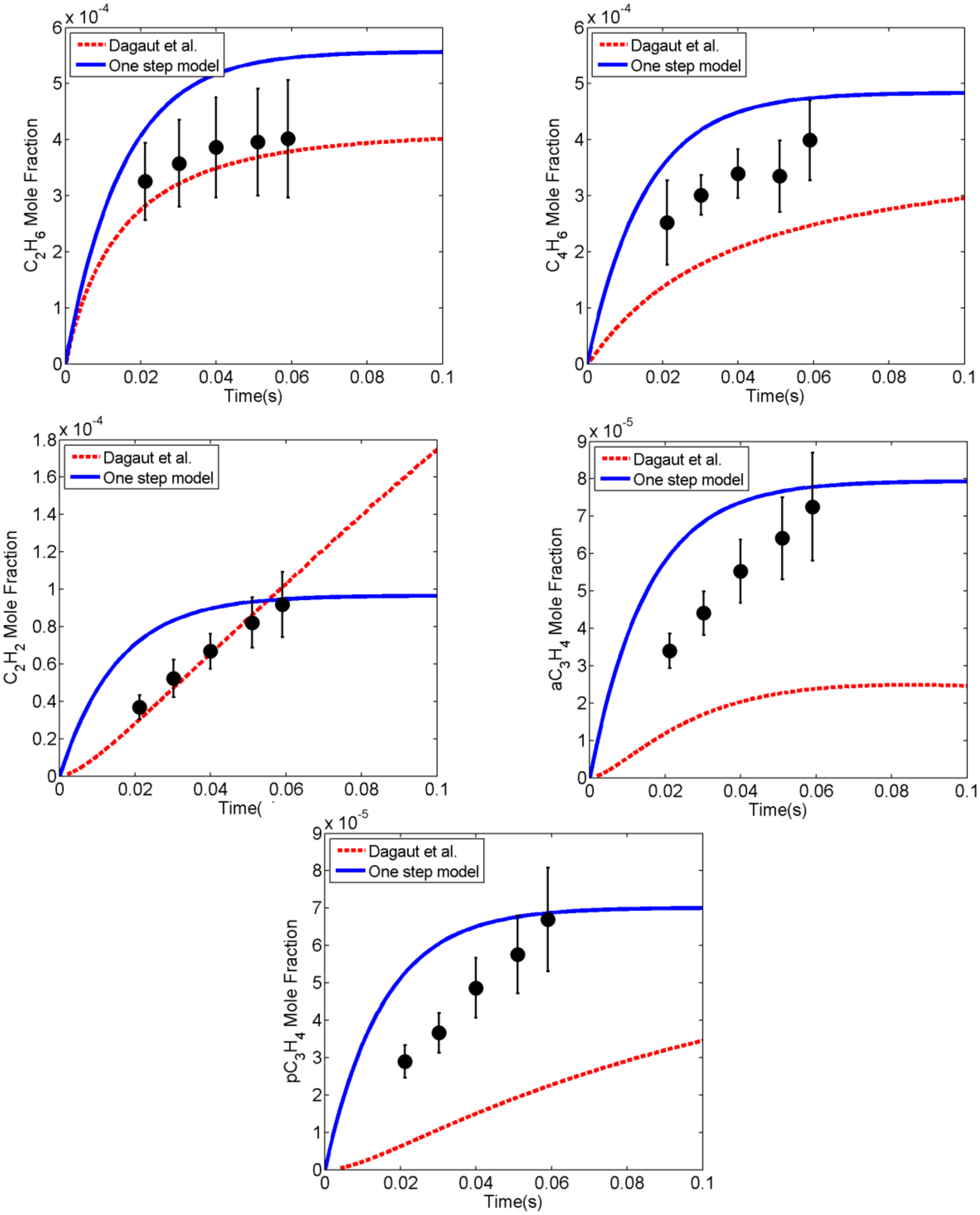

Figure 5.11: Comparison of species mole fraction (**minor species**) as a function of time for the hot section temperature of **1100 K**. Symbols represent experimental results and lines represent predictions with two models Dagaut et al. [95] and the one step model for inflow species compositions of $X_{C_{11}H_{22}} = 0.0025$, $X_{N_2} = 0.9975$ and p = 1 atm.

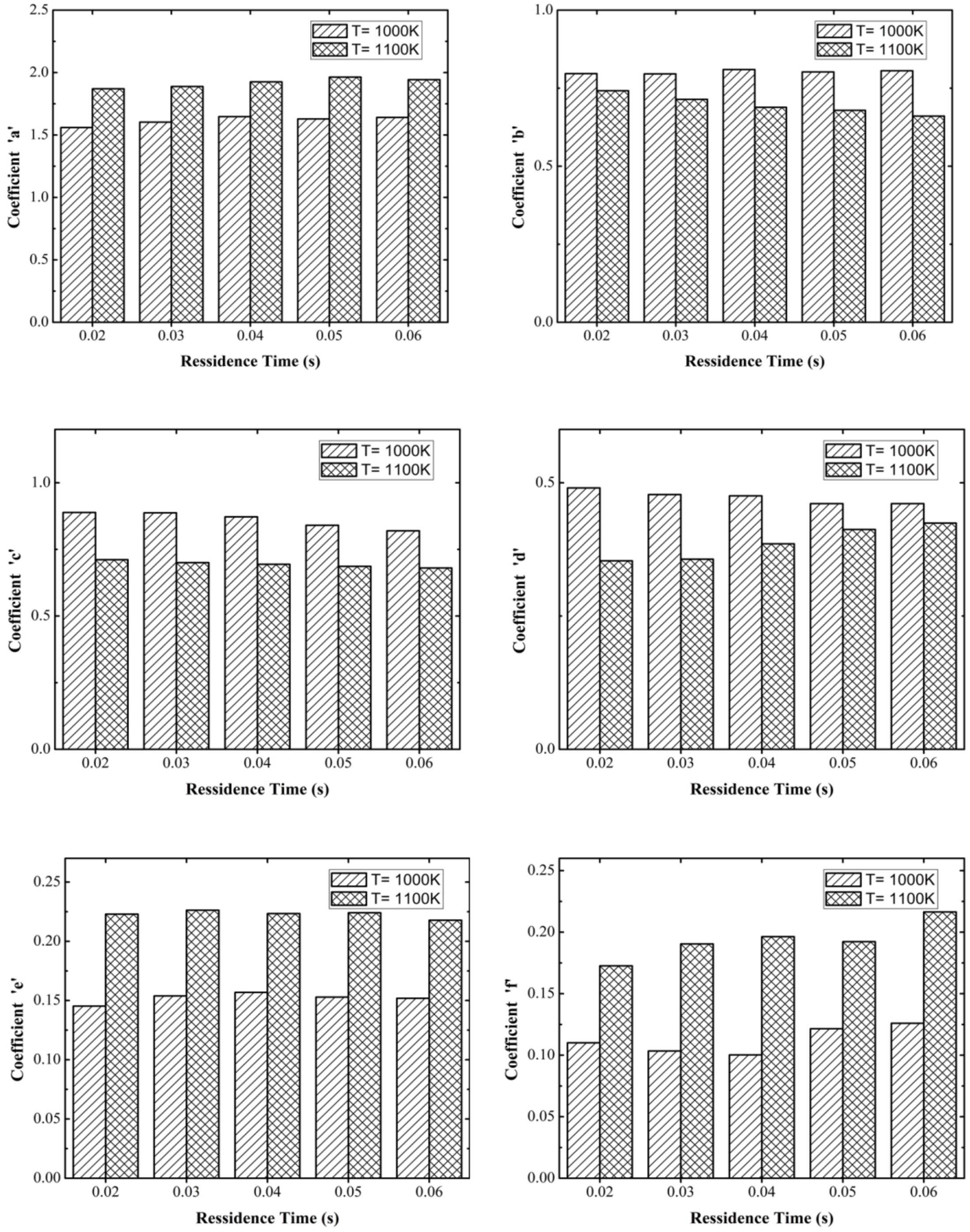

Figure 5.12: Comparison of stoichiometric coefficients (a-f) at residence times of 20-60 ms and temperatures 1000K and 1100K for inflow species compositions of $X_{C_{11}H_{22}} = 0.0025$, $X_{N_2} = 0.9975$ and p = 1 atm. The stoichiometric coefficients are defined by Eq.(5- 11) to (5- 21).

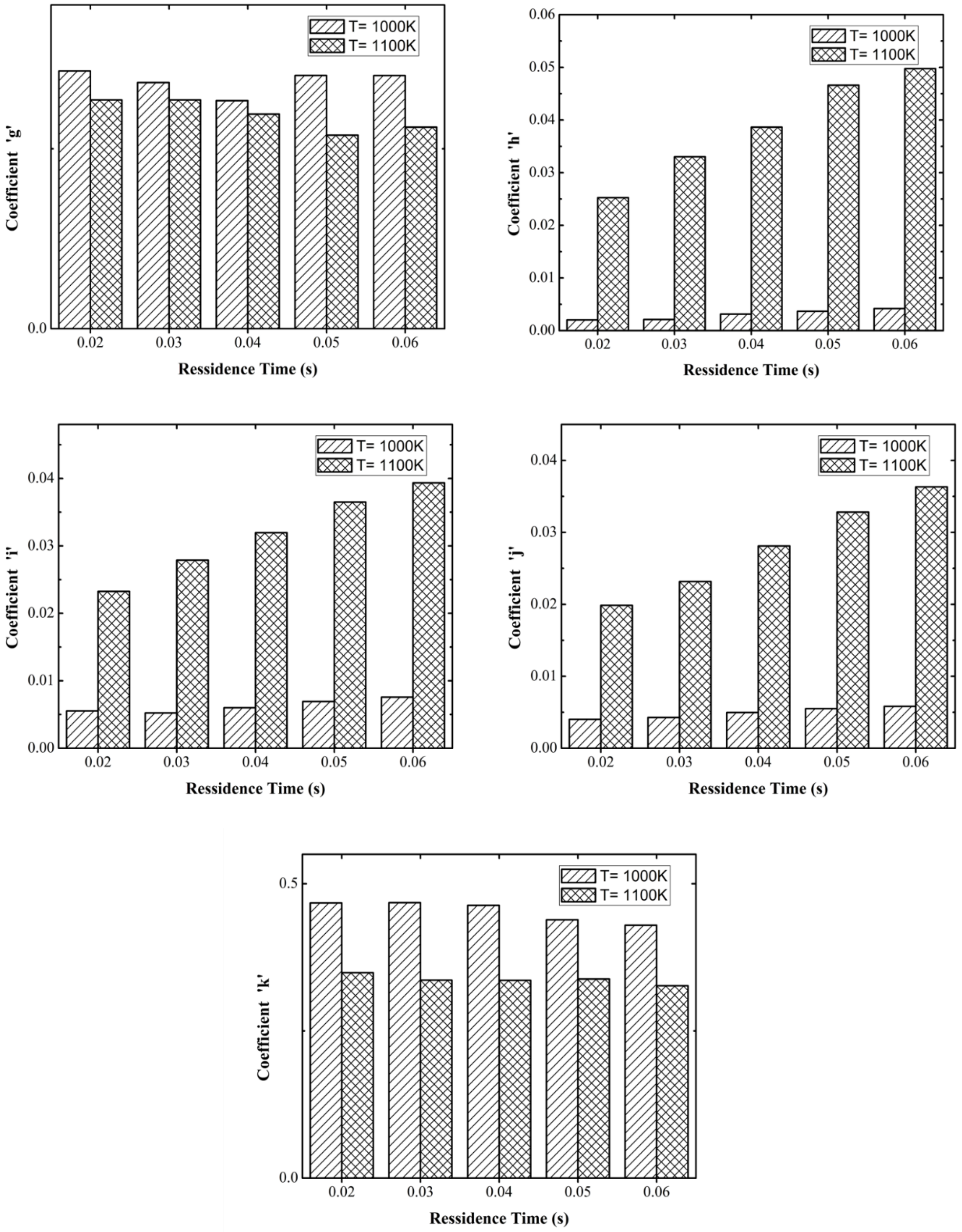

Figure 5.13: Comparison of stoichiometric coefficients (g-k) at residence times of 20-60 ms and temperatures 1000K and 1100K for inflow species compositions of $X_{C_{11}H_{22}}$ = 0.0025, X_{N_2} = 0.9975 and p = 1 atm. The stoichiometric coefficients are defined by Eq. (5- 11) to (5- 21).

5.3.3 Product Distribution Comparison of Fuels at Elevated Pressure

In order to investigate the variation of product distribution between various fuels, pyrolysis studies for four different fuels were conducted in the high-pressure reactor. This set of fuels includes a jet fuel surrogate (n-dodecane), a single component jet fuel (JP-10) and two batches of multi component JP-8 (A-1). Figure 5.14 and Figure 5.15 compare the product mole fraction of these fuels at several temperatures ranging from 950 to 1100K at 5 atm and at a residence time of 590 ms.

Based on the figures, it can be seen that all the fuels decompose into similar set of major product species. However, the concentration of product species varies significantly between these fuels indicating different pyrolysis pathways. While the variation between two batches of JP-8 is not prominent, significant differences are observed between n-dodecane, JP-8 and JP-10. Furthermore, JP-8 and dodecane also follow a similar trend for most of the products. However, JP-10 pyrolysis appears to follow a completely different pathway which is further analyzed in Section 5.4.2.

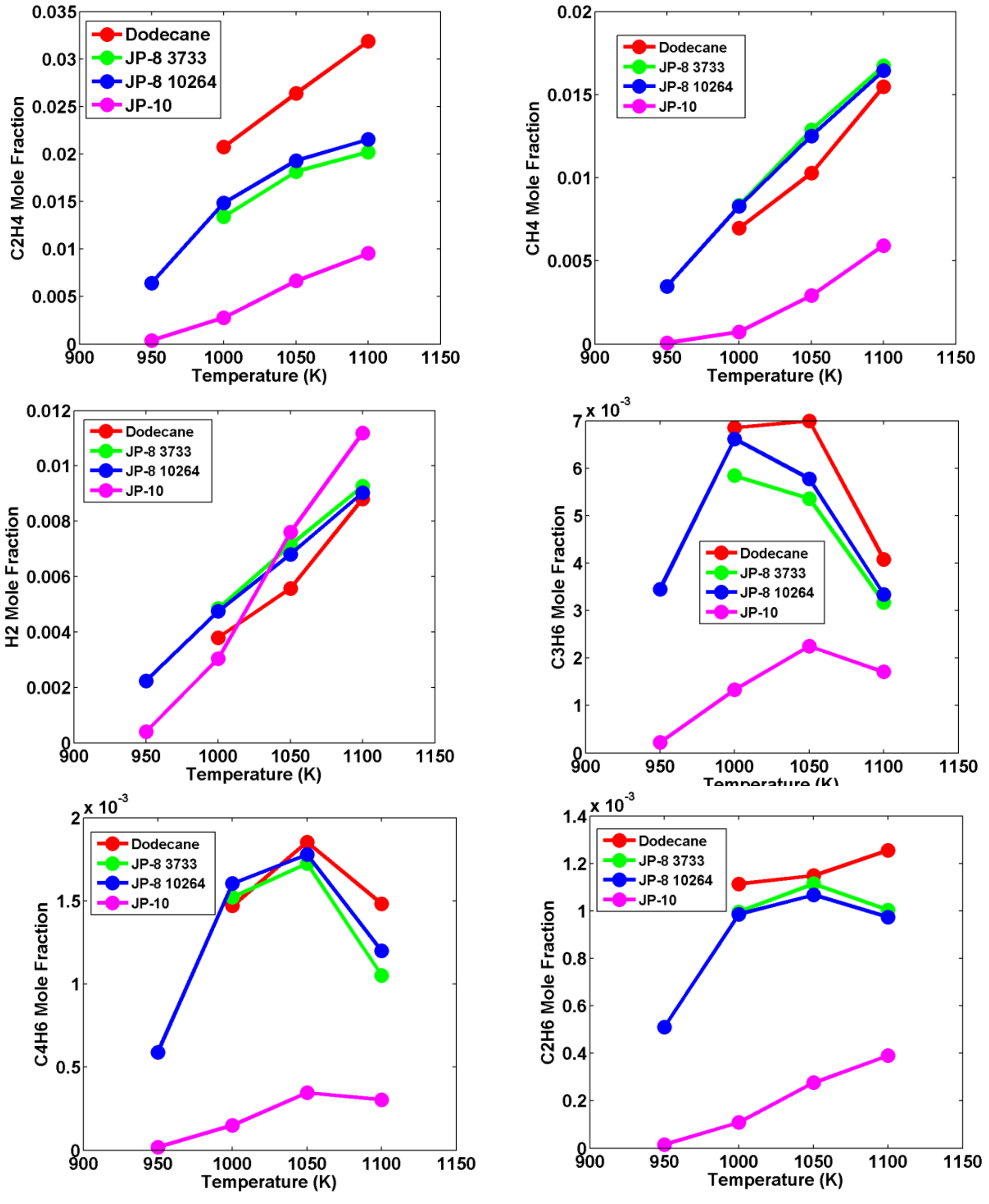

Figure 5.14: Comparison plot of **major** product distribution for various fuels (n-dodecane, two batches of JP-8 and JP-10) as a function of set temperature at residence time of 590 ms. $X_{\text{Fuel}} = 0.01$, $X_{N_2} = 0.99$ and p = 5 atm.

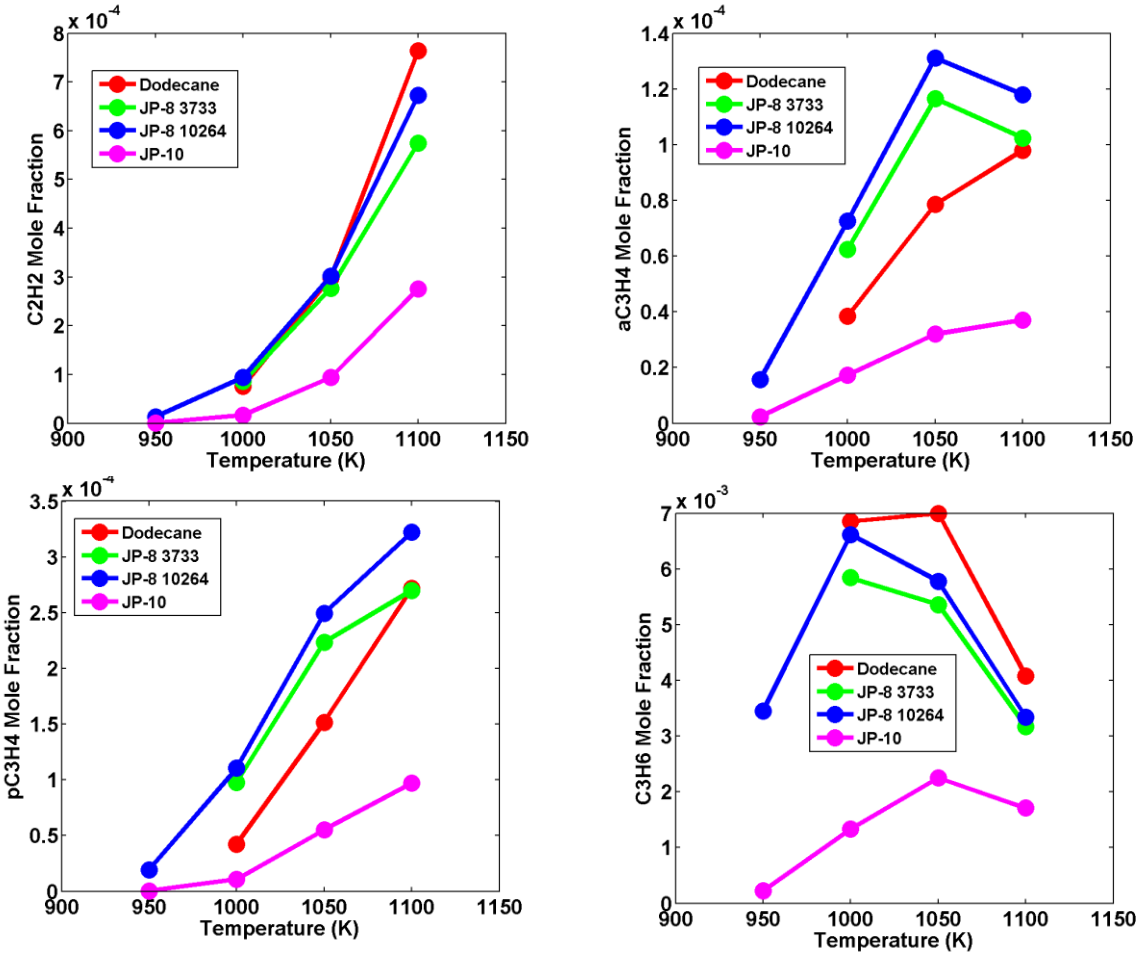

Figure 5.15: Comparison plot of **minor** product distribution for various fuels (n-dodecane, two batches of JP-8 and JP-10) as a function of set temperature at residence time of 590 ms. $X_{\mathrm{Fuel}} = 0.01$, $X_{N_2} = 0.99$ and p = 5 atm.

5.4 Catalytic Thermal Decomposition of JP-10 over H-Y zeolite

JP-10 is a single component synthetic aviation fuel with high energy density, high specific impulse, and low freezing point [102]–[108]. The heat of combustion of JP-10 (39.4 MJ/L) is considerable higher than JP-8 (34.5 MJ/L). JP-10 is currently used in missiles because of its high energy density which is favorable for high speed and long distance flights [109], [110]. It is also regarded as a potential fuel to be used as a heat sink or endothermic fuel

[104], [108] for hypersonic applications. Further, JP-10 is a single component fuel and thus the modeling of JP-10 is less complex compared to a multicomponent JP-8.

Recently, shock tube experiments and modelling studies of JP-10 were conducted by Gao et al [105]. The experiments were performed with 2000 ppm JP10 in a temperature range of 1000-1600K and pressure range of 6-8 atm. A homogeneous reaction model consisting of 691 species in 15,518 elementary reactions was also proposed. The model is an extended version of the improved pyrolysis model by Vandewiele et al. [111] which has been validated with experimental results from a continuous flow tubular reactor near atmospheric pressure and temperature range from 930-1080K [105]. A shock tube experimental study in combination with UV absorption spectrograph was conducted by Davidson et al. [112] in microsecond time scale (50-200 μs, T = 1100-1700K) and identified benzene, cyclopentene, propene, ethylene, acetylene, 1,3-butadiene and cyclopentadiene as decomposition products of JP-10. Also, cyclopentene was considered to be one of the major products. The experimental study conducted in a micro-flow tube reactor in by Nakra et al. [107] in ms scale range (2.6- 9.3 ms, T=293-1498 K) had similar products, namely cyclopentadiene, benzene, propyne, acetylene and ethylene. However, cyclopentene was not identified in the study [105].

In order to explore the applicability of the UVa MFTR for catalytic pyrolysis studies, JP-10 pyrolysis experiments were conducted in the atmospheric pressure reactor in presence and absence of H-Y zeolite catalyst. The selection of catalyst and fuel pairing between H-Y zeolite (30:1 Si: Al_2) and JP-10 was experimentally determined by Huang and Davis [113] in a fixed bed reactor system.

5.4.1 Wall-Coated Catalysis Experiments

The thermal decomposition of JP-10 (from Dixie Chemical Company) was conducted by placing three 1 mm clean quartz rods and H-Y zeolite coated quartz rods in the atmospheric pressure micro-flow tube reactor (see Figure 5.16). The quartz rods were fused together by a spacer at three points along the length to allow free flow of molecules between and around the rods.

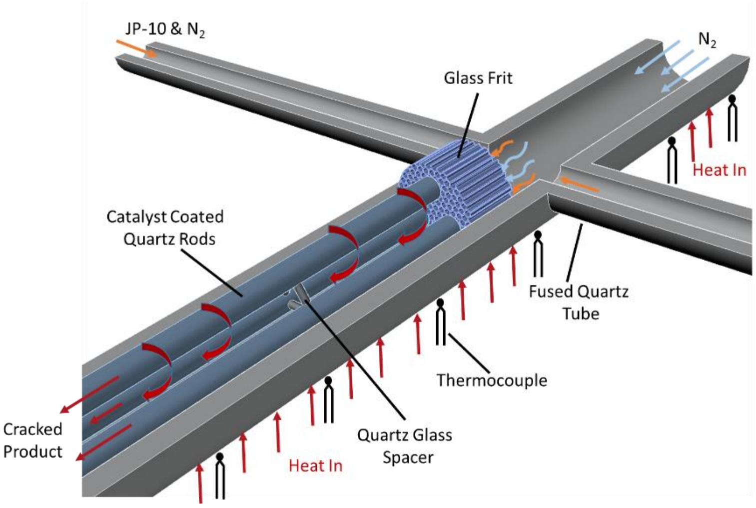

Figure 5.16: Schematic of atmospheric pressure micro flow tube reactor with three 1 mm coated quartz rods with H-Y zeolite and placed in the hot section.

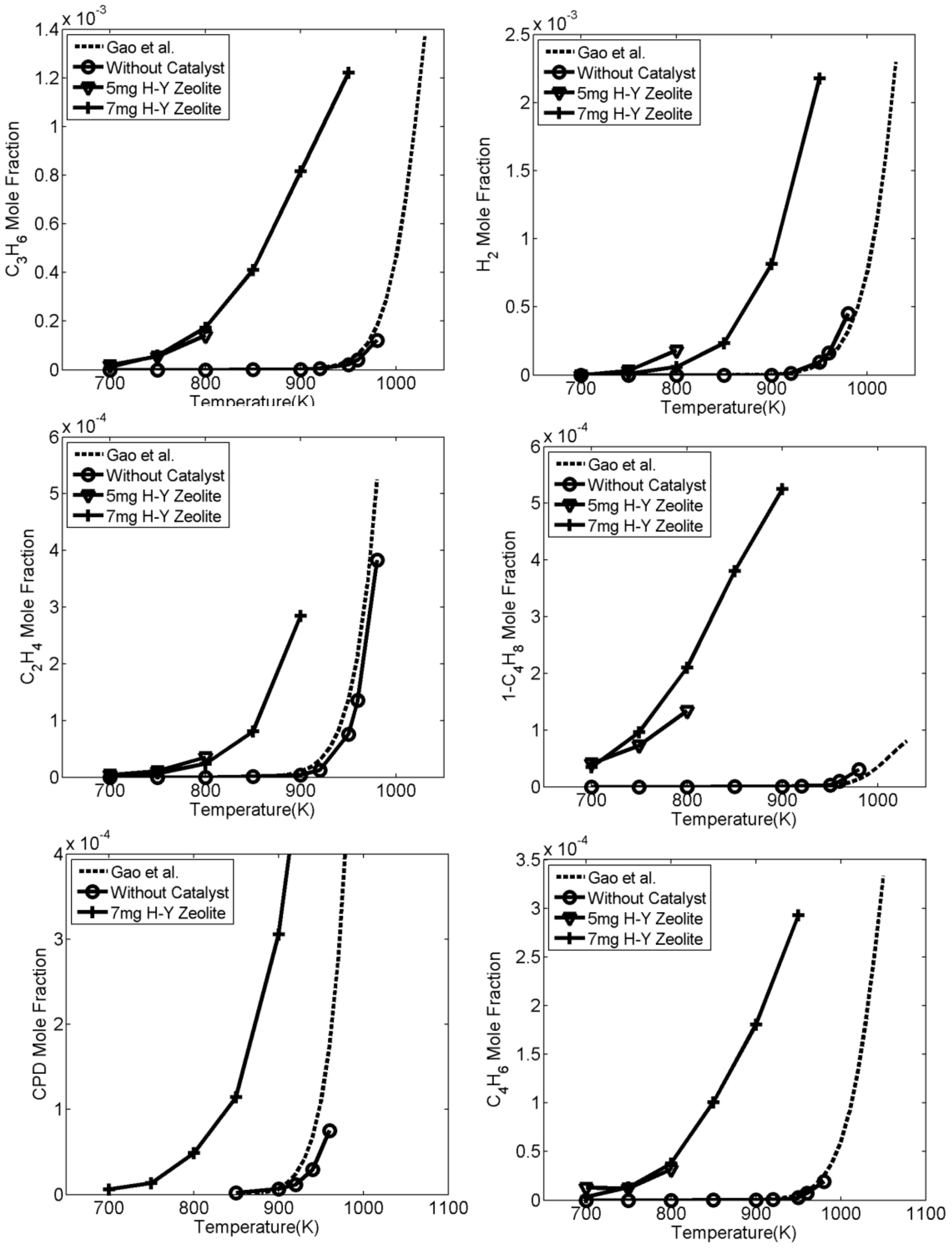

Figure 5.17: Comparison of **major** species yield from JP-10 pyrolysis as a function of hot-section temperature, for 1% JP-10 in nitrogen (by moles) at residence time 400 ms and pressure 1 atm. ∇ and + represents H-Y zeolite loadings of 5 mg and 7 mg, respectively; ○ represents without H-Y zeolite catalyst; dashed line represents numerical predictions using a detailed chemical kinetic model proposed by Gao et al. [105] without catalytic reactions.

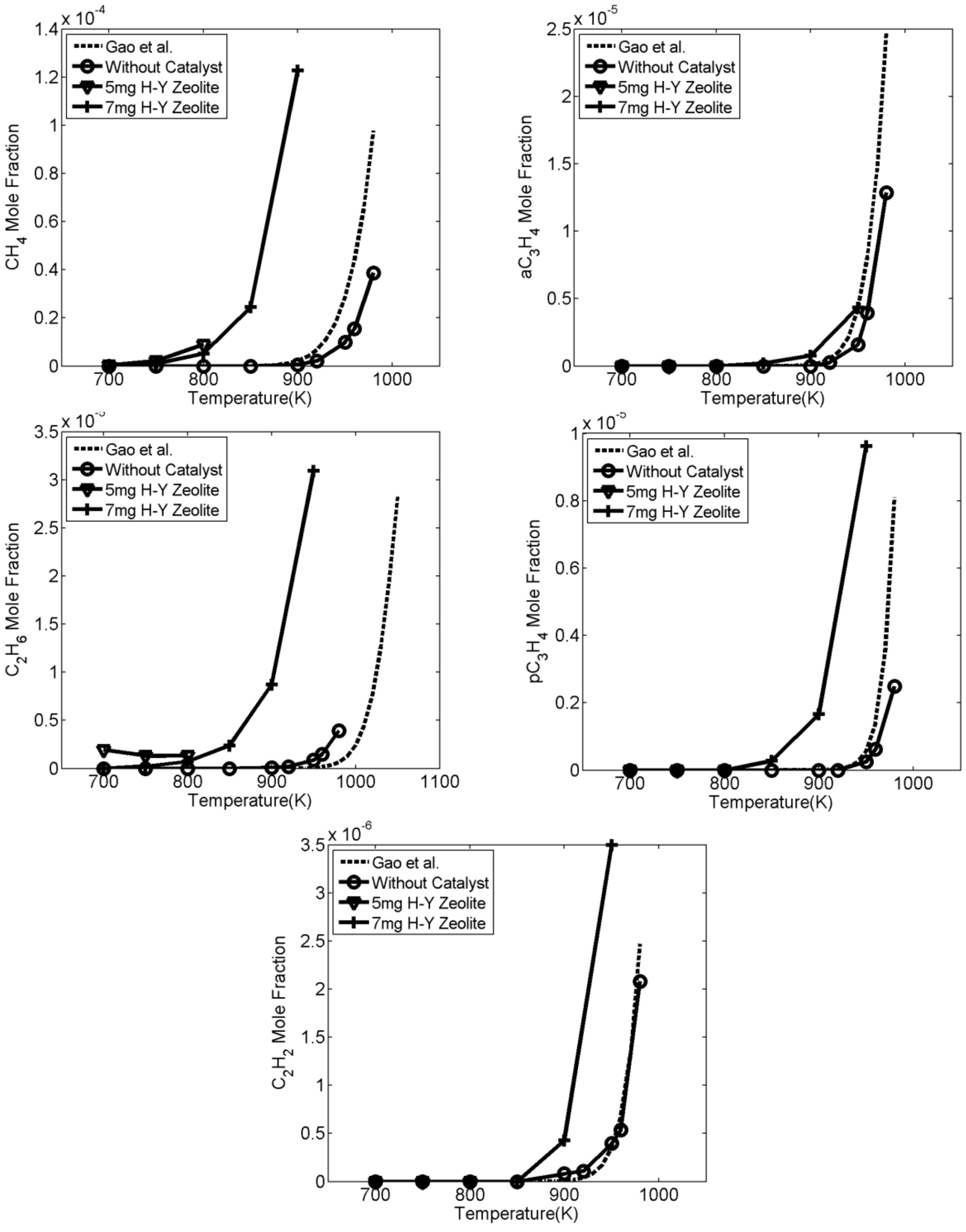

Figure 5.18: Comparison of **minor** species yield from JP-10 pyrolysis as a function of hot-section temperature, for 1% JP-10 in nitrogen (by moles) at residence time 400 ms and pressure 1 atm. ∇ and + represents H-Y zeolite loadings of 5 mg and 7 mg, respectively; **O** represents without H-Y zeolite catalyst; dashed line represents numerical predictions using a detailed chemical kinetic model proposed by Gao et al. [105] without catalytic reactions.

The experimental conditions explored for the present study are given in Table 5.3. In order to ensure sufficient interaction between fuel and catalyst, a relatively long residence time of 400 ms was selected. For the selected residence time the fuel flow rates required to attain 1% fuel mole fraction with the inserted rods were of the order 0.01- 0.014 ml/min. Other details for the experimental setup for the liquid fuel pyrolysis study can be found in Chapter 2.

Table 5.3: Experimental conditions for homogeneous and catalytic JP-10 pyrolysis study in MFTR.

JP-10 (% by moles)	**N_2 (% by moles)**	**Pressure (atm)**	**Temperature (K)**	**Residence time (s)**
1	99	1	700-980	0.4

5.4.2 Results and Discussion on Catalytic Pyrolysis of JP-10

Figure 5.17 and Figure 5.18 depict the comparison of experimental data obtained with and without catalyst and predicted results using detailed homogeneous kinetic model proposed by Gao et al. [105]. Figure 5.17 shows the major species, C_3H_6, H_2, C_2H_4, 1-C_4H_8, C_5H_6 CPD and C_4H_6, while Figure 5.18 shows the minor species, CH_4, aC_3H_4, C_2H_6, pC_3H_4, and C_2H_2. These species are consistent with the components identified in experiments conducted by Vandewiele et al. [108] and Gao et al. [105]. It can be observed from the figures that both the major and minor species agree well with the model. Another important conclusion that can be made from the figures is the shift of almost 188 K in decomposition temperature of the fuel with addition of catalyst. Also, 40% increase in catalyst loading brings no significant change in the results.

In addition to the species shown in the plots, species such as cyclopentene, benzene, 1, 3-hexadiene, cyclohexadiene and toluene are some of other major species observed in the experiments (See GC and GCMS chromatograms in Figure 5.19 and Figure 5.20 respectively). At similar product yield, the addition of the catalyst significantly changed the product distribution. It was observed that concentration of hydrogen, methane, ethylene, ethane, acetylene, allene, propyne, cyclopentadiene and cyclopentene were reduced with addition of catalyst. In contrast, propylene, 1,3-butadiene, 1-butene, cyclohexadiene and 1,3-hexadiene were significantly increased with the addition of catalyst.

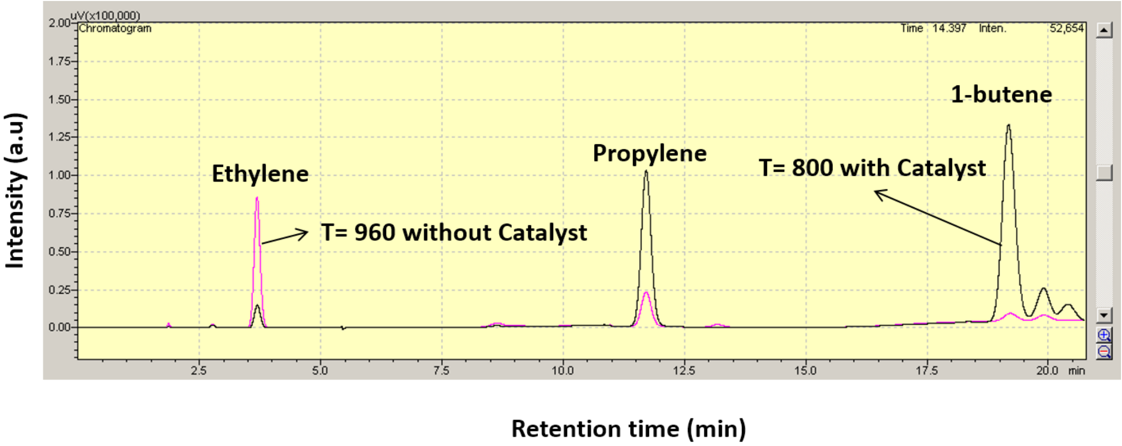

Figure 5.19: GC chromatogram during homogeneous and catalytic pyrolysis at T=800K and T=960 K respectively. The residence time is kept fixed at t_{res}=0.4 s.

As explained in Chapter 1, the chemical heat sink capacity offered by the fuel depends in product distribution. In order to calculate the heat sink capacity in both homogeneous and catalytic pyrolysis, the enthalpies were calculated using NASA thermochemical data base [114] given by:

$$\frac{h_k}{RT_k} = a_{1k} + \frac{a_{2k}}{2}T_k + \frac{a_{3k}}{3}T_k^2 + \frac{a_{4k}}{4}T_k^3 + \frac{a_{5k}}{5}T_k^4 + \frac{a_{6k}}{T_k} , \qquad (5\text{- }22)$$

where, $h_k$is the molar enthalpy of the kth species, R is the universal gas constant, T_k is the temperature and a_{1k}-$a_{6k}$are the numerical coefficients from Gao et al. [105].

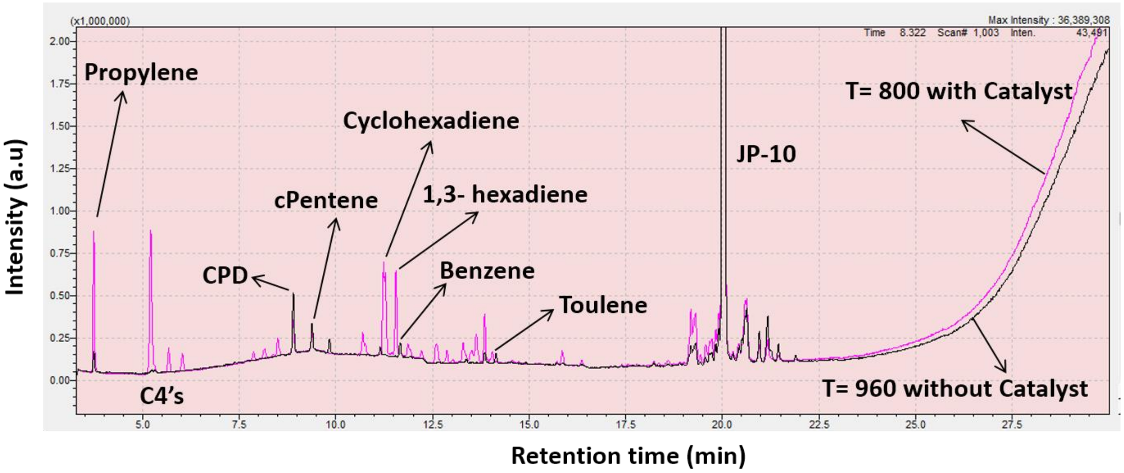

Figure 5.20: GC-MS chromatogram during homogeneous and catalytic pyrolysis at T=800K and T=960 K respectively. The residence time is kept fixed at t_{res}=0.4 s.

Table 5.4 shows a comparison of estimated endothermicity at iso-conversion level of 3.13 % with and without catalyst. Also, shown in the table is the sensible cooling capacity estimated from Δh_{sens} (see Eq. (1- 2)) between 298.15 K and iso-conversion temperature listed. The first key observation is that with catalyst the conversion occurs at a temperature about 188 K lower than without catalyst coating case. Second, at this small conversion level, the endothermic cooling capacity is very small when compared with the sensible cooling capacity. But more importantly, the species yield with catalyst results in no significant change in endothermic cooling capacity compared to without the catalyst.

Table 5.4: Comparison of endothermic vs. sensible enthalpy from JP-10 pyrolysis with and without catalyst

Condition	Iso-conversion T (K)	Endothermic cooling (J/mol)	Sensible cooling (J/mol)
Without catalyst	960	7656.49	3×10^5
With catalyst	772	7586.98	2.14×10^5

Figure 5.21 to Figure 5.24 show an attempt to describe the homogeneous reaction pathways that lead to the key species identified by the GC/FID/TCD/MS system at T=960K and residence time of 0.4 s. The reaction flux pathway were observed to be similar to JP-10 decomposition study reported by Gao et al. [105] at T=1000K.

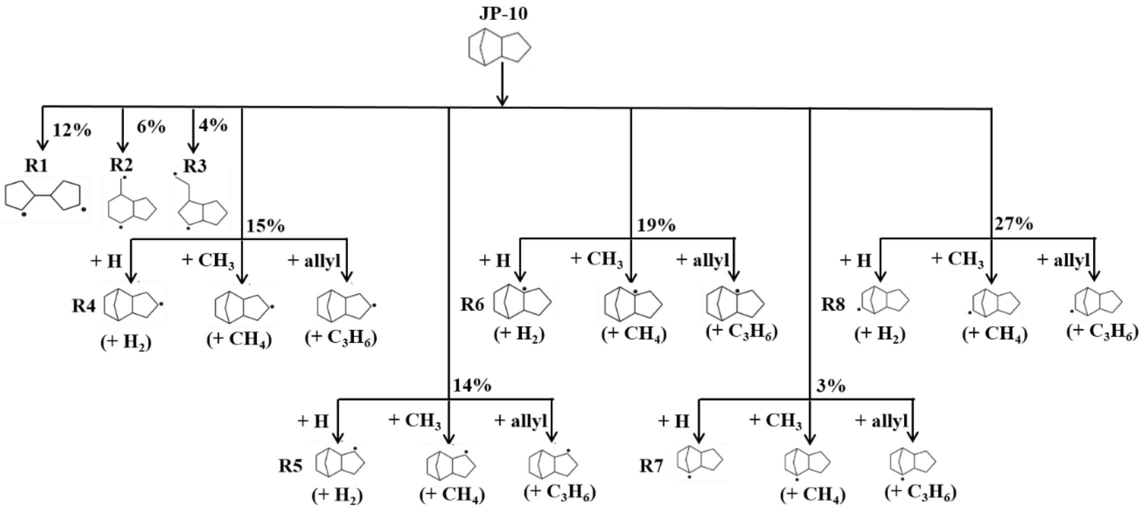

Figure 5.21: Reaction path flux analysis of JP-10 pyrolysis indicating the key reactions that JP-10 radical and key species such as hydrogen, methane and propylene identified in experiments at T=960K and residence time of 0.4 seconds

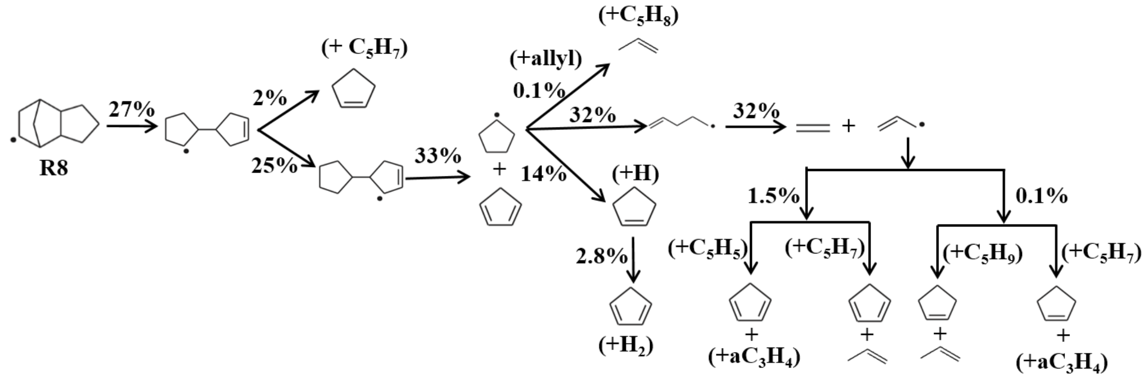

Figure 5.22: Reaction path flux analysis of R8 (JP-10 radical) pyrolysis indicating the key reactions that lead to the species such as allene, ethylene, cycopentadiene, and cyclopentene identified in experiments at T=960K and residence time of 0.4 seconds.

The main consumption of JP-10 occurs due to hydrogen abstraction to form JP-10 radicals (R1- R8) as shown in Figure 5.21 [105]. The hydrogen abstraction takes place due to the reaction of allyl, hydrogen and methyl radical with JP-10. Each hydrogen abstraction reaction follows a separate reaction pathways with different reaction flux to form JP-10 radicals, hydrogen, methane and propylene. These stable species are some of the major species observed in the present experiments (see Figure 5.17). Further, it can be observed from the figure that the most dominant channel that JP-10 decomposes into R8 (27%) and R6 (19%).

The reaction pathway analysis for channel R8 is shown in Figure 5.22. It can be observed from this analysis that 33% of JP-10 decomposes into cyclopentyl and cyclopentadiene.

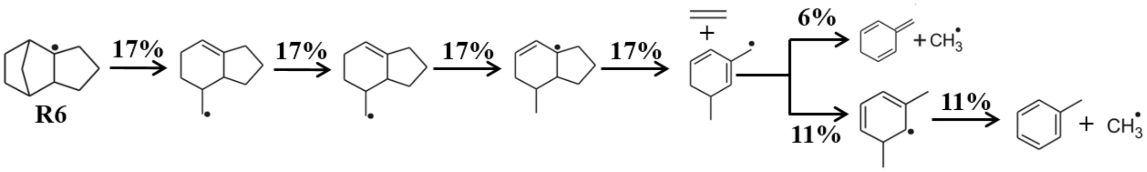

Figure 5.23: Reaction path flux analysis of R6 (JP-10 radical) indicating the key reactions that lead to toluene identified in experiments at T=960K and residence time of 0.4 seconds.

One of the pathways of cyclopentyl then leads to formation of 14% cyclopentene and the other leads to formation of ethylene and allyl radical. Both ethylene and cyclopentene were observed in the current experiments. Further, the allyl radical reacts with various C_5 molecules to form cyclopentadiene, cyclopentene, propylene and allene. These reaction pathways clearly explain the formation of ethylene, propylene and cyclopentadiene as major products and allene as minor products in the current experiments.

The reaction pathway analysis for the R6 radical is shown in Figure 5.23. The pathway depicts the decomposition of JP-10 into toluene and methyl radical which was also observed in the current study.

As explained earlier, with the addition of the catalyst, major species such ethylene and methane decreased while the species such as propylene, 1, 3-butadiene and cyclohexadiene increased. This change in species distribution indicates difference in major reaction pathways with addition of catalyst. Without the catalyst, around 14% of JP-10 decomposes into R5 (See Figure 5.21). The formation of 1,3-butadiene and cyclohexadiene can be observed by analysis of the R5 reaction pathway as shown in Figure 5.24. Around 1.8% on JP-10 decomposes into cyclohexenyl and 1-3, butadiene. Cyclohexenyl then converts into cyclohexadiene with H atom addition. Note this reaction pathway analysis is without the catalyst where the small concentration of these species is consistent with the homogeneous

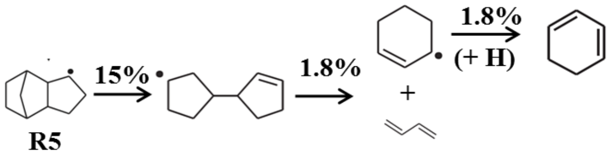

Figure 5.24: Reaction path flux analysis of R5 (JP-10 radical) indicating the key reactions that lead to toluene identified in experiments at T=960K and residence time of 0.4 seconds.

experiments. However, larger concentration of these species with addition of the catalyst indicated R5 as one of the major reaction pathways leading to cyclohexadiene and 1,3-butadiene.

5.5 Summary

The experimental set up for liquid fuel pyrolysis was validated by conducting pyrolysis study of n-dodecane which is a well-studied jet fuel surrogate component. In the process, the experimental results were compared with chemical kinetic models and experimental results in the literature. Similar to other fuels, available models showed variation between each other. Nevertheless, a recently published model by Mze-Ahmed et al. [94] showed a good agreement with the present results. With the validation of the experimental configuration, the work was extended to JP-8 pyrolysis experiments. Based on the observed product mole fractions, a one-step fast thermal pyrolysis was explored. The comparison of results with a surrogate model by Dagaut et al. [95] and the one step model indicated that the one-step model was capable of capturing the present MFTR data as good as the multi-step surrogate model. The good agreement of one step model with the experimental data indicated a potential use of the one step model in conjunction with available H_2, C_1-C_4 base models to form a complete set.

Finally, in order to show the applicability of MFTR to conduct heterogeneous pyrolysis studies, thermal decomposition of JP-10 was conducted by placing three 1 mm clean and H-Y zeolite coated quartz rods. In addition to the key products being consistent with literature studies, the product distribution matched the prediction by Gao et al. [105] very well. Furthermore, the addition of catalyst brought significant change in decomposition temperature (decreased by 188 K) of the fuel and product distribution. In order to understand the product distribution, reaction pathways analysis was conducted which indicated a change in pathway with and without catalyst.

Chapter 6: Summary and Future Recommendations

6.1 Summary

Besides providing energy, the liquid HC fuel in propulsion systems can also be used as coolant for critical engine components. Understanding fuel decomposition pathways and speciation are critical for determining the endothermic cooling capacity of the fuels as well as to understand the soot formation on a fundamental level. The reaction models defining these processes are large, complex, and have significant uncertainties. The present work aimed at understanding the fuel decomposition processes and reducing the uncertainties in these models by developing a well characterized experimental technique consisting of a MFTR and GC/FID/TCD/MS system and by investigating fuel pyrolysis experiments of various small and large hydrocarbon fuels.

In order to capture a wide range of temperatures, pressures, and residence times, two types of a novel MFTR (atmospheric and high pressure reactor) were designed and developed. Both the reactors are made up of 4mm i.d. quartz tubes with negligible catalytic effect. The main differences between the two rectors exist in the way how the fuel is fed and the presence of choked orifice at the exit of high pressure reactor. To minimize the effects of reaction initialization, the atmospheric pressure reactor featured a preheating helical section for supplying diluent, air cooled side tubes for supplying fuel, a small mixing volume, and a porous glass frit. The proper heating of the gases was assured by a well-controlled heating system with heaters, PID controllers, and thermocouples.

Experiments were performed to understand the uniformity of temperature along the length of the reactor, establish the degree of mixing of fuel and diluent after the frit, and to determine the presence of any catalytic/wall effects of quartz. Based on the traditional thermocouple measurement as well as by the chemical thermometer concept, no significant change in temperatures (±(5-10) K) along the controlled section were observed. While the atmospheric pressure reactor with a preheated helical section consisted of a uniform temperature profile, the high-pressure reactor consisted of a transient region of approximately 15 cm, due to the lack of the mentioned helical preheating section in that configuration. The results from the mixing study indicated well mixed fuel and diluent along the radial direction and a very well mixed mixture within 3.6% of the length in axial direction. Finally, a study performed by inserting three solid quartz rods, resulting in the increase of surface area to volume ratio by a factor of two, indicated no significant catalytic effect from quartz wall reactions.

The fidelity of the MFTR was tested conducting ethane and n-butane pyrolysis studies at various temperatures, pressures and residence times. The experimental results were compared with several model predictions as well as with available experimental results from the literature. Due to the small mixing volume of the reactor, one of the important factors concluded from the results is the fact that there is no issue of coordinate shifting or zero time shifting to match the experimental data with model predictions. For ethane pyrolysis, the experimental results show a very good agreement with the recently published AramcoMech model and product yield of ethylene and acetylene matched well with literature experimental data. However, for n-butane pyrolysis, none of the models captured the tube reactor data perfectly and show significant variation between themselves. The lack of experimental results for n-butane pyrolysis explained the discrepancy of current results for n-butane pyrolysis with the models.

n-Dodecane, JP-8 and JP-10 homogeneous pyrolysis experiments were performed at various temperatures, residence times and two different pressures. Pyrolysis and oxidation behavior of n-dodecane have been investigated by various groups. Thus, results from the n-dodecane experiments further validated the experimental set-up for liquid fuel pyrolysis. With the validation of the experimental configuration, the work was extended to JP-8 pyrolysis. A recently published model by Mze-Ahmed et al. [94] showed a good agreement with the present n-dodecane results and the surrogate model developed by Dagaut et al. [95] matched fairly well with present JP-8 results. In addition, based on the observed product mole fractions, a one-step fast thermal pyrolysis of JP-8 was also proposed. The comparison of results with a surrogate model by Dagaut et al. [95] and the one-step model indicated that the one-step model was capable of capturing the present MFTR data as good as the multi-step surrogate model. Finally, in order to show the applicability of MFTR to conduct heterogeneous pyrolysis studies, thermal decomposition of JP-10 was conducted by placing three 1 mm clean and H-Y zeolite coated quartz rods. In addition to the key products being consistent with literature studies, the product distribution agreed well with the predictions by a model proposed by Gao et al. [105]. Furthermore, the addition of catalyst brought significant change in decomposition temperature (decreased by 188 K) of the fuel and product distribution. In order to understand the product distribution, reaction pathways analysis was conducted which indicated a change in pathway with and without catalyst.

For all the experimental results, detailed uncertainty analysis was performed considering the calibration and measurement uncertainty.

6.2 Future Recommendations

With the validation of the experimental configuration, several future studies are recommended.

- The ideal configuration of the reactor with side tubes can be modified by adding a choked orifice at the exit and use to explore high pressure pyrolysis studied relevant to real propulsion systems.
- A calibration method developed to calibrate larger HCs in GCMS can be explored to quantify larger species in n-butane, n-dodecane, JP-8 and JP-10 pyrolysis. Carbon balance for these studies can be calculated including all the large HC's.
- Thermal decomposition experiments of category C fuels along with fast thermal pyrolysis model development can be investigated and compared with category A fuel.
- Fast thermal pyrolysis model can be combined with detailed oxidation models and the models can be validated with oxidation studies in MFTR.
- Pyrolysis study of JP-10 at wide range of temperatures, pressures and residence time can be performed to develop and validate a reduced model.
- Scanning Mobility Particle Sizer (SMPS) system along with in situ probe sampling technique can be utilized to study the size distribution of nano-particles in real fuels. The quantification of larger hydrocarbon such as benzene, pyrene, anthracene etc along with already quantified gas phase species can help in understanding the soot formation in these real fuels.

References

[1] U.S. Energy Information Administration, “Annual Energy Outlook 2015,” 2015.

[2] S. Dooley, S. H. Won, M. Chaos, J. Heyne, Y. Ju, F. L. Dryer, K. Kumar, C.-J. Sung, H. Wang, M. A. Oehlschlaeger, and others, “A jet fuel surrogate formulated by real fuel properties,” *Combust. Flame*, vol. 157, no. 12, pp. 2333–2339, 2010.

[3] T. Edwards and L. Maurice, “Hytech Fuels/Fuel System Research,” in *AIAA 98-1562 Aerospace Sciences Meeting*, 1998, pp. 296–306.

[4] N. Gascoin, P. Gillard, E. Daniau, S. Bernard, and M. Bouchez, “Pyrolysis of Supercritical Endothermic Fuel : Evaluation for Active Cooling Instrumentation,” *Int. J. Chem. React. Eng.*, vol. 6, no. A7, 2008.

[5] H. Huang, L. J. Spadaccini, and D. R. Sobel, “Fuel-Cooled Thermal Management for Advanced Aeroengines,” *J. Eng. Gas Turbines Power*, vol. 126, no. 2, p. 284, 2004.

[6] W. H. Heiser and D. T. Pratt, *Hypersonic Airbreathing Propulsion*. AIAA Education Series, 1994.

[7] R. Mohammad Javed, “Modeling and Analysis of Different Aspects of Finite-rate Chemical Kinetics in Hypersonic Combustors,” 2016.

[8] H. Huang, D. R. Sobel, L. J. Spadaccini, and E. Hartford, “Endothermic heat-sink of hydrocarbon fuels for scarmjet cooling,” in *38th AIAA Joint Propulsion Conference and Exihibit*, 2002.

[9] D. R. Sobel and L. J. Spadaccini, “Hydrocarbon Fuel Cooling Technologies for Advanced Propulsion,” *J. Eng. Gas Turbines Power*, vol. 119, no. 2, p. 344, 1997.

[10] D. S. Lee, D. W. Fahey, P. M. Forster, P. J. Newton, R. C. N. Wit, L. L. Lim, B. Owen, and R. Sausen, “Aviation and global climate change in the 21st century,” *Atmos. Environ.*, vol. 43, no. 22, pp. 3520–3537, 2009.

[11] A. Seaton, D. Godden, W. MacNee, and K. Donaldson, “Particulate air pollution and acute health effects,” *Lancet*, vol. 345, no. 8943, pp. 176–178, 1995.

[12] J. S. Kinsey, “Characterization of emissions from commercial aircraft engines during the Aircraft Particle Emissions eXperiment (APEX) 1 to 3,” Office of Research and Development, US Environmental Protection Agency, 2009.

[13] W. L. Chameides and M. Bergin, “Soot takes center stage,” *Science (80-.).*, vol. 297, no. 5590, pp. 2214–2215, 2002.

[14] J. E. Penner, D. H. Lister, D. J. Griggs, D. J. Dokken, and M. McFarland, “Aviation and the global atmosphere: A special report of intergovernmental panel on climate change working groups I and III.” Cambridge: Cambridge University Press, 1999.

[15] H. Richter and J. B. Howard, “Formation of polycyclic aromatic hydrocarbons and their growth to soot—a review of chemical reaction pathways,” *Prog. Energy Combust. Sci.*, vol. 26, no. 4, pp. 565–608, 2000.

[16] H. Bockhorn, *Soot formation in combustion: mechanisms and models*. Springer Science and Business Media, 2013.

[17] C. S. McEnally, L. D. Pfefferle, B. Atakan, and K. Kohse-Höinghaus, “Studies of aromatic hydrocarbon formation mechanisms in flames: Progress towards closing the fuel gap,” *Prog. Energy Combust. Sci.*, vol. 32, no. 3, pp. 247–294, Jan. 2006.

[18] M. Frenklach, “Reaction mechanism of soot formation in flames,” *Phys. Chem.*

Chem. Phys., vol. 4, no. 11, pp. 2028–2037, 2002.

[19] M. Frenklach, D. W. Clary, W. C. Gardiner, and S. E. Stein, "Detailed kinetic modeling of soot formation in shock-tube pyrolysis of acetylene," *Symp. Combust.*, vol. 20, no. 1, pp. 887–901, Jan. 1985.

[20] J. A. Miller and C. F. Melius, "Kinetic and thermodynamic issues in the formation of aromatic compounds in flames of aliphatic fuels," *Combust. Flame*, vol. 91, no. 1, pp. 21–39, Oct. 1992.

[21] R. Fournet, J. C. Bauge, and F. Battin-Leclerc, "Experimental and modeling of oxidation of acetylene, propyne, allene and 1, 3-butadiene," *Int. J. Chem. Kinet.*, vol. 31, no. 5, pp. 361–379, 1999.

[22] A. Gazi, G. Vourliotakis, G. Skevis, and M. A. Founti, "A Modelling Study of Allene and Propyne Combustion in Flames," *Proc. Eur. Combust. Meet.*, no. November 2016, 2011.

[23] L. Q. Maurice, H. Lander, T. Edwards, and W. E. Harrison, "Advanced aviation fuels: a look ahead via a historical perspective," *Fuel*, vol. 80, no. 5, pp. 747–756, 2001.

[24] T. Lu and C. K. Law, "Toward accommodating realistic fuel chemistry in large-scale computations," *Prog. Energy Combust. Sci.*, vol. 35, no. 2, pp. 192–215, 2009.

[25] M. B. Colket, J. Heyne, M. Rumizen, J. T. Edwards, M. Gupta, W. M. Roquemore, J. P. Moder, J. M. Tishkoff, and C. Li, "An Overview of the National Jet Fuels Combustion Program," in *54th AIAA Aerospace Sciences Meeting*, 2016, no. January, p. 177.

[26] H. Wang, E. Dames, B. Sirjean, D. A. Sheen, R. Tangko, A. Violi, J. Y. W. Lai, F. N. Egolfopoulos, D. F. Davidson, R. K. Hanson, C. T. Bowman, C. K. Law, W. Tsang, N. P. Cernansky, D. L. Miller, and R. P. Lindstedt, "A high-temperature chemical kinetic model of n-alkane (up to n-dodecane), cyclohexane, and methyl-, ethyl-, n-propyl and n-butyl-cyclohexane oxidation at high temperatures, JetSurF version 2.0." 2010.

[27] J. F. Roesler, "An experimental and two-dimensional modeling investigation of combustion chemistry in a laminar non-plug-flow reactor," in *Symposium (International) on Combustion*, 1998, vol. 27, no. 1, pp. 287–293.

[28] M. A. Mueller, T. J. Kim, R. A. Yetter, and F. L. Dryer, "Flow reactor studies and kinetic modeling of the H2/O2 reaction," *Int. J. Chem. Kinet.*, vol. 31, no. 2, pp. 113–125, 1999.

[29] T. B. Hunter, T. A. Litzinger, H. Wang, and M. Frenklach, "Ethane oxidation at elevated pressures in the intermediate temperature regime: experiments and modeling," *Combust. Flame*, vol. 104, no. 4, pp. 505–523, 1996.

[30] K. D. D. Dahm, P. S. S. Virk, R. Bounaceur, F. Battin-Leclerc, P. M. M. Marquaire, R. Fournet, E. Daniau, and M. Bouchez, "Experimental and modelling investigation of the thermal decomposition of n-dodecane," *J. Anal. Appl. Pyrolysis*, vol. 71, no. 2, pp. 865–881, Jun. 2004.

[31] S. Dooley, S. H. Won, J. Heyne, T. I. Farouk, Y. Ju, F. L. Dryer, K. Kumar, X. Hui, C.-J. Sung, H. Wang, and others, "The experimental evaluation of a methodology for surrogate fuel formulation to emulate gas phase combustion kinetic phenomena," *Combust. Flame*, vol. 159, no. 4, pp. 1444–1466, 2012.

[32] R. H. Natelson, M. S. Kurman, N. P. Cernansky, and D. L. Miller, "Low temperature

oxidation of n-butylcyclohexane," *Combust. Flame*, vol. 158, no. 12, pp. 2325–2337, 2011.

[33] D. N. Koert and N. P. Cernansky, "A flow reactor for the study of homogeneous gas-phase oxidation of hydrocarbons at pressures up to 20 atm (2 MPa)," *Meas. Sci. Technol.*, vol. 3, no. 6, p. 607, 1992.

[34] M. U. Alzueta, R. Bilbao, and M. Finestra, "Methanol oxidation and its interaction with nitric oxide," *Energy & fuels*, vol. 15, no. 3, pp. 724–729, 2001.

[35] Z. Li, J. Eckwert, A. Łapicki, and S. L. Anderson, "Low energy, high resolution ion scattering mass spectrometry of strained molecules and their isomers," *Int. J. Mass Spectrom. Ion Process.*, vol. 167, pp. 269–279, 1997.

[36] B. Van Devener and S. L. Anderson, "Breakdown and combustion of JP-10 fuel catalyzed by nanoparticulate CeO2 and Fe2O3," *Energy & fuels*, vol. 20, no. 5, pp. 1886–1894, 2006.

[37] S. Thomas and M. J. Wornat, "Effects of Acetylene Addition on Yields of the C1-C10 Hydrocarbon Products of Catechol Pyrolysis," *Energy & Fuels*, vol. 22, no. 2, pp. 976–986, 2008.

[38] H. Nakamura, R. Tanimoto, T. Tezuka, S. Hasegawa, and K. Maruta, "Soot formation characteristics and PAH formation process in a micro flow reactor with a controlled temperature profile," *Combust. Flame*, vol. 161, no. 2, pp. 582–591, 2014.

[39] C. L. Rasmussen, A. E. Rasmussen, and P. Glarborg, "Sensitizing effects of NO x on CH 4 oxidation at high pressure," *Combust. Flame*, vol. 154, no. 3, pp. 529–545, 2008.

[40] K. M. Walters and C. T. Bowman, "Vitiated ethane oxidation in a high-pressure flow reactor," *Combust. Flame*, vol. 156, no. 10, pp. 1886–1897, 2009.

[41] S. Banerjee, R. Tangko, D. A. Sheen, H. Wang, and C. T. Bowman, "An experimental and kinetic modeling study of n-dodecane pyrolysis and oxidation," *Combust. Flame*, vol. 163, pp. 12–30, 2016.

[42] A. E. Lutz, R. J. Kee, and J. A. Miller, "SENKIN: A FORTRAN program for predicting homogeneous gas phase chemical kinetics with sensitivity analysis," 1988.

[43] F. L. Dryer, F. M. Haas, J. Santner, T. I. Farouk, and M. Chaos, "Interpreting chemical kinetics from complex reaction--advection--diffusion systems: Modeling of flow reactors and related experiments," *Prog. Energy Combust. Sci.*, vol. 44, pp. 19–39, 2014.

[44] A. Laskin, H. Wang, and C. K. Law, "Detailed kinetic modeling of 1, 3-butadiene oxidation at high temperatures," *Int. J. Chem. Kinet.*, vol. 32, no. 10, pp. 589–614, 2000.

[45] J. Li, A. Kazakov, and F. L. Dryer, "Ethanol pyrolysis experiments in a variable pressure flow reactor," *Int. J. Chem. Kinet.*, vol. 33, no. 12, pp. 859–867, 2001.

[46] S. R. Turns, *An introduction to combustion*, vol. 287. McGraw-hill New York, 1996.

[47] J. C. Lee, R. a. Yetter, F. L. Dryer, a. G. Tomboulides, and S. a. Orszag, "Simulation and Analysis of Laminar Flow Reactors," *Combust. Sci. Technol.*, vol. 159, no. 1, pp. 199–212, 2007.

[48] A. H. Cutler, M. J. Antal Jr, and M. Jones Jr, "A critical evaluation of the plug-flow idealization of tubular-flow reactor data," *Ind. Eng. Chem. Res.*, vol. 27, no. 4, pp.

691–697, 1988.

[49] J. F. Stewart, *Supercritical pyrolysis of the endothermic fuels methylcyclohexane, decalin, and tetralin*. 1999.

[50] U. Shrestha, J. M. Rahimi, P. G. Simms, and K. H. Chelliah, "Fuel Pyrolysis in a Microflow Tube Reactor - Mesurement and Modeling Uncertainties of Ethane, n-Butane and n-Dodecane Pyrolysis," *Combust. Flame*, vol. 177, pp. 10–23, 2017.

[51] M. Araki, "PID Control," *Control Syst. Robot. Autom.*, vol. 2, no. 1–23, 2002.

[52] I. Manual, "Read the instruction manual thoroughly before you use the product. Keep this instruction manual for future reference.," 2010.

[53] W. C. Navidi, *Statistics for engineers and scientists*. McGraw-Hill New York, 2006.

[54] B. N. Taylor, *Guidelines for Evaluating and Expressing the Uncertainty of NIST Measurement Results (rev)*. DIANE Publishing, 2009.

[55] I. Coban, S. Sargin, M. S. Celiktas, and O. Yesil-Celiktas, "Bioethanol production from raffinate phase of supercritical CO2 extracted Stevia rebaudiana leaves," *Bioresour. Technol.*, vol. 120, pp. 52–59, 2012.

[56] W. Tsang and C. M. Rosado-Reyes, "Unimolecular Rate Expression for Cyclohexene Decomposition and Its Use in Chemical Thermometry under Shock Tube Conditions," *J. Phys. Chem. A*, p. 150217132232005, 2015.

[57] M. Nič, J. Jirát, B. Košata, A. Jenkins, and A. McNaught, Eds., *IUPAC Compendium of Chemical Terminology*. Research Triagle Park, NC: IUPAC, 2009.

[58] I. Stranic, D. F. Davidson, and R. K. Hanson, "Shock tube measurements of the rate constant for the reaction cyclohexene → ethylene + 1,3-butadiene," *Chem. Phys. Lett.*, vol. 584, pp. 18–23, 2013.

[59] J. H. Kiefer and J. N. Shah, "Unimolecular Dissociation of Cyclohexene at Extremely High Temperatures: Behavior of the Energy-Transfer Collision Efficiency," *J. Phys. Chem.*, vol. 91, no. 12, pp. 3024–3030, 1987.

[60] R. S. Tranter, R. Sivaramakrishnan, N. Srinivasan, and K. Brezinsky, "Calibration of reaction temperatures in a very high pressure shock tube using chemical thermometers," *Int. J. Chem. Kinet.*, vol. 33, no. 11, pp. 722–731, 2001.

[61] M. Uchiyama, T. Tomioka, and A. Amano, "Thermal Decomposition of Cyclohexene," vol. 68, no. 7, pp. 1878–1881, 1964.

[62] J. S. Heyne and F. L. Dryer, "Uncertainty Analysis in the Use of Chemical Thermometry: A Case Study with Cyclohexene.," *J. Phys. Chem.*, vol. 117, pp. 5401–5406, 2013.

[63] J. R. Mohammad, F. J. Ryan, and K. C. Harsha, "Numerical Modeling of Fuel Pyrolysis and Oxidation in a Laminar Micro-flow Tube Reactor," in *53rd AIAA Aerospace Sciences Meeting*, 2015, no. January, pp. 1–9.

[64] J. Li, A. Kazakov, and F. L. Dryer, "Experiments in a Variable Pressure Flow Reactor," 2001.

[65] P. Dagaut, M. Cathonnet, J. P. Rouan, R. Foulatier, A. Quilgars, J. C. Boettner, F. Gaillard, and H. James, "A jet-stirred reactor for kinetic studies of homogeneous gas-phase reactions at pressures up to ten atmospheres (≈ 1 MPa)," *J. Phys. E.*, vol. 19, no. 3, p. 207, 1986.

[66] J. M. Simmie, "Detailed chemical kinetic models for the combustion of hydrocarbon fuels," *Prog. Energy Combust. Sci.*, vol. 29, no. 6, pp. 599–634, 2003.

[67] H. J. Curran, "Detailed Chemical Kinetic Modeling ; Is There Life After Gri-Mech

3 . 0 ?," *Fuel*, vol. 49, no. 1, pp. 263–264, 2004.

[68] G. P. Smith, D. M. Golden, M. Frenklach, N. W. Moriarty, B. Eiteneer, M. Goldenberg, C. T. Bowman, R. K. Hanson, S. Song, W. C. Gardiner Jr, and others, "GRI-Mech 3.0," *URL http//www. me. berkeley. edu/gri_mech*, vol. 51, p. 55, 1999.

[69] H. Wang, X. You, A. V Joshi, S. G. Davis, A. Laskin, F. Egolfopoulos, and C. K. Law, "USC Mech Version II. High-Temperature Combustion Reaction Model of H2/CO/C1-C4 Compounds." 2007.

[70] C. W. Zhou, Y. Li, E. O'Connor, K. P. Somers, S. Thion, C. Keesee, O. Mathieu, E. L. Petersen, T. A. DeVerter, M. A. Oehlschlaeger, G. Kukkadapu, C. J. Sung, M. Alrefae, F. Khaled, A. Farooq, P. Dirrenberger, P. A. Glaude, F. Battin-Leclerc, J. Santner, Y. Ju, T. Held, F. M. Haas, F. L. Dryer, and H. J. Curran, "A comprehensive experimental and modeling study of isobutene oxidation," *Combust. Flame*, vol. 167, pp. 353–379, 2016.

[71] P. Dagaut, M. Cathonnet, and J. Boettner, "Kinetics of ethane oxidation," *Int. J. Chem. Kinet.*, vol. 23, no. 5, pp. 437–455, 1991.

[72] Y. Hidaka, K. Sato, H. Hoshikawa, T. Nishimori, R. Takahashi, H. Tanaka, K. Inami, and N. Ito, "Shock-tube and modeling study of ethane pyrolysis and oxidation," *Combust. Flame*, vol. 120, no. 3, pp. 245–264, 2000.

[73] R. S. Tranter, R. Sivaramakrishnan, K. Brezinsky, and M. D. Allendorf, "High pressure, high temperature shock tube studies of ethane pyrolysis and oxidation," *Phys. Chem. Chem. Phys.*, vol. 4, no. 11, pp. 2001–2010, 2002.

[74] R. S. Tranter, A. Raman, R. Sivaramakrishnan, and K. Brezinsky, "Ethane oxidation and pyrolysis from 5 bar to 1000 bar: Experiments and simulation," *Int. J. Chem. Kinet.*, vol. 37, no. 5, pp. 306–331, 2005.

[75] C. V Naik and A. M. Dean, "Detailed kinetic modeling of ethane oxidation," *Combust. Flame*, vol. 145, no. 1, pp. 16–37, 2006.

[76] C. V Naik and A. M. Dean, "Modeling high pressure ethane oxidation and pyrolysis," *Proc. Combust. Inst.*, vol. 32, no. 1, pp. 437–443, 2009.

[77] N. M. Marinov, W. J. Pitz, C. K. Westbrook, A. M. Vincitore, M. J. Castaldi, S. M. Senkan, and C. F. Melius, "Aromatic and polycyclic aromatic hydrocarbon formation in a laminar premixed n-butane flame," *Combust. Flame*, vol. 114, no. 1, pp. 192–213, 1998.

[78] P. Dagaut, J. Luche, and M. Cathonnet, "Reduction of NO by n-butane in a JSR: Experiments and kinetic modeling," *Energy & fuels*, vol. 14, no. 3, pp. 712–719, 2000.

[79] M. A. Oehlschlaeger, D. F. Davidson, and R. K. Hanson, "High-temperature thermal decomposition of isobutane and n-butane behind shock waves," *J. Phys. Chem. A*, vol. 108, no. 19, pp. 4247–4253, 2004.

[80] S. H. Pyun, W. Ren, D. F. Davidson, and R. K. Hanson, "Methane and ethylene time-history measurements in n-butane and n-heptane pyrolysis behind reflected shock waves," *Fuel*, vol. 108, pp. 557–564, 2013.

[81] L. Su and Z. Zhang, "In-situ quantitative measurement of ethylene from n-butane pyrolysis in a flow reactor," in *54th AIAA Aerospace Sciences Meeting*, 2016, no. January, pp. 1–7.

[82] W. K. Metcalfe, S. M. Burke, S. S. Ahmed, and H. J. Curran, "A hierarchical and comparative kinetic modeling study of C1 - C2 hydrocarbon and oxygenated fuels,"

Int. J. Chem. Kinet., vol. 45, no. 10, pp. 638–675, 2013.

[83] H. Wang, "A new mechanism for initiation of free-radical chain reactions during high-temperature, homogeneous oxidation of unsaturated hydrocarbons: Ethylene, propyne, and allene," *Int. J. Chem. Kinet.*, vol. 33, no. 11, pp. 698–706, 2001.

[84] V. J. Barwick, "Sources of uncertainty in gas chromatography and high-performance liquid chromatography," *J. Chromatogr. A*, vol. 849, no. 1, pp. 13–33, 1999.

[85] N. A. Dyson, *Chromatographic integration methods*. Royal Society of Chemistry, 1998.

[86] J. a Widegren Bruno, T.J., "Thermal decomposition kinetics of the aviation fuel Jet-A," *Ind. Eng. Chem. Res.*, vol. 47, no. 13, pp. 4342–4348, 2008.

[87] S. S. Vasu, D. F. Davidson, Z. Hong, V. Vasudevan, and R. K. Hanson, "n-dodecane oxidation at high-pressures: Measurements of ignition delay times and OH concentration time-histories," *Proc. Combust. Inst.*, vol. 32 I, no. 1, pp. 173–180, 2009.

[88] X. You, F. N. Egolfopoulos, and H. Wang, "Detailed and simplified kinetic models of n-dodecane oxidation: The role of fuel cracking in aliphatic hydrocarbon combustion," *Proc. Combust. Inst.*, vol. 32, no. 1, pp. 403–410, 2009.

[89] O. Herbinet, P.-M. Marquaire, F. Battin-Leclerc, and R. Fournet, "Thermal decomposition of n-dodecane: Experiments and kinetic modeling," *J. Anal. Appl. Pyrolysis*, vol. 78, no. 2, pp. 419–429, 2007.

[90] A. Agosta, N. P. Cernansky, D. L. Miller, T. Faravelli, and E. Ranzi, "Reference components of jet fuels: kinetic modeling and experimental results," *Exp. Therm. Fluid Sci.*, vol. 28, no. 7, pp. 701–708, 2004.

[91] A. Violi, S. Yan, E. G. Eddings, A. F. Sarofim, S. Granata, T. Faravelli, and E. Ranzi, "Experimental formulation and kinetic model for JP-8 surrogate mixtures," *Combust. Sci. Technol.*, vol. 174, no. 11–12, pp. 399–417, 2002.

[92] P. Dagaut, "On the kinetics of hydrocarbons oxidation from natural gas to kerosene and diesel fuel," *Phys. Chem. Chem. Phys.*, vol. 4, no. 11, pp. 2079–2094, 2002.

[93] T. Malewicki, S. Gudiyella, and K. Brezinsky, "Experimental and modeling study on the oxidation of Jet A and the n-dodecane/iso-octane/n-propylbenzene/1, 3, 5-trimethylbenzene surrogate fuel," *Combust. Flame*, vol. 160, no. 1, pp. 17–30, 2013.

[94] A. Mzé-Ahmed, K. Hadj-Ali, P. Dagaut, and G. Dayma, "Experimental and modeling study of the oxidation kinetics of n-undecane and n-dodecane in a jet-stirred reactor," *Energy and Fuels*, vol. 26, no. 7, pp. 4253–4258, 2012.

[95] P. Dagaut and M. Cathonnet, "The ignition, oxidation, and combustion of kerosene: A review of experimental and kinetic modeling," *Prog. energy Combust. Sci.*, vol. 32, no. 1, pp. 48–92, 2006.

[96] J. L. Moler't, E. M. Steward, and P. H. Taylor, "High temperature gas phase pyrolysis of JP-8," in *Abstract of papers of the american chemical society*, 1990, vol. 200, p. 102--FUEL.

[97] C.-M. Lee, K. Kundu, and B. Ghorashi, *Simplified jet-A kinetic mechanism for combustor application*. National Aeronautics and Space Administration, 1993.

[98] E. Ranzi, M. Dente, A. Goldaniga, G. Bozzano, and T. Faravelli, "Lumping procedures in detailed kinetic modeling of gasification, pyrolysis, partial oxidation and combustion of hydrocarbon mixtures," *Prog. Energy Combust. Sci.*, vol. 27, no.

1, pp. 99–139, 2001.

[99] Y. Zhu, R. Hanson, and D. Davidson, "Shock Tube/Laser Absorption Measurements of Jet Fuel Pyrolysis and Oxidation," *53rd AIAA Aerosp. Sci. Meet.*, 2015.

[100] R. P. L. B. Sirjean, E. Dames, D. A. Sheen, X.-Q. You, C. Sung, A. T. Holley, F. N. Egolfopoulos, H. Wang, S. S. Vasu, D. F. Davidson, R. K. Hanson, H. Pitsch, C. T. Bowman, A. Kelley, C. K. Law, W. Tsang, N. P. Cernansky, D. L. Miller, A. Violi, "A high-temperature chemical kinetic model of n-alkane oxidation, JetSurF version 1.0."

[101] Y. Zhu, W. Shengai, R. K. Hanson, and D. F. Davidson, "Shock Tube/Laser Absorption Measurements of Jet Fuel Pyrolysis and Oxidation," in *53rd AIAA Aerospace Sciences Meeting*.

[102] T. Bruno, M. Huber, a Laesecke, E. Lemmon, and R. Perkins, "Thermochemical and thermophysical properties of JP-10," *Adv. Sci. Tech.*, vol. 45, no. NISTIR 6640, pp. 1–67, 2006.

[103] H. S. Chung, G. S. H. Chen, R. A. Kremer, J. R. Boulton, and G. W. Burdette, "Recent developments in high-energy density liquid hydrocarbon fuels," *Energy and Fuels*, vol. 13, no. 3, pp. 641–649, 1999.

[104] D. F. Davidson, D. C. Horning, J. T. Herbon, and R. K. Hanson, "Shock tube measurements of JP-10 ignition," *Proc. Combust. Inst.*, vol. 28, no. 2, pp. 1687–1692, 2000.

[105] C. W. Gao, A. G. Vandeputte, N. W. Yee, W. H. Green, R. E. Bonomi, G. R. Magoon, H. W. Wong, O. O. Oluwole, D. K. Lewis, N. M. Vandewiele, and K. M. Van Geem, "JP-10 combustion studied with shock tube experiments and modeled with automatic reaction mechanism generation," *Combust. Flame*, vol. 162, no. 8, pp. 3115–3129, 2015.

[106] C. Joppin, "Cooling Performance of Storable Propellants for a micro rocket engine," Massachusetts Institute of Technology, 2002.

[107] S. Nakra, R. J. Green, and S. L. Anderson, "Thermal decomposition of JP-10 studied by micro-flowtube pyrolysis-mass spectrometry," *Combust. Flame*, vol. 144, no. 4, pp. 662–674, 2006.

[108] N. M. Vandewiele, G. R. Magoon, K. M. Van Geem, W. H. Green, and G. B. Marin, "Experimental and Modeling Study on the Thermal Decomposition of Jet Propellant-10," 2014.

[109] B. Van Devener and S. L. Anderson, "Breakdown and combustion of JP-10 fuel catalyzed by nanoparticulate CeO2 and Fe2O3," *Energy and Fuels*, vol. 20, no. 5, pp. 1886–1894, 2006.

[110] G. Li, C. Zhang, H. Wei, H. Xie, Y. Guo, and W. Fang, "Investigations on the thermal decomposition of JP-10/iso-octane binary mixtures," *Fuel*, vol. 163, pp. 148–156, 2016.

[111] N. M. Vandewiele, G. R. Magoon, M. Eestermans, K. M. Van Geem, M. Reyniers, W. H. Green, and B. Guy, "Thermal decomposition of JP-10 : Experimental and modeling study fuel."

[112] D. Davidson, D. Horning, M. Oehlschlaeger, and R. Hanson, "The decomposition products of JP-10," in *37th Joint Propulsion Conference and Exhibit*, 2001, pp. 1–7.

[113] B. Huang and R. Davis, "Private Communication," 2016.

[114] R. Kee, F. Rupley, E. Meeks, and J. Miller, “Chemkin: A software package for the analysis of gas phase chemical and plasma kinetics,” 2000.

[115] M. F. Meters, *SmartTrak ® 100 Series*, no. February. 2014.

[116] “What is a Mass Flow Controller?” [Online]. Available: http://www.horiba.com/horiba-stec/products/mass-flow-technology/what-is-a-mass-flow-controller/.

[117] M. Cooper and J. E. Shepherd, “Jp-10 for Pulse Detonation Engine Applications,” *Test*, no. 0, 2002.

[118] O. Sparkman, Z. Penton, and F. Kitson, *Gas chromatography and mass spectrometry: a practical guide*. Academic Press, 1996.

[119] D. A. Skoog, S. Universi, and S. R. Crouch, *Principles of Instrumental Analysis*. Saunders College Philadelphia, 1980.

[120] “Thermal conductivity detector - Wikipedia, the free encyclopedia.” [Online]. Available: https://en.wikipedia.org/wiki/Thermal_conductivity_detector.

[121] “Flame Ionisation Detector.” [Online]. Available: https://en.wikipedia.org/wiki/Flame_ionization_detector. [Accessed: 13-Feb-2017].

[122] “Methanizer (For low level CO and CO2 by FID).” [Online]. Available: http://www.srigc.com/home/product_detail/methanizer-for-low-level-co-and-co2-by-fid.

[123] “Basic Principle of Mass Spectrometry.” [Online]. Available: http://www.mhhe.com/physsci/chemistry/carey/student/olc/ch13ms.html.

[124] K. Neetu, G. Ankit, T. Ruchi, B. Ajay, and B. Prashant, “A review on mass spectrometry detectors,” *Int. Res. J. Pharm.*, vol. 3, no. 10, pp. 33–42, 2012.

[125] E. de Hoffmann and V. Stroobant, *Mass spectrometry : principles and applications*, Second. Toronto: Wiley, 2001.

[126] T. Lu and C. K. Law, “Toward accommodating realistic fuel chemistry in large-scale computations,” *Prog. Energy Combust. Sci.*, vol. 35, no. 2, pp. 192–215, 2009.

[127] W. Tsang, “Progress in the Development of Combustion Kinetics Databases for Liquid Fuels,” *Data Sci. J.*, vol. 3, no. January, pp. 1–9, 2004.

[128] T. Hasegawa and M. Sato, “Study of ammonia removal from coal-gasified fuel,” *Combust. Flame*, vol. 114, no. 1, pp. 246–258, 1998.

[129] “Pipeflow_intro - FLOW IN PIPES F luid flow in circular and noncircular pipes.” [Online]. Available: https://www.coursehero.com/file/9689755/Pipeflow-intro/.

[130] E. A. Nagley, “Fuel Composition Analysis of Endothermically Heated JP-8 Fuel For Use in a Pulse Detonation Engine,” 2003.

[131] “Introduction to Flame Ionization.” [Online]. Available: http://www.equipcoservices.com/support/tutorials/introduction-to-flame-ionization/. [Accessed: 13-Feb-2017].

[132] “Bristol University - Gas Chromatography Mass Spectrometry (GC/MS).” [Online]. Available: http://www.bris.ac.uk/nerclsmsf/techniques/gcms.html.

Appendix A: Mass Flow Controllers and GC System

A.1 Mass flow controller

The flow controllers work on the principle of heat transfer. The flow path of the gas consists of a laminar flow bypass which creates pressure drop across the bypass as shown in Figure A.1(a). This pressure-drop forces a small amount of gas flow $\dot{m}_1$ to pass through the capillary tube to the sensor tube.

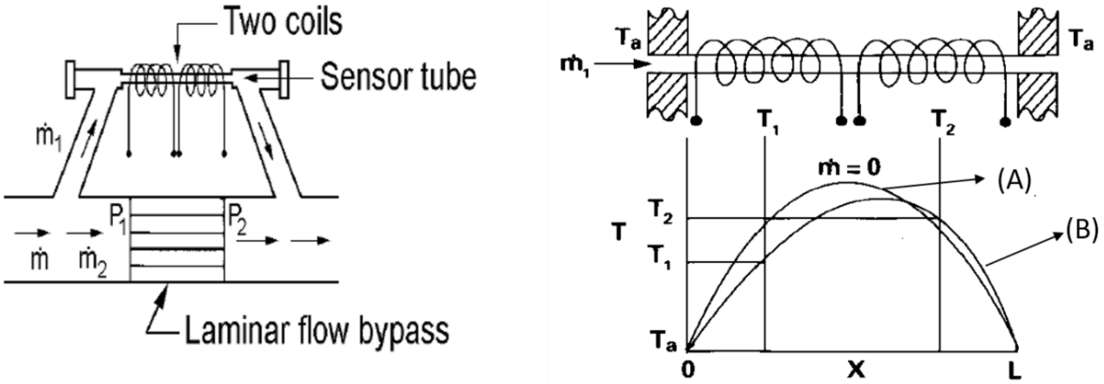

(a) **(b)**

Figure A.1: (a) Working principle of Sierra Flow controllers **(b)** Temperature profile of the gas flowing through the capillary tube [115].

The sensor tube consists of two resistance tube detectors (RTDs) which direct heat to the gas. With $\dot{m}_1 = 0$ the temperature profile of the sensor tube will be given by (A) as shown in Figure A.2 (b). With flow through the sensor tube the profile will be given by (B). The resulting temperature difference is proportional to the mass flow rate and is converted to an electrical signal by the bridge circuit.

This signal passes through the amplification circuits and is output as a linear voltage between 0 to 5V. A comparison between the flow rate setting signal and actual flow setting signal from the sensor is sent to a valve driving circuit. The electromagnetic valve is then adjusted to make this difference zero basically attaining the set point flow rate [115], [116]. The flow rate of the any gas is related to the calibrated gas by a K-factor given by:

$$\frac{Q_A}{Q_R} = \frac{K_A}{K_R} \quad , \tag{A-1}$$

where, Q and K are the flow rates and K-factors respectively. A represents actual and R represents reference gases. In general, the reference gas is either air or nitrogen with a K factor of one [23].

A.2 GC Theory

Gas Chromatography (GC) is the process of separation, identification and quantification of individual components from a volatile mixture. Separation occurs due to distribution of the components between two phases in the column namely stationary and mobile phase [117]. A typical GC system mainly consists of carrier gas supply, flow controller, injection port,

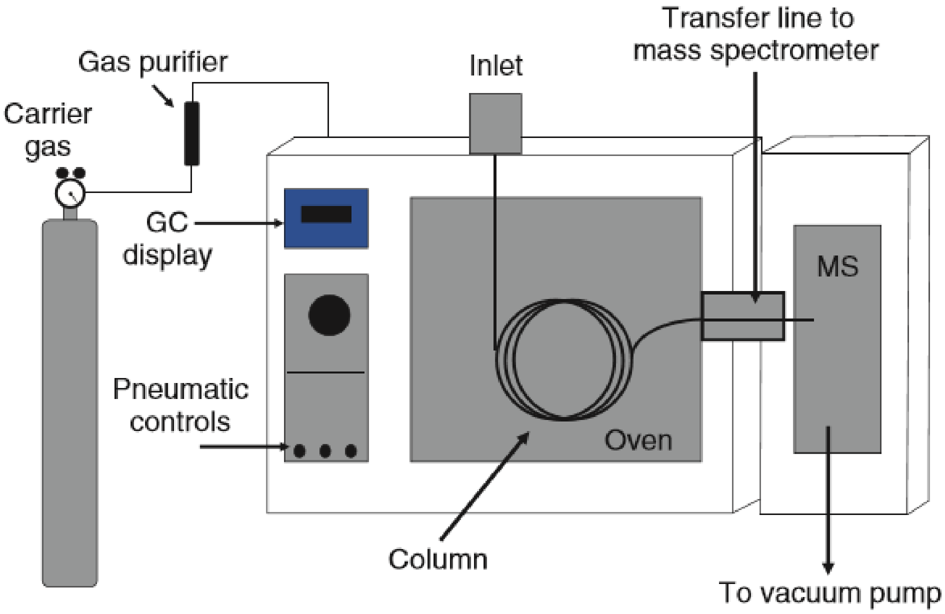

Figure A.2: Schematic of a typical GC with MS as a detector [118].

column/column oven, detectors and a computer as seen in Figure A.2 [118]. The sample is injected into the line through injection port/inlet which might be split or split less type or there may also be a gas sample valve consisting of a sample loop. High purity inert gas such as helium is used as a carrier gas which is the mobile phase. The sample to be measured is carried by the carrier gas through the column coated with absorbent stationary phase maintained at a certain temperature in a column oven. The molecules in the sample are distributed between the mobile and stationary phases as they passed through the column and travel at different rates depending upon their physical properties and temperature of the column.

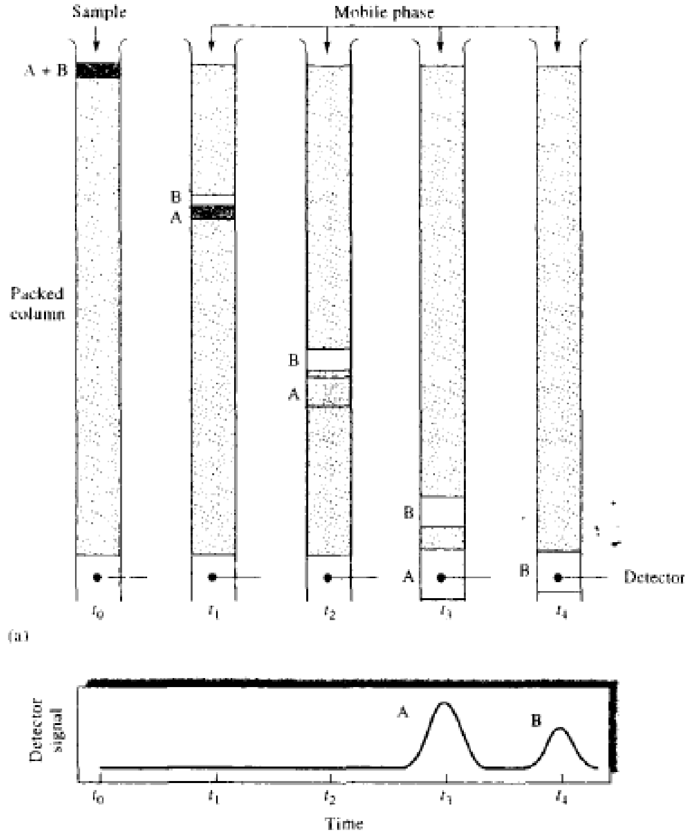

Figure A.3: Process showing separation of species A and B from a mixture of A+B in a column [119].

If we consider a solution A+B in the column at time t_0 as shown in Figure A.3. A continuous supply of mobile phase is maintained in the column and the species A and B distributes between stationary and mobile phases. The mobile phase carries the solute down the column in a continuous series of two phases. The fraction of time spent by the species in stationary phases depends on the affinity for that phase. In the particular example, component B has a stronger affinity towards the stationary phase and elutes later. The fastest molecule eluting will reach the detector first (A in this case) which depends on the temperature of the column, type of column material and type of sample to be handled. The detector then generates electrical signal and a chromatogram is plotted based on different elution time of the compounds. The time from point of injection to peak maximum is called the retention time (t_3 and t_4 for species A and B respectively) [119].

A.3 Detectors Used in GC Systems

In the current study, three types of detectors have been incorporated in GC systems: Thermal Conductivity Detector (TCD), Flame Ionization Detector (FID) and Mass Spectrometer (MS). TCD is a universal detector and can detect a range of species. On the other hand, FID can only detect hydrocarbons (HCs) accurately and is considered more sensitive than TCD with a capability to measure small concentrations of HCs.

A.3.1 Thermal Conductivity Detector (TCD)

TCD can be used to detect large concentrations of wide range of species such as H_2, O_2, CO, CO_2, N_2, HCs etc. It basically works on the principle of difference in thermal conductivity between the reference carrier gas and carrier gas with sample. It consists of four heated filaments (See Figure A.4) [120]. The sample from the column is allowed to flow through two of the filaments and reference carrier gas is allowed to flow through the other two, which are maintained in a Wheatstone bridge configuration. When there is no sample flown through the filaments there is balanced temperature across them and thus no change in thermal conductivities. As a compound is being eluted from the column, the temperature of the filament increases and unbalances the Wheatstone bridge which can be measured as a signal.

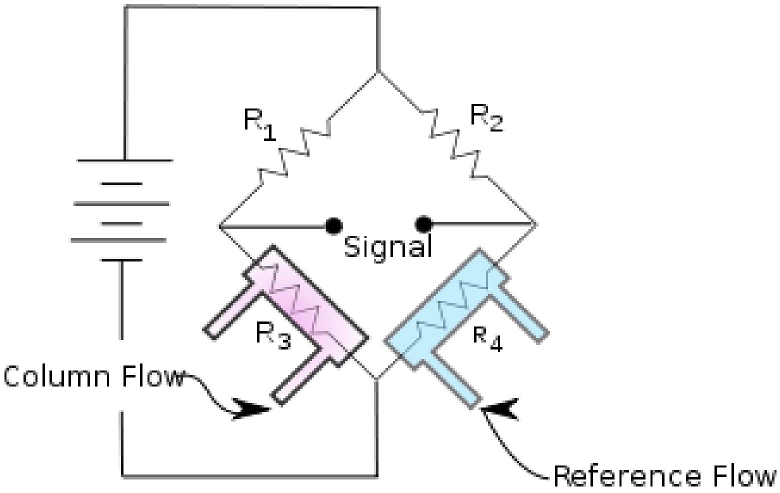

Figure A.4: working principle of TCD [120]**.**

A.3.2 Flame Ionization Detector (FID)

FID is a detector used to detect small concentrations of HCs based on ions formed in a hydrogen flame as shown in Figure A.5. Hydrogen –air flame ionizes the compounds and generates electrical current across electrodes proportional to the ions formed [121]. The current thus generated, appears as a chromatogram or as a peak.

In order to detect small concentrations of CO and CO_2, a methanizer (MTN) option is generally incorporated with the FID. The sample is mixed with hydrogen is delivered to the FID detector as shown in Figure A.6. The MTN consists of nickel catalyst powder on

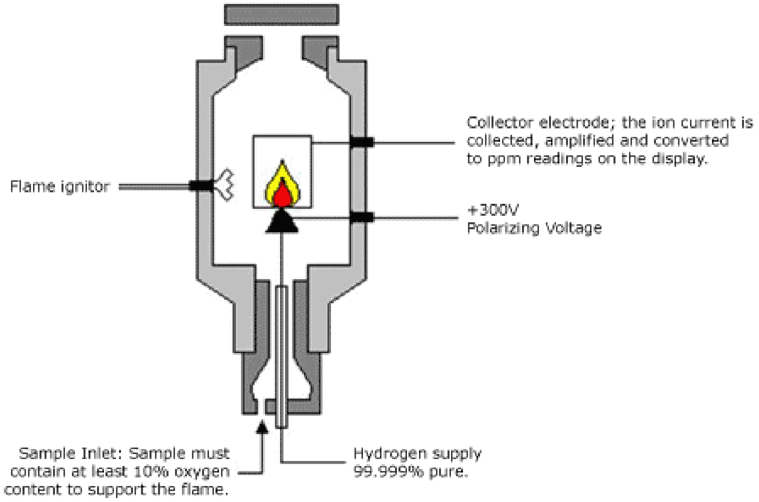

Figure A.5: Flame Ionization Detector [131] .

glass wool secured with two frits. It is generally heated to 380^{o}C with the FID detector body. When the sample passes through the MTN, CO and CO_2 are converted to methane which is detectable in FID [122].

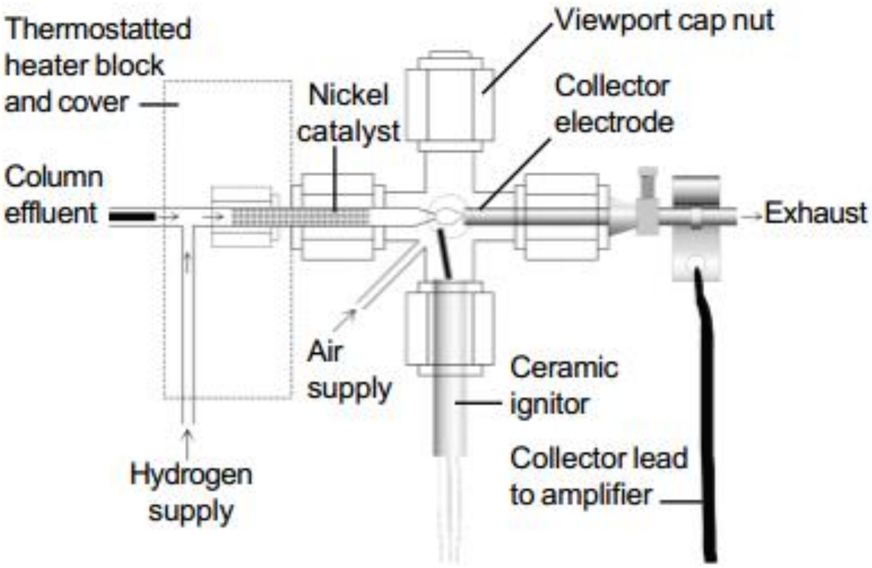

Figure A.6: FID with methanizer option [122].

A.3.3 Mass Spectrometer (MS)

Mass spectrometer is a detector which works on the principle of mass to charge ratio (m/z). The added advantage of MS is the identification of species based on unique mass spectrum of each individual molecule. It consists of three main components, ion source, mass analyzer (different types) and a detector (See Figure A.7(a)). In electron impact (EI) ionization, the ion source creates a high beam of electrons which displace electrons from vaporized sample molecules. The radical cation so formed is called the molecular ion (M^+). The molecular ion is unstable and fragments into even smaller ions called the fragment ions [123]. The ions formed are focused and accelerated into a beam through slits or lens by applying positive and negative charges.

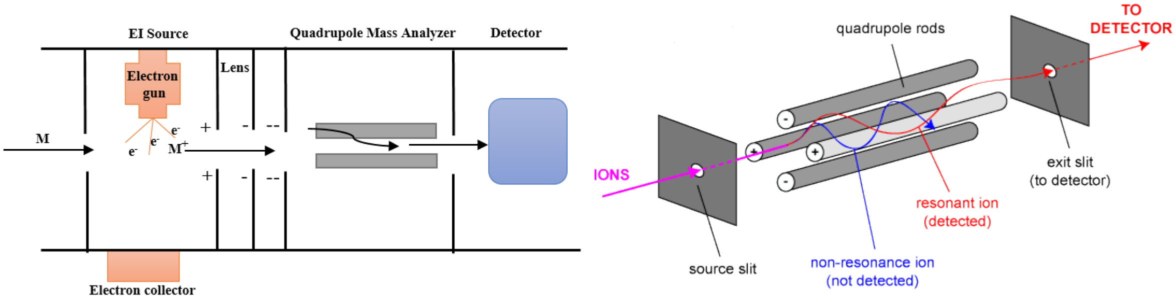

(a) (b)

Figure A.7: (a)Working principle of mass spectrometer with electron impact ionization and quadrupole mass analyzer (b) Quadrupole mass analyzer [132]**.**

The accelerated ions then enter the mass analyzer. There are various types of mass analyzers such as magnetic, time of flight, ion trap etc. [124]. Among them, GC 2014 consists of quadrupole mass analyzer which is one of the common and very efficient detectors. The quadrupole mass analyzer consists of four cylindrical rods parallel to each other as shown in Figure A.7(b). The opposite parallel rods are electrically connected together. A radio frequency (RF) with an offset DC voltage is applied between one pair of rods and the other forming high and low pass filters. Based on applied RF and DC voltages, only ions with certain m/z can reach the detector. Thus, a complete range of m/z can be scanned by applying variable voltages [125].

The separated ions are then passed to the detector which amplifies the signal. The computer records all the data and produces a visual display of chromatogram.

Appendix B: Calibration Curves and Uncertainties

B.1 Calibration curves for GC 2014

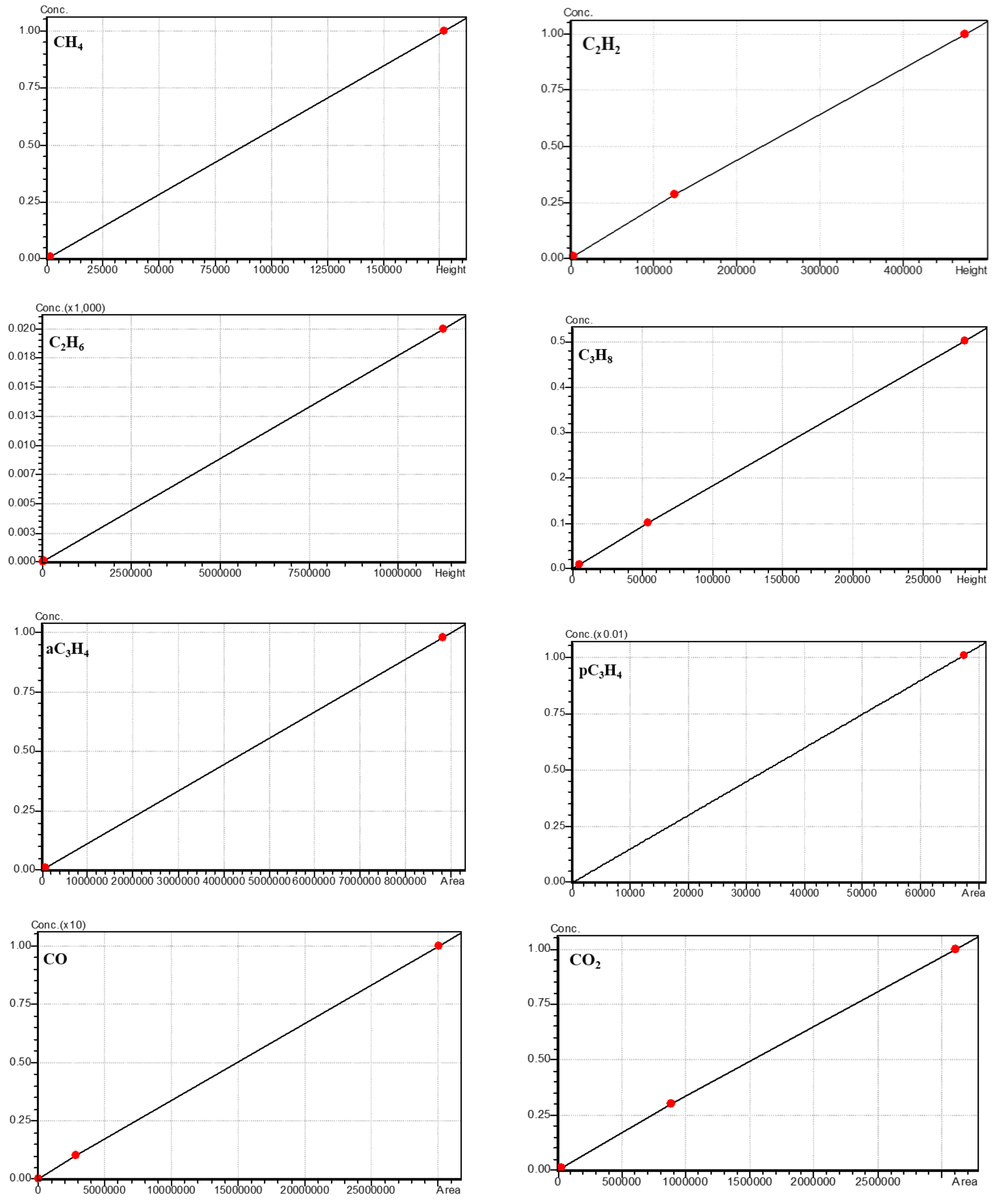

Figure B.1: Calibration curves (GC 2014) for C_1-C_3 species (ethylene and Hydrogen is given in Chaper 2, Figure 2.19).

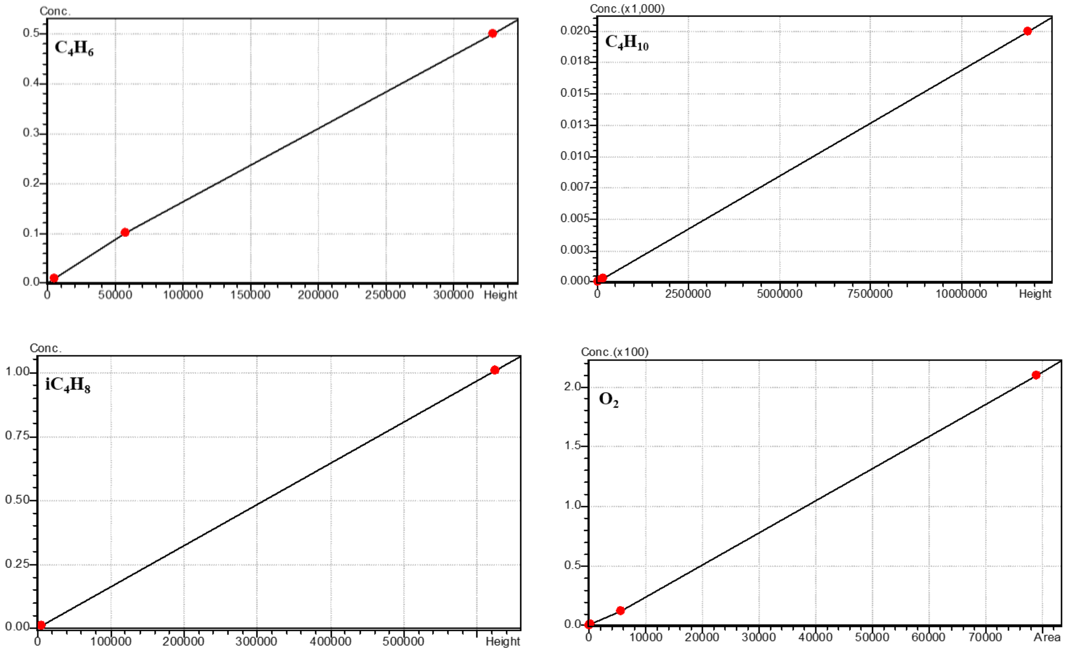

Figure B.2: Calibration curves (GC 2014) for C_4 species and O_2 (ethylene and Hydrogen is given in Chaper 2, Figure 2.19).

B.2 Uncertainties of standards and species calibrated by flow controllers

Table B.1: Calibration uncertainty of the species from standards with different concentrations

Species	Concentration (ppm)	Error% (+/-)	Species	Concentration (ppm)	Error % (+/-)
CO_2	10.1	5	CO	10.1	5
	302	2		1010	2
	1000	2		10000	2
C_2H_2	10.1	5	aC_3H_4	10	5
	287	2		980	2
	1000	2	iC_4H_8	10	2
C_3H_6	10	5		1010	2
	300	2	$2\text{-}C_4H_8$	10.5	5
	980	2		1030	2
	1000.3	2	$1\text{-} C_4H_8$	10.1	5
CH_4	10.2	5		1040	2
	1000	2	$p\text{-}C_3H_4$	10.1	5
C_3H_8	10	2	C_6H_{14}	10.3	5
	101	10		102	10
	503	2		290	2
C_4H_6	10	5	C_6H_6	20.5	10
	101	5		1010	2
	501	2			

Table B.2: Calibration uncertainty of the species from combination of standards and flow controllers with different concentrations

Species	Concentration (ppm)	Error% (+/-)	Species	Concentration (ppm)	Error% (+/-)
C_2H_4	9.99	5	O_2	100	2
	1000	2		1000	5
	19985	3.98		12000	8.9
	39966	5.7		210000	8.9
C_2H_6	10.1	2	H_2	10.2	5
	101	10		100	2
	20000	3.9		1000	2
C_4H_{10}	10	2		10000	6.1
	101	10		15000	4.9
	300	2			
	20000	4.8			

B.3 Calibration of large hydrocarbon molecules in GCMS 2010 plus

The GCMS 2010 plus is capable of identification and quantification of species larger than C_4. However, the calibration standard for species larger than C_7 and cyclopentadiene is not available as mentioned in Section 2.3.4. Thus, a calibration method was developed to calibrate the larger species including cyclopentadiene using liquid standards.

The GCMS system consists of separate sampling techniques for liquid and gaseous samples. While the liquid samples can be directly injected into the injection port using manual injection (micro syringe) or auto sampler. The gaseous samples are injected into the injection port via a valve assembly as explained in Section 2.2.5.2. During the sampling process, the sample is stored in a 1 ml loop before entering the column. The number of moles (n) of the sample in the loop can be calculated using the ideal gas law given as:

$$n = \frac{PV}{RT} \quad , \qquad \text{(B- 1)}$$

Where, P is pressure in the probing line, V is the volume of the loop, R is the universal gas constant and T is the temperature of gas in the loop. If X is the mole fraction of species to be calibrated, the number of moles of the species (n_s) is given by:

$$n_s = nX \quad , \qquad \text{(B- 2)}$$

In addition to a preinstalled thermocouple in insulated the valve box, a k-type thermocouple was added near to the loop for the calibration purpose.

With all these parameters, for a particular concentration, the required number of moles was calculated. The liquid samples were then prepared using a highly precise balance (accuracy of 0.1 mg) with same number of moles in methanol. For the purpose of establishing a relation between gas and liquid calibrations and to validate the method, benzene and 1-pentene were calibrated in gaseous form through the valve assemble and liquid form through the auto-sampler.

The GCMS response for 1000 ppm of each species is shown in Table B.3. It can be observed that, the ratio between the liquid and gas sample response is ~1.9 for both the species. The reason for this discrepancy between liquid and gaseous samples can be attributed to inaccuracies in temperature and volume of the gas in the loop. The other reason can be the difference in dilution of sample with carrier gas (helium) in valve configuration and auto-sampler injection in the equipment. Nevertheless, the ratio in response is very similar for both the species and can be used as a relation to calibrated species using liquid injection while keeping the experimental sampling in gaseous form. Further, no significant change in retention time was observed between the gaseous and liquid sampling. For the current study the process is used for calibration of cyclopentadiene. However, the process can be adapted to calibrate species such as anthracene, n-dodecane, nonene and other hydrocarbons in future.

Table B.3: GCMS response for 1000 ppm benzene and 1-pentene in liquid and gaseous form.

Species Types	**1000 ppm Benzene**		**1000 ppm 1-Pentene**	
Form	**Gas**	**Liquid**	**Gas**	**Liquid**
GCMS Response	8375954	15860997	5270421	10079056
Ratio (liquid to gas)	1.89		1.91	

B.4 Schematic of rods used in catalytic wall effect and catalytic pyrolysis studies

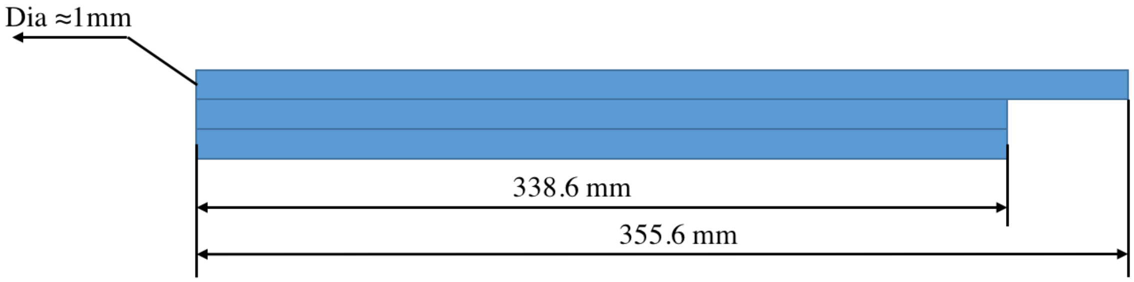

Figure B.3 Dimensions of quartz rods added to check catalytic wall effect and to conduct catalytic pyrolysis.

Appendix C:Ethane Pyrolysis at Elevated Pressure

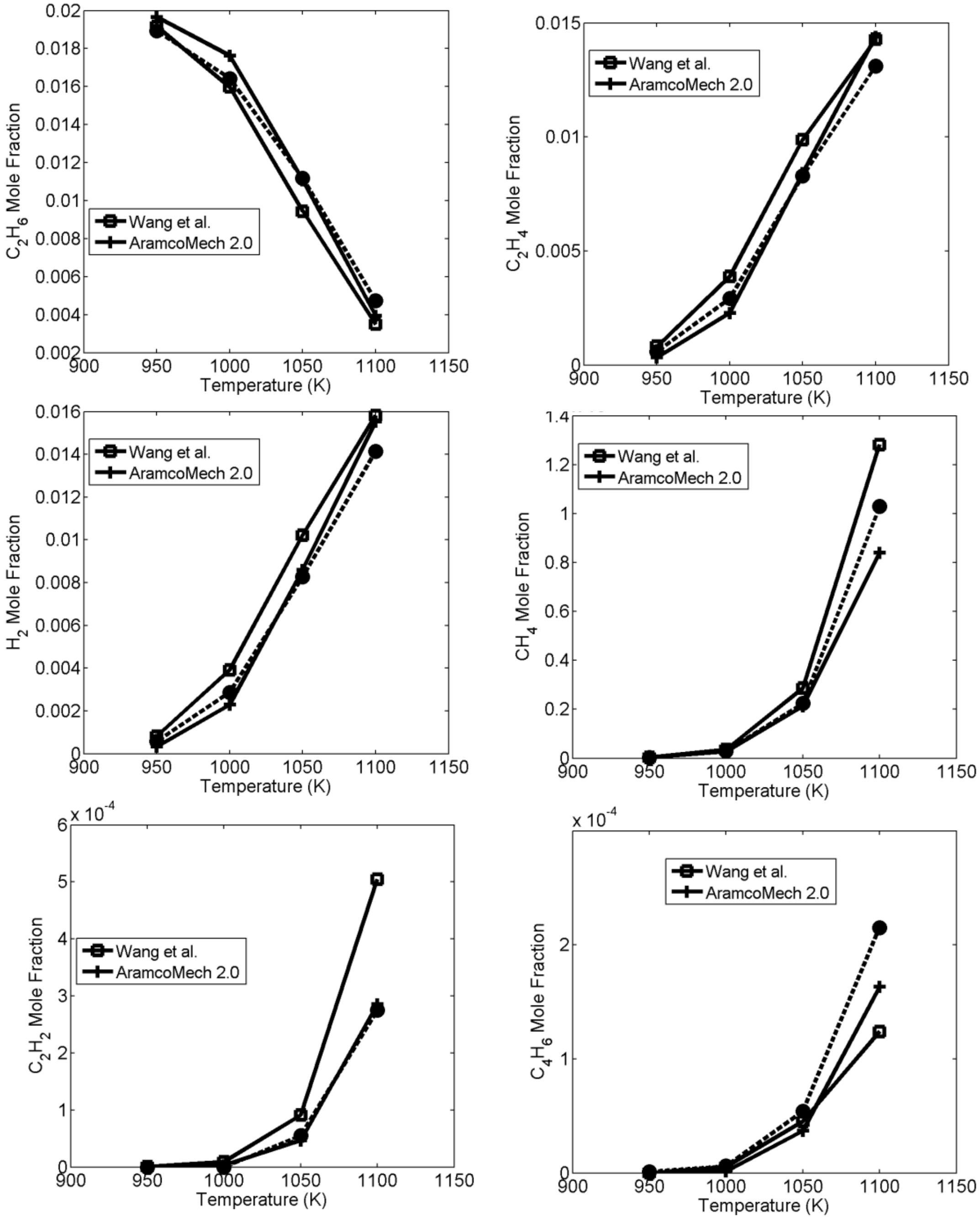

Figure C.1: Comparison of species mole fraction (**major species**) from the current experiments at **p=10 atm** as a function of temperature with two models by Wang et al. [26] and AramcoMech 2.0 [70]. Solid lines/square symbols represent prediction with model by Wang et al., solid lines/plus symbol represent prediction with AramcoMech 2.0 and dashed line/ filled circles represent present experimental results.for inflow species compositions of $X_{C_2H_6} = 0.02$, $X_{N_2} = 0.98$ and residence time ~ 590 ms.

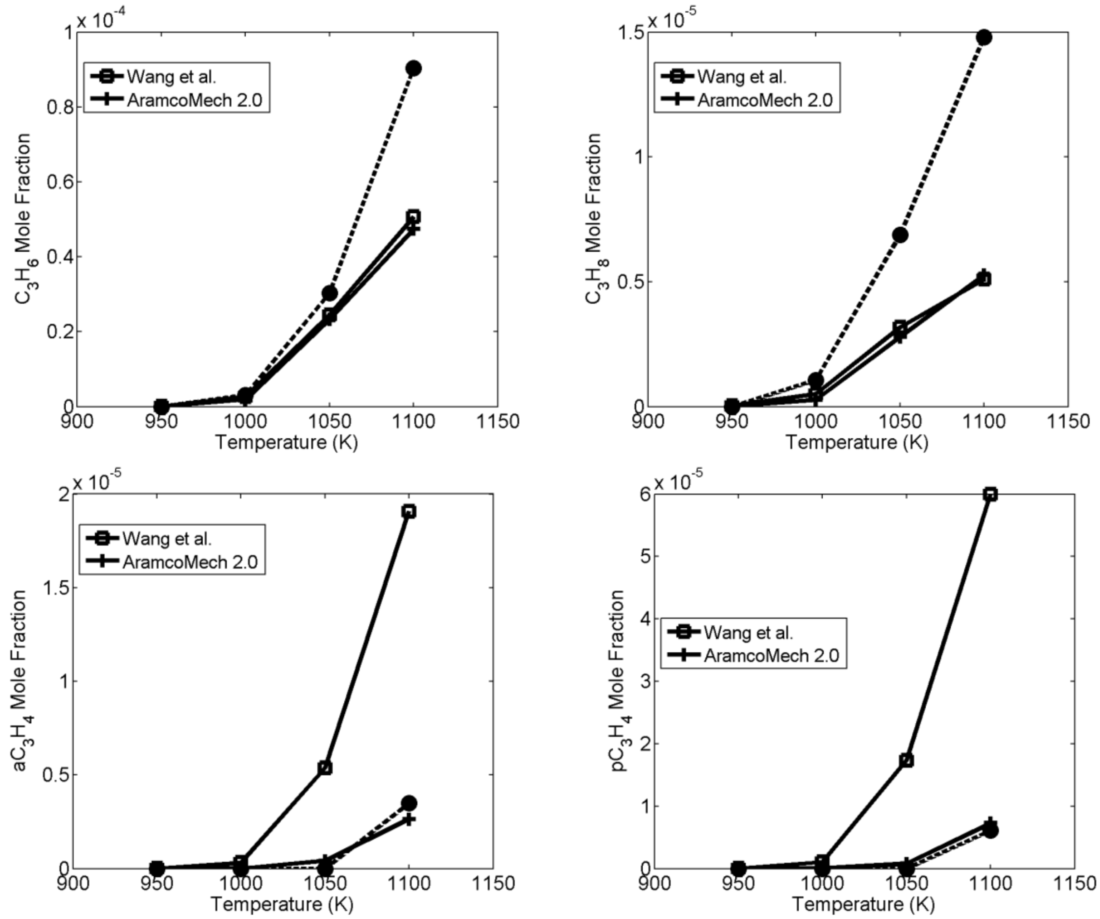

Figure C.2: Comparison of species mole fraction (**minor species**) from the current experiments at **p=10 atm** as a function of temperature with two models by Wang et al. [26] and AramcoMech 2.0 [70]. Solid lines/square symbols represent prediction with model by Wang et al., solid lines/plus symbol represent prediction with AramcoMech 2.0 and dashed line/ filled circles represent present experimental results.for inflow species compositions of $X_{C_2H_6} = 0.02$, $X_{N_2} = 0.98$ and residence time ~ 590 ms.

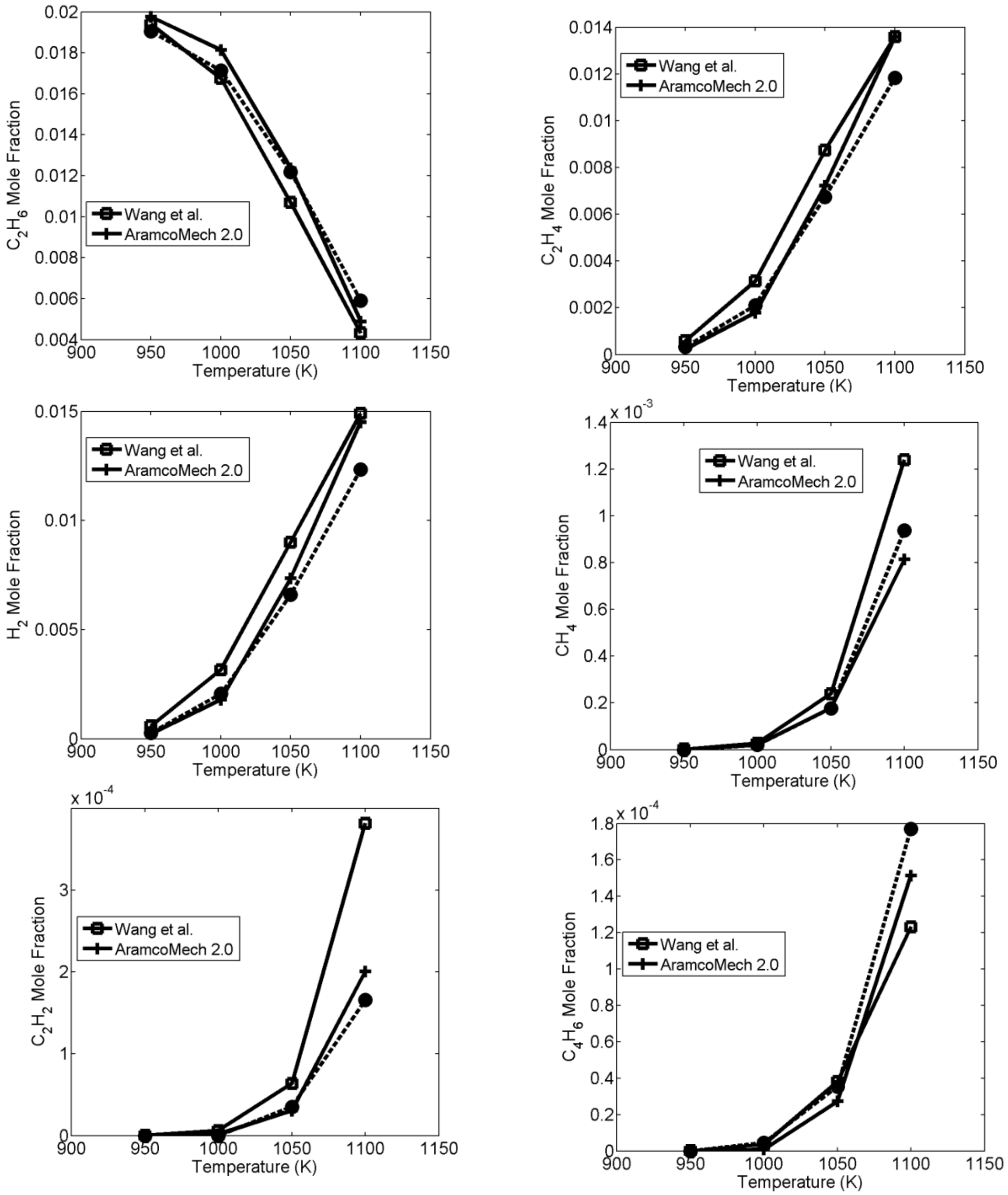

Figure C.3: Comparison of species mole fraction (**major species**) from the current experiments at **p=15 atm** as a function of temperature with two models by Wang et al. [26] and AramcoMech 2.0 [70]. Solid lines/square symbols represent prediction with model by Wang et al., solid lines/plus symbol represent prediction with AramcoMech 2.0 and dashed line/ filled circles represent present experimental results.for inflow species compositions of $X_{C_2H_6} = 0.02$, $X_{N_2} = 0.98$ and residence time ~ 590 ms.

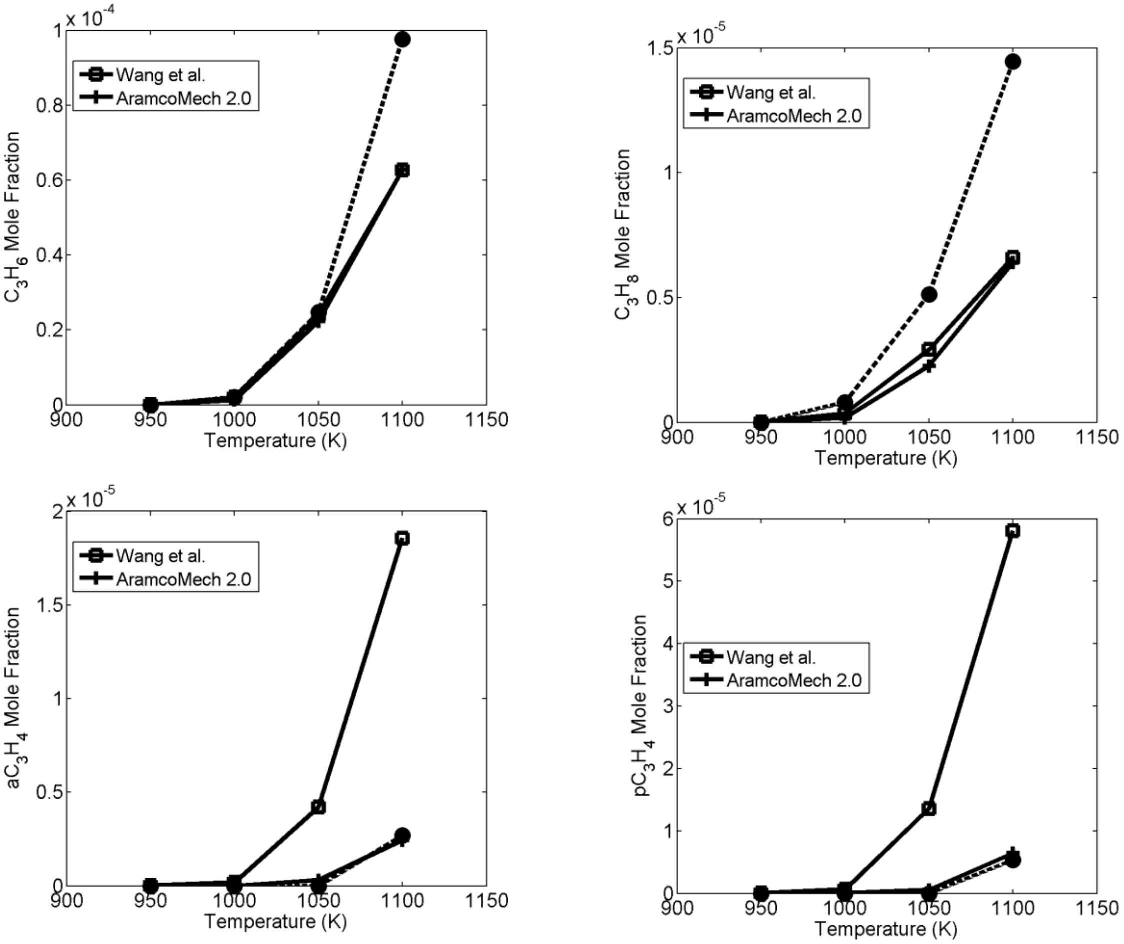

Figure C.4: Comparison of species mole fraction (**minor species**) from the current experiments at **p=15 atm** as a function of temperature with two models by Wang et al. [26] and AramcoMech 2.0 [70]. Solid lines/square symbols represent prediction with model by Wang et al., solid lines/plus symbol represent prediction with AramcoMech 2.0 and dashed line/ filled circles represent present experimental results.for inflow species compositions of X $_{C_2H_6}$ = 0.02, X_{N_2} = 0.98 and residence time ~ 590 ms.

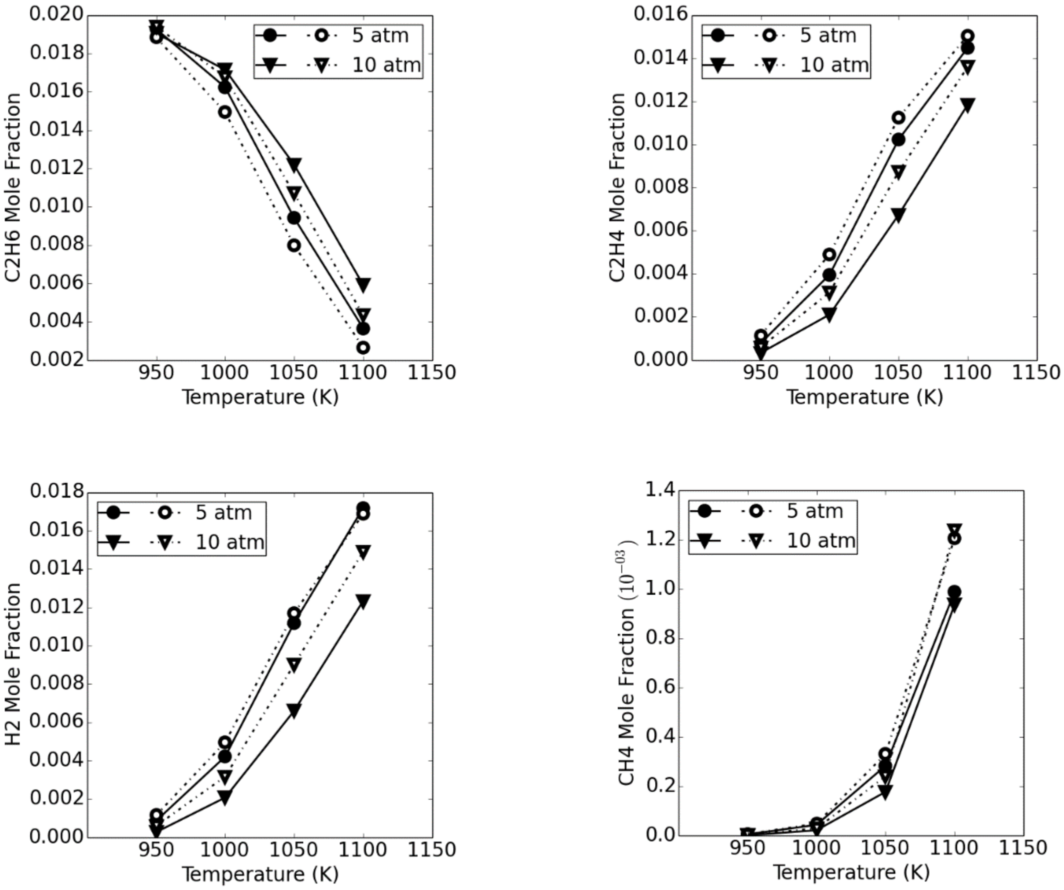

Figure C.5: Comparison of species mole fraction (**major species**) as a function of temperature for residence time ~ 590 ms. Solid line/ filled symbols represent experimental results and dashed line/open symbols represents model prediction by Wang et al. [26], for inflow species compositions of $X_{C_2H_6} = 0.02$, $X_{N_2} = 0.98$ and p = 5 and 15 atm.

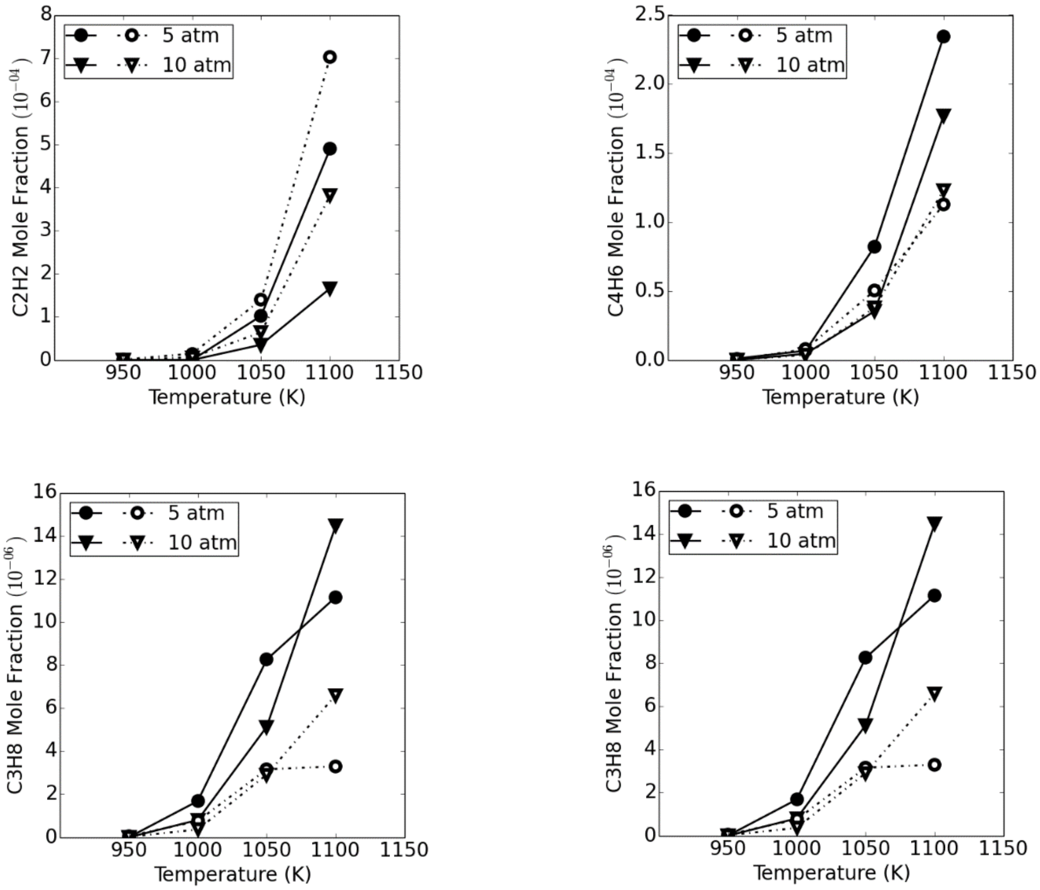

Figure C.6: Comparison of species mole fraction (**minor species**) as a function of temperature for residence time ~ 590 ms. Solid line/ filled symbols represent experimental results and dashed line/open symbols represents model prediction by Wang et al. [26], for inflow species compositions of $X_{C_2H_6}$ = 0.02, X_{N_2} = 0.98 and p = 5 and 15 atm.

Appendix D: n-Dodecane Pyrolysis

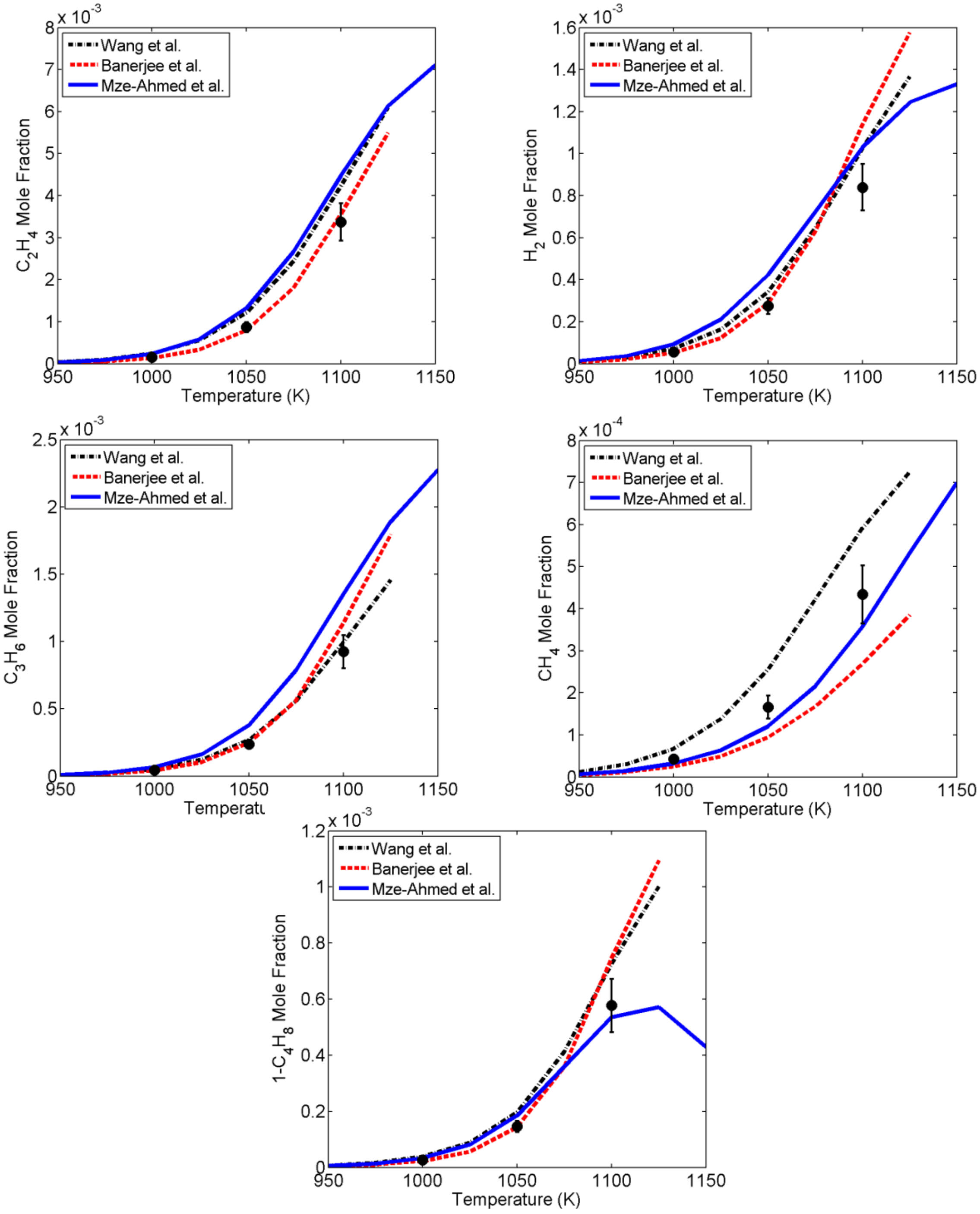

Figure D.1: Comparison of species mole fraction (**major species**) as a function of hot section temperature. Symbols represent experimental results and line represents prediction with three models by Wang et al. [26], Banerjee et al. [41] and Mze-Ahmed et al. [94] for inflow species compositions of $X_{C_{12}H_{26}} = 0.0025$, $X_{N_2} = 0.9975$ and residence time of 10ms.

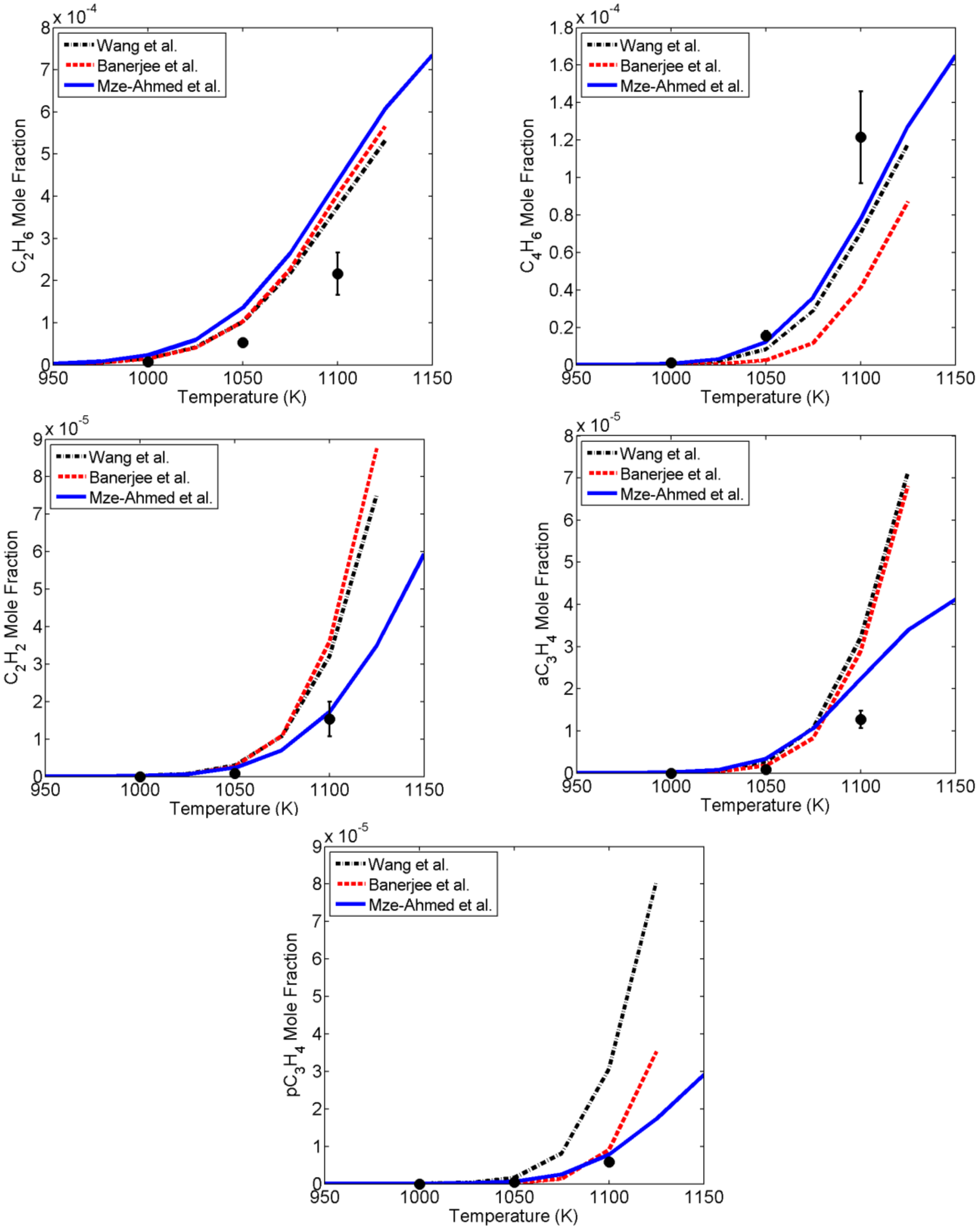

Figure D.2: Comparison of species mole fraction (**minor species**) as a function of hot section temperature. Symbols represent experimental results and line represents prediction with three models by Wang et al. [26], Banerjee et al. [41] and Mze-Ahmed et al. [94] for inflow species compositions of $X_{C_{12}H_{26}} = 0.0025$, $X_{N_2} = 0.9975$ and residence time of 10 ms.